

Advances in Civil Engineering

# Pavement Analysis and Design by Multiphysics

Lead Guest Editor: Xue Luo

Guest Editors: Robert L. Lytton, Yuqing Zhang, Fan Gu, Jinchang Wang,  
and Qiang Tang





---

# **Pavement Analysis and Design by Multiphysics**

Advances in Civil Engineering

---

## **Pavement Analysis and Design by Multiphysics**

Lead Guest Editor: Xue Luo

Guest Editors: Robert L. Lytton, Yuqing Zhang, Fan Gu,  
Jinchang Wang, and Qiang Tang



---

Copyright © 2019 Hindawi. All rights reserved.

This is a special issue published in “Advances in Civil Engineering.” All articles are open access articles distributed under the Creative Commons Attribution License, which permits unrestricted use, distribution, and reproduction in any medium, provided the original work is properly cited.

## Editorial Board

- Khalid Abdel-Rahman, Germany  
José Aguiar, Portugal  
Reza Akhavian, USA  
Maria Cruz Alonso, Spain  
Serji N. Amirkhania, USA  
P. Ch. Anastasopoulos, USA  
Venu G. M. Annamdas, Singapore  
Mehrdad Arashpour, Australia  
Pedro Arias-Sánchez, Spain  
Farhad Aslani, Australia  
Daniele Baraldi, Italy  
Emilio Bastidas-Arteaga, France  
Chiara Bedon, Italy  
Rafik Belarbi, France  
Rafael J. Bergillos, Spain  
Giovanni Biondi, Italy  
Hugo C. Biscaia, Portugal  
Giosuè Boscato, Italy  
Melina Bosco, Italy  
Jorge Branco, Portugal  
Emanuele Brunesi, Italy  
Alberto Campisano, Italy  
Francesco Canestrari, Italy  
Giulio Castori, Italy  
Robert Černý, Czech Republic  
Constantin Chalioris, Greece  
Noel Challamel, France  
Daniel W.M. Chan, Hong Kong  
Edwin H W Chan, Hong Kong  
Carlos Chastre, Portugal  
Ghassan Chehab, Lebanon  
Wensu Chen, Australia  
Nicholas Chileshe, Australia  
Heap-Yih (John) Chong, Australia  
Francesco Colangelo, Italy  
Ottavia Corbi, Italy  
Marco Corradi, Italy  
Mario D'Aniello, Italy  
Jorge de Brito, Portugal  
Gianmarco de Felice, Italy  
Stefano de Miranda, Italy  
Tayfun Dede, Turkey  
Angelo Di Egidio, Italy  
Luigi Di Sarno, Italy
- Giulio Dondi, Italy  
Mohamed ElGawady, USA  
Ahmed Elghazouli, UK  
Behzad Esmaeili, USA  
Flora Faleschini, Italy  
Harry Far, Australia  
Antonio Formisano, Italy  
Giovanni Garcea, Italy  
Emilio García-Taengua, UK  
Elhem Ghorbel, France  
Agathoklis Giaralis, UK  
Rodrigo Gonçalves, Portugal  
Arturo Gonzalez, Ireland  
Belén González-Fonteboa, Spain  
Salvatore Grasso, Italy  
Fan Gu, UK  
Kirk Hatfield, USA  
Khandaker Hossain, Canada  
Zahid Hossain, USA  
M. R. Hosseini, Australia  
Bon-Gang Hwang, Singapore  
Dong-Sheng Jeng, Australia  
Jian Ji, China  
Andreas Lampropoulos, UK  
Raffaele Landolfo, Italy  
Eul-Bum Lee, Republic of Korea  
Chun-Qing Li, Australia  
Dongsheng Li, China  
Li Li, Canada  
Xuemei Liu, Australia  
Zaobao Liu, China  
Davide Lo Presti, UK  
Cristiano Loss, Canada  
Sui Pheng Low, Singapore  
Lyan-Ywan Lu, Taiwan  
Eric Lui, USA  
Zhongguo John Ma, USA  
Lorenzo Macorini, UK  
Yann Malecot, France  
John Mander, USA  
Giuseppe Carlo Marano, Italy  
Fabio Mazza, Italy  
Claudio Mazzotti, Italy  
Ahmed Mebarki, France
- Shazim A. Memon, Kazakhstan  
Giovanni Minafò, Italy  
Hossein Moayedi, Iran  
Abbas Mohajerani, Australia  
Fabrizio Mollaioli, Italy  
Rosario Montuori, Italy  
Ayman S. Mosallam, USA  
Roberto Nascimbene, Italy  
Luís C. Neves, UK  
Trung Ngo, Australia  
Sanjay Nimbalkar, Australia  
Giuseppe Oliveto, Italy  
Alejandro Orfila, Spain  
Togay Ozbakkaloglu, Australia  
Hayri Baytan Ozmen, Turkey  
Alessandro Palmeri, UK  
Fabrizio Paolacci, Italy  
Fulvio Parisi, Italy  
Ignacio Paya-Zaforteza, Spain  
Arnaud Perrot, France  
Christophe Petit, France  
Giuseppe Piccardo, Italy  
Prodromos Psarropoulos, Greece  
Giuseppe Quaranta, Italy  
Carlo Rainieri, Italy  
Damien Rangaard, France  
Dimitris Rizos, USA  
Geoffrey W. Rodgers, New Zealand  
Hugo Rodrigues, Portugal  
Hamid Reza Ronagh, Australia  
Pier Paolo Rossi, Italy  
Lukasz Sadowski, Poland  
Anna Saetta, Italy  
Timo Saksala, Finland  
Evangelos J. Sapountzakis, Greece  
Vasilis Sarhosis, UK  
Halil Sezen, USA  
M. Shahria Alam, Canada  
Faiz U.A. Shaikh, Australia  
Mostafa Sharifzadeh, Australia  
Sanjay Kumar Shukla, Australia  
Amir Si Larbi, France  
Stefano Sorace, Italy  
Flavio Stochino, Italy



---

Claudio Tamagnini, Italy  
Yaya Tan, China  
Patrick W.C. Tang, Australia  
Yinshan Tang, UK  
Huu-Tai Thai, Australia  
Filippo Ubertini, Italy  
Humberto Varum, Portugal  
Castorina S. Vieira, Portugal  
C. Vipulanandan, USA  
Claudia Vitone, Italy  
Hao Wang, USA

Lei Wang, USA  
Linbing Wang, USA  
Wayne Yu Wang, UK  
Roman Wan-Wendner, Austria  
Bo Xia, Australia  
Wei-Chau Xie, Canada  
Michael Yam, Hong Kong  
Libo Yan, Germany  
Jian Yang, China  
Xu Yang, Australia  
Hui Yao, China

Victor Yepes, Spain  
Gürol Yildirim, Turkey  
Qingliang Yu, Netherlands  
Mariano Angelo Zanini, Italy  
Xiong Zhang, USA  
Yuqing Zhang, UK  
Dong Zhao, USA  
Xianbo Zhao, Australia  
Annan Zhou, Australia  
Abdul Aziz bin Abdul Samad, Malaysia

# Contents

## **Pavement Analysis and Design by Multiphysics**

Xue Luo , Robert L. Lytton, Yuqing Zhang , Fan Gu , Jinchang Wang , and Qiang Tang   
Editorial (2 pages), Article ID 3024138, Volume 2019 (2019)

## **A Synthesis of Computational and Experimental Approaches of Evaluating Chemical, Physical, and Mechanistic Properties of Asphalt Binders**

Kamal Hossain  and Zahid Hossain  
Review Article (20 pages), Article ID 1795958, Volume 2019 (2019)

## **Mechanical Evaluation of Bottom Ash from Municipal Solid Waste Incineration Used in Roadbase**

Qiang Tang , Fan Gu , Hui Chen, Cong Lu, and Yu Zhang  
Research Article (8 pages), Article ID 5694908, Volume 2018 (2019)

## **Exploration of Mechanisms of Joint Deterioration in Concrete Pavements regarding Interfacial Transition Zone**

Xin Wang, Jiake Zhang , Xuhao Wang , Peter Taylor, Kejin Wang, and Xinjian Sun  
Research Article (9 pages), Article ID 3295954, Volume 2018 (2019)

## **The State-of-the-Art Review on Molecular Dynamics Simulation of Asphalt Binder**

Xin Qu, Dawei Wang , Linbing Wang , Yucheng Huang , Yue Hou , and Markus Oeser  
Review Article (14 pages), Article ID 4546191, Volume 2018 (2019)

## **Moisture Susceptibility of Sustainable Warm Mix Asphalt**

Amjad H. Albayati , Hasan M. Al-Mosawe, Abbas A. Allawi , and Nazar Oukaili  
Research Article (9 pages), Article ID 3109435, Volume 2018 (2019)

## **Investigation of Thermal Cooling Effectiveness of RRVCs for Permafrost Protection under Wide Expressway Embankment**

Tao Tang , Tao Ma , Xiaoming Huang , Qiuming Xiao , Hao Wang, and Guangji Xu  
Research Article (11 pages), Article ID 2196459, Volume 2018 (2019)

## **Measurement of Degree of Compaction of Fine-Grained Soil Subgrade Using Light Dynamic Penetrometer**

Junhui Zhang , Yongsheng Yao , Jianlong Zheng, Xiangqun Huang, and Tian Lan  
Research Article (8 pages), Article ID 1364868, Volume 2018 (2019)

## **Investigating the Pavement Vibration Response for Roadway Service Condition Evaluation**

Zhoujing Ye , Yang Lu , and Linbing Wang   
Research Article (14 pages), Article ID 2714657, Volume 2018 (2019)

## **Estimation of Soil-Water Characteristic Curve for Cohesive Soils with Methylene Blue Value**

Junhui Zhang , Junhui Peng , Yejuan Chen, Jue Li, and Feng Li  
Research Article (7 pages), Article ID 9213674, Volume 2018 (2019)

## **Application of the Bipotential Theory to a Nonassociated Drucker–Prager Model**

Yang-Jing Zhou, Zhi-Qiang Feng , Juan Antonio Rojas Quintero, Jian-Bo Zhou, and Hui-Jian Chen  
Research Article (11 pages), Article ID 4534750, Volume 2018 (2019)

**Pavement Analysis and Design by Multiphysics Reconstructing Algorithm for the Virtual Asphalt Mixture Based on the Discrete-Element Method**

Danhua Wang, Xunhao Ding , Tao Ma , Weiguang Zhang, and Deyu Zhang

Research Article (11 pages), Article ID 5180562, Volume 2018 (2019)

**An Equal-Strain Analytical Solution for the Radial Consolidation of Unsaturated Soils by Vertical Drains considering Drain Resistance**

Feng Zhou , Zheng Chen , and Xudong Wang

Research Article (9 pages), Article ID 5069159, Volume 2018 (2019)

**Study on Relaxation Damage Properties of High Viscosity Asphalt Sand under Uniaxial Compression**

Yazhen Sun, Zhangyi Gu, Jinchang Wang, Chenze Fang , and Xuezhong Yuan 

Research Article (12 pages), Article ID 1498480, Volume 2018 (2019)

**A Study on Dynamic Amplification Factor and Structure Parameter of Bridge Deck Pavement Based on Bridge Deck Pavement Roughness**

Fei Han , Dan-hui Dan , and Hu Wang

Research Article (8 pages), Article ID 9810461, Volume 2018 (2019)

## Editorial

# Pavement Analysis and Design by Multiphysics

**Xue Luo** <sup>1</sup>, **Robert L. Lytton**,<sup>2</sup> **Yuqing Zhang** <sup>3</sup>, **Fan Gu** <sup>4</sup>, **Jinchang Wang** <sup>1</sup>,  
and **Qiang Tang** <sup>5</sup>

<sup>1</sup>Zhejiang University, Hangzhou, China

<sup>2</sup>Texas A&M University, College Station, TX, USA

<sup>3</sup>Aston University, Birmingham, UK

<sup>4</sup>National Center for Asphalt Technology, Auburn, AL, USA

<sup>5</sup>Soochow University, Suzhou, China

Correspondence should be addressed to Xue Luo; xueluo@tamu.edu

Received 23 October 2018; Accepted 23 October 2018; Published 28 February 2019

Copyright © 2019 Xue Luo et al. This is an open access article distributed under the Creative Commons Attribution License, which permits unrestricted use, distribution, and reproduction in any medium, provided the original work is properly cited.

Reliable and sustainable pavement infrastructure is critical for present economic and environmental challenges. The complexity of pavement analysis and design stems from diverse pavement materials, heavy traffic, and changing climate. The reliability of a pavement design depends on the extent of representation of this complexity in the prediction of various forms of distress that limit the effective service life of the pavement. The pavement materials need to be treated as they actually are, and the analysis should take into account the actual coupled behaviors of materials, structures, traffic, and environmental conditions.

From a physical point of view, prediction of pavement performance is a multiphysics problem. Questions still remain about appropriate representation and characterization of each physical process and integration of multiple physical processes to predict pavement material deterioration and structural distresses as an analysis and design platform.

Thus, this special issue provides a collection of presentation and discussion of applications of multiphysical concepts and approaches to characterize pavement materials and predict pavement responses as well as performance. It includes a variety of pavement materials such as asphalt, concrete, soils, and recycled materials.

A. H. Albayati et al. discussed the application of the recycled concrete aggregate in warm mix asphalt and how to improve the moisture susceptibility of the mixture. The replacement of the original aggregates with the recycled concrete aggregate had shown a significant improvement in moisture susceptibility. A paper by K. Hossain and Z. Hossain provides a synthesis of computational and experimental approaches to

characterize chemical, physical, and mechanical properties for asphalt binders. A paper by D. Wang et al. presents an algorithm to construct virtual asphalt mixtures using the discrete element method and predicts the mechanical responses of the mixture. Y. Sun et al. conducted laboratory investigations of relaxation damage properties of high-viscosity asphalt sand and used the modified generalized Maxwell model to simulate coupled viscoelasticity and damage. The results showed that the proposed approach could effectively predict the relaxation damage process and provide a theoretical support for crack control of asphalt pavements. A review paper by X. Qu et al. presents a comprehensive view of the development, establishment, and application of molecular dynamics to simulate the behaviors of asphalt materials.

A paper by J. Zhang et al. presents a method to measure and predict the degree of compaction of fine-grained subgrade using a light dynamic penetrometer. A prediction equation was developed that contained the penetration ratio and the numerically calculated water content of subgrade. J. Zhang et al. developed a method to estimate the soil water characteristic curve of cohesive soils using a simple test with methylene blue. A paper by F. Zhou et al. presents an equal-strain model for the radial consolidation of unsaturated soils by vertical drains. The solutions were verified, and parametric studies regarding the drain resistance effect were graphically presented. T. Tang et al. investigated the thermal cooling effects of reflective-resistant-ventilated coupling structure in permafrost zones. It was recommended that such a structure could be used as a protective measure to improve the thermal stability of wide embankment.

Q. Tang et al. investigated the possibility of using bottom ash from the incineration of municipal solid waste as partial aggregate alternative. The laboratory test results indicated that bottom ash is suitable to be used as road base materials. X. Wang et al. studied the mechanisms of premature deterioration of concrete at joints in cold weather regions and carried out experimental work to verify the hypothesis. It was found that interfacial transition zone could be the weak point for cracking. Y. Zhou et al. applied the bipotential theory to the Drucker–Prager model and proposed dual constitutive cones with five forms of the bipotential function. The accuracy and stability of the developed algorithm was verified for civil engineering applications.

F. Han et al. studied the dynamic amplification factor due to surface roughness of bridge deck pavements. The roughness of the bridge deck pavement and the vehicle speed are two main factors that affect the dynamic amplification factor, which is closely related to driving comfortableness and service life of deck pavement. A paper by Z. Ye et al. presents a numerical model to analyze pavement vibration due to the dynamic load of passing vehicles. The vibration signals reflected the level of road roughness, the stiffness of the pavement materials, and the integrity of pavement structure, which could provide recommendations for early warning and timely maintenance of pavements.

### **Conflicts of Interest**

The editors declare that there are no conflicts of interest regarding the publication of this special issue.

*Xue Luo*  
*Robert L. Lytton*  
*Yuqing Zhang*  
*Fan Gu*  
*Jinchang Wang*  
*Qiang Tang*

## Review Article

# A Synthesis of Computational and Experimental Approaches of Evaluating Chemical, Physical, and Mechanistic Properties of Asphalt Binders

Kamal Hossain <sup>1</sup> and Zahid Hossain<sup>2</sup>

<sup>1</sup>Department of Civil and Environmental Engineering, University of Illinois at Urbana-Champaign, Urbana, IL, USA

<sup>2</sup>Department of Civil and Environmental Engineering, Arkansas State University, Jonesboro, AR, USA

Correspondence should be addressed to Kamal Hossain; [kamalh@mun.ca](mailto:kamalh@mun.ca)

Received 6 February 2018; Revised 10 May 2018; Accepted 4 June 2018; Published 3 February 2019

Academic Editor: Yuqing Zhang

Copyright © 2019 Kamal Hossain and Zahid Hossain. This is an open access article distributed under the Creative Commons Attribution License, which permits unrestricted use, distribution, and reproduction in any medium, provided the original work is properly cited.

Asphalt binder is a very complex chemical compound. Much work has been done to understand and model its chemical, morphological, rheological, and mechanical features. This paper synthesizes and presents findings from pertinent studies available in the public domain. Understanding of asphalt characteristics at the very finite level is the first critical step to develop a better macroscopic- or pavement-level performance model. This paper showcases a summary of current knowledge gained on (a) how chemical elemental compositions and molecular groups play critical roles in asphalt binder's performance in pavement composites; (b) morphological properties and their relationships with the asphalt's structural performance; and (c) mechanistic characteristics of asphalt binder's at nanoscopic, mesoscopic, and microscopic levels, and how they are related to macroscopic- or pavement-level performance.

## 1. Introduction

About 96% of paved roads in the U.S. are made of asphalt [1]. Most of these roads were built during and immediately after the Second World War. They demand major rehabilitation or reconstruction services. The most expensive element in asphalt pavement is the asphalt binder. Government agencies not only in the U.S. but also around the world spend significant resources to develop a total design package that can result in a longer lasting pavement and be economic to build and maintain. In the recent decades, a common practice that many agencies adopted to reduce expenditure is recycling of existing old pavements by reducing the amount of new asphalt binder. Asphalt researchers have expressed their concerns to this strategy because the use of high-grade asphalt binder from existing asphalt pavements can have detrimental effects on the longevity of the new pavement. Valid reasons for this concern are the blending and performance issues of the aged binder, which comes from old or aged pavements.

Asphalt is also a very complex nonlinear chemical material [2]. It is complex because of its highly variable

chemical constituents that change with source, process of extraction, temperature, ambient environment, and elapsed time. To better understand asphalt binder's behavior, a significant number of chemistry-based researches have been conducted in Europe and North America. In the late 1980s and early 1990s, Jennings et al. [3, 4] initiated chemical studies of asphalt binders and proposed average molecular structures for them. The ultimate goal of these research studies is to develop multiscale pavement models. The developed models should link and communicate the performance of the constituent materials among different scales (nano-, micro-, meso-, and macroscale/pavement). Pavement model features such as stiffness, rutting, and cracking performance should be found on the enhanced understanding from the finite level possible for each constituent and for all phases [5]. With the advent of new technologies, capturing of rich information of materials at micro- or nanoscale levels has become easy in the recent time, and it has successfully been utilized in other natural science and engineering disciplines. Asphalt researchers have also recently advanced knowledge related to binder

performance at much needed microscopic level, which is more important than meso- or macroscale [6–8]. Based on findings of the existing literature, it is clear that the behavior of asphalt pavement materials depends highly on their microstructure. For instance, cracks and voids at the microstructure level can eventually lead to failures of the material under loads [9]. Thus, understanding the deterioration process and improving the materials at the microstructure level can help in constructing longer lasting pavement. A better understanding of microstructure of asphalt binders is also expected to help researchers to develop better models for predicting pavement performance.

The main goal of this study is to synthesize the understanding of asphalt binder at microscopic level. To accomplish the aforementioned goal, a thorough review of pertinent literature has been conducted and presented in a coherent format. This paper is organized in multiple sections. As seen here, the current section provides an introduction to the topic. The second section presents a summary of understanding of chemical constituents and chemical models of asphalt binder. The third section discusses the morphological models and how these models correlate with chemical models. The fourth section presents the mechanistic models and their relationship with macroscopic or pavement models. Finally, the concluding section presents an overall development in the topic and gives a future research direction.

## 2. Chemical Models of Asphalt

A very rich amount of information is available in the literature on the chemistry of asphalt. The information includes the types and percentages of elemental constituents, molecular groups and structures, and polarity and non-polarity behaviors of the molecules. These chemical properties govern the performance of asphalt. One behavior of asphalt that is very interesting to researchers and pavement professionals is viscoelasticity; at high temperature, asphalt is a viscous liquid, and at low temperature, it behaves like an elastic solid and becomes fragile. Chemical properties of an asphalt binder are also highly depended on the sources and processes employed.

*2.1. Functional Groups and Chemical Families.* Many chemistry-based techniques such as elemental analysis, Fourier transform infrared (FTIR) spectroscopy, gel permeation chromatography (GPC), thin layer chromatography (TLC), and high-performance liquid chromatography (HPLC) are commonly used in chemical characterizations of asphalt binders. For instance, as part of a comprehensive study of multiscale modeling, Stangl et al. [5] performed elemental analysis of an asphalt sample following the ASTM D5291-02 method, and some of the results are presented in Table 1. As indicated earlier, the chemical compositions of asphalt vary with the source of asphalt, processes adopted to manufacture it, analytic techniques utilized in elemental analysis, and chemical solvents and adsorbents used to obtain the compositional information. However, the

variability among dominating elements such as carbon, hydrogen, and oxygen is less observed than that of foreign elements such as vanadium, nitrogen, and sulphur, as presented in Table 1. At a molecular level, researchers have proposed various structural models of asphalt. Such a structure for the strategic highway research program's asphalt sample (AAD-1 also known as California Coastal AAD-1) is presented in Figure 1, where a long chain of hydrocarbon along with some other chemical elements such as nitrogen and sulphur is modeled.

In the real world, asphalt binder interacts with a large number of environmental and mechanical factors such as oxygen, heat radiation, UV radiation, moisture, and traffic factor. These factors often act in a conjoint environment that affects the asphalt at the compositional, molecular, and macro levels. The consequential performance due to changes in chemical compositions and molecular structures should be taken in consideration when using the binder in a new pavement construction.

*2.1.1. Molecular Groups of Asphalt.* At molecular level, asphalt can be considered a complex organic compound consisting of groups of different molecules. Based on the size and polarity, they can be grouped as saturate, aromatic, resin, and asphaltene (often called SARA). Together they form a colloidal system—where asphaltene is a relatively stiffer and disperse domain, and later, three form a liquid substance that holds the asphaltene. The later three compositions are also called maltene. There have been many methods employed to better understand the characteristics of these fractionates and to quantify their share in asphalt. A rapid and inexpensive characterization method is thin-layer chromatography (TLC). This technique separates asphalt fractionates by some organic solvents. For example, asphaltene is precipitable by n-heptane where maltene dissolves, saturate by cyclohexane, aromatic by dichloromethane, and finally, resin by methanol or isopropanol [11, 12]. In this test process, a mobility parameter ( $R_f$ ) for the fractionate is determined using a model, as shown in equation (1). Table 2 presents the approximate  $R_f$  value for four fractionates. However,  $R_f$  from one lab testing may not match with that of another since this parameter is also dependent on the sample size (thickness and diameter), solvent type, and so on, which are used in the characterization process. To obtain the SARA information, another method the so-called Iatroscan method that combines thin-layer chromatography and flame ionization is also employed frequently.

$$R_f = \frac{D_s}{D_m}, \quad (1)$$

where  $R_f$  = mobility parameter of the asphalt fraction,  $D_s$  = distance moved from point of application by solute, and  $D_m$  = distance moved from point of application by mobile size.

Technology has also made possible to physically visualize these fractionates. When a maltene fractionate is irradiated by an UV ray with an appropriate wavelength, a chromatograph of maltene can be obtained, as shown in

TABLE 1: Asphalt chemical constituents and their share. The table is reproduced from Stangl et al. [5] (under the creative commons attribution license/public domain).

Asphalt state	Chemical constituents (mass %)					
	Carbon	Hydrogen	Oxygen	Nitrogen	Sulphur	Total
Neat asphalt (British specification B50/70)	83.90	10.40	<0.1	0.40	5.00	99.70
After RTFO	83.80	10.40	<0.1	0.40	5.00	99.60
After RTFO + PAV	83.70	10.50	<0.1	0.50	4.90	99.60

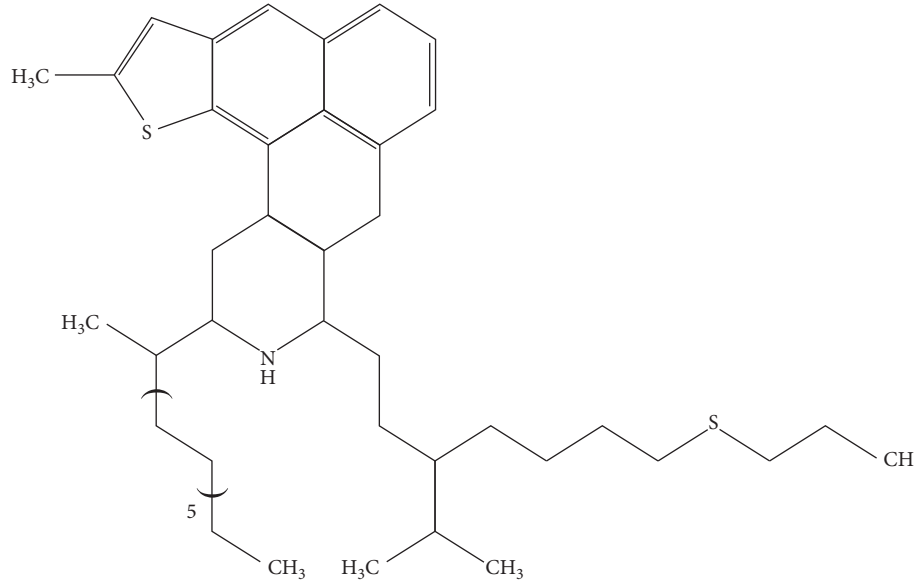


FIGURE 1: Average structure of California Coastal (aad-1) asphalt molecules. The figure is obtained from Lesueur [10] (under the creative commons attribution license/public domain).

TABLE 2:  $R_f$  value for asphalt fractions.

Asphalt fractions	$R_f$ value
Asphaltene	0.20–0.21
Resin	0.45–0.47
Saturate	0.90–0.92
Aromatic (mono, di, or poly)	0.68–0.83

Figure 2(a). Physically, saturate (S) has yellowish color, and the color of aromatics (A) ranges from light yellow to light reddish based on polarity of the molecules, and finally resin (R) appeared as dark black color [14]. Figure 2(b) shows the Yen–Mullins model of asphaltene (AS). This model specifies that asphaltene can be present in bituminous materials as an isolated molecule or as a colony of six to eight molecules or clusters of about eight molecules. Figure 3 displays how a vital engineering property (in this case, viscosity) varies with SARA fractionates of an asphalt sample collected from California Valley. In a related study, Hofko [16] reported that among SARA fractionates, the asphaltene fractionate significantly influences the viscoelastic behavior of asphalt. Therefore, understanding of these fractionates in regard to chemical formation, behavioral characteristics, and, more importantly, engineering properties such as stiffness, creep, and viscoelasticity are critical and can be utilized to develop a model at microscale and thereafter to the full pavement model.

### 3. Morphological Models of Asphalt

3.1. Overview. Morphological studies deal with understanding of structural form of a matter, and they attempt to link the formation of the matter to its structural performance. To have a better understanding of morphology of a matter at microscale, a superior technology is needed. With the advent of new micro- and nanoscopic technologies, pavement researchers around the world added a rich amount of information on the body of knowledge in last two decades. Technologies used by researchers included, but not limited to, scanning electron microscope (SEM), fluorescence microscope, atomic force microscope (AFM), transmission electron microscope (TEM), and environmental scanning electron microscope (ESEM) with various advance engineering fixtures at different capacities. As previously mentioned, researchers now have been trying to connect this morphological information of asphalt binder to better predict the pavement performance over its design life.

In recent years, researchers predominately used AFM and SEM techniques. The AFM has some advantages and disadvantages over the SEM and vice versa. The AFM can provide three-dimensional morphological images of a binder sample, whereas the SEM provides two-dimensional images. The AFM sample preparation does not require a sputtering sample coating, which is required in SEM

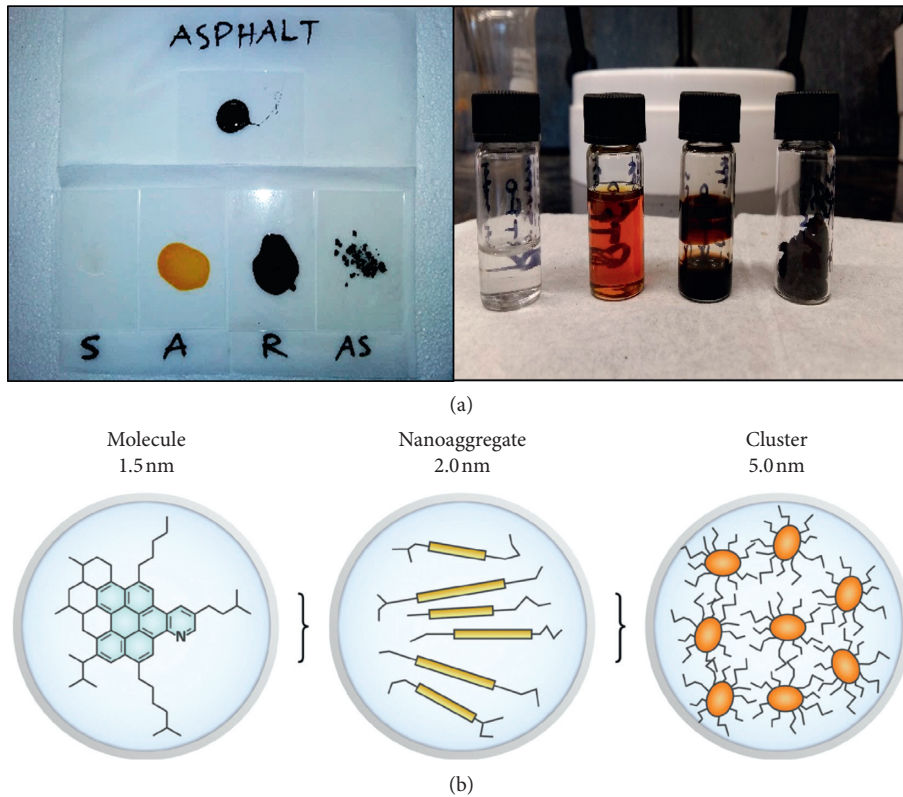


FIGURE 2: (a) Maltene (S = saturate, A = aromatic, R = resin), and (b) asphaltene (AS). The figure is reproduced from Mullins et al. (under the creative commons attribution license/public domain) [13].

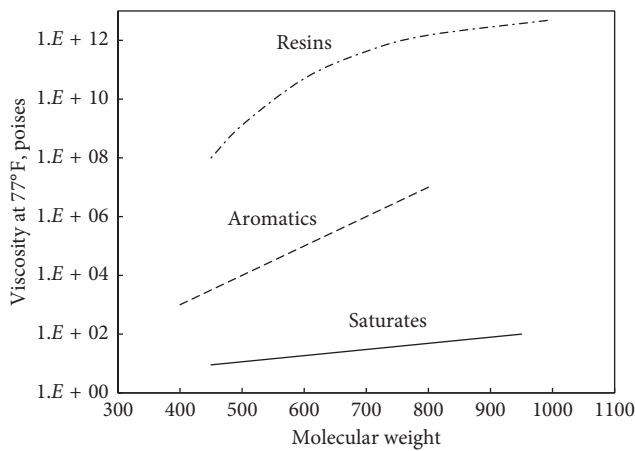


FIGURE 3: Changes in viscosity for different asphalt fractions under different molecular weights. The left figure is obtained from Griffin et al. (under the creative commons attribution license/public domain) [15].

analyses. A comparative advantage of the SEM is that it can image a large area (on the order of square millimeters), whereas the AFM can only image a maximum scanning area of about  $150 \times 150$  micrometers. Furthermore, the scan rate of an AFM is relatively lower than that of an SEM. Figure 4 shows microscopic views of an asphalt sample under fluorescence [17] and atomic force microscopes. A pioneer study on asphalt morphology is conducted by Loeber et al. [18]. From inspecting these microscopic

images, one can easily see that there is a circular kind of particles in a matrix system. The particles are of different sizes and are randomly placed within a couple of micrometers. Interestingly, these particles are available in both images obtained from two different microscopes that completely utilize different techniques; however, they still presented similar results in terms of sizes for the particles, orientation, and matrix design. For brevity, the current study is not focusing the techniques behind the different microscopes. Many studies also investigated the pattern, thickness, resistance force, deformation, stiffness, and other engineering properties of this circular domain in asphalt material, and that will be discussed in the following sections.

**3.2. Analysis of Morphological Phases of Asphalt.** It is generally believed that asphalt has three morphological phases (also called microdomains): a disperse phase, a relatively larger phase than disperse phase surrounding to the disperse phase, and finally a continuous phase. A better understanding of the engineering properties of these morphological phases of asphalt is expected to help scientists to develop better models for predicting pavement performance [19–22]. In a recent study, Pauli et al. [20] reported how the morphological phases affect microstructure of asphalt and how some external variables inherited to microstructure influence the morphology. Figure 5 shows images obtained through an AFM,

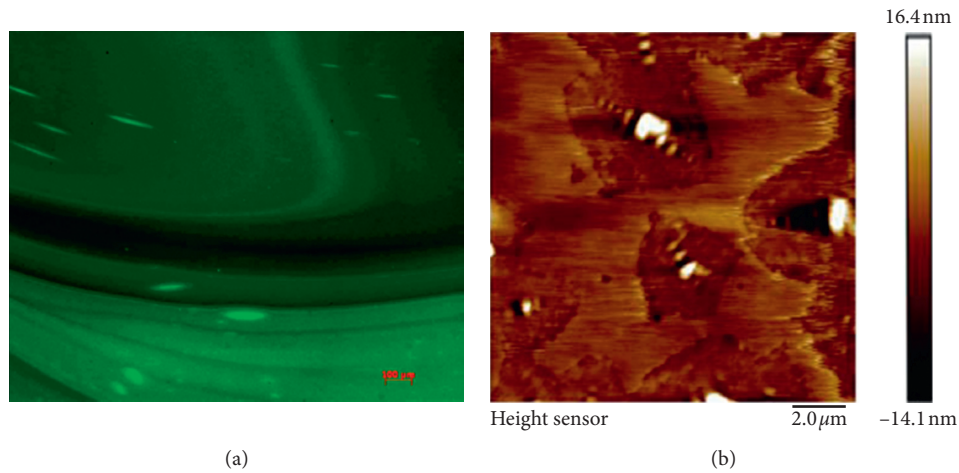


FIGURE 4: Asphalt sample view obtained from a fluorescence microscope on the left and an atomic force microscope on the right. The left figure is obtained from Kraus [17] (under the creative commons attribution license/public domain).

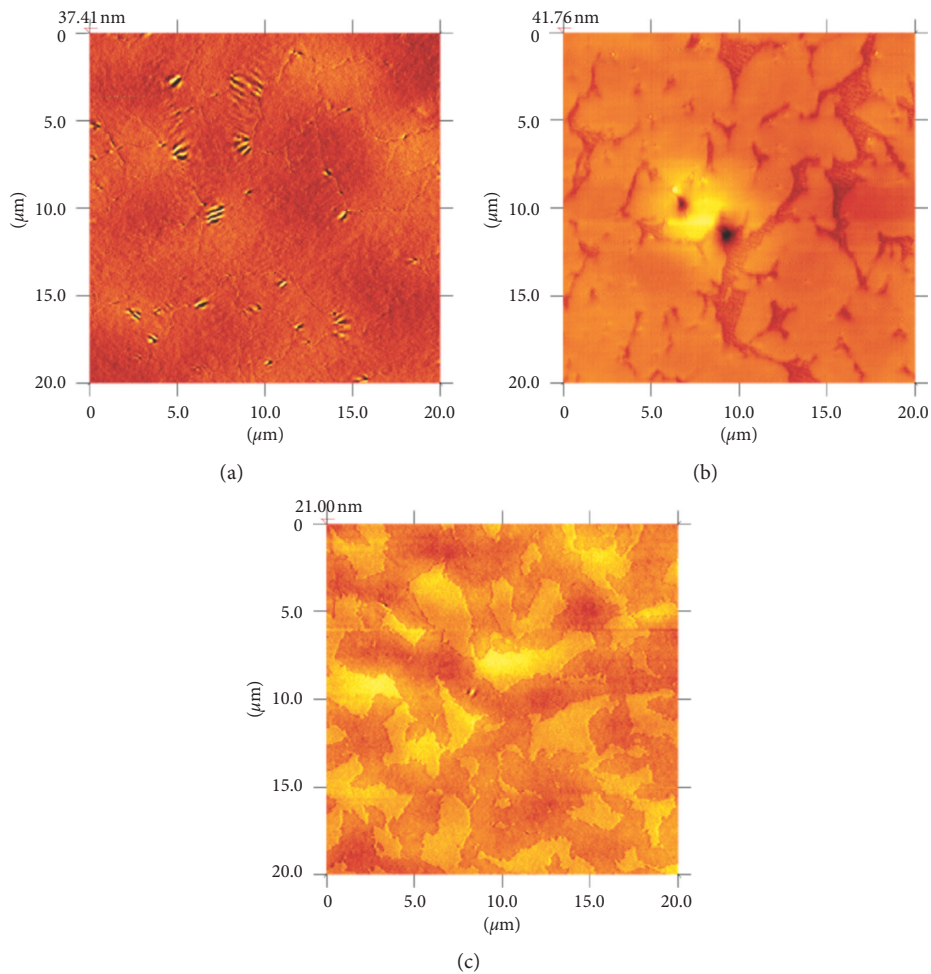


FIGURE 5: Images of asphalt morphology (AAK-1 sample, size  $20\ \mu\text{m} \times 20\ \mu\text{m}$ ) of film thickness of 1600 nm (a), 1000 nm (b), and 600 nm (c). The figure is obtained from Pauli [23] (under the creative commons attribution license/public domain).

and it displays changes in morphological phases as a function of asphalt film thickness [23]. It can be seen that the disperse domain significantly varies as the sample thickness changes; the thinner the sample is, the lesser the presence of

disperse domain is. However, some studies also concluded otherwise that the microstructure is independent of asphalt film thickness. Therefore, further research is needed to clarify this issue.

The disperse phase in the asphalt microstructure is considered as a “bee”-like structure with ridges and valleys within this phase. A bird’s eye view of an AFM specimen of  $15\ \mu\text{m} \times 15\ \mu\text{m}$  can be seen in Figure 6(a), and details of this bee structure are presented in Figure 6(b), where the depth and spacing of valleys and ridge scan can be observed.

Some studies [25] named these three phases differently. The central part (disperse) within each highlighted area is also called the catana phase (so-called, bee), immediately around the catana phase is called the interstitial/periphase, and both of these phases are suspended from another phase called the perpetua phase or matrix (Figure 7). It has been reported that periphase and perpetua phase change with temperature; as the temperature increases, these phases interconvert from one to another, which has been observed in differential scanning calorimetry study by Soenen [26].

A few studies initially assumed a link on the relationship between the catana phase and asphaltene [18]. However, later other studies found this relationship is not statistically significant, while there is a highly plausible evidence that the catana phase is highly related to the presence of metal elements (e.g., nickel and iron) in the asphalt [24].

Menapace et al. [27] has investigated on the growth and height of the catana phase, and the study found that both are affected by the testing temperature in an AFM investigation. Table 3 presents that in general, the average diameter of bee structure increased as temperature increased for selected types of asphalt tested, and the same trend can be noticed for the area covered by the bee structure phase for one asphalt grade (PG 76-22), whereas a mix result was observed for another asphalt grade (Pen 60/70). The increased size of “bee structure” could be due to the disintegration of bees due to increased temperatures. Allen et al. reported that the dispersed phase (i.e., bee) increased as saturate fractionate in the asphalt increased [28]. The dispersed phase can completely change when a virgin asphalt is mixed with aged asphalt binder from either recycled asphalt pavement or roof shingles; microparticles found in the interfacial zone ranged from 160 nm to  $2.07\ \mu\text{m}$  by recent multiple studies [29, 30], as presented in Figure 8 [31].

All these research results suggest that asphalt binder has complex phases, which are influenced by many experimental and environmental factors. However, if we can obtain generalized information on these phases and if they are based on good amount of data, a link can ultimately be developed between microcharacteristic and macrolevel pavement performance.

Soenen et al. [25] reported that morphologies of the asphalt sample are highly influenced by the temperature employed to prepare the sample, the elapsed time in that temperature after isothermal condition reached, and other experimental factors. Surface morphologies changed in terms of network structural forms and sizes between the samples when tested at an isothermal condition for different temperatures (Figure 9). Perhaps, this is why, asphalt binder’s rheological performance changes due to thermal aging.

*3.3. Effect of Aging, Additives, and Rejuvenators on Asphalt Morphology.* When asphalt is utilized in real-world applications (e.g., pavement), it experiences a very complex environment throughout its life. Some major chemical compounds or environmental factors that asphalt interacts with are atmospheric oxygen, dissolved oxygen, UV radiation, and other hundreds of known and unknown solid, liquid, and gaseous compounds. As a consequence of the interactions between asphalt and surrounding chemical compounds, asphalt loses its some vital rheological properties over time, which is termed as aging of asphalt. Many researches have been conducted to mimic the aging processes in laboratories, to model field aging and finally to deter aging by using additives such as polymers and rejuvenators. Two aging processes for asphalt binder are commonly employed in laboratory testing: one is the rolling thin-film oven test (RTFOT) process to simulate preservice aging and other is the pressurized aging vessel (PAV) process that simulates in-service aging.

Figure 10 shows that the catana phase is very dominant in an aged sample than that of an unaged sample, indicating significant differences in the phase angle (i.e., higher changes in elevation) between disperse domain (catana) and continuous matrix (peri and perpetua). Moreover, the percentage of area covered by disperse domain reduces significantly with the PAV process compared to the RTFOT aging. To better understand the engineering properties of these phases for “before” and “after” aging conditions, Allen et al. [32] conducted a comprehensive research study on the subject matter and developed an improved technique to obtain microrheological property of the phases such as creep information of asphalt fraction morphologies. This study reported that the creep was affected by the aging and can be noticed in Figure 11. The asphalt binder sample shown in Figure 11 is a SHRP’s AAD sample. In this figure, Phases 1, 2, and 3 refer to catana, peri, and perpetua phases, respectively.

In Brazil, Rebelo et al. [34] recently investigated on how RTFOT and PAV processes affect the morphologies of asphalt using an atomic force microscope. These researchers reported that there was no catana phase observed in the sample after both aging processes. Interestingly, these researchers did not see the catana phase before aging the sample too. Figure 12 presents the topographic and phase contrast images of asphalt sample with various recycled binders (RAP) after different aging conditions. The lateral dimensions of the AFM-based images shown in Figure 12 are  $10\ \mu\text{m} \times 10\ \mu\text{m}$ . The scale of the topography images is 20 nm. Absence of the catana phase in the unaged sample is not new. For example, the study conducted by Qin et al. also supports the observation of the Rebelo study [35]. In addition to thermal and oxidative effects on asphalt binder, various forms of moisture precipitate from atmosphere also damage asphalt pavement significantly. Dos Santos et al. [36] reported that the catana and perpetua phases are significantly affected by moisture that, in turn, affects the rheological and adhesive properties of asphalt binder.

In the recent years, to improve pavement performance, the addition of different polymers or additives in asphalt binders has become a common practice in the industry. In

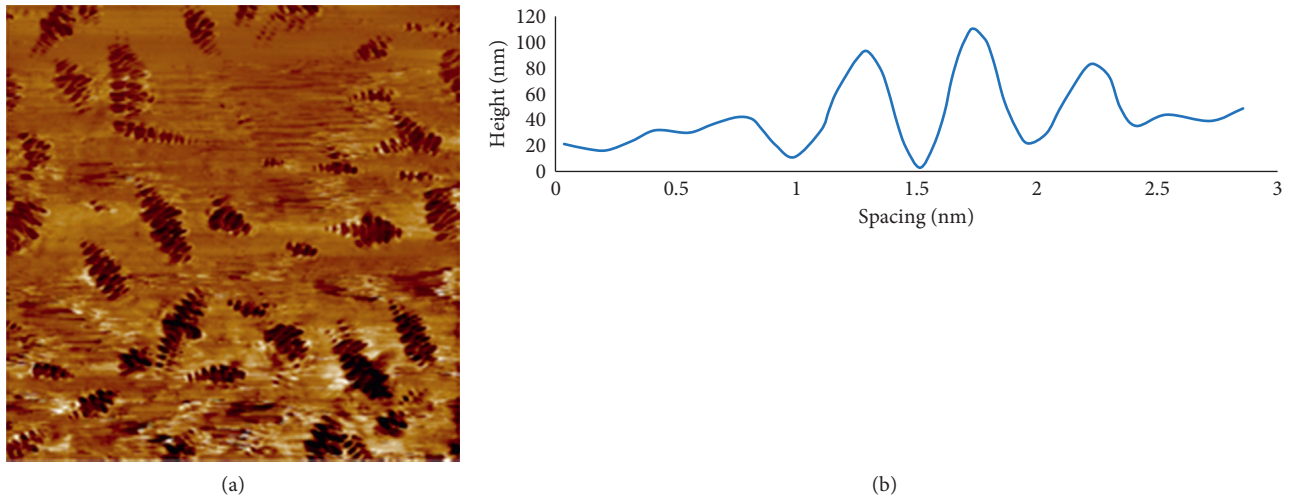


FIGURE 6: (a) A bird eye view of asphalt sample under AFM, and (b) a tentative topographic profile of bee structure. The Figure 6(b) is reproduced from the data reported by Masson et al. [24] (under the creative commons attribution license/public domain).

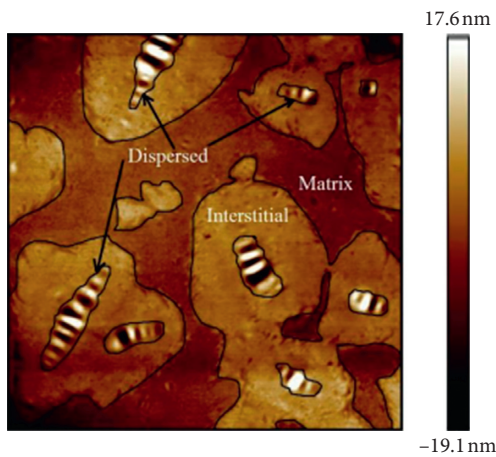


FIGURE 7: A detail view of all morphological phases in asphalt.

TABLE 3: Effect of temperature on diameter and area coverage of bee structure in asphalt. The table is reproduced from Menapace [27] (under the creative commons attribution license/public domain).

Treatment temperature	Pen 60/70		PG 76-22	
	Average diameter ( $\mu\text{m}$ )	% area covered	Average diameter ( $\mu\text{m}$ )	% area covered
Room temperature	0.27	22	0.27	35
50°C	0.58	56	0.56	53
70°C	1.07	66	0.99	60
100°C	1.64	55	2.06	63
130°C	1.54	51	2.13	69
150°C	1.48	43	1.83	60

microstructure investigation, it was found the addition of polymer basically changes the microstructure of the original binder, and the improvement in modified binder in regard to rheological or adhesive property is strongly associated with changes in microstructure or new morphologies developed in the modified binder [35, 37, 38]. Another study [25] also reported that asphalt morphology is influenced by the UV aging.

The main consequence of various aging is formation of crack in asphalt. Researchers have been trying to use a rejuvenator in a capsule (very fine shell) during pavement construction. The idea is when a microcrack initiates and passes through randomly spread rejuvenator shells, the shell breaks and liquid rejuvenators spread in the microcracks [39]. Morphologies of asphalt with asphalt modifiers and closer view of the cracks has been shown in Figure 13. Depending on morphologies of the crack surfaces, appropriate rejuvenators can improve both adhesive and cohesive bond properties of asphalt binders, and thereby crack propagation is deterred. All of these studies strongly demonstrate the strong association between the morphological properties and microstructural performance of asphalt. The authors also believe that the understanding of this association can be linked to macrolevel performance of the pavement in the real world.

**3.4. Network Structure of Asphalt Molecules.** To better understand the architectural pattern, i.e., the design of network of molecular compounds and how the network is associated with asphalt binder’s fundamental properties (e.g., adhesibility and stiffness), a few studies have been done. To capture the network design of asphalt molecules, electron micrograph drawn by utilizing scanning electron or environmental scanning electron microscopes is common in the literatures. Between these two systems, literatures have come to a point that, to realize the goal of understating of surface network morphology, the environmental scanning electron microscope does a better job than that of scanning electron. In the latter technique (i.e., scanning electron), an asphalt sample is distorted by the evaporation of some hydrocarbon molecules with the heat radiated from the electron beam [41]. To avoid the evaporation of some molecules, thereby, maintaining the integrity of the testing sample, a carbon coating on the sample is done when a scanning electron microscope is utilized in network structure study. However, this takes meticulous sample preparation efforts and

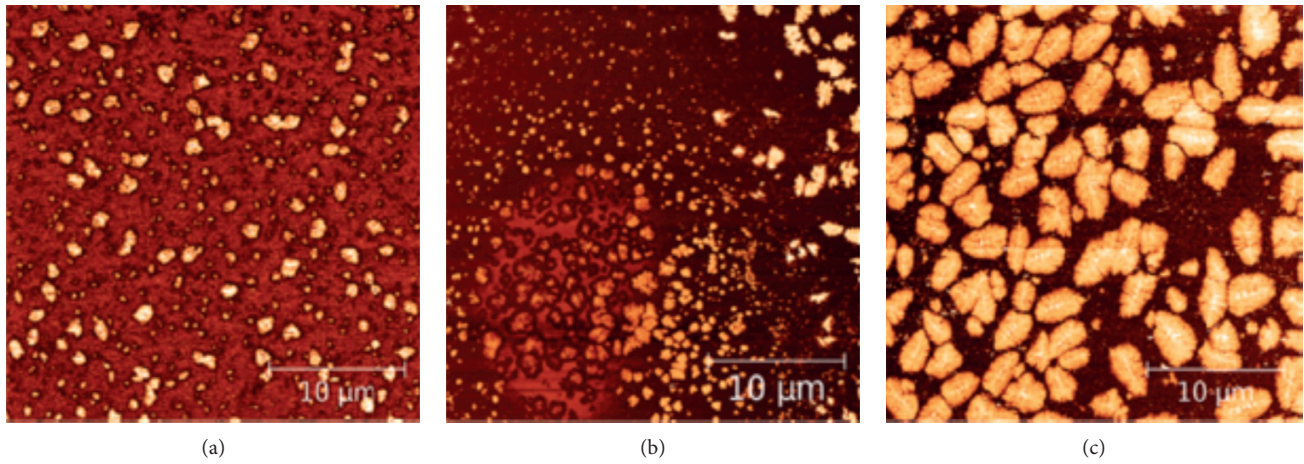


FIGURE 8: (a) Micrographs of RAP asphalt binder, (b) RAP and virgin asphalt binder's interfacial zone, and (c) virgin asphalt. The figure is obtained from Nahar [31] (under the creative commons attribution license/public domain).

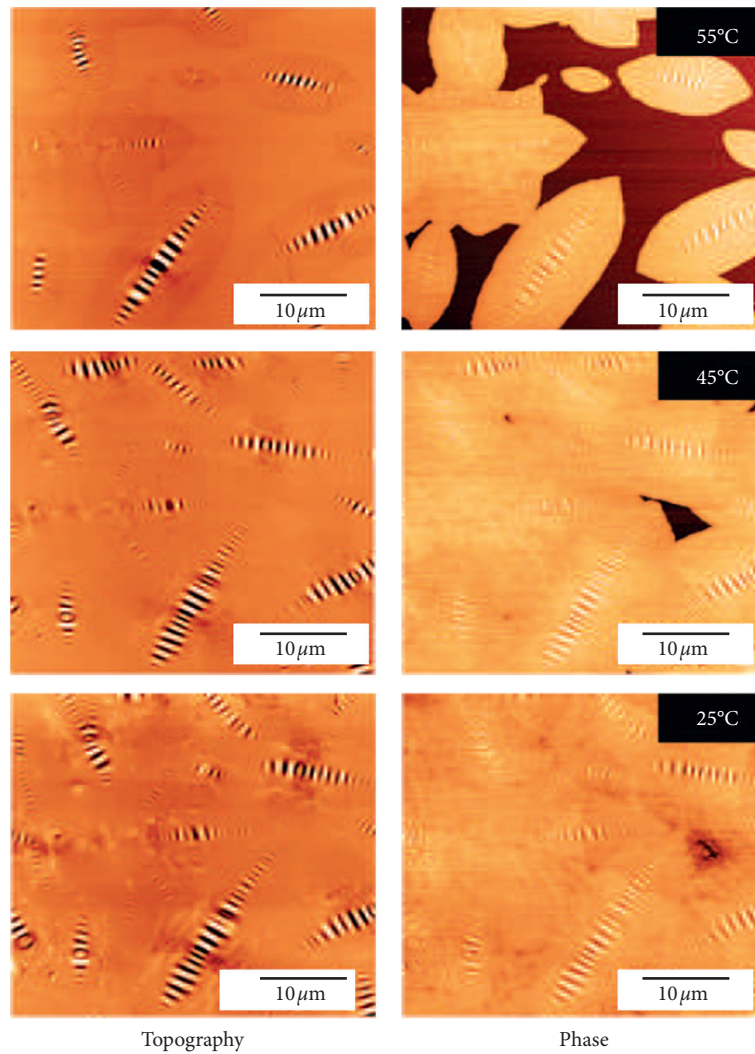


FIGURE 9: Microscopic images of asphalt morphologies under different temperatures. The figure is obtained from Nahar [31] (under the creative commons attribution license/public domain).

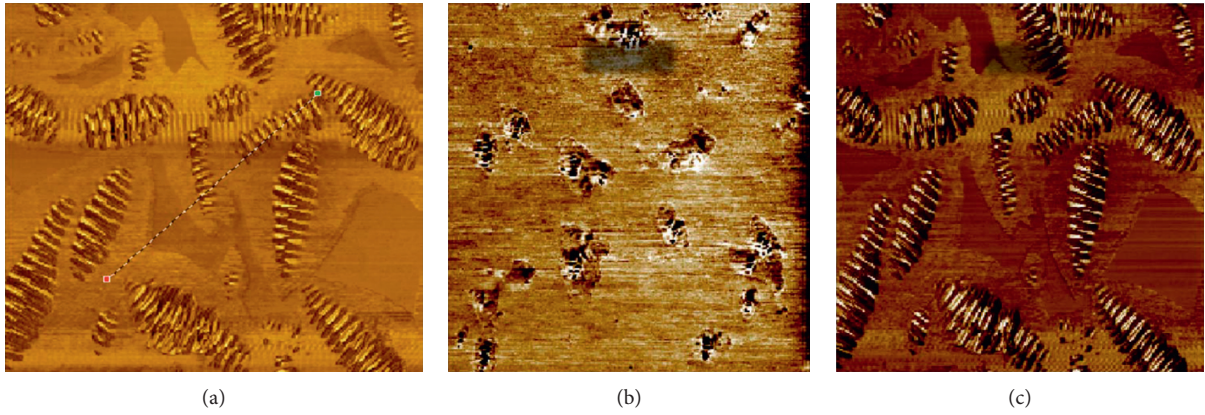


FIGURE 10: (a) AFM micrograph of asphalt showing catana, peri, and perpetua phases, (b) micrograph before aging, and (c) micrograph after aging. The figure is obtained from Allen [33] (under the creative commons attribution license/public domain).

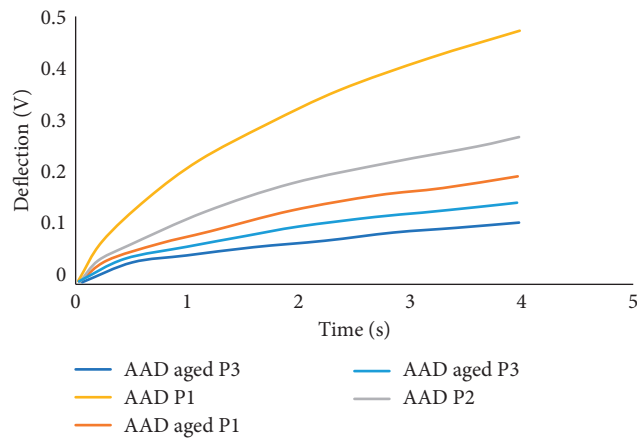


FIGURE 11: Effect of aging on asphalt phases. The figure is obtained from Allen et al. [33] (under the creative commons attribution license/public domain).

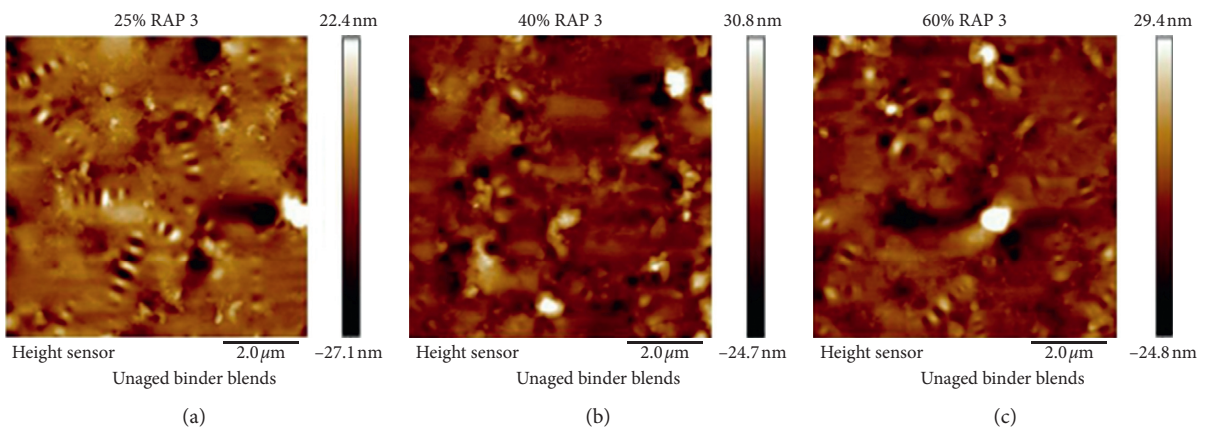


FIGURE 12: Continued.

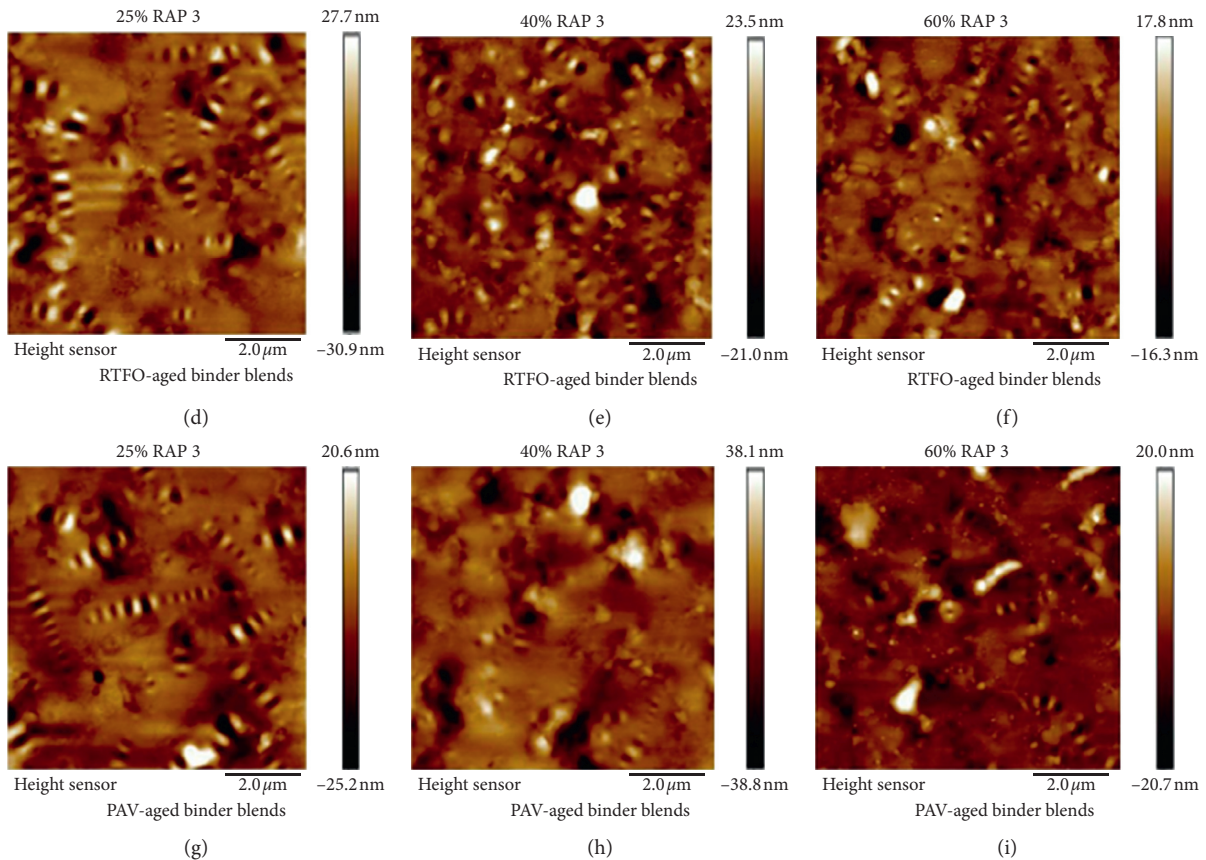


FIGURE 12: Morphology of RAP-asphalt blends: (a–c) 25%, 40%, and 60% unaged blends, (d–f) 25%, 40%, and 60% RTFO-aged blends, and (g–i) 25%, 40%, and 60% PAV-aged blends, respectively.

extended time to test [42]. Detail information on how these microscopy works and advantages and disadvantages are available in [43].

Figure 14 shows micrographs of asphalt binder's molecular network captured by an environmental scanning electron microscope [44]. A network entanglement that consists of thousands of rope-like elements (also called network strand or fibril) can be observed. The average diameter of this fibril is reported 10 micrometers for an unaged sample [45]. But, when an aged sample was tested, observed fibrils were found to be a bit coarser than that of an unaged sample. Rozeveld et al. [42] also investigated the network structure of asphaltene fraction (phase with heavy molecular weight) after fractionating by n-heptane and reported the presence of a network of interconnected lentil-like particles than a network of smooth fibrils. This individual chemical family (asphaltene fractions) had an average size of 0.2 to 0.3 micrometer before aged, whereas after aged, the fractions became significantly larger in size (0.8 to 1.2 micrometer). The increase in size was attributed to the change in molecular structure by oxidation during aging. The observation made by Khattak et al. [46] supported the findings of Rozeveld et al. [42], which reported a network of interconnected lentil particles (asphaltene particles). The study [45] also included time-dependency effect on network design in their experimental matrix. Interestingly, distinct differences in the network structure were observed for

different level of interaction between asphaltene molecule group and n-heptane, as can be seen in Figure 15 [47].

Figure 16 shows an ESEM image of asphalt sample tested under irradiation loading [44]. When the asphalt sample is loaded under tensile loading, the fibril network was found well aligned [42]. This observation suggests that when asphalt is loaded, the fibril network provides the resistance force and that ultimately help contribute to prevent deformation, and, also possibly, the fibrils act as a stitching between the microcracks and participate to reduce crack propagation under the loading. Some studies also reported that the network structures were changed with the addition of polymer and its dosages (Figure 17) and indicated that rheological properties and microperformances changed after the addition of polymers could be linked to the modified network of the fibrils [11, 42, 48]. Similar observations were made by some other researchers who compared the morphological structure of a neat asphalt and the asphalt binder modified with carbon nanofibers. However, this was not the case for the study conducted by Stangl et al. [5]; this group did not find any significant difference between the network structures with and without polymer modification of asphalt binders. The effects of aging on network structure were observed significant, only after long-term aging (PAV) in the Stangl et al. study [5], however other study reported aging changed asphalt ESEM profiles as tested for different temperature and duration, as displayed in Figure 18. To be

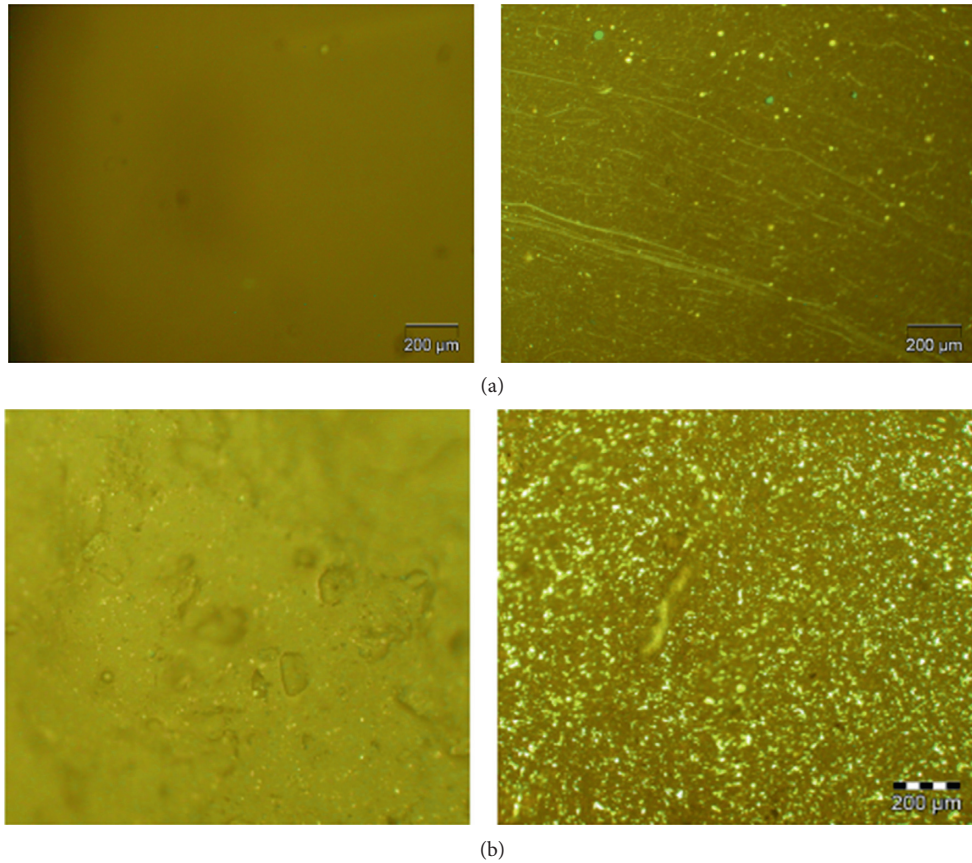


FIGURE 13: (a) Fluorescence microscopy of pure bitumen (left) and SBS modified bitumen (right). (b) Fluorescence microscopic pictures of the cross section of the PBmas (left) and the SBSmas (right) directly after being broken at 0°C. This figure is obtained from Qiu [40] (under the creative commons attribution license/public domain).

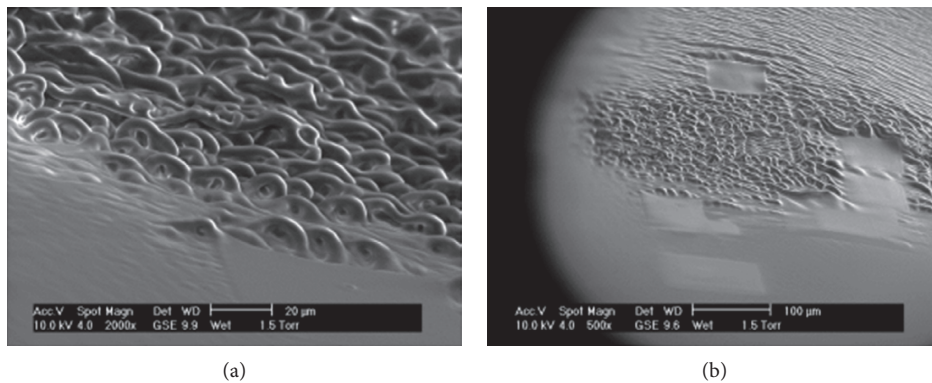


FIGURE 14: (a) Micrograph of an asphalt sample after 2 minutes irradiation. (b) Electron effects in that asphalt due to double irradiation. The figure is obtained from Gaskin [44] (under the creative commons attribution license/public domain).

precise, little to no change was noticed in the RTFOT sample, a contrast to the Shin et al.’s study [45] which suggests that a systematic standard test method for aging effect needs to be developed for improving reproducibility, which can be utilized to predict micro level performance with statistical reliability. Thus, results from micro- or nanolevel investigation can be helpful and can be connected to pavement-level model—a driving force of this review.

#### 4. Micromechanistic Characteristics of Asphalt

This section summarizes micromechanistic characteristics and performances of asphalt binders and how they are influenced by chemomorphological properties that have been previously presented. Among many fundamental properties of asphalt binders, adhesibility, elastic and composite moduli, creep and deformation behavior, and

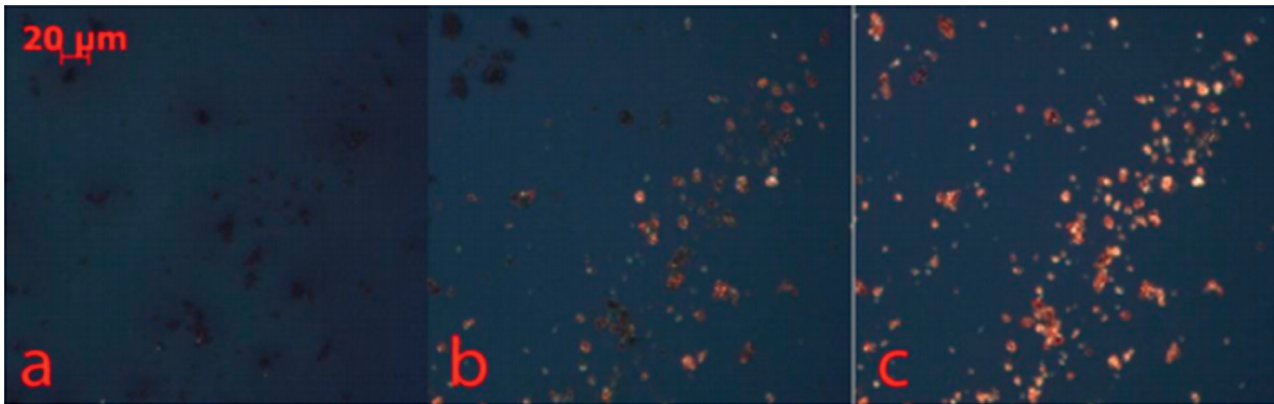


FIGURE 15: Topographic images showing the interaction between n-heptane and asphaltenes. (a) Asphaltene with n-heptane, (b) asphaltene during n-heptane evaporation, and (c) asphaltene after evaporation of n-heptane. The figure is obtained from Nikooyeh [47] (under the creative commons attribution license/public domain).

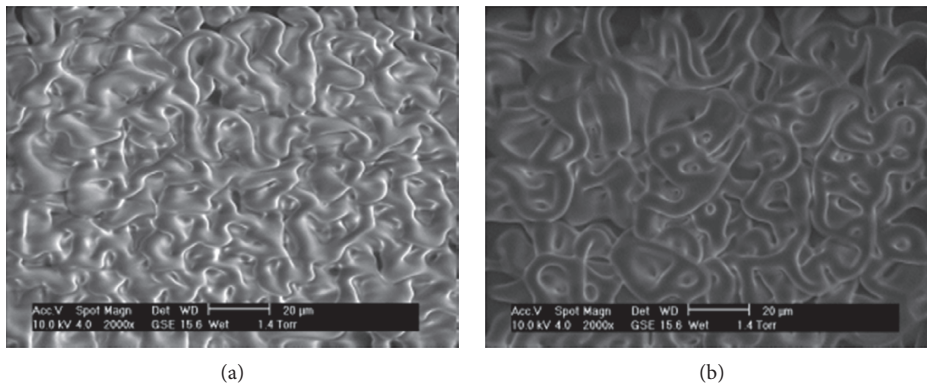


FIGURE 16: Figure micrograph of maltene fraction after irradiation for 1 minute (a) and after 2 minutes (b). The figure is obtained from Gaskin [44] (under the creative commons attribution license/public domain).

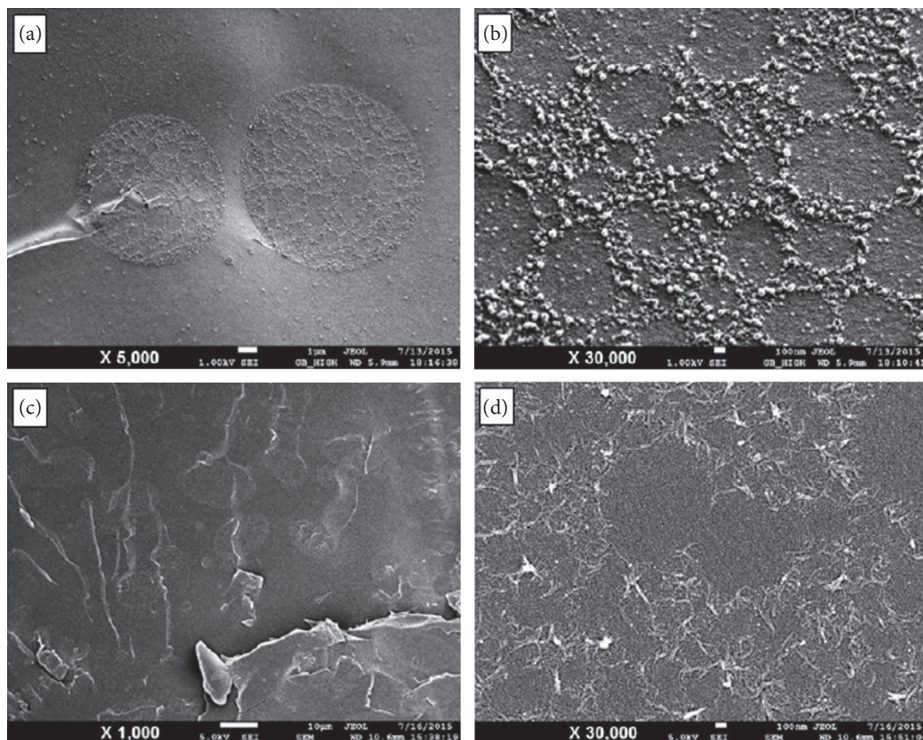


FIGURE 17: ESEM scan of modified asphalt (3% SBS) (a) 5000x and (b) 30000x. ESEM scan of modified asphalt (5% SBS) (a) 5000x and (b) 30000x. The figure is obtained from Jasso [48] (under the creative commons attribution license/public domain).

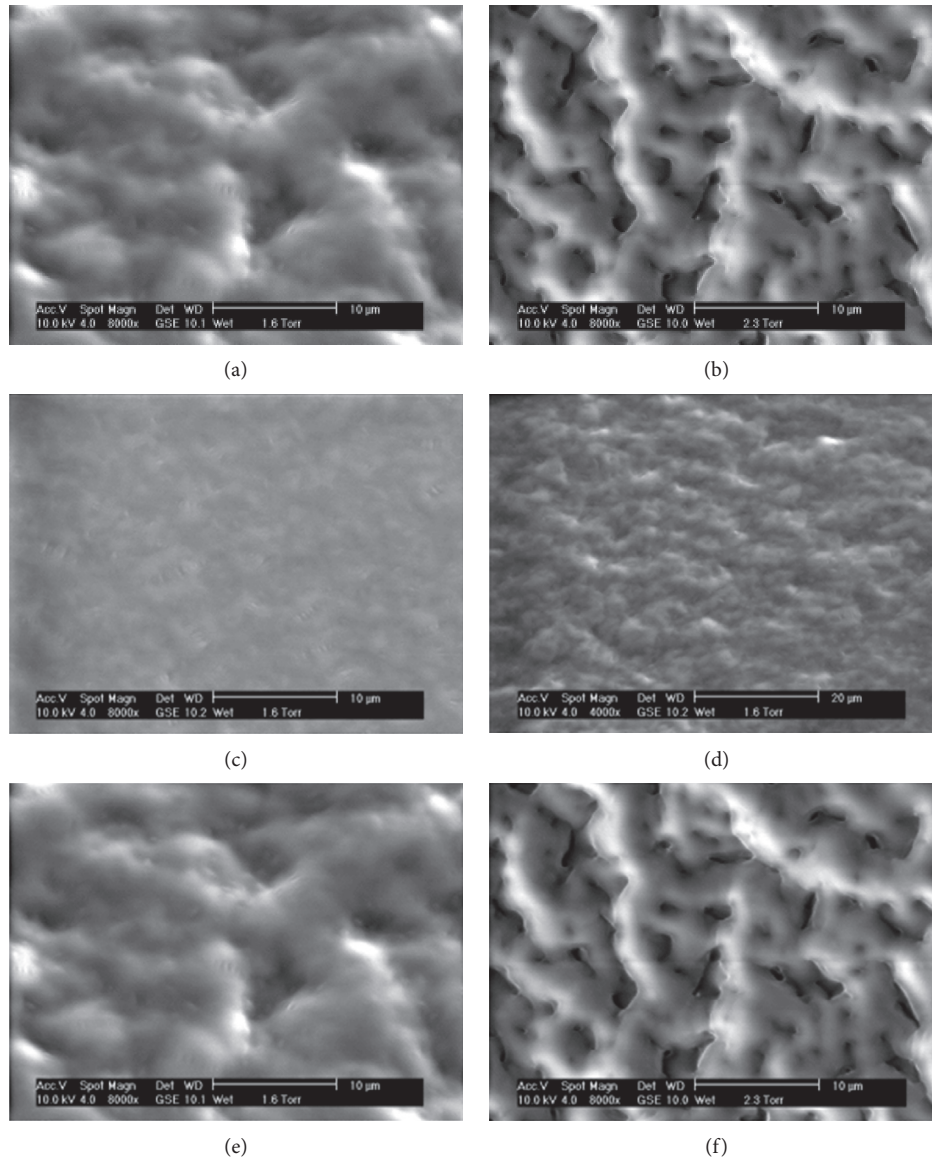


FIGURE 18: (a) ESEM profile of asphalt after aging at 0°C for 2 minutes, (b) after aging at 5°C for 2 minutes, (c) 10°C for 2 minutes, (d) 15°C for 2 minutes, (e) 20°C for 2 minutes, and (f) 25°C for 2 minutes. The figure is obtained from Gaskin [44] (under the creative commons attribution license/public domain).

frictional properties are often considered critical by the pavement community, and they are discussed in the following sections.

**4.1. Adhessibility of Asphalt Phases.** A number of studies have attempted to investigate the adhesion property of asphalt binders and their various microphases [49–55]. The adhessibility of an asphalt binder is found to significantly vary with asphalt source, chemical compositions, and types, and they are influenced by environmental factors such as temperature and moisture. These studies reported that the aforementioned factors also influence the adhesive force of various microphases of asphalt binders. In micro- and nanoscales adhesive force is estimated from the force-distance curve obtained in experimental results of the atomic

force technique—the PFQNM™ (PeakForce quantitative nanomechanical) property mapping. In the PFQNM™ technique, the Derjaguin–Muller–Toporov (DMT) model, shown in equation (2), is utilized to predict adhesive forces. Detail technique can be found in many literatures [21, 40]. Figure 19 presents the variation of adhesion force within a 20-micrometer square asphalt fraction. In Figure 19, regions with white patches exhibiting bee structure (catana phase) have the weakest adhesive force than other phases. The color variation indicates force differences from none to about 242 nN. However, studies [55] found that, in general, some phases of asphalt have a distinctive pattern of adhesion forces. Figure 20 shows a tentative height profile indicating adhesion force over the profile of an asphalt sample. In general, the catana phase has the weakest adhesive force, while periphase has the highest adhesive force as reported by

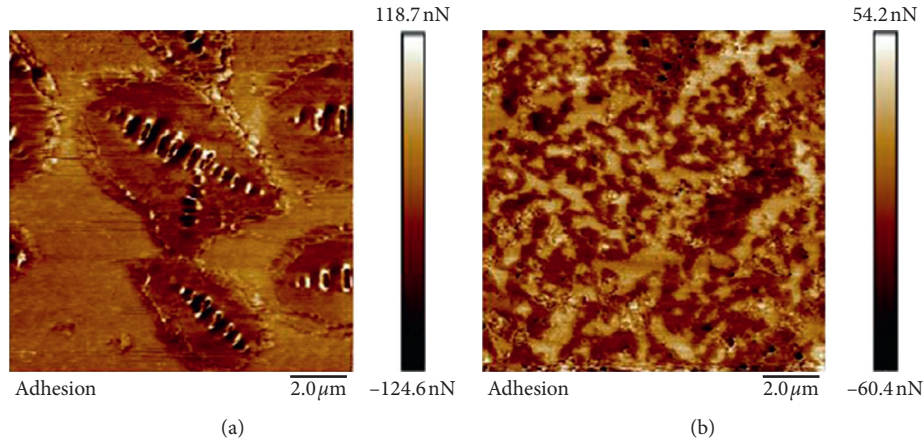


FIGURE 19: Micrograph of asphalt showing adhesion force overlay on a  $20 \times 20$  micrometer sample.

Fischer et al. [49]. However, the third phase (perpetua) can exhibit adhesive force as high as periphase.

$$F_{\text{Adh}} = F - \frac{4}{3}E^r \sqrt{R(d-d_0)^3}, \quad (2)$$

where  $F_{\text{Adh}}$  = adhesion force,  $F$  = applied force,  $R$  = radius of the curvature developed due to the force,  $d - d_0$  = deformation of the sample, and  $E^r$  = Young's modulus of the sample.

Within the catana phase of an asphalt binder, Dourado et al. [52] found that the adhesion force is very consistent; to be precise, the data had just a coefficient of variation of 16%. After conducting studies on a number of asphalt samples, Yu et al. [51] found that there was a statistically significant difference in adhesive force between two areas (raised and recessed) in asphalt, as shown in Figures 21(b) and 21(c). Chemomechanical properties of these morphological regions in the sample may be accounted for this difference are critical and needed to be better understood if adheability is sought to be enhanced for improving pavement performance. And, indeed, some improvement in adhesion force was noticed at nanoscale where the sample studied was modified by some hydrocarbon additives that can be seen in Rebelo's study [22]. Also, Tarefder et al. [56, 57] found this adhesion force enhancement occurred, in general, when asphalt was modified with common styrene-butadiene (SB), SBS polymers, and limes.

**4.2. Modulus Behavior of Asphalt Micro Phases.** With the development of the PFQNM technique in atomic force microscopy, it became possible to obtain nanomechanical properties of asphalt, on top of topographic height profile. Among three morphological phases discussed earlier, Fisher et al. reported that the periphase surrounding the catana phase is stiffer than the perpetua phase (smooth matrix), and the perpetua was found more viscous than the periphase. In this investigation for the modulus profile of an asphalt sample, two groups of moduli were noticed clearly: one group with a low modulus value, ranging from 300 to 450 MPa and the other group with a high modulus value, ranging from 500 to

750 MPa. It was also reported that low modulus zone corresponds to the perpetua phase while the high modulus zone corresponds to both catana phase and periphases [49]. Similar observations were made in the Lyne's work [55]. Surprisingly, later some other researchers [50] found that the perpetua phase had a higher DMT modulus value than that of peri/catana phase using (Figure 22).

Dourado et al. estimated elastic modulus of an asphalt sample on five different spots, which were mostly selected in bee areas [52]. Those spots were tested with varying loads ranging from 10 nN to 40 nN. Elastic moduli in these spots were estimated with equation (3), and it was observed that moduli values varied from 0.29 GPa to 2.0 GPa, with trend of the higher the load, the lower the modulus value, an opposite trend that is generally seen at a macroscopic scale. The perpetua phase (smooth matrix) was noticed to be stiffer than the catanaphase/periphase that supports Hossain et al.'s findings [50].

Allen et al. [58] examined viscoelastic/composite moduli of asphalt phases for aged and unaged conditions. A significantly higher modulus value was reported for all three phases in aged asphalt sample than that of the unaged sample. When an additive is added to modify an asphalt binder to improve its mechanistic behavior, the additive changes its morphological network as discussed in the previous section. In turn, the modified morphology helps improve the mechanistic performance. Such behavior was also seen in the microscopic scale—in terms of modulus of the asphalt phases. Besides, modulus values of asphalt phases in this very small scale is also significantly affected by the testing temperature. As expected, moduli of asphalt phases decrease as temperature increases, in general. Figure 23 presents a two-dimensional model and shows how modulus of catana, peri, and perpetua phases changes under a wide range of temperature.

$$E = \frac{4(1-\vartheta^2)F_{\text{max}}}{3\delta_{\text{max}}^2 \tan \alpha}, \quad (3)$$

where  $E$  = elastic modulus,  $F$  = maximum applied force,  $\alpha$  = half angle in the tip of cantilever in atomic force microscopy,  $\delta$  = indentation depth, and  $\vartheta$  = Poisson's ratio.

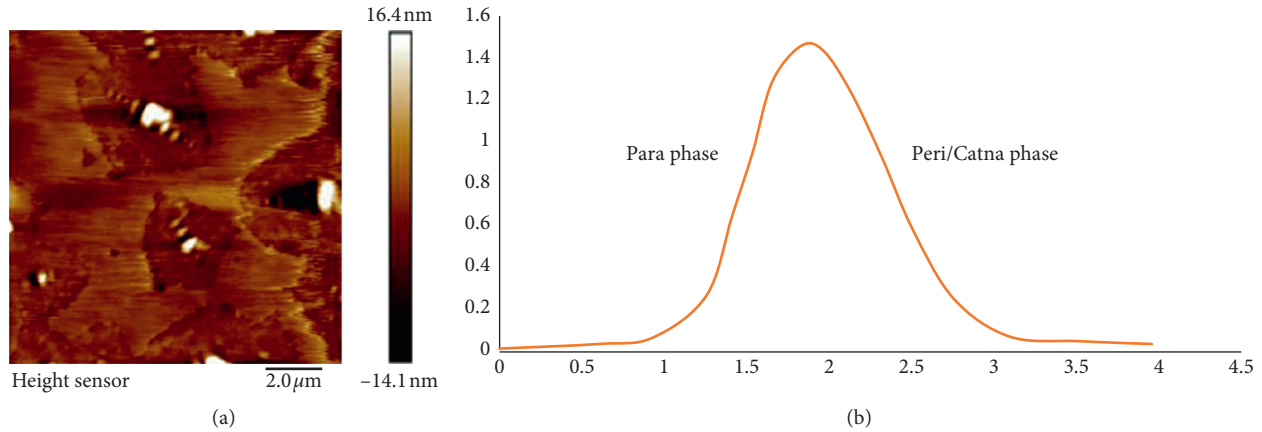


FIGURE 20: Different phases exhibit different adhesion force in the left image (a). Frequency distribution of adhesion forces (b). The Figure 20(b) is reproduced from Fischer et al. [49] (under the creative commons attribution license/public domain).

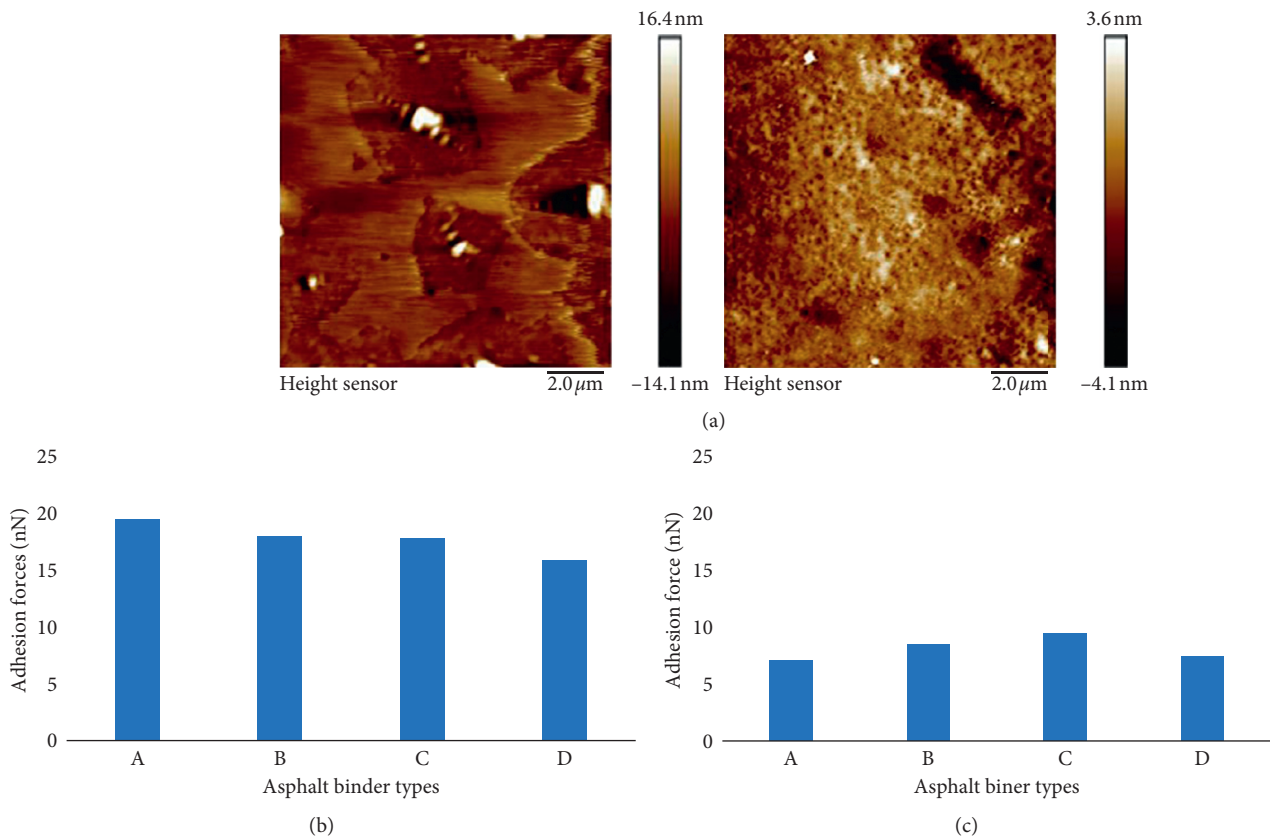


FIGURE 21: (a) Topographic image of asphalt sample with varying height, (b) adhesion force values (in nN) obtained in raised area from different samples, and (c) adhesion force values (in nN) obtained in recessed area. The Figures 21(b) and 21(c) is reproduced from Yu et al. [51] (under the creative commons attribution license/public domain).

**4.3. Creep and Deformation Characteristics of Asphalt Phases.** Asphalt is fundamentally a viscoelastic material—exhibiting the behavior of an elastic solid and a viscous liquid. When it is placed under a mechanical loading, it deforms instantly and also over time. When load is removed, some part of the deformation rebounds. Many studies have been conducted to understand this viscoelastic behavior of asphalt from micro- and nanoscopic scales [19, 35, 50, 52, 58]. Dourado

et al. [52] examined how asphalt’s morphological surface changes under mechanical loading (10 nN) over time with the AFM technique. It was reported that, after 12 minutes from loading, a dark zone appeared that reflected changes in morphology for an imposed load, but it is reduced significantly after an hour. Qtaish [59] also found similar results (Figure 24). Figure 25 displays how the phase deformation changes over time. Clearly, it can be noticed first

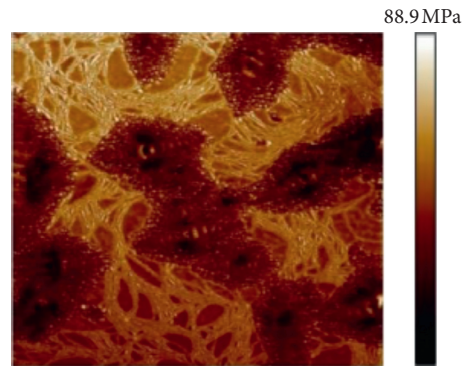


FIGURE 22: Modulus profile of an asphalt sample of  $20 \times 20$  micrometer.

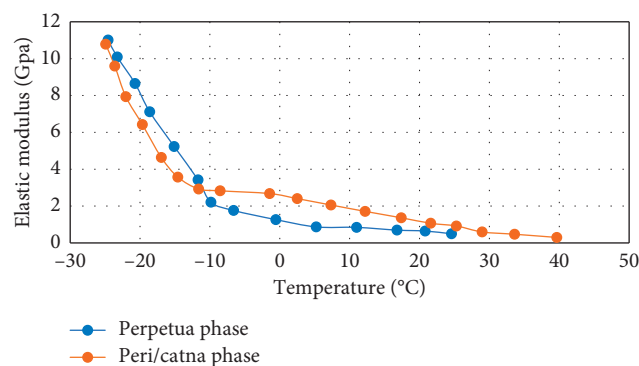


FIGURE 23: Effect of temperature on asphalt phases. The figure is reproduced from Fischer et al. [49] (under the creative commons attribution license/public domain).

deformation was increasing under the loading that could be attributed to the tensile effect on the surface, whereas after reaching the peak deformation, it decreased over time that can be attributed to elastic recovery after the load is removed.

Allen et al. [33] estimated deformation characteristics of asphalt phases for aged and unaged conditions for different asphalt samples and found different creep performance between the asphalts. Figure 26 shows deformation profiles of two phases (continuous phase/smooth matrix and dispersed phase/surrounding of bee) of SHRP ABD asphalt. For the unaged sample, higher deformation was observed in smooth matrix than the dispersed phase under a creep static loading of 5 nN, while almost similar deformation trend was observed for both phases in the aged sample, suggesting morphological changes of the phases during aging processes. Interestingly, aged phases exhibited an elastic solid material behavior—a linear deformation with time while unaged phases showed a lag in deformation response for the creep loading. Study also found that the deformation value of asphalt phases, that is critical for understanding nucleation of microcracks and developing prevention mechanisms, is changed with the additives added for asphalt modification or when a neat asphalt is blended with aged asphalt from recycled pavement [50]. Figure 27 shows asphalt phases after straining. Crack is nucleated around the bee areas at different scales and with different geometrical blocks—such differences can be attributed to the heterogeneity in the

asphalt phases that induce differential local stress and strain with various amplitude leading to microcracks.

## 5. Concluding Remarks

Asphalt binder is a vital component for asphalt pavement and dictates the overall performance of pavement. Much research studies have been done to better understand the behavior and properties of binder. In the recent years, a number of studies have also been conducted to understand asphalt binder at molecular/nanoscale level. A thorough review on asphalt binder's binder properties at different scale levels has been conducted in this study. Based on the review of the literature, the following can be concluded:

- (i) To better understand and predict the performance of pavement, it is important to understand the behavior and performance of asphalt binder at molecular and nanoscales. This became even more important with the increased trends in modification of asphalt binders and utilization of recycled asphalts in new pavement constructions.
- (ii) Asphalt molecular models are widely varied depending on origins, chemical processing, and so on.
- (iii) At the nano level, an asphalt binder has three major microdomains: catana phase (also called dispersed

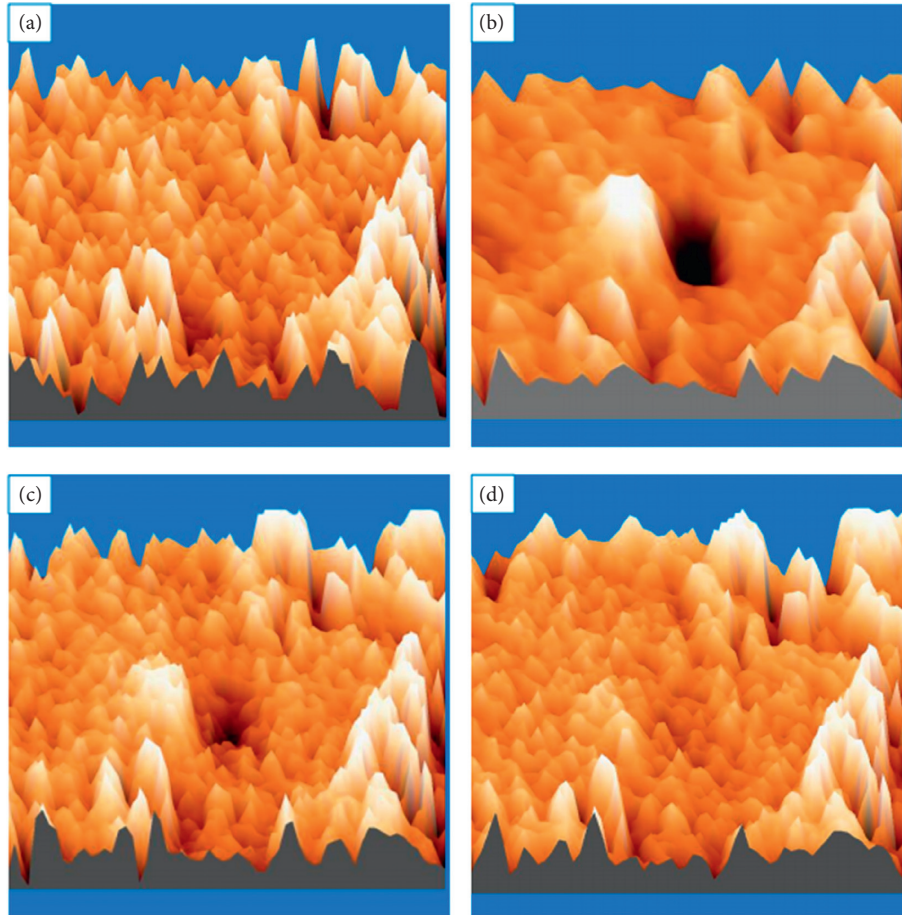


FIGURE 24: Asphalt micrograph: (a) directly before loading, (b) 163 sec after loading, (c) 350 sec after loading, and (d) 800 sec after loading. The figure is obtained from Qtaish [59] (under the creative commons attribution license/public domain).

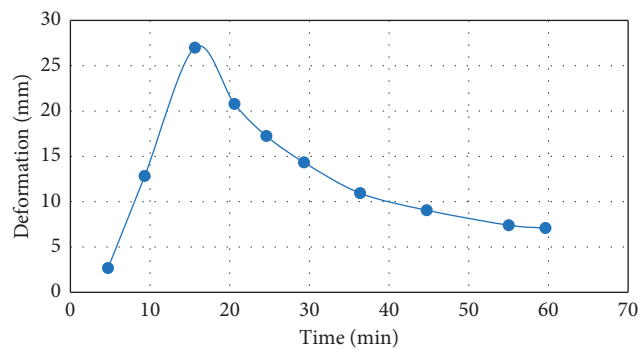


FIGURE 25: Changes in deformation in the asphalt phase under a mechanical loading of 25 nN. The figure is reproduced from Dourado et al. [52] (under the creative commons attribution license/public domain).

phase), periphase (phase surrounding dispersed phase), and perpetua phase (continuous phase). It is reported that the existence and dominance of these microdomains can be highly influenced by aging, environmental factors, and asphalt modification types.

(iv) Many studies also reported that an asphalt binder consists of network of molecular compounds, observed through electron microscopes. When asphalt is loaded, the fibril network provides the resistance

force and contribute to prevent deformation and act as a stitching between the microcracks. The average diameter of molecule fibril of a typical asphalt molecule is 10 micrometers. However, the size of the fibrils can vary due to aging and modification types.

(v) Adhesibility is a very important performance property of asphalt binder that is highly varied depending source, and chemical compositions and types. The adhesive property of asphalt microdomains can be

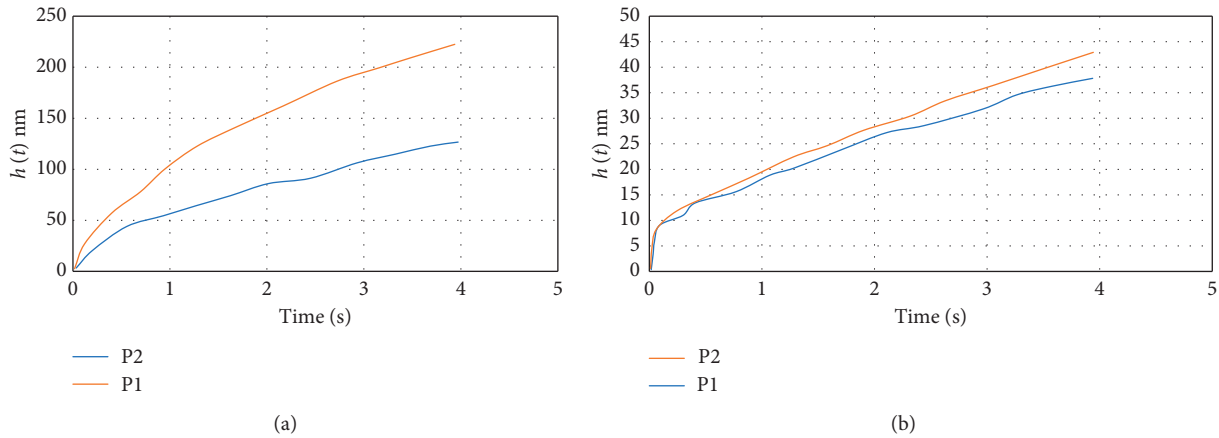


FIGURE 26: Deformation over time of perpetua (P1) and peri (P2) phases under a creep load of 5 nanonewtons for unaged (a) and aged (b) asphalt samples. The figure is reproduced from Allen [33] (under the creative commons attribution license/public domain).

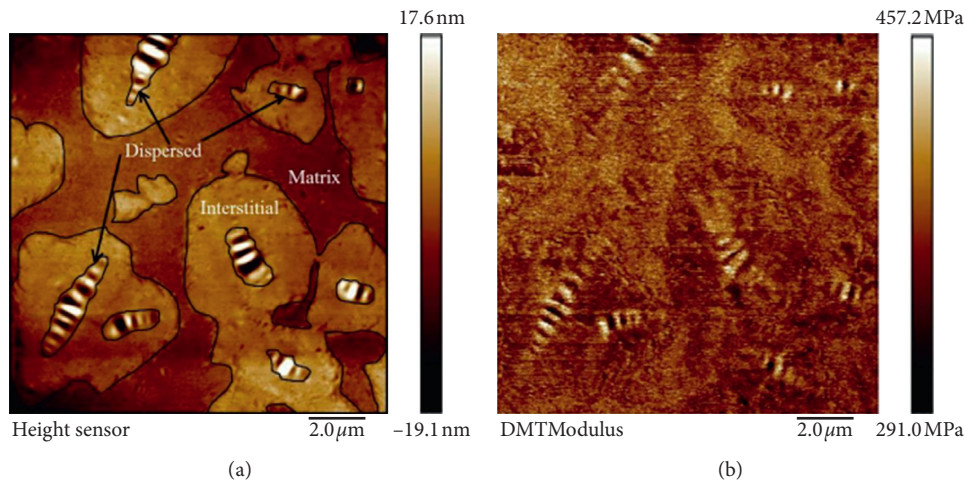


FIGURE 27: (a) Micrographs of asphalt phases before application of strain and (b) after straining.

estimated using the atomic force technique, and studies reported that the property is significantly varied among the microdomains and the catana phase has the weakest adhesive force component.

- (vi) From stiffness perspective, the catana phase is stiffer than perpetua phase, while the perpetua phase was found more viscous than periphase. However, under creep loading, a higher deformation was found in the perpetua phase compared to the catana phase.

### Conflicts of Interest

The authors declare that they have no conflicts of interest.

### Acknowledgments

The authors would like to acknowledge the contribution of their graduate students in preparation of this manuscript for capturing some of the images in the laboratory or creating the charts after collecting data from the existing literature. They include Mr. M. M. Tariq Morshed, Mr. Feroze Rashid, Mr. Shahriar Alam, Mr. Sumon Roy from Arkansas State

University in USA, and Farhana Akter from Memorial University in Canada. Also, the authors would like to acknowledge all the researchers and their great works that generated a great amount of data to understand asphalt binder at molecular level.

### References

- [1] UPM, *Unique Paving Materials Corp*, 2018, <https://www.uniquepavingmaterials.com/asphalt-paving-throughout-history/>.
- [2] E. R. Brown, P. S. Kandhal, F. L. Roberts et al., *Hot Mix Asphalt Materials, Mixture Design and Construction*, Worldcat, National Asphalt Pavement Association Research and Education Foundation, Lanham, MD, USA, 2nd edition, 1996.
- [3] P. W. Jennings, J. A. Pribanic, M. A. Desando et al., *Binder Characterization and Evaluation by Nuclear Magnetic Resonance Spectroscopy*, National Research Council, Washington, DC, USA, 1993.
- [4] P. Jennings, M. Desando, M. Raub, R. Moats, T. Mendez, and F. F. Stewart, "NMR spectroscopy in the characterization of

- eight selected asphalts," *Fuel Science and Technology International*, vol. 10, pp. 887–907, 1992.
- [5] K. Stangl, A. Jäger, and R. Lackner, "Microstructure-based identification of bitumen performance," *Road Materials and Pavement Design*, vol. 7, pp. 111–142, 2006.
- [6] P. K. Das, H. Baaj, S. Tighe, and N. Kringos, "Atomic force microscopy to investigate asphalt binders: a state-of-the-art review," *Road Materials and Pavement Design*, vol. 17, no. 3, pp. 693–718, 2016.
- [7] Y. Veytskin, C. Bobko, and C. Castorena, "Nanoindentation and atomic force microscopy investigations of asphalt binder and mastic," *Journal of Materials in Civil Engineering*, vol. 28, no. 6, article 04016019, 2016.
- [8] M. Guo, Y. Tan, J. Yu, Y. Hou, and L. Wang, "A direct characterization of interfacial interaction between asphalt binder and mineral fillers by atomic force microscopy," *Materials and Structures*, vol. 50, no. 2, pp. 1–12, 2017.
- [9] L. D. Poulikakos and M. N. Partl, "Investigation of porous asphalt microstructure using optical and electron microscopy," *Journal of Microscopy*, vol. 240, no. 2, pp. 145–154, 2010.
- [10] D. Lesueur, "The colloidal structure of bitumen: consequences on the rheology and on the mechanisms of bitumen modification," *Advances in Colloid and Interface Science*, vol. 145, no. 1–2, pp. 42–82, 2009.
- [11] L. Champion, J. F. Gerard, J. P. Planche, D. Martin, and D. Anderson, "Low temperature fracture properties of polymer-modified asphalts relationships with the morphology," *Journal of Materials Science*, vol. 36, no. 2, pp. 451–460, 2001.
- [12] K. Dunn, G. V. Chilingarian, H. Lian, Y. Y. Wang, and T. F. Yen, "Chapter 11 analysis of asphalt and its components by thin-layer chromatography," in *Developments in Petroleum Science*, Elsevier, Amsterdam, Netherlands, 2000.
- [13] O. C. Mullins, A. E. Pomerantz, A. B. Andrews, and J. Y. Zuo, "Asphaltenes explained for the nonchemist," *Petrophysics*, vol. 56, no. 3, pp. 266–275, 2015.
- [14] L. Eberhardsteiner, F. Josef, B. Hofko et al., "8th international RILEM symposium on testing and characterization of sustainable and innovative bituminous materials, SIB 2015," *International Journal of Pavement Research and Technology*, vol. 7, no. 1, pp. 411–421, 2014.
- [15] R. L. Griffin, W. C. Simpson, and T. K. Miles, "Influence of composition of paving asphalt on viscosity, viscosity-temperature susceptibility, and durability," *Journal of Chemical & Engineering Data*, vol. 4, no. 4, pp. 349–354, 1959.
- [16] B. Hofko, L. Eberhardsteiner, J. Füssl et al., "Impact of maltene and asphaltene fraction on mechanical behavior and microstructure of bitumen," *Materials and Structures*, vol. 49, no. 3, pp. 829–841, 2016.
- [17] Z. Kraus, *The Morphology of Polymer Modified Asphalt and Its Relationship to Rheology and Durability*, Texas A&M University, College Station, TX, USA, 2008.
- [18] L. Loeber, O. Sutton, and J. Morel, "New direct observations of asphalts and asphalt binders by scanning electron microscopy and atomic force microscopy," *Journal of Microscopy*, vol. 182, pp. 32–39, 1996.
- [19] R. Jahangir, D. Little, and A. Bhasin, "Evolution of asphalt binder microstructure due to tensile loading determined using AFM and image analysis techniques," *International Journal of Pavement Engineering*, vol. 16, no. 4, pp. 337–349, 2014.
- [20] A. T. Pauli, R. W. Grimes, A. G. Beemer, T. F. Turner, and J. F. Branthaver, "Morphology of asphalts, asphalt fractions and model wax-doped asphalts studied by atomic force microscopy," *International Journal of Pavement Engineering*, vol. 12, no. 4, pp. 291–309, 2011.
- [21] H. R. Fischer, E. C. Dillingh, and C. G. M. Hermse, "On the microstructure of bituminous binders," *Road Materials and Pavement Design*, vol. 15, no. 1, pp. 1–15, 2014.
- [22] L. M. Rebelo, P. N. Cavalcante, J. S. De Sousa, J. M. Filho, S. A. Soares, and J. B. Soares, "Micromorphology and microrheology of modified bitumen by atomic force microscopy micromorphology and microrheology of modified bitumen by atomic force microscopy," *Road Materials and Pavement Design*, vol. 15, no. 2, pp. 300–311, 2014.
- [23] A. T. Pauli, *Chemomechanics of Damage Accumulation and Damage-Recovery Healing in Bituminous Asphalt Binders*, Delft University of Technology, Delft, Netherlands, 2014.
- [24] J. F. Masson, V. Leblond, and J. Margeson, "Bitumen morphologies by phase-detection atomic force microscopy," *Journal of Microscopy*, vol. 221, no. 1, pp. 17–29, 2006.
- [25] H. Soenen, X. Lu, and P. Redelius, "The morphology of bitumen-SBS blends by UV microscopy," *Road Materials and Pavement Design*, vol. 9, no. 1, pp. 97–110, 2008.
- [26] H. Soenen, J. Besamusca, H. R. Fischer et al., "Laboratory investigation of bitumen based on round robin DSC and AFM tests," *Materials and Structures*, vol. 47, no. 7, pp. 1205–1220, 2013.
- [27] I. Menapace, E. Masad, and A. Bhasin, "Effect of treatment temperature on the microstructure of asphalt binders: insights on the development of dispersed domains," *Journal of Microscopy*, vol. 262, no. 1, pp. 12–27, 2016.
- [28] R. G. Allen, D. N. Little, A. Bhasin, and C. J. Glover, "The effects of chemical composition on asphalt microstructure and their association to pavement performance," *International Journal of Pavement Engineering*, vol. 15, no. 1, pp. 9–22, 2014.
- [29] S. N. Nahar, M. Mohajeri, A. J. M. Schmetts, A. Scarpas, M. F. C. van de Ven, and G. Schitter, "First observation of blending-zone morphology at interface of reclaimed asphalt binder and virgin bitumen," *Transportation Research Record: Journal of the Transportation Research Board*, vol. 2370, no. 1, pp. 1–9, 2013.
- [30] S. Zhao, S. N. Nahar, A. J. M. Schmetts, B. Huang, X. Shu, and T. Scarpas, "Investigation on the microstructure of recycled asphalt shingle binder and its blending with virgin bitumen," *Road Materials and Pavement Design*, vol. 16, no. 1, pp. 21–38, 2015.
- [31] S. N. Nahar, *Phase-Separation Characteristics of Bitumen and Their Relation to Damage-Healing*, Delft University of Technology, Delft, Netherlands, 2016.
- [32] R. G. Allen, D. N. Little, D. M. Asce, and A. Bhasin, "Structural characterization of micromechanical properties in asphalt using atomic force microscopy," *Journal of Materials in Civil Engineering*, vol. 24, no. 10, pp. 1317–1327, 2012.
- [33] R. Allen, *Structural Characterization of Micromechanical Properties in Asphalt Using Atomic Force Microscopy*, Texas A&M University, College Station, TX, USA, 2010.
- [34] L. M. Rebelo, J. S. De Sousa, A. S. Abreu et al., "Aging of asphaltic binders investigated with atomic force microscopy," *Fuel*, vol. 117, pp. 15–25, 2014.
- [35] Q. Qin, M. J. Farrar, A. T. Pauli, and J. J. A. Morphology, "Thermal analysis and rheology of sasobit modified warm mix asphalt binders," *Fuel*, vol. 115, pp. 416–425, 2014.
- [36] S. Dos Santos, M. N. Partl, and L. D. Poulikakos, "Newly observed effects of water on the microstructures of bitumen

- surface,” *Construction and Building Materials*, vol. 71, pp. 618–627, 2014.
- [37] X. Yu, Y. Wang, and T. Wei, “The viscosity-reducing mechanism of organic wax additive on CRMA,” *Journal of Wuhan University of Technology*, vol. 28, no. 4, pp. 726–732, 2013.
- [38] M. Nazzal, S. Kaya, and L. Abu-qaish, *Evaluation of WMA Healing Properties Using Atomic Force Microscopy*, Springer, Berlin, Germany, 2012.
- [39] J.-F. Su, J. Qiu, E. Schlangen, and Y.-Y. Wang, “Experimental investigation of self-healing behavior of bitumen/microcapsule composites by a modified beam on elastic foundation method,” *Materials and Structures*, vol. 48, no. 12, pp. 4067–4076, 2014.
- [40] J. Qiu, *Self Healing of Asphalt Mixtures: Towards a Better Understanding of the Mechanism*, Delft University of Technology, Delft, Netherlands, 2012.
- [41] R. Kim, D. Little, and R. Burghardt, “SEM Analysis on Fracture and Healing of Sand-Asphalt Mixture,” *Journal of Materials in Civil Engineering*, vol. 3, no. 2, pp. 140–153, 1991.
- [42] S. J. Rozeveld, E. Eugene Shin, A. Bhurke, L. France, and L. T. Drzal, “Network morphology of straight and polymer modified asphalt cements,” *Microscopy Research and Technique*, vol. 38, no. 5, pp. 529–543, 1997.
- [43] Thermofisher. Nanodevices, 2018, <https://www.fei.com/materials-science/nanodevices/>.
- [44] J. Gaskin, *On Bitumen Microstructure and the Effects of Crack Healing*, University of Nottingham, Nottingham, UK, 2013.
- [45] E. Shin, A. Bhurke, E. Scott, S. Rozeveld, and L. Drzal, “Microstructure, morphology, and failure modes of polymer-modified asphalts,” *Transportation Research Record: Journal of the Transportation Research Board*, vol. 1535, pp. 61–73, 1996.
- [46] M. J. Khattak, A. Khattab, P. Zhang, H. R. Rizvi, and T. Pesacreta, “Microstructure and fracture morphology of carbon nano-fiber modified asphalt and hot mix asphalt mixtures,” *Materials and Structures*, vol. 46, no. 12, pp. 2045–2057, 2013.
- [47] K. Nikooyeh, *Phase Behavior of Asphaltenes in Organic Media*, University of Alberta, Edmonton, AB, Canada, 2012.
- [48] M. Jasso, *The Mechanism of Modification and Properties of Polymer Modified Asphalts*, University of Calgary, Calgary, AB, Canada, 2016.
- [49] H. Fischer, H. Stadler, and N. Erina, “Quantitative temperature-depending mapping of mechanical properties of bitumen at the nanoscale using the AFM operated with PeakForce Tapping™ mode,” *Journal of Microscopy*, vol. 250, no. 3, pp. 210–217, 2013.
- [50] Z. Hossain, F. Rashid, I. Mahmud, and M. Rahaman, “Morphological and nanomechanical characterization of industrial and agricultural waste-modified asphalt binders,” *International Journal of Geomechanics*, vol. 17, no. 3, article 04016084, 2016.
- [51] X. Yu, N. A. Burnham, R. B. Mallick, and M. Tao, “A systematic AFM-based method to measure adhesion differences between micron-sized domains in asphalt binders,” *Fuel*, vol. 113, pp. 443–447, 2013.
- [52] E. R. Dourado, R. A. Simao, and L. F. M. Leite, “Mechanical properties of asphalt binders evaluated by atomic force microscopy,” *Journal of Microscopy*, vol. 245, no. 2, pp. 119–128, 2012.
- [53] T. Pauli, W. Grimes, A. Cookman, S. Huang, and M. Asce, “Adherence Energy of Asphalt Thin Films Measured by Force-Displacement Atomic Force Microscopy,” *Journal of Materials in Civil Engineering*, vol. 26, no. 12, pp. 1–11, 2014.
- [54] A. S. Al-rawashdeh and S. Sargand, “Performance assessment of a warm asphalt binder in the presence of water by using surface free energy concepts and nanoscale techniques,” *Journal of Materials in Civil Engineering*, vol. 26, no. 5, pp. 803–811, 2014.
- [55] Å. L. Lyne, V. Wallqvist, and B. Birgisson, “Adhesive surface characteristics of bitumen binders investigated by atomic force microscopy,” *Fuel*, vol. 113, pp. 248–256, 2013.
- [56] R. A. Tarefder and A. Zaman, “Characterization of asphalt materials for moisture damage using atomic force microscopy and nanoindentation,” in *Nanotechnology in Civil Infrastructure*, pp. 237–256, Springer, Berlin, Germany, 2011.
- [57] R. A. Tarefder and S. Ahsan, “Neural network modelling of asphalt adhesion determined by AFM,” *Journal of Microscopy*, vol. 254, no. 1, pp. 31–41, 2014.
- [58] R. G. Allen, D. N. Little, A. Bhasin, and R. L. Lytton, “Identification of the composite relaxation modulus of asphalt binder using AFM nanoindentation,” *Journal of Materials in Civil Engineering*, vol. 25, no. 4, pp. 530–539, 2012.
- [59] L. A. Qtaish, *The Use of Atomic Force Microscopy in Evaluating Warm Mix Asphalt*, Ohio University, Athens, OH, USA, 2013.

## Research Article

# Mechanical Evaluation of Bottom Ash from Municipal Solid Waste Incineration Used in Roadbase

Qiang Tang <sup>1,2,3</sup>, Fan Gu <sup>4</sup>, Hui Chen,<sup>3</sup> Cong Lu,<sup>5</sup> and Yu Zhang<sup>3</sup>

<sup>1</sup>Key Laboratory of Ministry of Education for Geomechanics and Embankment Engineering, Hohai University, Nanjing, China

<sup>2</sup>Jiangsu Research Center for Geotechnical Engineering Technology, Hohai University, Nanjing, China

<sup>3</sup>School of Rail Transportation, Soochow University, Suzhou, China

<sup>4</sup>National Center for Asphalt Technology, Auburn University, Auburn, AL, USA

<sup>5</sup>School of Civil Engineering, Suzhou University of Science and Technology, Suzhou, China

Correspondence should be addressed to Fan Gu; [tracygufan@tamu.edu](mailto:tracygufan@tamu.edu)

Received 16 February 2018; Revised 3 July 2018; Accepted 25 July 2018; Published 5 December 2018

Academic Editor: Kirk Hatfield

Copyright © 2018 Qiang Tang et al. This is an open access article distributed under the Creative Commons Attribution License, which permits unrestricted use, distribution, and reproduction in any medium, provided the original work is properly cited.

As a by-product from the incineration of municipal solid waste, bottom ash has a broad application prospect of resource utilization. In this study, bottom ash was selected as partial aggregate alternative and used as roadbase materials. The cemented aggregate containing bottom ash was evaluated through both experimental and numerical analysis. According to the results, the unconfined compressive strength of samples increases with the curing time, and the failure strain of sample decreases with the curing time. The unconfined compressive strength and failure strain of samples are influenced by the types of bottom ash. The increase of compressive strength with the curing time can be attributed to that the hydration reaction of cement will be more complete when the curing time is longer. The representative value (7 days) of unconfined compressive strength of samples meets the strength requirement ( $\geq 2.5$  MPa) of the road subbase layer of heavy traffic highway in China. Subsequently, the surface settlement decreases with the increase of the modulus and thickness of roadbase and the distance from the centerline, while the settlement increases with vehicle load increasing. The modulus of the roadbase is not the main influences on the pavement settlement, under the condition that the strength of samples meets the requirements. However, increasing the thickness of roadbase can reduce the settlement at the center of the pavement effectively.

## 1. Introduction

Nowadays, the amount of municipal solid waste is significantly increasing in China [1, 2]. From 2004 to 2015, the municipal solid wastes increased from 155.1 to 191.4 megatons. Conventional treatment methods for municipal solid waste include reusing and recycling, composting, anaerobic digestion, incineration, and land disposal [3–5]. Among them, incineration treatment is the most effective method in terms of energy saving and reduction of the volume and weight of waste [6–8]. In Holland, the incineration percentage of solid waste reached 40% in 2000, while in Sweden, Denmark, Luxembourg, Japan, and Switzerland, such incineration percentage even reached 60–80% [6, 9]. In China, the incineration percentage of municipal solid wastes also increased

from 2.90% in 2004 to 34.3% in 2015. Obviously, incineration technique has become more and more prevalent to dispose municipal solid waste.

However, incineration technique also generates other types of solid wastes, primarily including bottom ash, fly ashes, and air pollution control (APC) ashes [10, 11]. Fly ash and APC ash usually consist of high percentage of chlorides, heavy metals, or other organic compounds, which are harmful to environment [12–14], while bottom ash is mainly composed of noncombustible materials such as glass, ceramics, and unburned matter. The amount of chlorides and hazardous chemicals in bottom ash is typically significantly lower than that in fly ash and APC ash [12]. In addition, bottom ash accounts for 25% of the amount of total municipal solid waste and represents 80% of the total ash

[15–17]. Due to the high cost of treatment and disposal, the environment-friendly recycling of bottom ash has attracted more and more attention in recent years [12].

Some studies reported that the recycled bottom ash was applied to many construction projects [12, 18]. In Germany and France, the recycling rate of bottom ash was more than 60%, and in Denmark and Holland, this rate even reached 80% [12], while in China, the recycling rate of bottom ash is still low [19]. The municipal solid waste incineration bottom ash is widely used as soil improvement materials, concrete aggregate, and roadbed stuffing [16, 20–24]. In China, bottom ash is mainly used as concrete aggregate, supplementary cementitious material [25, 26]. These existing studies demonstrated that bottom ash could partially replace natural aggregate, which could save natural resources and energy. Moreover, the cement is capable of fixing the bottom ash-containing contaminant by adsorption or surface complexation, which promotes the environment-friendly recycling of bottom ash [10, 11].

To address the aforementioned research needs, this study aimed at recycling the bottom ash from municipal solid waste incineration to partially replacing natural aggregates. The ordinary Portland cement (OPC) was used as a binder material in the bottom ash-aggregate mixture. This study investigated the effects of curing time and mixture ratio on the mechanical behavior of the bottom ash-aggregate mixture. MIDAS GTS was used to simulate the pavement settlement when using the bottom ash in roadbase. The influence factors included the axle load and the modulus and thickness of roadbase. Finally, both the laboratory and simulation results advocated the use of bottom ash in roadbase.

## 2. Materials and Methods

**2.1. Materials.** The bottom ash used in this study was collected from Taizhou municipal solid waste incineration power plant in Jiangsu Province, China. Approximately 800 tons/day of municipal solid wastes were incinerated for electricity generation in this plant. As a kind of renewable resources, the bottom ash includes the original bottom ash and cracked bottom ash. As shown in Figure 1, original bottom ash was crushed into smaller particles that is called cracked bottom. Four types of limestone aggregates were used in the study, which are labeled as 1#, 2#, 3#, and 4#, respectively. The particle size distributions of original bottom and cracked bottom ash and limestone aggregates are shown in Table 1. As presented, 96% of 1# aggregates are distributed within the range of 9.5 mm~31.5 mm; 95.8% of 2# aggregates are within the range of 4.75 mm~19 mm; 97.3% of 3# aggregates are within the range of 0.075 mm~9.5 mm; and 84.5% of 4# aggregates are within the range of 0.075 mm~4.75 mm. The particles of cracked bottom ash are smaller than the original bottom ash.

The physical properties of original bottom ash and cracked bottom ash and limestone aggregate are presented in Table 2. Note that the current Chinese standard JTG/F20 only requires to measure the apparent density for aggregates. As shown in Table 2, the apparent density of the original bottom ash and cracked bottom ash is less than that of



(a)



(b)

FIGURE 1: Examples of bottom ash. (a) Original bottom ash. (b) Cracked bottom ash.

TABLE 1: Particle size distribution of 1#, 2#, 3#, and 4# aggregates, original bottom, and cracked bottom ash (%).

Aggregate	Unit	Particle size (mm)							
		31.5	26.5	19	9.5	4.75	2.36	0.6	0.075
1# aggregate	%	100	95.9	55	4	1	0.9	0.9	0.9
2# aggregate	%	100	100	100	56	4.2	0.9	0.9	0.9
3# aggregate	%	100	100	100	100	92	47.3	14.2	2.7
4# aggregate	%	100	100	100	100	98.5	65.8	31.3	14.0
Cracked bottom ash	%	100	100	100	99.5	79.8	49.9	22.2	3.2
Original bottom ash	%	100	98.6	91.9	71.1	50.9	35.5	19.9	3.9

limestone aggregate. Due to the porous structure of the bottom ash, the water absorption of original bottom ash and cracked bottom ash are much higher than that of the limestone aggregates. According to the JTGE42-2005, the crushing value is an index to evaluate the mechanical properties of aggregates, which describes the resistance of aggregate to crushing under the increasing load. The crushing values of the original bottom ash and cracked bottom ash are over 30%, which are also greater than that of the limestone aggregates. Apparently, the hardness of the original bottom ash and cracked bottom are lower than that of the limestone aggregates.

As a binder material, the commercially available ordinary Portland cement (OPC) 42.5 was prepared, which consisted of 6%–15% active additive and 85%–94% cement. The cement consisted of 60.48% CaO, 20.85% SiO<sub>2</sub>, 5.71%

TABLE 2: Physical properties of aggregates.

Aggregate	Sizes (mm)	Crushing value (%)	Apparent density ( $\text{g}/\text{cm}^3$ )		Water absorption rate (%)
		T0350-2005	T0328-2005		T0330-2005
Standard (JTG E42-2005)	T0302-2005	T0350-2005	T0328-2005		T0330-2005
Original bottom ash	(2.36~4.75)	30.6	2.412		9.647
	(4.75~9.5)	32.5	2.458		7.74
	(9.5~19.0)	33.1	2.318		6.23
	( $\geq 19$ )	43.6	2.253		6.75
Cracked bottom ash	(2.36~4.75)	32.3	2.468		8.89
	(4.75~9.5)	34.7	2.402		6.41
Limestone aggregate	(2.36~4.75)	25.3	2.733		0.81
	(4.75~9.5)	18.2	2.715		0.62
	(9.5~19.0)	22.6	2.726		0.74
	( $\geq 19$ )	24.9	2.731		0.70

$\text{Al}_2\text{O}_3$ , 3.33%  $\text{Fe}_2\text{O}_3$ , 2.28%  $\text{MgO}$ , 2.84%  $\text{SO}_3$ , and 1.43%  $\text{Na}_2\text{O}$  [10].

**2.2. Method.** The aggregate-bottom ash mixture consists of limestone aggregates and cracked bottom ash or original bottom ash, in which the cracked bottom ash and original bottom ash account for 20% of the weight of limestone aggregate [27]. The aggregate-bottom ash mixtures are recorded as PS-20 and YZ-20 as shown in Table 3. Note that the current Chinese standard JTJG/F20 recommends using mass fraction in the mix design. According to Liu et al., the control sample without bottom ash is recoded as LZ-0 [27]. With the bottom ash joining, the number of feed hopper increases accordingly. Therefore, reducing variation of the aggregate yields fast construction speed, simple operation, and low construction cost. As shown in Table 1, the particle size distribution of 3# aggregate is similar to cracked bottom ash. With the amount of cracked bottom ash kept constant, the 3# aggregate is replaced by cracked bottom ash. The combined aggregate is simply regarded as PSS-20. The proportion of PS-20, YZ-20, and PSS-20 combined aggregates is shown in Table 3. As shown in Figure 2, the gradation of different designed mixtures (LZ-0, PS-20, YZ-20, and PSS-20) is similar to each other [27], which all meet the requirement (JTJG D50-2006). In addition, the cement content accounts for 4% of combined aggregates. According to JTJG E51-2009, the maximum dry density and the optimum water content of PS-20, YZ-20, and PSS-20 combined aggregates with cement content 4% were determined by the compaction tests. The maximum dry density of LZ-0, PS-20, YZ-20, and PSS-20 is  $2.401 \text{ g}/\text{cm}^3$ ,  $2.293 \text{ g}/\text{cm}^3$ ,  $2.293 \text{ g}/\text{cm}^3$ , and  $2.308 \text{ g}/\text{cm}^3$ , respectively. The corresponding optimum water contents are 5.3%, 5.1%, 5.1%, and 5.2% [27].

Limestone aggregate, cracked bottom ash, original bottom ash, and OPC samples were oven-dried at  $105^\circ\text{C}$  for 24 hours ( $h$ ) (101-A, Leao, China). Subsequently, they were cooled down to room temperature in a desiccator. In order to mix thoroughly, the limestone aggregates and cement were first homogenized with cracked bottom ash or original bottom ash at three different ratios (as shown in Table 3 by dry mass) manually in the vessel. According to the optimum water content, the distilled water produced by a water distillation apparatus (JYCS-0.02 T, China) was added slowly into the dry mix for the mixing process. After the

TABLE 3: Proportion of combined aggregates (%).

Combined aggregates	Limestone aggregate				Crushed bottom ash	Original bottom ash
	1#	2#	3#	4#		
PS-20	47	14.7	6	15.6	16.7	/
YZ-20	42.2	14.6	8.4	18.1	/	16.7
PSS-20	47	14.7	/	21.6	16.7	/

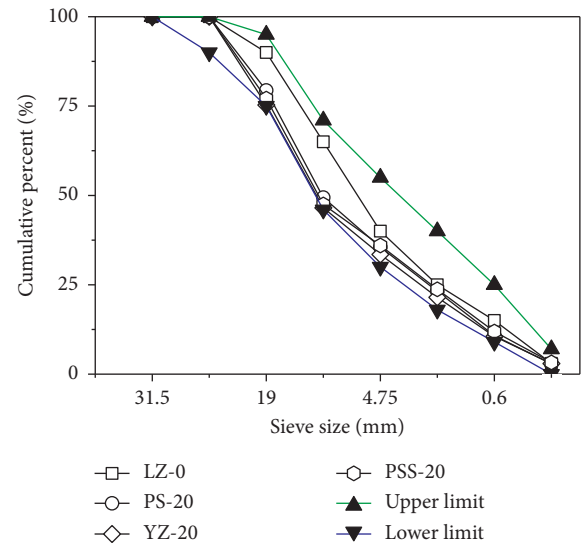


FIGURE 2: Grain size distributions of LZ-0, PS-20, YZ-20, and PSS-20 and standard limits.

mixing procedure, the mixture was transferred into the molds ( $\Phi 150 \text{ mm} \times h 150 \text{ mm}$ , Boyuan, China) with 98% of the maximum dry density at the optimum moisture content. Afterwards, the samples were demolded and wrapped by the polyethylene film. After the period, the mixtures were cured ( $\geq 95\%$  humidity,  $20 \pm 2^\circ\text{C}$ ) for 7, 14, and 28 days in the standard curing room (BYS-40, Huanan, China).

Electrohydraulic pressure-testing machine (DYE-2000, Huaxi, China) was used to obtain the compressive strength ( $f_{cu}$ ) of samples. The diameter of loading platform was 15 cm, and the range was fixed at 0~20000 kN during the test. Total maximum loads were recorded, and the compressive strength was determined using the following formula:

$$f_{cu} = \frac{F}{A} \quad (1)$$

where  $F$  is the total maximum load (N) and  $A$  is the area of loaded surface ( $\text{mm}^2$ ) [1]. Meanwhile, the failure strain ( $\varepsilon_f$ ) was measured by displacement meter (KTR11, MIRAN, China). Six replicates were analyzed for each trial.

**2.3. Numerical Simulation Model.** The roadbase is a supporting layer for road structure. Its main function is to bear the traffic load and disperse the stress generated from pavement surface to underlying layers [28–31]. At present, semirigid base course materials (e.g., cement-, lime-, or fly ash-stabilized aggregates) are widely used in highway construction.

This research adopts the MIDAS/GTS finite element software to simulate cemented aggregate containing bottom ash used in ordinary municipal roadbase. The influence of mix proportion, roadbase thickness, and vehicle load on the structural deformation of the road surface is analyzed. In this paper, the schematic plot of road structure is shown in Figure 3. The simulation was made on an axisymmetric finite element model [32].

In this model, the road width is 5 meters. The calculation range of the soil foundation is triple the distance of the half road surface. The calculation depth of the model is from the pavement to 3 meters below the surface in the model. The pavement structure consists of some layers as follows: asphalt layer, cement-treated aggregate containing bottom ash, and soil foundation. The basic dimensions and parameter of model (constitutive model, thickness, and basic properties of each layer) are shown in Table 4.

In pavement structure design, it is generally assumed that the axial load is uniformly distributed on the contact area [33]. In BZZ-100 standard axle load, axle load is 100 kN and contact pressure is 0.7 MPa. The contact area of wheels and road surface is  $0.134 \text{ m}^2$  (JTG D50-2006). The road position is shown in Figure 3, and the radius is 0.152 m in a single round contact.

The subsidence of the simulated surface of the road is only caused by the traffic axle load. Model boundary conditions are that the bottom boundary is completely fixed and that the side boundary is horizontal fixed. The model assumes this simulation is a plane strain problem.

Note that the development of elastic modulus may be inferred from the characteristics of strength development. Lim and Dan investigated relationship between the measured compressive strength and elastic modulus of cemented aggregate containing bottom ash mixtures [34]. Equation (2) is used for predicting elastic modulus of cemented aggregate containing bottom ash materials [34]:

$$E = 635.26 \cdot (16.0256w)^{1.5} \cdot (0.0069f_{cu})^{0.75}, \quad (2)$$

where  $E$  is the elastic modulus (MPa);  $w$  is the mixture density ( $\text{g/cm}^3$ ); and  $f_{cu}$  is the unconfined compressive strength (MPa) after 28 days' curing. The elastic modulus is applied to the numerical simulation in this paper.

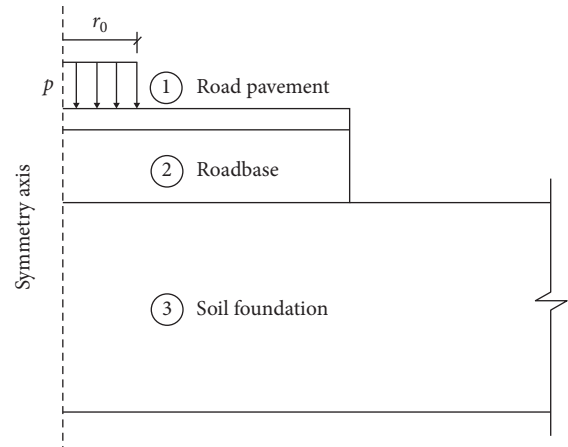


FIGURE 3: Schematic plot of road structure.

### 3. Experimental Results and Analysis

The unconfined compressive strength values and the failure strain of the cemented aggregate containing bottom ash sample under different curing periods are presented in Figures 4 and 5, respectively.

The unconfined compressive strength of samples increase with the curing time, while the failure strain of samples decrease with the curing time. The unconfined compressive strength and failure strain of samples are also influenced by the types of bottom ash. Compared to the 7 days' curing, the compressive strength of LZ-0, YZ-20, PS-20, and PSS-20 after 14 days' curing increased by 47.8%, 23.9%, 31.1%, and 30.3%, and the failure strain of YZ-20, PS-20, and PSS-20 decreased by 20.6%, 16.8%, and 22.9%. After 28 days' curing, the compressive strength of LZ-0, YZ-20, PS-20, and PSS-20 increased by 73.9%, 49.9%, 41.7%, and 47.8%, and the failure strain of YZ-20, PS-20, and PSS-20 decreased by 27.3%, 22.5%, and 21.1%.

Figures 4 and 5 show that the compressive strength of mixtures increases and the failure strain decreases with the curing time. This is because the hydration reaction is more adequate with a longer curing time. During the period of cement hydration reaction, two processes are involved. One is through-solution hydration, which involves several factors such as dissolution of anhydrous compounds into their ionic constituents, formation of hydrates in the solution, and eventual precipitation of hydrates from the supersaturated solution. The other is solid-state hydration of cement, and the reactions occur directly at the surface of the hydrous cement compounds. During this period, no compounds dissolve into solution. In the early stage of cement hydration, through-solution hydration is dominant. At the poststage of cement hydration, the hydration of residual cement particles may occur by the solid-state reactions, and the migration of ions in the solution becomes restricted [35]. As presented in Figure 4, LZ-0 has higher compressive strength values than other materials at all the three curing times. The reason is that the strength of the bottom ash is lower than that of the limestone aggregate, and the partial replacement of limestone aggregate

TABLE 4: Parameters of finite element model.

Material	① Asphalt mixture	② Cemented aggregate containing bottom ash	③ Silty clay
Constitutive model	Elasticity	Elasticity	Mohr–Coulomb
Thickness (m)	0.18	0.4	2.42
Bulk density (kN/m <sup>3</sup> )	19.6	22.9	17.4
Elasticity modulus (MPa)	1400	13823	22
Cohesive force (kPa)	/	/	24
Internal friction angle (°)	/	/	30
Poisson's ration	0.25	0.2	0.32

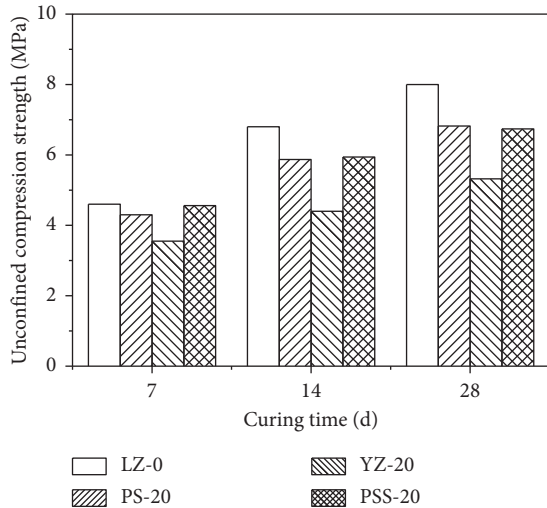


FIGURE 4: The unconfined compression strength of samples under different conditions (mixture ratio and curing time).

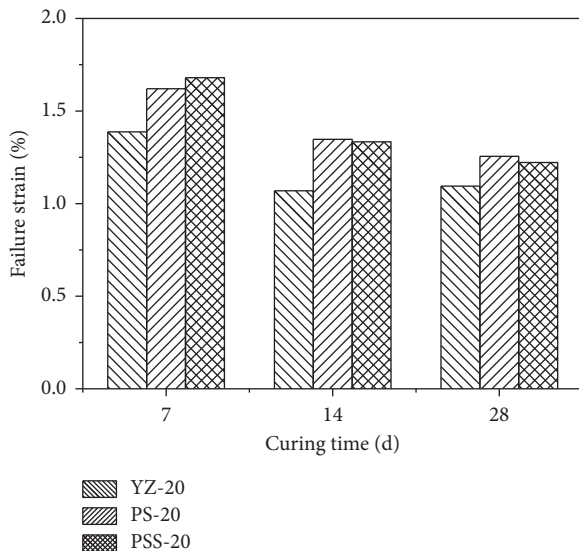


FIGURE 5: The failure strain of samples under different conditions (mixture ratio and curing time).

affects the compressive strength of the sample. According to Table 2, the crushing value of bottom is lower than the limestone aggregate, which further explains the strength of LZ-0 is higher than other samples [27].

The unconfined compressive strength of mixtures and the failure strain are influenced by the types of bottom ash. Compared to the YZ-20 samples, PS-20 samples and PSS-20 samples have higher strength under the same condition. This is because PS-20 samples and PSS-20 samples have more 1# and 2# limestone aggregate than YZ-20 samples from Table 3. The strength of the granular material grows with the increase of the maximum particle size, especially for comparable gradation curves [36]. The unconfined compressive strength of samples PSS-20 is slightly higher than that of samples PS-20, under the same condition. According to Table 3, PSS-20 has more fine aggregate than PS-20. The fine aggregate has a certain viscosity and plasticity, which will affect the suction in the structure. Meanwhile, the increase of fine particle content results in a higher suction and pore-filling degree and increases the stability between coarse aggregates [22], which further explains that the unconfined compressive strength of samples PSS-20 is slightly higher. Because of premature destruction of large-sized original bottom, the failure strain of the original bottom ash samples is lower than that of the cracked bottom ash samples at the same age.

When the bottom ash content is 20% and the cement content is 4%, the representative value (7 days) of the unconfined compressive strength are 3.35~4.56 MPa, which can meet the strength requirement ( $\geq 2.5$  MPa) of the road subbase layer of heavy traffic highway in China. Under the same condition, the samples containing cracked bottom ash also meet the strength requirements ( $\geq 3.5$  MPa) of the subbase layer and the base layer (JTG/T F20-2015).

#### 4. Simulation Results and Analysis

This research used the cement-treated aggregate containing bottom ash as roadbase and explored the influence of base modulus, base thickness, and vehicle load on settlement deformation of pavement.

**4.1. Analysis of the Influence of Roadbase Modulus.** Due to the cemented aggregate containing bottom ash sample with different conditions, the elasticity moduli of roadbase also vary in most cases. According to the experimental results, the elasticity moduli of cemented aggregate containing bottom ash of LZ-0, PSS-20, PS-20, and YZ-20 after 28 days' curing are 17267 MPa, 14311 MPa, 13823 MPa, and 11867 MPa. Figure 6 shows the surface settlement of pavement using different roadbase materials.

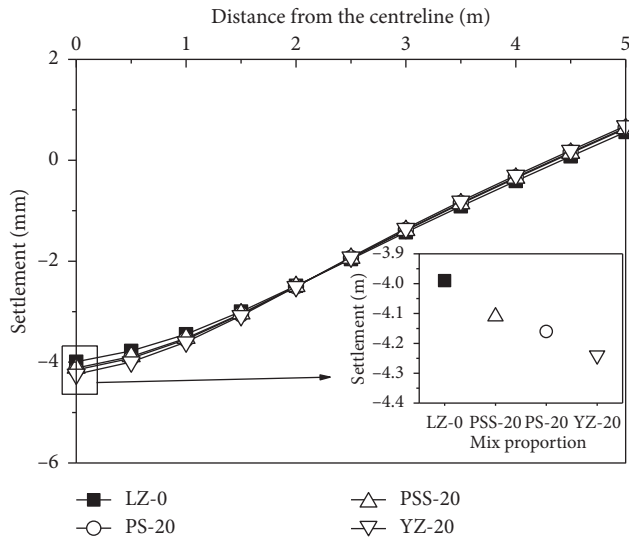


FIGURE 6: Settlement of the pavement with different base materials.

The surface settlement of the pavement decreases when increasing the elastic modulus and also decreases when the distance is away from the load center. Compared to the load center, the settlement of pavement that is 2.5 meter away from the center reduces by 50% approximately, and the settlement at the edge decreases by 115–145%. Compared to LZ-0, the use of YZ-20, PS-20, and PSS-20 increases the settlement of pavements at the load center by 6.2%, 4.1%, and 3.2%. This indicates that different combinations of aggregates (LZ-0, YZ-20, PS-20, and PSS-20) have negligible effects on pavement settlement. Therefore, the modulus of the roadbase is not the primary factor affecting the pavement settlement, if the base material meets the standard requirements.

**4.2. Analysis of the Influence of Roadbase Thickness.** According to the JTG D50-2006, the minimum compaction thickness of the single cemented structure layer is 150 mm. In this paper, the base and subbase layer are merged into one layer. The designed thickness of the roadbase layer is 300 mm, 400 mm, and 500 mm, respectively. The settlement of pavement with different thickness of the roadbase layer is shown in Figure 7.

The surface settlement of the pavement with different roadbase thicknesses decreases with increasing roadbase thickness and distance away from the centerline. Compared to the center settlement for 300 mm thick roadbase, the center settlement for 400 mm and 500 mm thick roadbase decreases by 15.8% and 27.9%, respectively. Compared to the surface settlement at the center, the settlement at the edge with 300 m, 400 mm, and 500 mm roadbase thickness decreases by 116.5%, 115.5%, and 109.9%, respectively. The influence of the thickness of roadbase on the reduction of the surface settlement is more effective than the roadbase modulus.

**4.3. Analysis of the Influence of Traffic Load.** Considering the influence of traffic load on the settlement of the pavement,

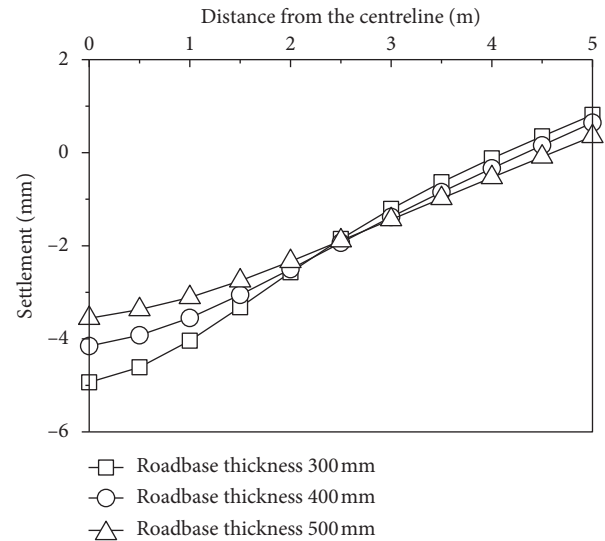


FIGURE 7: Settlement of the pavement with different roadbase thicknesses.

the designed axle load of the vehicle is  $p = 0.7$  MPa (BZZ-100 standard axle load),  $p = 1.05$  MPa (overload 50%), and  $p = 1.4$  MPa (overload 100%). The settlement of pavements with different traffic loads are shown in Figure 8.

The surface settlement of the pavement with different loads decreases with increasing the distance away from the centerline and increases with increasing the traffic load. Compared to the surface settlement at the center, the settlement of the pavement (2.5 meter away from the center) with standard axle load, overload 50%, and overload 100% increases by 53.4%, 53.5%, and 52.6%; the settlement of the pavement at the edge with standard axle load, overload 50%, and overload 100% increases 115.5%, 116.0%, and 116.7%. Compared to the surface settlement with BZZ-100 standard axle load, the surface settlement with overload 50%, 100% increases by 51.2%, 103.7%. Under this scenario, the pavement settlement at the centerline  $o$  is linearly proportional to the axle load.

## 5. Conclusions

- (1) Municipal solid waste bottom ash is suitable to use as roadbase materials to partially replace aggregates. The physical properties and the designed gradation of aggregate-bottom ash mixtures (LZ-0, PS-20, YZ-20, and PSS-20) meet the standard requirements.
- (2) The unconfined compressive strength of cement-treated aggregate containing bottom ash samples increases with curing time, and the failure strain decreases with curing time. Under the same condition, the strength of samples with original bottom ash was significantly lower than that within cracked bottom ash samples. The unconfined compressive strength representative value (7 days) could meet the strength requirement of the subbase and base layer of heavy traffic highway in China.

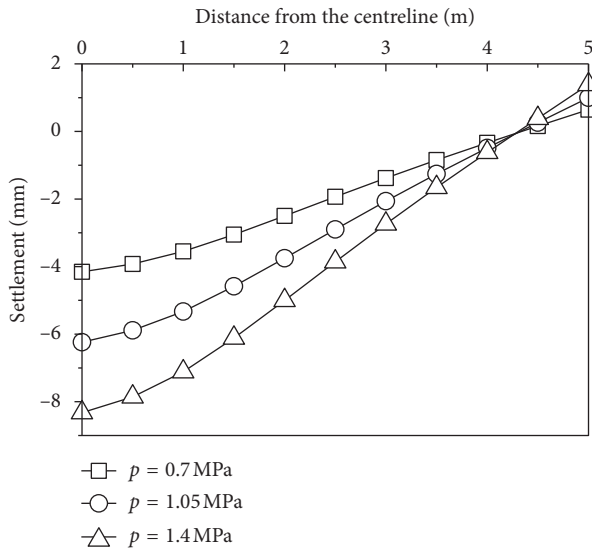


FIGURE 8: Settlement of the pavement with different axle loads.

- (3) The surface settlement decreases with the increase of base modulus, base thickness, and distance away from the centerline, but increases with increasing traffic loads. The modulus of the roadbase was not the primary factor affecting the pavement settlement, if the base material meets the standard requirements. The influence of the thickness of roadbase on the reduction of surface settlement is more effective than the roadbase modulus.

## Data Availability

The data used to support the findings of this study are available from the corresponding author upon request.

## Conflicts of Interest

The authors declare that there are no conflicts of interest regarding the publication of this paper.

## Acknowledgments

This research was supported by the National Nature Science Foundation of China (51708377 and 41630633), Natural Science Foundation of Jiangsu Province (BK20170339), China Postdoctoral Science Foundation funded project (2016M591756), Natural Science Fund for Colleges and Universities in Jiangsu Province (17KJB560008), Jiangsu Planned Projects for Postdoctoral Research Funds (1601175C), and project from Jiangsu Provincial Department of Housing and Urban-Rural Development (2016ZD18). This research was also supported by the Jiangsu Provincial Transport Bureau (2016T05), Six Talent Peaks Project in Jiangsu Province, China (2015-JNHB-018), and Bureau of Housing and Urban-Rural Development of Suzhou.

## References

- [1] Q. Tang, W. Liu, H. Y. Wang, R. Cheng, and Y. F. Qian, "Membrane behavior of bentonite-amended Fukakusa clay under K, Na and Ca solutions," *Journal of Central South University*, vol. 23, no. 12, pp. 3122–3131, 2016.
- [2] Q. Tang, T. Katsumi, T. Inui, and Z. Z. Li, "Influence of pH on the membrane behavior of bentonite amended Fukakusaclay," *Separation and Purification Technology*, vol. 141, pp. 132–142, 2015.
- [3] Q. Tang, F. Gu, Y. Zhang, Y. Q. Zhang, and J. L. Mo, "Impact of biological clogging on the barrier performance of landfill liners," *Journal of Environmental Management*, vol. 222, pp. 44–53, 2018.
- [4] Q. Tang, H. J. Kim, K. Endo, T. Katsumi, and T. Inui, "Size effect on lysimeter test evaluating the properties of construction and demolition waste leachate," *Soils and Foundations (JGS)*, vol. 55, no. 4, pp. 720–736, 2015.
- [5] Q. Tang, T. Katsumi, T. Inui, and Z. Z. Li, "Membrane behavior of bentonite amended compacted clay," *Soils and Foundations (JGS)*, vol. 54, no. 3, pp. 329–344, 2014.
- [6] H. U. Hartenstein and M. Horvay, "Overview of municipal waste incineration industry in west Europe (based on the German experience)," *Journal of Hazardous Materials*, vol. 47, no. 1–3, pp. 19–30, 1996.
- [7] Y. L. Galiano, C. F. Pereira, and J. Vale, "Stabilization/solidification of a municipal solid waste incineration residue using fly ash-based geopolymers," *Journal of Hazardous Materials*, vol. 185, no. 1, pp. 373–381, 2011.
- [8] K. Anastasiadou, K. Christopoulos, E. Mousios, and E. Gidaracos, "Solidification/stabilization of fly and bottom ash from medical waste incineration facility," *Journal of Hazardous Materials*, vol. 207–208, no. 6, pp. 165–170, 2012.
- [9] Waste treatment in Japan, Ministry of Environment, Waste Management and Recycling Unit, 2011, in Japanese.
- [10] Q. Tang, Y. Liu, F. Gu, and T. Zhou, "Solidification/stabilization of fly ash from a municipal solid waste incineration facility using Portland cement," *Advances in Materials Science and Engineering*, vol. 2016, Article ID 7101243, 10 pages, 2016.
- [11] Q. Tang, Y. Zhang, Y. F. Gao, and F. Gu, "Use of cement-chelated, solidified, municipal solid waste incinerator (MSWI) fly ash for pavement material: mechanical and environmental evaluations," *Canadian Geotechnical Journal*, vol. 54, no. 11, pp. 1553–1566, 2017.
- [12] M. Margallo, M. B. M. Taddei, A. Hernández-Pellón, R. Aldaco, and A. Irabien, "Environmental sustainability assessment of the management of municipal solid waste incineration residues: a review of the current situation," *Clean Technologies and Environmental Policy*, vol. 17, no. 5, pp. 1333–1353, 2015.
- [13] Q. Tang, F. Gu, Y. F. Gao, T. Inui, and T. Katsumi, "Desorption characteristics of Cr(III), Mn(II) and Ni(II) in contaminated soil using citric acid and citric acid containing wastewater," *Soils and Foundations (JGS)*, vol. 58, no. 1, pp. 50–64, 2018.
- [14] Q. Tang, X. W. Tang, M. M. Hu, Z. Z. Li, Y. M. Chen, and P. Lou, "Removal of Cd(II) from aqueous solution with activated Firmiana Simplex Leaf: behaviors and affecting factors," *Journal of Hazardous Materials*, vol. 179, no. 1–3, pp. 95–103, 2010.
- [15] D. S. Kosson, H. A. V. D. Sloop, and T. T. Eighmy, "An approach for estimation of contaminant release during

- utilization and disposal of municipal waste combustion residues,” *Journal of Hazardous Materials*, vol. 47, no. 1–3, pp. 43–75, 1996.
- [16] C. C. Wiles, “Municipal solid waste combustion ash: state-of-the-knowledge,” *Journal of Hazardous Materials*, vol. 47, no. 1–3, pp. 325–344, 1996.
- [17] R. Forteza, M. Far, C. Seguí, and V. Cerda, “Characterization of bottom ash in municipal solid waste incinerators for its use in road base,” *Waste Management*, vol. 24, no. 9, pp. 899–909, 2004.
- [18] C. Ferreira, A. Ribeiro, and L. Ottosen, “Possible applications for municipal solid waste fly ash,” *Journal of Hazardous Materials*, vol. 96, no. 2, pp. 201–216, 2003.
- [19] D. Q. Zhang, S. K. Tan, and R. M. Gersberg, “Municipal solid waste management in China: status, problems and challenges,” *Journal of Environmental Management*, vol. 91, no. 8, pp. 1623–1633, 2010.
- [20] S. Sakai, S. E. Sawell, A. J. Chandler, T. T. Eighmy, D. S. Kosson, and J. Vehlow, “World trends in municipal solid waste management,” *Waste Management*, vol. 16, no. 5–6, pp. 341–350, 1996.
- [21] R. Sinquin, G. Valentis, and I. Pari, “Testing and use of bottom ash in France,” in *Proceedings of 7th International Conference on Municipal Solid Waste Combustor Ash Utilization*, pp. 32–48, Arlington, VA, USA, 1997.
- [22] U. Müller and K. Rübner, “The microstructure of concrete made with municipal waste incinerator bottom ash as an aggregate component,” *Cement and Concrete Research*, vol. 36, no. 8, pp. 1434–1443, 2006.
- [23] M. Arm, “Variation in deformation properties of processed MSWI bottom ash: results from triaxial tests,” *Waste Management*, vol. 24, no. 10, pp. 1035–1042, 2004.
- [24] M. Abdulahi, “Municipal solid waste incineration bottom ash as road construction material,” *AU Journal of Technology*, vol. 13, no. 2, pp. 121–128, 2009.
- [25] X. G. Li, Y. Lv, B. G. Ma, Q. B. Chen, X. B. Yin, and S. W. Jian, “Utilization of municipal solid waste incineration bottom ash in blended cement,” *Journal of Cleaner Production*, vol. 32, pp. 96–100, 2012.
- [26] H. Zhang, P. J. He, L. M. Shao, and X. J. Li, “Leaching behavior of heavy metals from municipal solid waste incineration bottom ash and its geochemical modeling,” *Journal of Material Cycles and Waste Management*, vol. 10, no. 1, pp. 7–13, 2008.
- [27] D. Liu, L. Li, and H. Cui, “Pavement performance of cement stabilized municipal solid waste incineration bottom ash aggregate and crushed stones,” *Journal of Tongji University*, vol. 43, no. 3, pp. 405–415, 2015.
- [28] F. Gu, Y. Zhang, C. V. Drodody, R. Luo, and R. L. Lytton, “Development of a new mechanistic empirical rutting model for unbound granular material,” *Journal of Materials in Civil Engineering*, vol. 28, no. 8, article 04016051, 2016.
- [29] J. Zhang, J. Peng, J. Li, and J. Zheng, “Characterization of stress and moisture-dependent resilient behaviour for compacted clays in South China,” *Road Materials and Pavement Design*, pp. 1–14, 2018.
- [30] J. Zhang, J. Li, Y. Yao, J. Zheng, and F. Gu, “Geometric anisotropy modeling and shear behavior evaluation of graded crushed rocks,” *Construction and Building Materials*, vol. 183, pp. 346–355, 2018.
- [31] F. Gu, H. Sahin, X. Luo, R. Luo, and R. Lytton, “Estimation of resilient modulus of unbound aggregates using performance-related base course properties,” *Journal of Materials in Civil Engineering*, vol. 27, no. 6, article 04014188, 2014.
- [32] F. Gu, X. Luo, R. Luo, R. L. Lytton, E. Y. Hajj, and R. V. Siddharthan, “Numerical modeling of geogrid-reinforced flexible pavement and corresponding validation using large-scale tank test,” *Construction and Building Materials*, vol. 122, pp. 214–230, 2016.
- [33] K. Himeno, T. Kamijima, T. Ikeda, and T. Abe, “Distribution of tire contact pressure of vehicles and its influence on pavement distress,” in *Proceedings of Eighth International Conference on Asphalt Pavements Federal Highway Administration*, Seattle, WA, USA, August 1997.
- [34] S. Lim and G. Z. Dan, “Estimation of the compressive strength and modulus of elasticity of cement-treated aggregate base materials,” *Transportation Research Record Journal of Transportation Research Board*, vol. 1837, no. 1, pp. 30–38, 2003.
- [35] P. K. Mehta and P. J. M. Monteiro, *Concrete: Microstructure, Properties, and Materials*, McGraw-Hill Education, New York City, NY, USA, 4th edition, 2014.
- [36] P. Chindaprasirt, S. Hatanaka, N. Mishima, Y. Yuasa, and T. Chareerat, “Effects of binder strength and aggregate size on the compressive strength and void ratio of porous concrete,” *International Journal of Minerals, Metallurgy and Materials*, vol. 16, no. 6, pp. 714–719, 2009.

## Research Article

# Exploration of Mechanisms of Joint Deterioration in Concrete Pavements regarding Interfacial Transition Zone

Xin Wang,<sup>1</sup> Jiake Zhang ,<sup>2</sup> Xuhao Wang ,<sup>3,4</sup> Peter Taylor,<sup>5</sup> Kejin Wang,<sup>6</sup> and Xinjian Sun<sup>7,8</sup>

<sup>1</sup>Ph.D. Student, Civil, Construction and Environmental Engineering, Town Engineering Building, Iowa State University, Ames, Iowa 50014, USA

<sup>2</sup>Research Associate, College of Transportation Engineering, Tongji University, Shanghai, China

<sup>3</sup>Associate Research Scientist, Qinghai University-Tsinghua University Sanjiangyuan University Sanjiangyuan Research Institute, Qinghai University, Xinning, China

<sup>4</sup>Associate Professor, School of Highway Chang'an University, Xi'an, China

<sup>5</sup>Director, National Concrete Pavement Technology Center, Ames, Iowa 50014, USA

<sup>6</sup>Professor, Civil, Construction and Environmental Engineering, Town Engineering Building, Iowa State University, Ames, Iowa 50014, USA

<sup>7</sup>Associate Professor, School of Hydraulic and Electric Engineering, Qinghai University, Xinning, China

<sup>8</sup>State Key Laboratory of Plateau Ecology and Agriculture, Xinning, China

Correspondence should be addressed to Xuhao Wang; wangxh@chd.edu.cn

Received 26 February 2018; Accepted 16 September 2018; Published 27 November 2018

Guest Editor: Jinchang Wang

Copyright © 2018 Xin Wang et al. This is an open access article distributed under the Creative Commons Attribution License, which permits unrestricted use, distribution, and reproduction in any medium, provided the original work is properly cited.

As a common issue for cold weather regions, premature deterioration of concrete at joints has been reported in many states. In this paper, the mechanisms of joint deterioration were investigated, and then, experimental investigations were conducted to further verify some of the mechanisms. It was found that freeze-thaw (F-T) damage and salt crystallization are not enough to cause the observed deterioration, but the deterioration near the interfacial transition zone (ITZ) may be the cause of some of the observed phenomena. In the experimental work, samples were tested at 40°F in salt solutions to observe the deterioration in the ITZ using the scanning electron microscope (SEM). Concrete tested in MgCl<sub>2</sub> solution indicated distress in ITZ under SEM. It was found that ITZ may act as a shortcut for ion transfer to surrounding concrete near the joints and may also be the weak point for cracking due to expansion of the paste.

## 1. Introduction

Sawn joints in concrete pavements are used to control both transverse and longitudinal cracking, which are induced by shrinkage or contraction of the pavement. According to the American Concrete Pavement Association [1], an efficient joint system should accommodate slab movements, transfer load between pavement segments, and divide the concrete slab into practical construction increments. Contraction joints are normally made by saw cutting, with a minimum depth of ¼ the thickness of slab but not less than 25.4 mm and a minimum width of 3.18 mm. Saw cutting is conducted when the concrete is mature enough to be cut without

spalling, but not too late to allow random cracks in the slab. A sealant is often placed to prevent water from getting into the joint. However, sealants may deteriorate and so allow water to penetrate the saw cut over time, thus increasing the risk of damage within the kerf.

Performance and service life of concrete pavements are heavily dependent on the performance of the joints. Hence, premature joint deterioration is a great concern, particularly in cold weather regions. Figure 1 shows multiple forms of pavement joint deterioration observed in different states [2]. To control or eliminate such pavement deterioration, it is necessary to understand the mechanisms of joint damage.

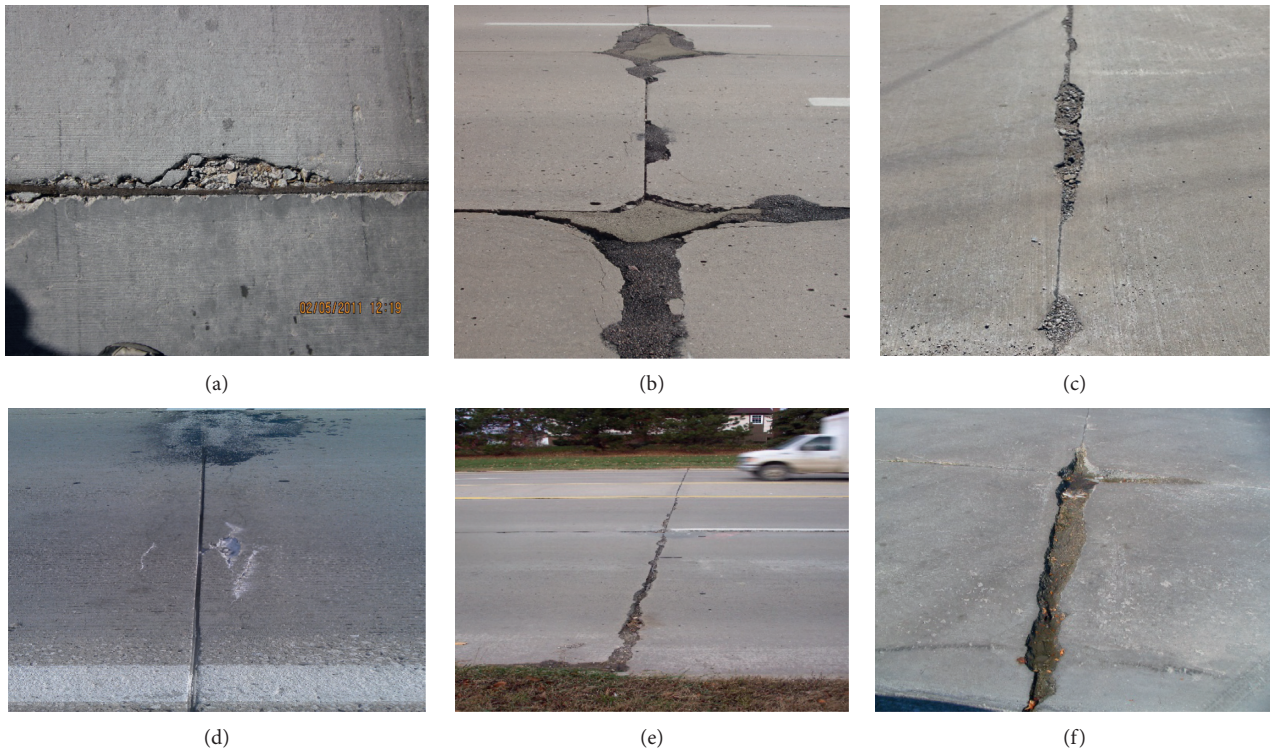


FIGURE 1: Photos of joint deterioration from multiple states. (a) Arizona, 2011. (b) Colorado, 2010. (c) Illinois, 2014. (d) Kansas, 2012. (e) Missouri, 2005. (f) Nebraska, 2010.

The objective of this research was to review the current state of knowledge of possible causes of joint deterioration and further investigate the mechanism behind this form of deterioration.

## 2. Mechanisms of Joint Deterioration

Damage is typically observed in two different forms. The first is the formation of small flakes in the paste near the joint (Figure 2(a)). The other form is where cracks form about 25.4 mm from the exposed face, and exposed aggregate particles are observed (Figure 2(b)). In the latter case, the concrete between the crack and the face is often in good condition. Typically, the crack will form around the coarse aggregate leaving it unusually free of mortar. The cause of this distress has been less well understood.

The current knowledge of joint deterioration indicates that there are four major mechanisms by which concrete joints may deteriorate:

- (1) Freezing-thawing (F-T) damage
- (2) Salt crystallization
- (3) Oxychloride expansion
- (4) Interfacial transition zone damage

**2.1. Freezing-Thawing Damage.** It is widely accepted that the freeze-thaw mechanism is typically associated with concrete that contains marginal air-void systems that are exposed to

abundant moisture. Moisture in a joint may be higher than that at the surface because water is trapped due to insufficient drainage of the base layer or the cracks not opening up. Li et al. [3] have observed that for samples with a degree of saturation higher than a critical value of 86–88%, concrete may exhibit damage in a few freeze-thaw cycles. They also found that saturated concrete is unable to resist cyclic F-T, regardless of the air content of concrete, although a properly entrained-air system is effective at delaying critical saturation.

**2.2. Salt Crystallization.** Deicing salts are applied to roadways in areas that experience snow and ice in order to ensure the safety of traffic on roadways. Salts in pore solutions may crystallize out and form crystals due to changes in external humidity or temperature. A state of supersaturation is required for crystallization to occur. Under supersaturation, the cumulative crystals generate stress on the confining pore walls and cause damage in the solid matrix of a concrete mixture [4]. Using an equation proposed by Correns in 1949 [5] which describes the growth and dissolution of crystals under pressure (Equation (1)), Thaulow and Sahu [4] concluded that potential pressure created by crystallization (159 atm) could be 5 to 10 times the tensile strength of concrete in their example:

$$P = \frac{RT}{V_s} * \ln \frac{C}{C_s}, \quad (1)$$

where  $P$  is the pressure exerted by growing crystals,  $R$  is the gas constant, 0.082 L-atm/mol,  $T$  is the absolute

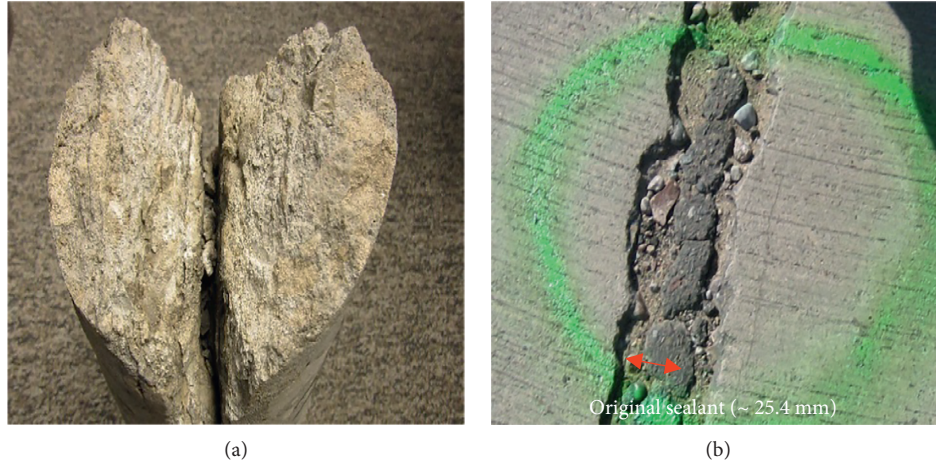
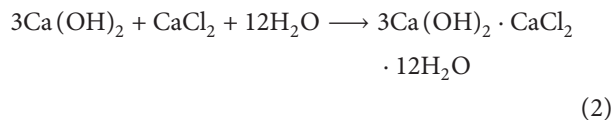


FIGURE 2: Typical F-T deterioration: (a) F-T damage and (b) joint deterioration.

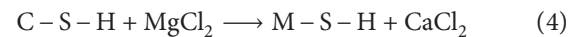
temperature,  $K$ ,  $V_s$  is the molar volume of solid salt in L/mole, and  $C/C_s$  is the degree of supersaturation, where  $C$  is the existing solute concentration and  $C_s$  is the saturation concentration.

**2.3. Oxychloride Formation.** Certain deicers contain chemicals that may deteriorate concrete pavement. Chloride deicers will increase the concentration of calcium and magnesium in pore water of concrete. At the same time, the chloride is able to react with cement paste and forming a new expansive phase that may be expansive, calcium chloride [6]. The expansive nature of calcium oxychloride can block the concrete pore connection, decrease the fluid transfer property in concrete, and influence the entire concrete matrix [6–8].

Formation of calcium oxychloride occurs at temperature just above freezing [6, 8]. Both calcium chloride and magnesium chloride can form calcium oxychloride by reacting with calcium hydroxide from the cement paste. Though various forms of calcium oxychloride can be produced based on environmental conditions such as temperature and relative humidity, a common reaction is illustrated in Equation (2). The reaction between magnesium chloride and calcium hydroxide is complex, producing not just calcium oxychloride but also magnesium chloride in secondary reactions [9]:

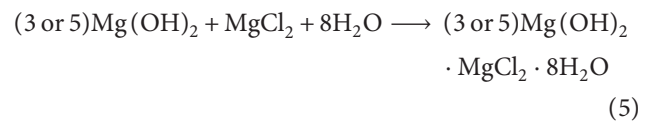


When  $\text{MgCl}_2$  is used as a deicer on concrete pavements, a reaction between  $\text{Ca}(\text{OH})_2$  from cement hydration and magnesium chloride will produce brucite ( $\text{Mg}(\text{OH})_2$ ) (Equation (3)). At the same time, the calcium in calcium silicate hydrate (C-S-H) will be replaced by magnesium to produce noncementitious magnesium silicate hydrate (M-S-H) (Equation (4)) [8]:



As the secondary reaction, brucite produced from Equation (3) will react with remaining  $\text{MgCl}_2$  to produce magnesium oxychloride (Equation (5)). Two phases of magnesium oxychloride are reported to exist, with either 3 or 5  $\text{Mg}(\text{OH})_2$  molecules ((3 or 5)  $\text{Mg}(\text{OH})_2 \cdot \text{MgCl}_2 \cdot 8\text{H}_2\text{O}$ ) [8].

$\text{CaCl}_2$  produced from Equation (3) may also contribute to formation of calcium oxychloride [10], and the process of calcium oxychloride formation is in a similar stepwise reaction as  $\text{MgCl}_2$  solutions (Equation (2)). Both calcium oxychloride and magnesium oxychloride have been reported to be expansive and destructive in the concrete system [8, 11]:



Formation of magnesium oxychloride is dependent on the concentration of magnesium chloride [12, 13]. M-S-H and  $\text{Mg}(\text{OH})_2$  are thermodynamically more stable than C-S-H and  $\text{Ca}(\text{OH})_2$ , so it is preferable for C-S-H and  $\text{Ca}(\text{OH})_2$  to change into M-S-H and  $\text{Mg}(\text{OH})_2$ , both of which are expansive. Monosi and Collepari also reported that the oxychloride formation proceeds faster at temperatures between 4 and 10°C, while Peterson et al. [13] proposed that a phase change of calcium oxychloride may occur between 0°C and 50°C.

**2.4. Interfacial Transition Zone Damage.** The interfacial transition zone (ITZ) in concrete is a 10–50  $\mu\text{m}$  zone between cement paste and coarse aggregates formed during hydration of cement particles against aggregate surfaces [14, 15]. ITZ has a higher porosity than bulk-hydrated cement paste. Due to the high porosity and their high connectivity, property of transportation of fluids is increased in the ITZ,

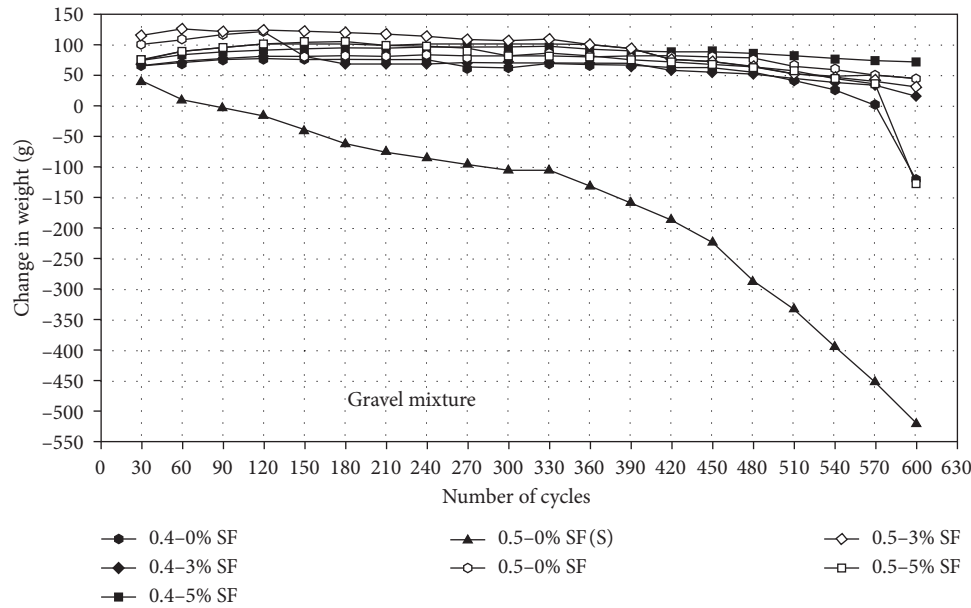


FIGURE 3: Weight change of beams for 600 freezing and thawing cycles (W/C ratio 0.4/0.5; silica fume content 0%, 3%, and 5%; 0.5-0% SF (S) sample with W/C = 0.5, 0% silica fume, soaked in NaCl).

facilitating movement of chloride ions [16] thus increasing the amount of paste that may react with the chlorides as discussed above.

In a previously reported project, Taylor et al. [17] observed mass loss in samples cycled in 3% sodium chloride solution using ASTM C666 (Figure 3). In comparing with samples with no silica fume, samples with an improved ITZ by silica fume were more durable. It was also reported that chloride and calcium ions appeared concentrated in the ITZ near the surface in these samples, indicating that the interfacial transition zone could be preferentially penetrated and attacked by deicers (Figure 4). They concluded that the ITZ is playing a significant part in the formation of incremental cracks about 25.4 mm from, and parallel to, the joint surface.

It is well known that the solubility of calcium solutions increases with decreasing temperature. It was hypothesized that, as temperatures are reduced in a freezing system, then an ITZ containing high amounts of  $\text{Ca}(\text{OH})_2$  might tend to dissolve more readily than the bulk C-S-H system nearby. Such dissolution would encourage separation of the coarse aggregate particles from the paste. In addition, chloride ions can penetrate into hydrated cement pastes [18], and leach out  $\text{Ca}(\text{OH})_2$ , consequently increasing porosity and susceptibility to freeze-thaw deterioration [19].

**2.5. Summary of Mechanisms.** The F-T damage and salt crystallization stresses discussed above can be quantified. Based on an equation proposed by Correns [5], Zhang [21] calculated the crystallization pressure to be about 2600 kPa in the ITZ. The osmotic pressure is about 1100 kPa according to Valenza and Scherer [20]. The total pressure due to these mechanisms is thus about 3700 kPa.

Figure 5 shows a deteriorated sample exposed to 3% NaCl solution, and part of aggregate on the corner is smooth and

clean with no mortar after 10 cycles of F-T. This is a concrete sample with 0.45 water-to-cementitious material ratio and 10% silica fume. The flexural strength of the sample was likely above 4500 kPa [22] which is greater than the imposed stress. The cumulative pressure caused by osmotic pressure and salt crystallization is therefore not enough to cause the deterioration in Figure 5. This suggests that some other mechanism is in play, such as calcium oxychloride expansion, resulting in the paste being separated from the aggregate in the ITZ.

### 3. Materials and Methods

Therefore, the purpose of the work discussed below was to study whether the formation and expansion of oxychloride was a part of mechanism causing the deterioration observed in Figures 2 and 5.

**3.1. Materials, Mix Proportion, Curing Condition, and Specimen Preparation.** Materials used in this study include the following:

- (i) Coarse aggregate: one inch nominal maximum size of round gravel (specific gravity (SpG) = 2.66, absorption = 0.3%, and dry-rodded unit weight =  $1541 \text{ kg/m}^3$ )
- (ii) Fine aggregate: No. 4 sieve size nominal maximum size river sand (SpG = 2.68, absorption = 0.6%, and fineness modulus = 3.08)
- (iii) Portland cement: ASTM C150 Type I
- (iv) Supplementary cementitious materials (SCMs): ASTM C618 Class C fly ash and silica fume

Mixtures used in this study had a constant water-to-cementitious material ratio (w/cm) of 0.45 and

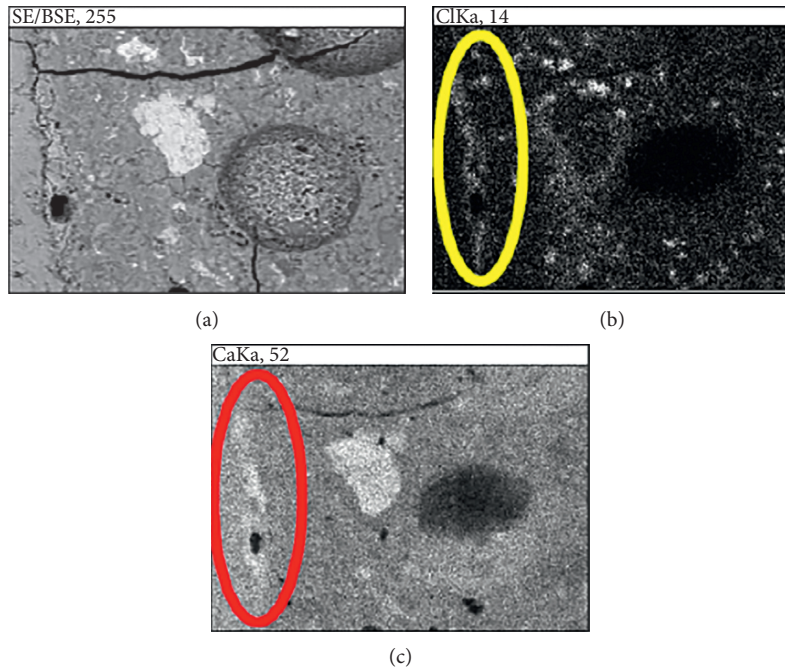


FIGURE 4: SEM map analysis on distressed samples under cyclic freeze thaw in  $\text{CaCl}_2$  (calcium and sodium).



FIGURE 5: Sample exposed to 3% NaCl solution showing washed aggregate on the corner.



FIGURE 6: Saw cut slice sample from concrete beam.

TABLE 1: Mixture proportions.

Material	Quantity
Cementitious materials ( $\text{kg}/\text{m}^3$ )	335
Type I cement	80%
C fly ash	20%
Water ( $\text{kg}/\text{m}^3$ )	151
Water-to-cementitious material ratio	0.45
Course aggregate ( $\text{kg}/\text{m}^3$ )	1125
Fine aggregate ( $\text{kg}/\text{m}^3$ )	666

a cementitious material content of  $335 \text{ kg}/\text{m}^3$ . Mixture parameters are shown in Table 1.

Concrete mixing and curing were conducted in accordance with ASTM C 192. Air content, slump, and unit weight were measured after mixing. Two  $7.6 \times 10.2 \times 40.6 \text{ cm}$  beams were cast from each mix. Sample preparation comprised 3 days wet curing followed by exposure to air until 28 days of age. Beams were cut into  $7.6 \times 10.2 \times 6.35 \text{ cm}$  prisms using



FIGURE 7: Samples partially immersed in deicers.

a diamond saw at 28 days (Figure 6). The section thickness was selected to increase the likelihood that a single aggregate, and its associated ITZ, would percolate from face to face thus accelerating distress effects associated with the ITZ.

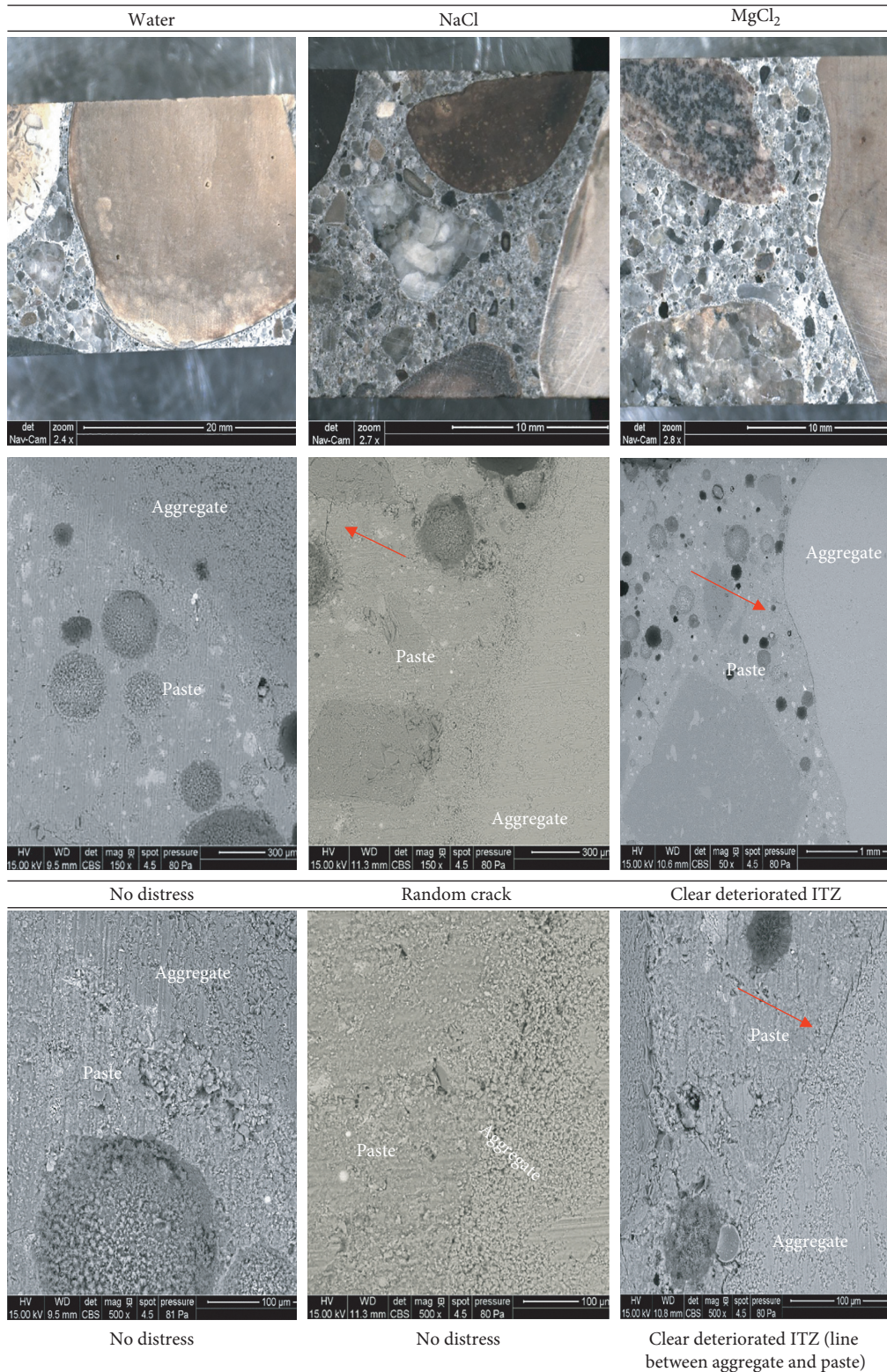


FIGURE 8: SEM images of sample soaked in water, NaCl, and MgCl<sub>2</sub> for 56 days.

All samples were vacuum saturated in accordance with ASTM C1202 for 24 hours using the following solutions: 3% sodium chloride (NaCl), 3% magnesium chloride (MgCl<sub>2</sub>), and water.

3.2. Test Procedures. Six slices were placed in a pan, partially submerged in assigned solutions (Figure 7), and stored at 4°C for 56 days. The low, constant temperature was selected to remove the effects of freezing, while enhancing potential



FIGURE 9: Photo of sample after 56 days in  $MgCl_2$ ; paste was pushed above aggregate.

dissolution of calcium compounds and formation of oxy-chloride compounds. The temperature was also selected based on distress reported by Sutter et al. [6]. Photos were taken regularly to track the condition of the sample surface. After 56 days of testing, specimens were split and polished before being examined in a scanning electron microscope. Samples were examined under FEI Quanta 250 FE-SEM at a voltage of 15 kV. SEM images from samples are presented in Figure 8.

#### 4. Results and Discussion

It is observed that the samples soaked in water did not exhibit any distress, as was expected, since no F-T cycles were applied. Likewise, neither osmotic pressure nor critical saturation should occur.

For samples soaked in NaCl, there was some micro-cracking in the paste matrix, and the zone between paste and aggregate was undamaged. A possible explanation for this damage is the reactions between aluminate phases of the matrix and deicer solutions [8].

SEM images of samples soaked in  $MgCl_2$  showed cracking in the boundary between aggregate and paste (Figure 8). In addition, Figure 9 shows that the paste was pushed above the aggregate, indicating expansion in the paste. It is likely that the damage is due to the paste expanding away from the aggregate particles. This type of deterioration was more prevalent closer to the face of the sample exposed to solution, which is consistent with distress being associated with solutions penetrating the system from an exposed face.

Zhang et al. [23] used the same mix proportions and materials to observe the influence of the ITZ on F-T resistance of concrete mixtures. Samples with 0, 5, and 10% silica fume were tested in a variety of salt solutions ( $NaCl$ ,  $MgCl_2$ ,  $CaCl_2$ , and water) in F-T cycles. They found that samples tested in water for 35 cycles remained in good condition. This indicated that the paste system was able to resist F-T cycling without becoming critically saturated as discussed in F-T damage.

For samples soaked in 3%  $MgCl_2$ , whole aggregate particles were observed to be removed in several samples

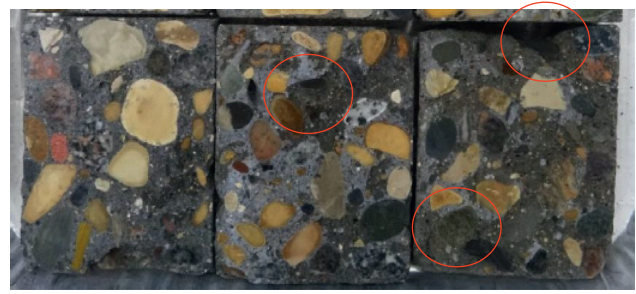
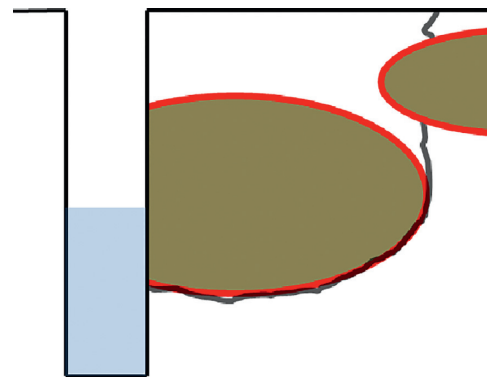


FIGURE 10: Samples exposed to  $MgCl_2$  solution during F-T. Left to right: 10%, 5%, and 0% silica fumes [23]; sample on right with no silica fume lost some aggregates during F-T.



(a)



(b)

FIGURE 11: Crack developing out of a saturated ITZ. (a) Schematic sketch of the theory. (b) Laboratory observation supporting the theory.

(Figure 10). This is again an indicative of aggregate particles being separated from the paste, likely due to expansion of the paste tied with damage in the ITZ.

To explain the phenomenon in Figure 2(b), the following mechanisms may be occurring:

- (i) Salt solution is trapped in the kerf of a sawn joint, either because it has not cracked out or the base material below the crack is impermeable.
- (ii) Salt solution is preferentially transported around coarse aggregate particles through the ITZ.

- (iii) Oxychloride compounds are formed in the paste around and near the aggregate particles.
- (iv) The paste expands, setting up tensile stresses and so cracking in the ITZ. Any dissolution of the ITZ will accelerate this damage.
- (v) Cracks are propagated under traffic through the paste to the top surface, typically parallel to and about 1.9 to 2.5 cm from the sawn face. Aggregates are either removed and left, paste free, loose in the joint, or remained in the concrete, projecting into the joint.

## 5. Conclusion

Joint deterioration in sawn pavements has been found in many cold regions of the United States. The major mechanisms by which concrete joints may deteriorate include (1) freezing-thawing (F-T) damage, (2) salt crystallization, and (3) oxychloride expansion. The interfacial transition zone (ITZ) between cement paste and aggregate permits more salt solution to penetrate around aggregate particles and potentially accelerates the joint deterioration.

By reviewing the previous work and testing samples subjected to soaking and F-T cycles, a mechanism has been described that explains the observed formation of so-called incremental cracks at joints. Solutions containing magnesium and calcium chloride appear to be penetrating the exposed ITZ around coarse aggregate particles in non-draining joints (Figure 11). The solution is reacting with hydrated cement paste to form oxychloride compounds near the aggregate particles. The paste expands, separating from the aggregates and causing cracks to propagate to the surface under traffic.

## Data Availability

The data generated from this research are available upon request to the corresponding author.

## Conflicts of Interest

The authors declare that they have no conflicts of interest.

## Acknowledgments

The present study is an extension of Dr. Jiake Zhang's PhD work "Investigation of deterioration of joints in concrete pavements" (2013). This work was funded by the National Concrete Pavement Center, Ames, Iowa. This study was also partially supported by the National Natural Science Foundation Project (NSFC 51868066) and the Qinghai Science & Technology Department Natural Science Foundation Project (2018-ZJ-931Q).

## References

- [1] American Concrete Pavement Association, *Design and Construction of Joints for Concrete Streets*, ACPA, Washington, DC, USA, 1992.
- [2] P. Taylor, L. Sutter, and J. Weiss, "Investigation of deterioration of joints in concrete pavements," Tech. Rep. 09-361, Iowa State University, Ames, IA, USA, 2012.
- [3] W. Li, M. Pour-Ghaz, J. Castro, and J. Weiss, "Water absorption and critical degree of saturation relating to freeze-thaw damage in concrete pavement joints," *Journal of Materials in Civil Engineering*, vol. 24, no. 3, pp. 299–307, 2012.
- [4] N. Thaulow and S. Sahu, "Mechanism of concrete deterioration due to salt crystallization," *Materials Characterization*, vol. 53, no. 2-4, pp. 123–127, 2004.
- [5] G. A. Julio-Betancourt, *Effect of de-icer and anti-icer chemicals on the durability, microstructure, and properties of cement-based materials*, Ph.D. dissertation, University of Toronto, Toronto, ON, Canada, 2009.
- [6] L. Sutter, K. Peterson, S. Houton, T. Van Dam, and D. Johnston, "Petrographic evidence of calcium oxychloride formation in mortar exposed to magnesium chloride solution," *Cement and Concrete Research*, vol. 36, no. 8, pp. 1533–1541, 2006.
- [7] W. A. Tasong, J. C. Cripps, and C. J. Lynsdale, "Aggregate-chemical interactions," *Cement and Concrete Research*, vol. 28, no. 7, pp. 1037–1048, 1998.
- [8] Y. Farnam, A. Wiese, D. Bentz, J. Davis, and J. Weiss, "Damage development in cementitious materials exposed to magnesium chloride deicing salt," *Construction and Building Materials*, vol. 93, pp. 384–392, 2015.
- [9] J. Weiss and Y. Farnam, "Concrete pavement joint deterioration recent findings to reduce the potential for damage," in *Map Brief June, CP Road Map*, FHWA, Washington, DC, USA, 2015.
- [10] H. Lee, R. D. Cody, A. M. Cody, and P. G. Spry, "Effects of various deicing chemicals on pavement concrete deterioration," in *Proceedings of Mid-Continent Transportation Symposium Proceeding*, p. 151, Ames, IA, USA, May 2000.
- [11] L. Sutter, T. Van Dam, K. R. Peterson, and D. P. Johnston, "Long-Term effects of magnesium chloride and other concentrated salt solutions on pavement and structural Portland and structural Portland cement concrete," *Journal of the Transportation Research Board*, vol. 1979, pp. 60–68, 2006.
- [12] S. Monosi and M. Collepardi, "Chemical attack of magnesium chloride on the Portland cement paste," *IL Cemento*, vol. 90, pp. 169–173, 1993.
- [13] K. Peterson, G. Julio-Betancourt, L. Sutter, R. D. Hooton, and D. Johnston, "Observations of chloride ingress and calcium oxychloride formation in laboratory concrete and mortar at 5°C," *Cement and Concrete Research*, vol. 45, pp. 79–90, 2013.
- [14] D. M. Roy, M. W. Grutzeck, D. Shi, and G. Lui, *Cement Paste Aggregate Interface Microstructure*, SHRP-C-629, 1993.
- [15] C. W. Correns, "Growth and dissolution of crystals under linear pressure," *Discussions of the Faraday Society*, vol. 5, pp. 267–271, 1949.
- [16] A. Delagrave, J. P. Bigas, J. P. Ollivier, J. Marchand, and M. Pigeon, "Influence of the interfacial transition zone on the chloride diffusivity of mortars," *Advanced Cement Based Materials*, vol. 5, no. 3-4, pp. 86–89, 1997.
- [17] P. Taylor, J. K. Zhang, and X. Wang, *Investigation of Deterioration of Joints in Concrete Pavements*, Tech. Rep. TPF-5(224), Iowa State University, Ames, IA, USA, 2015.
- [18] P. Gegout, E. Revertegat, and G. Moine, "Chloride ion attack on low water-cement ratio pastes containing silica fume," in *Proceedings of the Fourth International Conference on the Use of Fly Ash, Silica Fume, Slag and Natural Pozzolans in Concrete*, ACI SP-132, V. Malhotra, Ed., pp. 1471–1490, Istanbul, Turkey, 1992.

- [19] D. Hoffmann, "Changes in structure and chemistry of cement mortars stressed by a sodium chloride solution," *Cement and Concrete Research*, vol. 14, no. 1, pp. 49–56, 1984.
- [20] J. J. Valenza II and G. W. Scherer, "A review of salt scaling: II. Mechanisms," *Journal of Cement and Concrete Research*, vol. 37, no. 7, pp. 1022–1034, 2007.
- [21] J. Zhang, *Investigation of deterioration of joints in concrete pavements*, Ph.D. dissertation, Iowa State University, Ames, IA, USA, 2013.
- [22] S. Bhanja and B. Sengupta, "Influence of silica fume on the tensile strength of concrete," *Cement and Concrete Research*, vol. 35, no. 4, pp. 743–747, 2005.
- [23] J. Zhang, P. C. Taylor, and C. Shi, "Investigation of approaches for improving interfacial transition zone-related freezing-and-thawing resistance in concrete pavements," *ACI Materials Journal*, vol. 112, no. 5, 2013.

## Review Article

# The State-of-the-Art Review on Molecular Dynamics Simulation of Asphalt Binder

Xin Qu,<sup>1,2</sup> Dawei Wang ,<sup>1,2,3</sup> Linbing Wang ,<sup>4,5</sup> Yucheng Huang ,<sup>4</sup> Yue Hou ,<sup>3</sup>  
and Markus Oeser<sup>2</sup>

<sup>1</sup>School of Transportation Science and Engineering, Harbin Institute of Technology, Harbin 150090, China

<sup>2</sup>Institute of Highway Engineering, RWTH Aachen University, D52074 Aachen, Germany

<sup>3</sup>Department of Road and Railway Engineering, College of Metropolitan Transportation, Beijing University of Technology, Beijing 100124, China

<sup>4</sup>Gemini Technology, 3103 Harbors Avenue, Eggs Harbor, NJ 08315, USA

<sup>5</sup>Department of Civil Engineering, Virginia Polytechnic Institute and State University, Blacksburg, VA, USA

Correspondence should be addressed to Dawei Wang; wang@isac.rwth-aachen.de and Yue Hou; alladin@outlook.com

Received 22 February 2018; Revised 4 June 2018; Accepted 20 June 2018; Published 3 September 2018

Academic Editor: Xue Luo

Copyright © 2018 Xin Qu et al. This is an open access article distributed under the Creative Commons Attribution License, which permits unrestricted use, distribution, and reproduction in any medium, provided the original work is properly cited.

Asphalt pavement has been widely used in the world. As the main components of asphalt pavement, the asphalt binder is crucial to the service performance and life of the road. In the past decades, numerous studies were conducted on technical performance, aging, and modification of the asphalt binder. With the development of modern technology, it was discovered that the microscopic properties, aging mechanism, and modification mechanism of the asphalt binder affect the macroscopic performance of asphalt pavement significantly. As a new emerging powerful numerical tool, the molecular dynamics (MD) simulation has been developed to study the asphalt binder material from a micro perspective. Based on the previous studies, some average asphalt binder models, fractional asphalt binder models, aged asphalt binder models, and modifier models were proposed by many researchers, which have made remarkable progress in asphalt studies; the microproperties, aging mechanism, and modification mechanism of the asphalt binder can also be analyzed using the MD simulation. Overall, the state-of-the-art review provides a comprehensive view for the readers to better understand the development, establishment, and application of the asphalt molecular model.

## 1. Background and Introduction

With the rapid development of modern transportation in the world, the asphalt pavement structure has become one of the most preferred structures of highways due to its advantages for comfortable driving and fast traffic opening [1]. Since the asphalt binder is the main bonding material for the road, its properties are crucial to the service performance and service life of the pavement, that is, the quality of the pavement in service life depends largely on the quality of the asphalt binder [2, 3]. So far, many scholars have studied the technical performance of asphalt [4–20], including aging resistance [21–25], adhesion property [26–28] self-healing behavior [29–32], fatigue-resistance performance [33–39],

modified improvement [40–47], and so on. However, most of these investigations are based on the macroscale experiments including the penetration test, ductility test, softening point test, DSR, and BBR. In a recent investigation on asphalt microproperties, it was discovered that the microscopic properties of asphalt significantly affect the macroscopic properties. Because the asphalt microproperties have a strong relationship with the chemical composition, which is considered to be the main reason for its microscopic properties, it has attracted the attention of many scholars. Since the asphalt binder itself is a by-product of the petrol industry, there exists more than a million chemical compositions in the asphalt binder. Therefore, it is necessary to simplify and separate the asphalt binder into a few fractions

for the basic investigation. The mainstream method separates the asphalt binder into aliphatics, naphthene aromatics, polar aromatics, and asphaltenes according to different polarities created by Corbett [48]. With this method, the chemical properties of each fraction can be studied, and some chemical structures are proposed to explain the mechanism of properties of the asphalt binder at a molecular scale.

However, the chemical composition separation can only study the asphalt binder from static state and cannot dynamically describe the chemical structure, whereas a molecular dynamics (MD) simulation can reflect the thermodynamic behaviors of asphalt molecules and has therefore been developed. The MD simulation was firstly employed in biology in terms of protein molecules and nutrition; then it was developed by the field of petroleum to study the properties of petroleum; later, in the asphalt industry, the MD simulation was also developed to solve many problems at microscale [49, 50]. Greenfield has made significant contributions in this area [51–53]. The research progress is shown in Figure 1.

MD simulation is conducted at microscale to analyze the main physical and mechanical properties of the asphalt binder based on the molecular interaction and local dynamics of particles. Some research studies in terms of MD application were investigated by us: the effect of wasting cooking oil on the macro- and microproperties of the asphalt binder, nanocracking under external loading conditions in the asphalt binder, and hardening effect on asphalt binder during the aging process as well as the effect of paraffin on the microproperties of the asphalt binder [49, 54–58]. In this study, we would like to describe the development status and some applications of this technology; some specific research of asphalt binder models is also described in this paper. The main properties of the binder including density, glass transition temperature, diffusion coefficient, adhesion, self-healing behavior, and so on can be calculated. The objective of this paper is to introduce the state-of-the-art research process on the molecular models of the asphalt binder, as well as the applications of MD simulation, based on which further research on the asphalt microscopic properties investigation at microscale is expected to be conducted. A schematic view of the MD simulation in the asphalt binder is shown in Figure 2.

## 2. Chemistry and Structure of Asphalt Binder and Fractions

**2.1. Asphalt Binder Molecular Structure.** To investigate the asphalt binder from a microscopic perspective, Jennings et al. [59] built eight average molecular structures for the core asphalt binders in the Strategic Highway Research Program (SHRP) (Figure 3). The physical properties of those core asphalt binders have been investigated by Pauli et al. [60], and an alicyclic sheet molecule was recommended to represent the asphalt binder. Based on their research results, the physical properties of those real asphalts were studied by the corresponding average models.

However, the asphalt binder consists of millions of kinds of original components [61]. To study the components in the asphalt binder in depth, the asphalt binder was separated

into aliphatics, naphthene aromatics, polar aromatics, and asphaltenes according to the Corbett method [48], which is a mainstream method in the field of crude oil. The four fractions have their own unique properties.

**2.2. Chemical Composition.** Based on previous research, the chemical structure of each fraction in the asphalt binder was investigated, and then reasonable microscopic structures for different asphalt binders were created to represent the asphalt binder accurately.

**2.2.1. Aliphatics.** At room temperature, aliphatics form a light-coloured liquid [48]. By means of the Fourier transform infrared spectroscopy (FTIR), it is known that there are different kinds of branching structures and some aliphatic chains in the aliphatics structure, almost all atoms and aromatic rings are nonpolar, and the average molar mass of aliphatics is 600 g/mol approximately [62].

The aliphatics is the fraction with the least polarity, and compared with the other fractions, the chemical properties of aliphatics is the most stable [63, 64]; oxidation or dehydrogenation reactions are difficult to carry out [65] because there is only a few polar atoms or aromatic rings on aliphatics [62]. In terms of chemical structure, n-docosane ( $n\text{-C}_{22}\text{H}_{46}$ ) was chosen as a representative aliphatics by Kowalewski et al. [66]. Later, an aliphatic structure squalane was obtained from animal sources and plant; it can also be found in petroleum [67, 68]. In addition, another aliphatic structure hopane was derived from crude oils and biodegraded oil shales commonly, which were constituents of bacterial cell membranes [69]. These typical molecular structures for aliphatics are shown in Figure 4.

**2.2.2. Naphthene Aromatics.** At room temperature, naphthene aromatics are liquid with the colour yellow to red [48]. Compared with the aliphatics, naphthene aromatics behave more viscous at the room temperature. There are very few aliphatics with lightly condensed aromatic rings on their carbon skeleton, and the average molar mass of the fraction is about 800 g/mol [62]. In addition, previous research demonstrates that some naphthene aromatics have negative impacts on human health, such as impaired lung function in asthmatics, and is even the cause of cancer in laboratory animals [70].

The glass transition temperature ( $T_g$ ) of naphthene aromatics is around  $-20^\circ\text{C}$ , which is consistent with that of the bitumen parent; hence, at the same temperature, naphthene aromatics have a higher viscosity than the aliphatics due to its  $T_g$  [71, 72].

Some aromatic, naphthenic, and paraffinic compounds are in naphthene aromatics component [73]. 1,7-Dimethylnaphthalene was selected to represent naphthene aromatics [74]. The alkane/aromatic ratio of 1,7-dimethylnaphthalene is 16.7:83.3, which is different from the overall 58:42 balance [74]. There are some side chains and aromatic rings on the 1,7-dimethylnaphthalene, the number of which can make 1,7-dimethylnaphthalene intermediate between aliphatics and asphaltenes. Later, another structure of naphthene aromatics

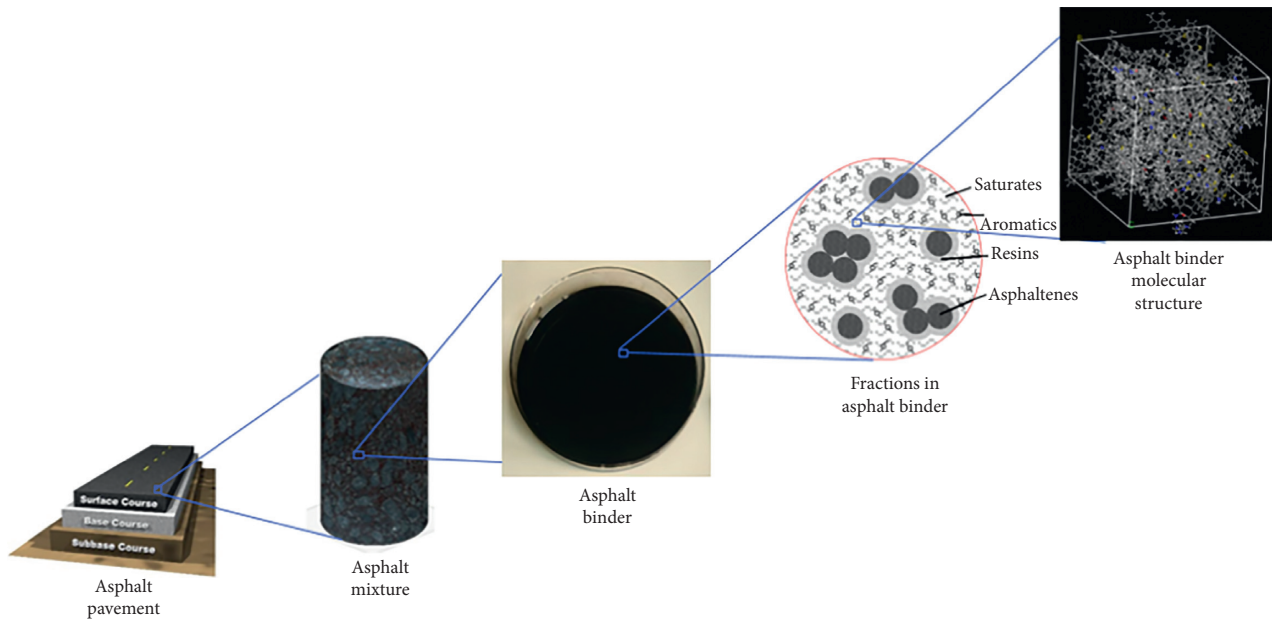


FIGURE 1: Asphalt research from macrolevel to microlevel.

called perhydrophenanthrene-naphthalene (PHPN) was proposed by Lira-Galeana and Hammami, which contained aromatic rings joined with naphthenic rings [75]. Simanzhenkov and Idem found that dioctyl-cyclohexane-naphthalene (DOCHN) can represent an average naphthene aromatic structure by means of n-d-M method; the DOCHN structure was consistent with the mass ratio of carbons on aromatics, naphthenes, and paraffins in crude oils, and its rationality was validated using some parameters, such as the measurements of refractive index, density, and molecular weight of the fraction [76]. So, naphthene aromatics can be represented by three kinds of molecular structures, which are shown in Figure 5.

**2.2.3. Polar Aromatics.** Polar aromatics form black-coloured solid at normal temperature [48], the molar mass of them is less than asphaltenes, but their composition is close [77]. The glass transition temperature of polar aromatics is still not confirmed [71, 72]. The typical structure of polar aromatics contains fused aromatic rings with 2–4 fused rings [62]. They are important for the stability of asphalt binder, because in asphalt binder, polar aromatics are a stabilizer for the asphaltenes [78].

Koots and Speight found that the composition of polar aromatics and asphaltenes were similar [77]. Pieri found that the polarity of polar aromatics could be larger than that of asphaltenes sometimes, although having less condensed aromatic rings [62]. Average polar aromatics molecule structures were built by Murgich et al. to analyze molecular recognition [79]. These structures derived from fresh water lacustrine source rocks were identified by Oldenburg et al. by means of gas chromatography-mass spectrometry (GC-MS) [69]. Koopmans et al. studied the alkylsulfide fraction of sedimentary rock samples and extracted a polar aromatics component thio-isorenieratane by means of gas chromatography

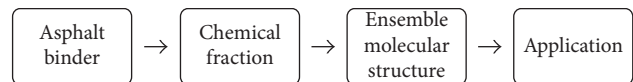


FIGURE 2: Schematic view of MD simulation in asphalt binder.

(GC) [80]; later, they identified another polar aromatics component trimethylbenzene-oxane in shale rocks using GC [81]. Then, benzobisbenzothiophene was identified in organic extractions from sedimentary rocks using GC-MC methods. Lira-Galeana and Hammami [75, 82] built average polar aromatics molecule structures containing two organic groups connected by sulfur elements. These typical molecular structures for polar aromatics are shown in Figure 6.

**2.2.4. Asphaltenes.** At room temperature, fraction asphaltenes are black powder [48]. They do not have any thermal transition up to 200°C [71]. Asphaltenes are defined as the fraction which is an insoluble part in *n*-heptane but soluble in toluene [84]. So a colloid model was proposed for the asphalt binder, in which asphaltenes are covered with polar aromatics and suspended in naphthene aromatics and an aliphatic medium [85]. The asphaltenes are crucial for the technical properties of the asphalt binder, so they are by far the most studied fraction in asphalt binders [86]. Their average molar mass is about 800–3500 g/mol [87, 88]. Furthermore, Van Hamme et al. found that there were many aromatic rings and aggregates in hydrocarbon solvents in asphaltenes [89]. Brandt et al. predicted that asphaltenes could stack in some solvents using thermodynamic modeling, and the maximum number of aggregated asphaltenes molecules was five [90].

Pacheco-Sánchez et al. found that the number of asphaltenes aggregation decreased as temperature increased

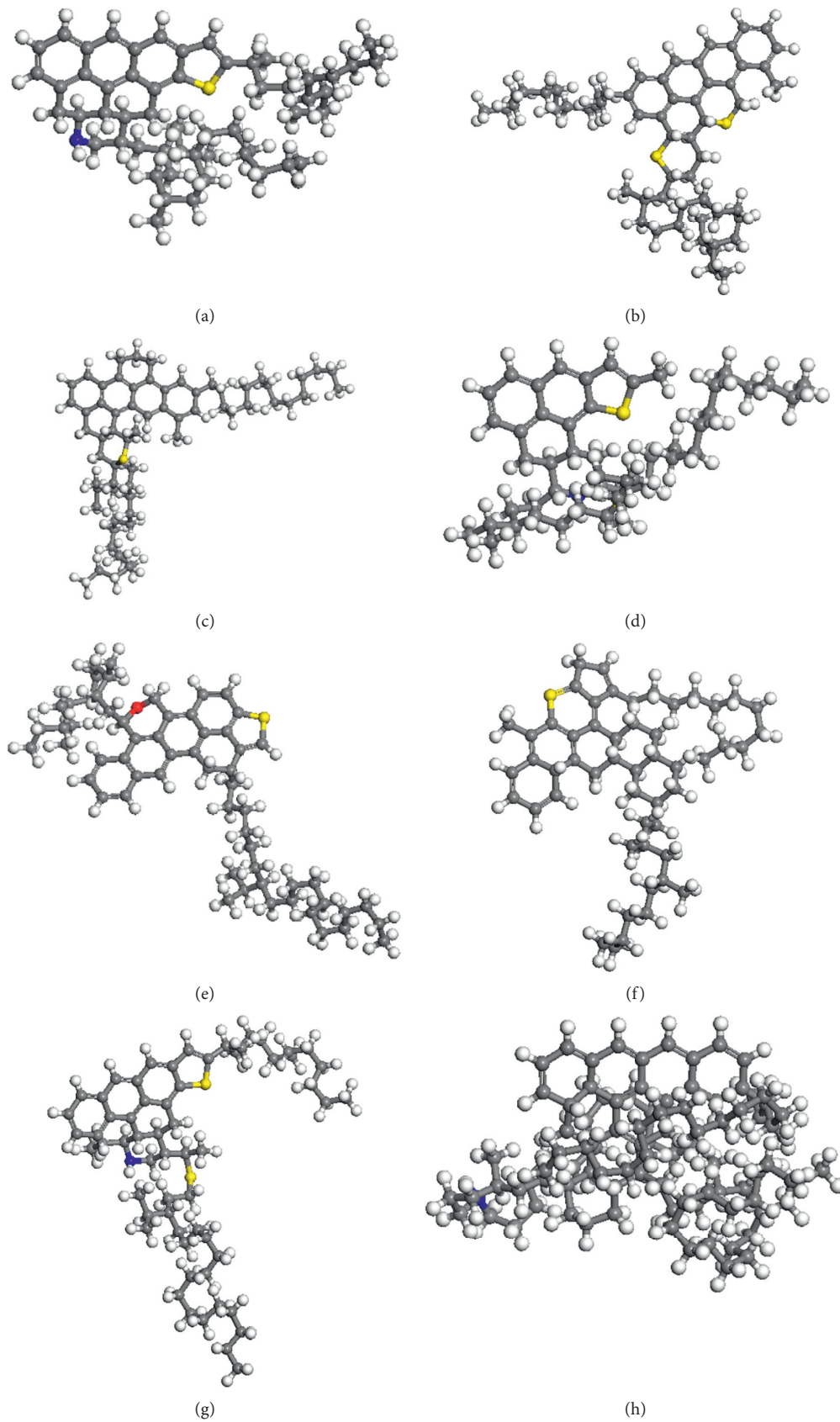


FIGURE 3: Average molecule for each of the SHRP binders [59]: (a) AAA-1, (b) AAB-1, (c) AAC-1, (d) AAD-1, (e) AAF-1, (f) AAG-1, (g) AAK-1, and (h) AAM-1.

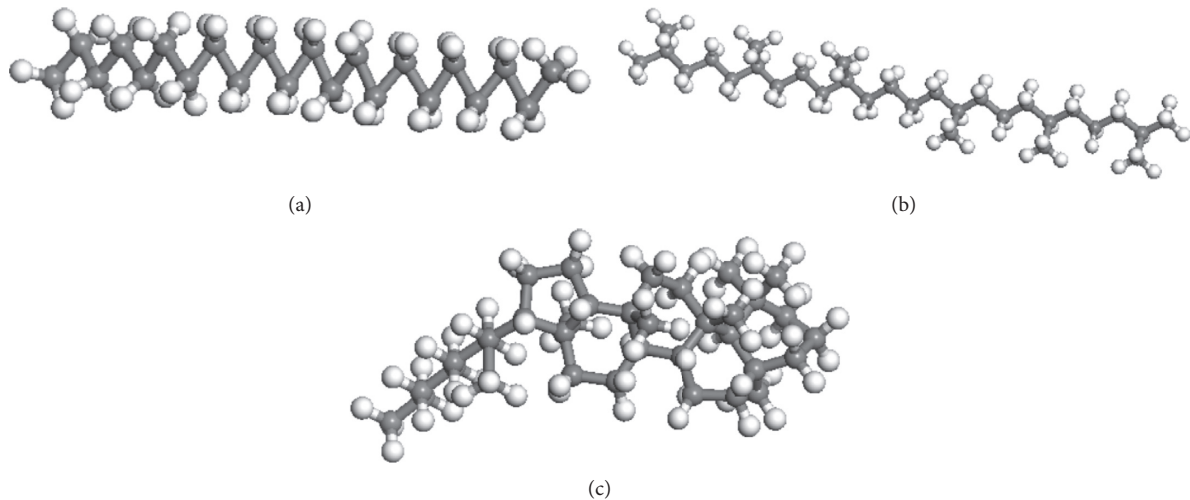


FIGURE 4: Typical molecular structures for aliphatics [33–35].

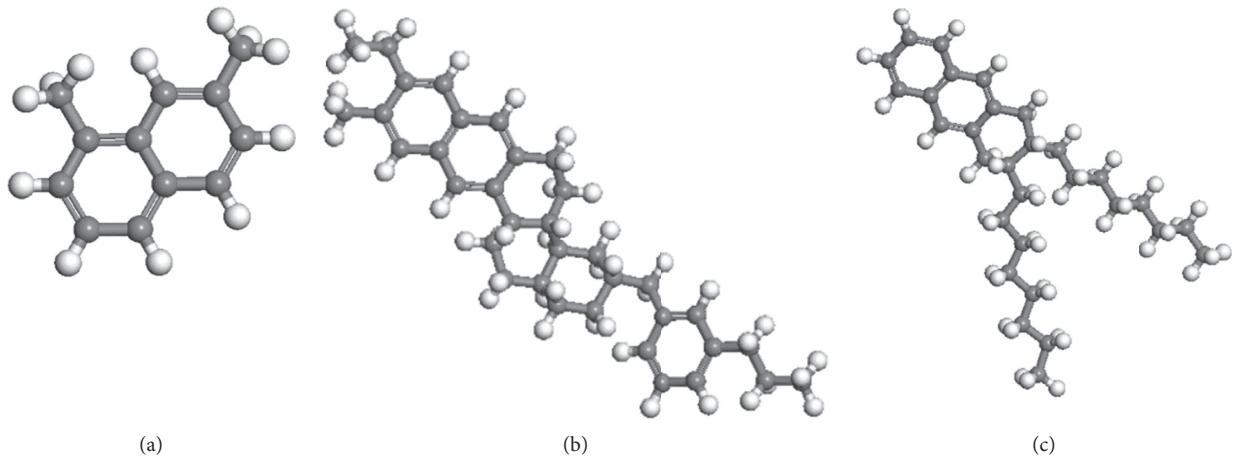


FIGURE 5: Typical molecular structures for naphthene aromatics [37, 38].

[91] and mostly the characteristics of crude oil determine the aggregate orientation [92]. Yen et al. investigated the structure of asphaltenes and found that the interlayer distance between aggregated asphaltene molecules was 3.5–3.8 Å using X-ray diffraction ( $1 \text{ \AA} = 10^{-1} \text{ nm}$ ) [93].

Murgich et al. built an average chemical molecule structure for asphaltene to investigate the mechanism of asphaltene aggregation [79]. Artok et al. built several asphaltene chemical structures containing a moderate-size aromatic core with small branches based on experimental data [94]. Groenzin and Mullins [95] recommended more models with smaller aromatic core and much longer alkane side branches for asphaltene structures by means of fluorescence measurements.

Yen assumed that the asphaltene was composed of extensive condensation of aromatic rings [96]. Afterwards, Groenzin and Mullins proposed a kind of this structure with lower molecular molar weight based on spectroscopic studies. Compared with the structures proposed earlier [56],

this molecular structure was closer to the true asphaltene. Siskin et al. investigated different asphaltene from different production areas and their chemical properties and then proposed six average molecular structures for asphaltene [97]. Some typical asphaltene models are shown in Figure 7.

### 3. Molecular Model

**3.1. Creation of Fractional Asphalt Binder Model.** Based on the chemical structures of each fraction, some chemical models of the asphalt binder are proposed.

**3.1.1. Three-Component Asphalt Binder Model.** In the field of asphalt binder materials, two asphalt binder models were created by Zhang and Greenfield to investigate the properties of asphalt binders [100–102], one of which contained 5 asphaltene proposed by Artok et al. [94], 27 1,7-dimethylnaphthalene, and 41  $n\text{-C}_{22}$  molecules, and the other of which consisted of 5 asphaltene proposed by Groenzin and

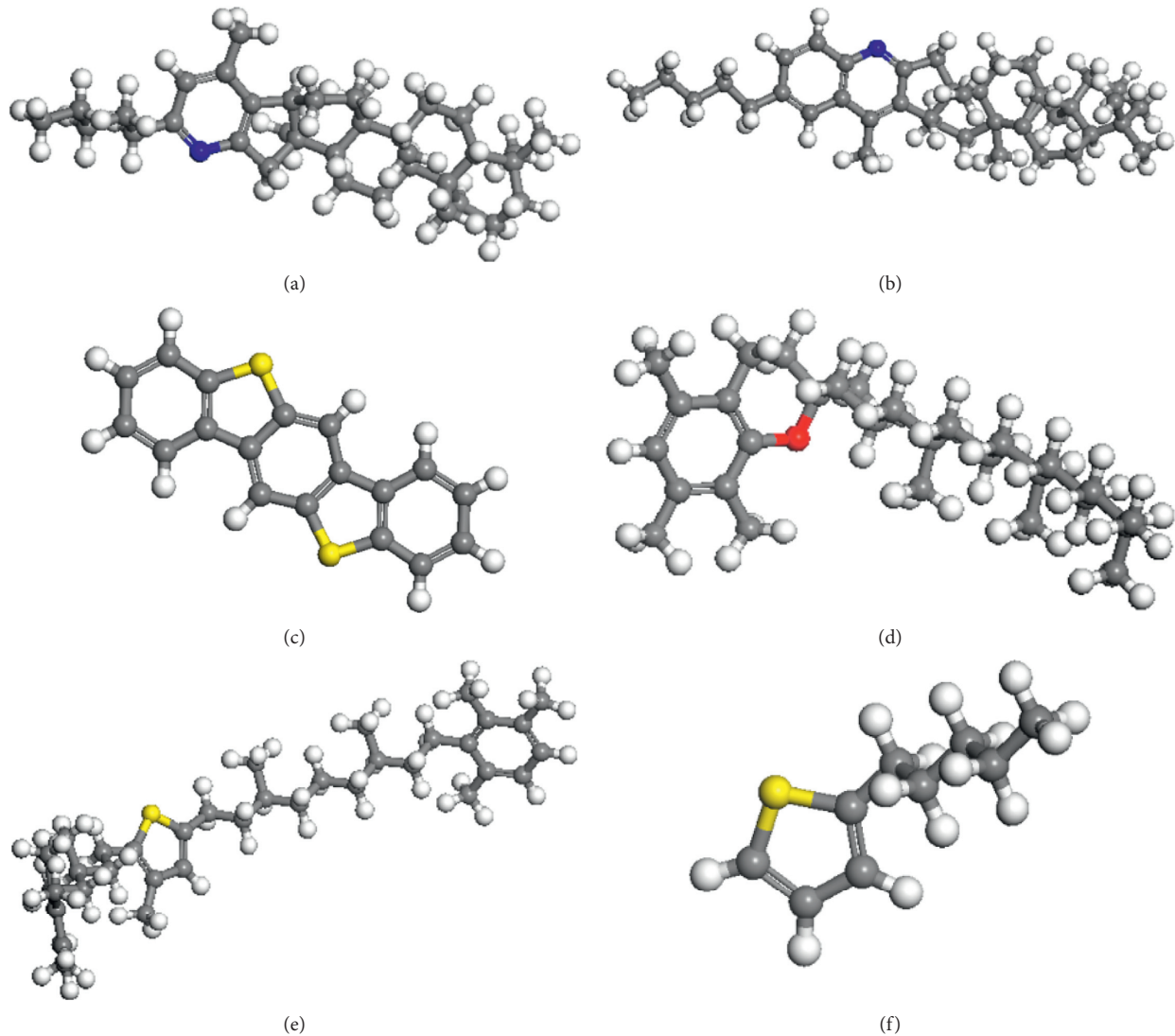


FIGURE 6: Typical molecular structures for polar aromatics [35, 40, 42, 43, 83].

Mullins [95], 30 1,7-dimethylnaphthalene, and 45 n-C<sub>22</sub> molecules. The two asphalt binder models consist of 21% asphaltenes and 59–60% aliphatics, which is consistent with the content of the total C/H ratio reported for a real asphalt [74, 103].

These asphalt binder models have been used in some research: the effect of fractions on the micromechanical behaviors of the asphalt binder [49], the influence of SBS modifier on molecular agglomeration behavior of the asphalt binder using the radial distribution function data [104], the micromechanism of self-healing behavior of the asphalt binder using the morphology of the molecules in the asphalt binder [105], and the interactive response between the asphalt binder and different aggregate [106].

These asphalt binder models were the first molecular model for the asphalt binder, which helped researchers solve a lot of mechanism problems from a micro perspective, and the models had landmark meaning. However, only three fractions exist in the model; there are possibilities for improvement.

**3.1.2. Twelve-Component Asphalt Binder Model.** With the development of molecular simulation technology, more accurate asphalt binder models were established. Li and Greenfield [99] created three kinds of asphalt binder systems (AAA-1, AAK-1, and AAM-1) with 12 chemical components according to the ratio of the four fractions, mass percentage of element of carbon, hydrogen, oxygen, nitrogen and sulfur, atomic H/C ratio, and aromatic and aliphatic percentage of carbon and hydrogen, and they are the widely used asphalt binder models. Compared with the previous asphalt binder models, these models with 12 components are more reasonable and closer to the nature of the real asphalt binder. The only disadvantage is that these models cannot represent the other kinds of asphalt binder.

The twelve-component asphalt binder model was used for some scientific issue: the cohesive and adhesive properties of asphalt binder, including the adhesion between asphalt binder and aggregate; the influence of moisture on their adhesive property [107]; the mechanical performance and modified modification of the asphalt binder with

different waste cooking oil contents [57]; and the oxidative aging effect of asphalt binder, including the influence of aging on the self-healing behavior and moisture damage behavior of asphalt [108].

**3.1.3. Aged Asphalt Binder Model.** Based on the asphalt binder models mentioned above, some aged asphalt binder models were proposed. Generally, the aged asphalt binder model can be divided into two ways to characterize it. The first approach is to adjust the proportion of asphaltene structures [109], which is consistent with the increases of asphaltene content after aging. However, it is not taken into account that some oxidation reaction occurs during the aging procedure. So another approach has been proposed by Yao et al. [110] and Xu and Wang [108]. Yao added a carboxylic acid group on the asphaltene molecule to represent aged asphaltene. Xu and Wang added some oxygen atoms on the asphaltene, naphthalene aromatics, and polar aromatic molecular structures, and the molecular structure of aliphatics remained unchanged, because the content of polar atoms and aromatic rings was too small [108].

**3.2. Creation of Modifier Model.** In recent years, the modified asphalt binder has been used widely in the pavement area due to its excellent technical performance. So it is necessary to investigate the modifier for the asphalt binder.

**3.2.1. Polymer.** Currently, the simulated modifier in the asphalt binder is SBS, graphene, and carbon nanotubes. Ding et al. studied two kinds of SBS modifiers in the asphalt binder and based on the radial distribution function (RDF) data to analyze the impact of these two kinds of SBS on the molecular agglomeration state of asphalt binders [104].

Zhang and Greenfield [101] investigated the effects of polystyrene modification on properties and the microstructure of asphalt system models because polystyrene is part of the common modifier SBS.

**3.2.2. Graphene and Carbon Nanotubes.** Yao et al. compared the two models of the asphalt binder with exfoliated graphite nanoplatelets (xGNP) and control asphalt binder by means of MD simulation to study the physical and thermal properties of the xGNP-modified asphalt binder [110].

A comparative study was employed to study the effects of graphene and carbon nanotubes (CNTs) on the mechanical and thermal properties of the asphalt binder using molecular simulations, and in experiments by Zhou et al. they found that the excess graphene in modified asphalt remained as aggregated particles, while most carbon nanotubes were dispersed in modified asphalt [111].

**3.2.3. Rejuvenator.** The effect of different rejuvenators on recycled asphalt mixtures was investigated using MD simulation by Ding et al. [109], and they found that the interdiffusion rate between asphalt binders at different aging stages could be accelerated to the maximum rate when

adding a rejuvenator into the aged binder, which can improve the efficiency of recycling.

Xiao et al. investigated the diffusion behavior of two different rejuvenators in an aged asphalt binder at the molecular scale. Meanwhile, dynamic shear rheometer (DSR) was employed to determine the recovery influence of aged bitumen resulting from rejuvenators [112]. The test results validated the accuracy of the model simulation results and indicated that the aging state of asphalt binders greatly influenced the rejuvenating effect [113].

Some typical molecular structures for modifier are shown in Figure 8.

## 4. Applications

**4.1. Nanocracking Behavior.** Fatigue damage is the main distress in asphalt pavement; it influences the fatigue life of pavement significantly [114–119], and the fatigue damage gradually generates with the appearance and development of macro- and microcracks under the loading of vehicle and temperature [120]. In order to study the fundamental asphalt binder material properties for the crack, a pair of big enough-opposing forces is applied on the molecular boundaries, then the molecules are pulled by an external force, and a crack appearance can be observed. The stress state of the molecules in an asphalt binder model can be observed with the MD simulation; in addition, the process of molecules being pulled apart can also be observed by some visual software. Hou et al. studied the initiation and propagation of crack in asphalt binder applying tension force on the molecular boundaries, and they found that the natural distribution of atoms at microscale would affect the intrinsic defects and further influence initiation and propagation of crack in the asphalt binder [58]. Nishimura and Miyazaki have used the MD simulation of a-Fe to investigate the mechanical behaviors under cyclic loading from a micro perspective. They made a crack on the boundary of a 2D material, then cyclic loading was applied to the system 12 times, and generation of several vacancies around the crack tip and the crack propagation under cyclic loading were observed [121]. Shang and Kitamura studied the onset of fracture at the free edges of bimaterial interfaces; crack initiation at interface edge models with different contact angle were created to clarify the relationship between crack initiation, contact angle, and maximum stresses [122]. This investigation is meaningful for the research of adhesion between the aggregate and asphalt binder.

**4.2. Tire-Aggregate Friction.** The tire-pavement friction is a complicated mechanism affected by a variety of factors composed of tire type, pavement surface macrotexture and microtexture, wet and dry conditions, and vehicle speed. Adhesion and hysteresis are primary frictional force components for tire-pavement friction, which are critical to roadway safety. Many numerical approaches have been used to analyze the pavement friction including the finite element method [123–125], discrete element method [126, 127], and

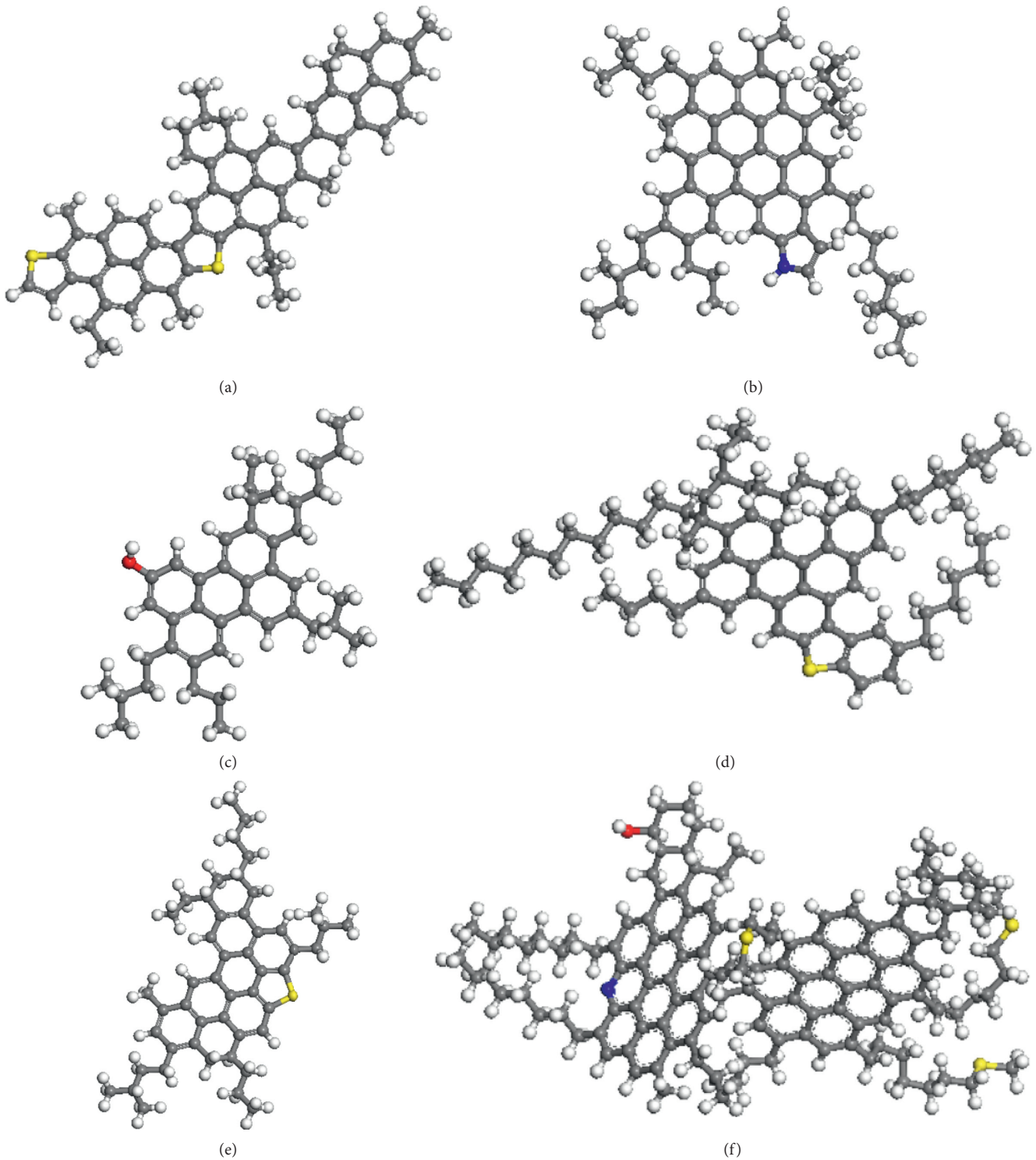


FIGURE 7: Typical molecular structures for asphaltenes [94, 95, 98, 99].

boundary element method [128, 129], at macro-, micro-, and nanoscales. Most of the previous studies on the mechanisms focus on the macro friction behavior based on continuum mechanics. However, the traditional friction analysis cannot reveal the mechanism of tire friction on pavement fully at macro scale.

Recently, some studies have been conducted on the tire friction behavior on pavement at nanoscale [130]. The molecular dynamics method was used to simulate the friction process between the diamond matrix and amorphous carbon probes by Mo et al. [131]. Grierson et al. used the atomic force microscope (AFM) test to study the

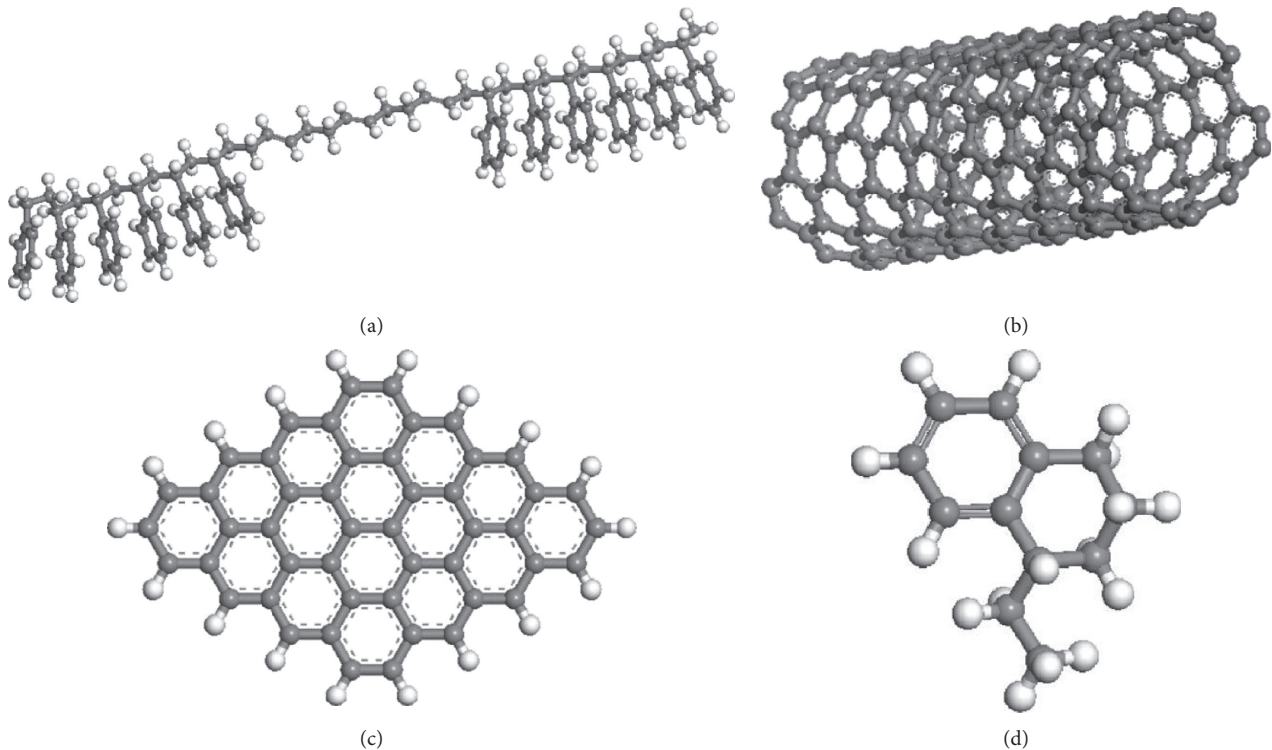


FIGURE 8: Typical molecular structures for modifier [104, 109–111]: (a) SBS, (b) CNT, (c) graphene, and (d) rejuvenator.

adhesion and friction properties at nanoscale [132]. It is found that the friction force has a linear relationship with contact area at the nanoscale. The friction force changes from nonlinear to linear with the decrease of the adhesion between the contacting surfaces [133, 134]. The tribometer, a sophisticated device, is used to clarify the friction coefficient ( $\mu T$ ) from the nano-, micro-, and macroscopic texture of a surface [112]. Hou et al. applied the MD simulation to study the microscopic friction of tire on the asphalt pavement, where the MD simulation was conducted under different environments [135]. There are still some MD simulations about the friction proposed for the other material, and these MD simulations are meaningful to review, because these studies can provide some new methodologies for the tire-pavement friction in terms of MD simulation. For example, Shimizu et al. created two molecular models to represent the slider of AFM and specimen, and the friction during the test and the major influencing factors were investigated using MD simulation combining the constitutive model [136].

## 5. Conclusion

The above review explains that the microscale properties of the asphalt binder significantly affect the macroscale properties with the fast development of technology. The chemical properties of each fraction are therefore studied, and some chemical structures are proposed to study the mechanism of properties of the asphalt binder at molecular scale. Later, the molecular dynamics (MD) simulation was developed because the MD simulation can reflect the

thermodynamics behaviors of asphalt molecules in a dynamic process. MD simulation is a kind of an effective research tool that explores the properties of asphalt binder material from a microscopic perspective.

Using the molecular structure of the asphalt binder and aggregate, the interaction energy between them can be characterized. It is known that the aggregate mineral influences the work of adhesion obviously. It is also employed to explore the influence of water on the adhesion behavior from a micro perspective; some research shows that the interface between the asphalt binder and calcite is susceptible due to moisture damage at small moisture content.

The model of aged the asphalt binder is created by changing the ratio of each fraction, adding some functional groups, or adding some oxygen elements. Then the asphalt binder is studied before and after aging at a molecular scale based on the aged asphalt binder model; meanwhile, the aging mechanism can be also investigated. Based on some microstudy on aging of the asphalt binder, it is seen that there are two reasons for the decrease of molecular diffusion of aged asphalt: on the one hand, the molecular size of asphaltene, resin, and aromatic decreases; on the other hand, free volume space for saturate reduces.

In terms of mechanism of crack, applying some tension on different asphalt binder models, it is found that the atoms distribution at microscale would influence the intrinsic defects of the asphalt binder, and the crack initiation and propagation would be further affected in the asphalt binder.

The modifier is also an important research region of the asphalt MD simulation. The influence law of different modifiers on physical parameters, such as the density and

glass transition temperature of the asphalt binder can be investigated, and the modification characteristics of different modifiers on asphalt performance and their respective modification mechanisms can be further researched. In terms of rejuvenator, its diffusion behavior in the asphalt binders at different aging states can be studied to guide the use of regenerative agents.

As the supercomputer can be used in the future, the model size and the time scale would be increased obviously. In this case, the simulation process will be closer to the macro test, and the simulation result will be closer to the test results.

## Disclosure

The authors are solely responsible for the content.

## Conflicts of Interest

The authors declare that they have no conflicts of interest.

## Acknowledgments

This paper is based on a part of the research project carried out at the request of the German Research Foundation (DFG) under Research Project no. OE 514/1-2 (FOR 2089) and National Natural Science Foundation of China (Grant no. 51708026). The China Scholarship Council (CSC no. 201408080059) is also gratefully acknowledged.

## References

- [1] A. Horvath and C. Hendrickson, "Comparison of environmental implications of asphalt and steel-reinforced concrete pavements," *Transportation Research Record: Journal of the Transportation Research Board*, vol. 1626, no. 1, pp. 105–113, 1998.
- [2] J. Howson, E. Masad, D. Little, and E. Kassem, "Relationship between bond energy and total work of fracture for asphalt binder-aggregate systems," *Road Materials and Pavement Design*, vol. 13, no. 1, pp. 281–303, 2012.
- [3] Y. Sun, B. Huang, J. Chen, X. Jia, and Y. Ding, "Characterizing rheological behavior of asphalt binder over a complete range of pavement service loading frequency and temperature," *Construction and Building Materials*, vol. 123, pp. 661–672, 2016.
- [4] M. Oeser, T. Pellinen, T. Scarpas, and C. Kasbergen, "Studies on creep and recovery of rheological bodies based upon conventional and fractional formulations and their application on asphalt mixture," *International Journal of Pavement Engineering*, vol. 9, no. 5, pp. 373–386, 2008.
- [5] M. Oeser and B. Möller, "3D constitutive model for asphalt pavements," *International Journal of Pavement Engineering*, vol. 5, no. 3, pp. 153–161, 2004.
- [6] S. Zhao, J. Liu, P. Li, and T. Burritt, "Asphalt binder adaption for climatic conditions in cold regions: Alaska experience," *Journal of Materials in Civil Engineering*, vol. 29, no. 1, article 4016184, 2016.
- [7] L. Wang, Y. Hou, L. Zhang, and G. Liu, "A combined static-and-dynamics mechanics analysis on the bridge deck pavement," *Journal of Cleaner Production*, vol. 166, pp. 209–220, 2017.
- [8] Y. Hou, W. Sun, L. Wang, Y. Huang, and M. Guo, "A multi-scale approach of mode I crack in ettringite," *Road Materials and Pavement Design*, vol. 18, no. 3, pp. 33–42, 2017.
- [9] H. R. Zhu, L. Sun, and Y. T. Zhu, "Viscoelastic-viscoplastic damage constitutive model based on thermodynamics for asphalt mixtures," *China Journal of Highway and Transport*, vol. 40, no. 3, pp. 81–100, 2013.
- [10] H. Xu, F. Chen, X. Yao, and Y. Tan, "Micro-scale moisture distribution and hydrologically active pores in partially saturated asphalt mixtures by X-ray computed tomography," *Construction and Building Materials*, vol. 160, pp. 653–667, 2018.
- [11] H. Xu, W. Guo, and Y. Tan, "Internal structure evolution of asphalt mixtures during freeze-thaw cycles," *Materials and Design*, vol. 86, pp. 436–446, 2015.
- [12] H. Xu, J. Zhou, Q. Dong, and Y. Tan, "Characterization of moisture vapor diffusion in fine aggregate mixtures using Fickian and non-Fickian models," *Materials and Design*, vol. 124, pp. 108–120, 2017.
- [13] P. Liu, D. Wang, and M. Oeser, "Application of semi-analytical finite element method coupled with infinite element for analysis of asphalt pavement structural response," *Journal of Traffic and Transportation Engineering*, vol. 2, no. 1, pp. 48–58, 2015.
- [14] E. Hesami, D. Jelagin, N. Kringos, and B. Birgisson, "An empirical framework for determining asphalt mastic viscosity as a function of mineral filler concentration," *Construction and Building Materials*, vol. 35, pp. 23–29, 2012.
- [15] A. H. De Bondt and A. P. Scarpas, "Design of (reinforced) asphaltic overlays," in *Proceedings of the 8th International Conference on Asphalt Pavements*, Seattle, WC, USA, August 1997.
- [16] A. Collop, A. Scarpas, C. Kasbergen, and A. De Bondt, "Development and finite element implementation of stress-dependent elastoviscoplastic constitutive model with damage for asphalt," *Transportation Research Record: Journal of the Transportation Research Board*, vol. 1832, no. 1, pp. 96–104, 2003.
- [17] D. Wang, X. Chen, C. Yin, M. Oeser, and B. Steinauer, "Influence of different polishing conditions on the skid resistance development of asphalt surface," *Wear*, vol. 308, no. 1-2, pp. 71–78, 2013.
- [18] E. Kassem, L. G. Cicalon, E. Masad, and D. Little, "Effect of warm mix additives on the interfacial bonding characteristics of asphalt binders," *International Journal of Pavement Engineering*, pp. 1–14, 2016.
- [19] B. Huang, X. Chen, X. Shu, E. Masad, and E. Mahmoud, "Effects of coarse aggregate angularity and asphalt binder on laboratory-measured permanent deformation properties of HMA," *International Journal of Pavement Engineering*, vol. 10, no. 1, pp. 19–28, 2009.
- [20] J. Liu, S. Zhao, L. Li, P. Li, and S. Saboundjian, "Low temperature cracking analysis of asphalt binders and mixtures," *Cold Regions Science and Technology*, vol. 141, pp. 78–85, 2017.
- [21] T. A. N. Yi-qiu, W. Jia-ni, F. Zhong-liang, Z. Xing-ye, and X. U. Hui-ning, "Ultraviolet aging mechanism of asphalt binder," *China Journal of Highway and Transport*, vol. 21, no. 1, pp. 19–24, 2008.
- [22] F. Zhang, J. Yu, and S. Wu, "Influence of ageing on rheology of SBR/sulfur-modified asphalts," *Polymer Engineering and Science*, vol. 52, no. 1, pp. 71–79, 2012.
- [23] P. E. Yuhong Wang, Y. Wen, K. Zhao, D. Chong, and A. S. T. Wong, "Evolution and locational variation of asphalt

- binder aging in long-life hot-mix asphalt pavements,” *Construction and Building Materials*, vol. 68, pp. 172–182, 2014.
- [24] Y. Wang, Y. Wen, K. Zhao, D. Chong, and J. Wei, “Connections between the rheological and chemical properties of long-term aged asphalt binders,” *Journal of Materials in Civil Engineering*, vol. 27, no. 9, article 04014248, 2015.
- [25] R. K. Dong and L. J. Sun, “Low temperature susceptibility indexes of asphalt binder with different aging degree,” *China Journal of Highway and Transport*, vol. 19, no. 4, pp. 34–39, 2006.
- [26] M. Guo, Y. Tan, L. Wang, and Y. Hou, “A state-of-the-art review on interfacial behavior between asphalt binder and mineral aggregate,” *Frontiers of Structural and Civil Engineering*, vol. 12, no. 2, pp. 1–12, 2017.
- [27] W. Sun, Y. Liu, D. S. Lane, H. Nair, and L. Wang, “Experimental investigation of the relationship between mineral content and aggregate morphological characteristics using the improved FTI system and XRD method,” *Construction and Building Materials*, vol. 155, pp. 981–991, 2017.
- [28] M. Guo, Y. Tan, L. Wang, and Y. Wang, “Improvement of evaluation indicator of interfacial interaction between asphalt binder and mineral fillers,” *Construction and Building Materials*, vol. 151, no. 200, pp. 236–245, 2017.
- [29] S. Shen, H. M. Chiu, and H. Huang, “Characterization of fatigue and healing in asphalt binders,” *Journal of Materials in Civil Engineering*, vol. 22, no. 9, pp. 846–852, 2010.
- [30] X. Luo and R. L. Lytton, “Characterization of healing of asphalt mixtures using creep and step-loading recovery test,” *Journal of Testing and Evaluation*, vol. 44, no. 6, article 20150135, 2015.
- [31] X. Luo, R. Luo, and R. L. Lytton, “Mechanistic modeling of healing in asphalt mixtures using internal stress,” *International Journal of Solids and Structures*, vol. 60–61, pp. 35–47, 2015.
- [32] D. X. Cheng, D. Little, R. Lytton, and J. Holste, “Surface energy measurement of asphalt and its application to predicting fatigue and healing in asphalt mixtures,” *Transportation Research Record: Journal of the Transportation Research Board*, vol. 1810, no. 1, pp. 44–53, 2002.
- [33] L. Shan, Y. Tan, S. Underwood, and Y. R. Kim, “Application of thixotropy to analyze fatigue and healing characteristics of asphalt binder,” *Transportation Research Record: Journal of the Transportation Research Board*, vol. 2179, no. 1, pp. 85–92, 2010.
- [34] L. Shan, Y. Tan, B. S. Underwood, and Y. R. Kim, “Separation of thixotropy from fatigue process of asphalt binder,” *Transportation Research Record: Journal of the Transportation Research Board*, vol. 2207, no. 1, pp. 89–98, 2011.
- [35] C. Wang, C. Castorena, J. Zhang, and Y. R. Kim, “Unified failure criterion for asphalt binder under cyclic fatigue loading,” *Road Materials and Pavement Design*, vol. 16, no. 2, pp. 125–148, 2015.
- [36] C. Wang, H. Zhang, C. Castorena, J. Zhang, and Y. R. Kim, “Identifying fatigue failure in asphalt binder time sweep tests,” *Construction and Building Materials*, vol. 121, pp. 535–546, 2016.
- [37] H. U. Bahia, H. Zhai, K. Bonnetti, and S. Kose, “Non-linear viscoelastic and fatigue properties of asphalt binders,” *Journal of Association of Asphalt Paving Technologists*, vol. 68, 1998.
- [38] X. Luo, R. Luo, and R. L. Lytton, “Characterization of fatigue damage in asphalt mixtures using pseudostrain energy,” *Journal of Materials in Civil Engineering*, vol. 25, no. 2, pp. 208–218, 2012.
- [39] X. Luo, F. Gu, and R. L. Lytton, “Mechanistic composition-specific fatigue life of asphalt pavements,” *Journal of Engineering Mechanics*, vol. 143, no. 12, article 04017136, 2017.
- [40] R. Zhang, H. Wang, Z. You, X. Jiang, and X. Yang, “Optimization of bio-asphalt using bio-oil and distilled water,” *Journal of Cleaner Production*, vol. 165, pp. 281–289, 2017.
- [41] J. Gao, H. Wang, Z. You, and M. R. M. Hasan, “Research on properties of bio-asphalt binders based on time and frequency sweep test,” *Construction and Building Materials*, vol. 160, pp. 786–793, 2018.
- [42] R. Roque, B. Birgisson, C. Drakos, and G. Sholar, “Guidelines for use of modified binders,” Final report 4910-4504-964-12, University of Florida, Gainesville, FL, USA, 2005.
- [43] H. U. Bahia, D. I. Hanson, M. Zeng, H. Zhai, M. A. Khatri, and R. M. Anderson, “Characterization of modified asphalt binders in superpave mix design,” NHCR Report 459, National Cooperative Highway Research Program, Washington, DC, USA, 2001.
- [44] J. Wei, Z. Liu, and Y. Zhang, “Rheological properties of amorphous poly alpha olefin (APAO) modified asphalt binders,” *Construction and Building Materials*, vol. 48, no. 19, pp. 533–539, 2013.
- [45] J. Wei, Y. Li, F. Dong, H. Feng, and Y. Zhang, “Study on the amorphous poly alpha olefin (APAO) modified asphalt binders,” *Construction and Building Materials*, vol. 66, no. 1, pp. 105–112, 2014.
- [46] H. Yu, Z. Leng, and Z. Gao, “Thermal analysis on the component interaction of asphalt binders modified with crumb rubber and warm mix additives,” *Construction and Building Materials*, vol. 125, pp. 168–174, 2016.
- [47] Z. Leng, A. Gamez, and I. L. Al-Qadi, “Mechanical property characterization of warm-mix asphalt prepared with chemical additives,” *Journal of Materials in Civil Engineering*, vol. 26, no. 2, pp. 304–311, 2014.
- [48] L. W. Corbett, “Composition of asphalt based on generic fractionation, using solvent deasphalting, elution-adsorption chromatography, and densimetric characterization,” *Analytical Chemistry*, vol. 41, no. 4, pp. 576–579, 1969.
- [49] Y. Hou, L. Wang, D. Wang, M. Guo, P. Liu, and J. Yu, “Characterization of bitumen micro-mechanical behaviors using AFM, phase dynamics theory and MD simulation,” *Materials*, vol. 10, no. 2, 2017.
- [50] M. Guo, Y. Tan, L. Wang, and Y. Hou, “Diffusion of asphaltene, resin, aromatic and saturate components of asphalt on mineral aggregates surface: molecular dynamics simulation,” *Road Materials and Pavement Design*, vol. 18, no. 3, pp. 149–158, 2017.
- [51] L. Zhang and M. L. Greenfield, “Rotational relaxation times of individual compounds within simulations of molecular asphalt models,” *Journal of Chemical Physics*, vol. 132, no. 18, article 184502, 2010.
- [52] D. D. Li and M. L. Greenfield, “Viscosity, relaxation time, and dynamics within a model asphalt of larger molecules,” *Journal of Chemical Physics*, vol. 140, no. 3, article 034507, 2014.
- [53] L. Zhang and M. L. Greenfield, “Molecular orientation in model asphalts using molecular simulation,” *Energy and Fuels*, vol. 21, no. 2, pp. 1102–1111, 2007.
- [54] X. Qu, D. Wang, Y. Hou, M. Oeser, and L. Wang, “Application on self-healing behavior of six-fraction molecular model of asphalt binder,” *Journal of Materials in Civil Engineering*, 2018.

- [55] X. Qu, Q. Liu, M. Guo, D. Wang, and M. Oeser, "Study on the effect of aging on physical properties of asphalt binder from a microscale perspective," *Construction and Building Materials*, vol. 187, pp. 718–729, 2018.
- [56] X. Qu, D. Wang, Y. Hou, M. Oeser, and L. Wang, "Influence of paraffin on the microproperties of asphalt binder using MD simulation," *Journal of Materials in Civil Engineering*, vol. 30, no. 8, article 04018191, 2018.
- [57] X. Qu, Q. Liu, C. Wang, D. Wang, and M. Oeser, "Effect of co-production of renewable biomaterials on the performance of asphalt binder in macro and micro perspectives," *Materials*, vol. 11, no. 2, p. 244, 2018.
- [58] Y. Hou, L. Wang, D. Wang, X. Qu, and J. Wu, "Using a molecular dynamics simulation to investigate asphalt nano-cracking under external loading conditions," *Applied Science*, vol. 7, no. 8, p. 770, 2017.
- [59] P. W. Jennings, J. A. S. Pribanic, M. A. Desando et al., "Binder characterization and evaluation by nuclear magnetic resonance spectroscopy," SHRP-A-335, Montana State University, Bozeman, MT, USA, 1993.
- [60] A. T. Pauli, W. Grimes, S. C. Huang, and R. E. Robertson, "Surface energy studies of SHRP asphalts by AFM," *American Chemical Society, Division of Petroleum Chemistry*, vol. 48, no. 1, pp. 14–18, 2003.
- [61] I. A. Wiehe and K. S. Liang, "Asphaltenes, resins, and other petroleum macromolecules," *Fluid Phase Equilibria*, vol. 117, no. 1-2, pp. 201–210, 1996.
- [62] N. Pieri, "Etude du vieillissement simulé et in situ des bitumes routiers par IRTF et fluorescence UV en excitation-émission synchrones: détermination des relations structures chimiques-propriétés rhéologiques par analyse en composantes principales," Aix-Marseille University, Provence, France, 1994.
- [63] R. Hunter and P. Culley, *Shell Bitumen Handbook*, ICE Publishing, London, UK, 2015.
- [64] D. Lesueur, "The colloidal structure of bitumen: consequences on the rheology and on the mechanisms of bitumen modification," *Advances in Colloid and Interface Science*, vol. 145, no. 1-2, pp. 42–82, 2009.
- [65] J. R. Wright, "Weathering: theoretical and practical aspects of asphalt durability," *Bituminous Materials: Asphalts, Tars and Pitches*, vol. 2, no. 1, pp. 249–306, 1965.
- [66] I. Kowalewski, M. Vandenbroucke, A.-Y. Huc, M. J. Taylor, and J. L. Faulon, "Preliminary results on molecular modeling of asphaltenes using structural elucidation programs in conjunction with molecular simulation programs," *Energy and Fuels*, vol. 10, no. 1, pp. 97–107, 1996.
- [67] X. Lu, B. Kalman, and P. Redelius, "A new test method for determination of wax content in crude oils, residues and bitumens," *Fuel*, vol. 87, no. 8, pp. 1543–1551, 2008.
- [68] P. M. Gardner and E. V. Whitehead, "The isolation of squalane from a Nigerian petroleum," *Geochimica et Cosmochimica Acta*, vol. 36, no. 2, pp. 259–263, 1972.
- [69] T. B. P. Oldenburg, H. Huang, P. Donohoe, H. Willsch, and S. R. Larter, "High molecular weight aromatic nitrogen and other novel hopanoid-related compounds in crude oils," *Organic Geochemistry*, vol. 35, no. 6, pp. 665–678, 2004.
- [70] K.-H. Kim, S. A. Jahan, E. Kabir, and R. J. C. Brown, "A review of airborne polycyclic aromatic hydrocarbons (PAHs) and their human health effects," *Environment International*, vol. 60, pp. 71–80, 2013.
- [71] P. Claudy, J. Letoffe, G. N. King, and J. Planche, "Caractérisation des bitumes routiers par analyse calorimétrique différentielle (ACD). Analyse thermo-optique (ATO). Corrélation entre propriétés physiques et résultats ACD," *Bulletin de Liaison des Laboratoires des Ponts et Chaussées*, vol. 45, p. 177, 1992.
- [72] P. Claudy, J. M. Letoffe, G. N. King, and J. P. Planche, "Characterization of asphalt cements by thermomicroscopy and differential scanning calorimetry: correlation to classic physical properties," *Fuel Science and Technology International*, vol. 10, no. 4–6, pp. 735–765, 1992.
- [73] F. Roberts, *Hot Mix Asphalt Materials, Mixture Design, and Construction*, NAPA Education Foundation, Napa, CA, USA, 1991.
- [74] D. A. Storm, J. C. Edwards, S. J. DeCanio, and E. Y. Sheu, "Molecular representations of Ratawi and Alaska north slope asphaltenes based on liquid- and solid-state NMR," *Energy and Fuels*, vol. 8, no. 3, pp. 561–566, 1994.
- [75] C. Lira-Galeana and A. Hammami, *Wax Precipitation from Petroleum Fluids: A Review*, Elsevier Science and Technology, New York, NY, USA, 2000.
- [76] V. Simanzhenkov and R. Idem, *Crude Oil Chemistry*, CRC Press, Boca Raton, FL, USA, 2003.
- [77] J. A. Koots and J. G. Speight, "Relation of petroleum resins to asphaltenes," *Fuel*, vol. 54, no. 3, pp. 179–184, 1975.
- [78] J. M. Swanson, "A contribution to the physical chemistry of the asphalts," *Journal of Physical Chemistry*, vol. 46, no. 1, pp. 141–150, 1942.
- [79] J. Murgich, Rodríguez, and Y. Aray, "Molecular recognition and molecular mechanics of micelles of some model asphaltenes and resins," *Energy and Fuels*, vol. 10, no. 1, pp. 68–76, 1996.
- [80] M. P. Koopmans, J. W. De Leeuw, M. D. Lewan, and J. S. S. Damste, "Impact of diagenesis and catagenesis on sulphur and oxygen sequestration of biomarkers as revealed by artificial maturation of an immature sedimentary rock," *Organic Geochemistry*, vol. 25, no. 5–7, pp. 391–426, 1997.
- [81] M. P. Koopmans, J. W. De Leeuw, and J. S. S. Damsté, "Novel cyclised and aromatised diagenetic products of  $\beta$ -carotene in the Green River Shale," *Organic Geochemistry*, vol. 26, no. 7-8, pp. 451–466, 1997.
- [82] L. Marynowski, M. J. Rospondek, R. M. Z. Reckendorf, and B. R. T. Simoneit, "Phenyldibenzofurans and phenyldibenzothiophenes in marine sedimentary rocks and hydrothermal petroleum," *Organic Geochemistry*, vol. 33, no. 7, pp. 701–714, 2002.
- [83] H. Zhu and L. Sun, "A viscoelastic-viscoplastic damage constitutive model for asphalt mixtures based on thermodynamics," *International Journal of Plasticity*, vol. 40, no. 1, pp. 81–100, 2013.
- [84] ASTM, *Standard Test Method for n-Heptane Insolubles; D3279*, ASTM, West Conshohocken, PA, USA, 2012.
- [85] D. N. Little, S. Prapnnachari, A. Letton, and Y. R. Kim, *Investigation of the Microstructural Mechanism of Relaxation and Fracture Healing in Asphalt*, Texas Transportation Institute Station, 1993.
- [86] J. Branthaver, J. Petersen, and R. Robertson, "Binder characterization and evaluation: volume 2: chemistry," SHRP report A-367, National Research Council, Washington, DC, USA, 1993.
- [87] J. G. Speight, *The Chemistry and Technology of Petroleum*, CRC press, Boca Raton, FL, USA, 2014.
- [88] J. G. Speight and H. Plancher, "Molecular models for petroleum asphaltenes and implications for asphalt science and technology," in *Proceedings of the International Symposium on the Chemistry of Bitumens*, Rome, Italy, June 1991.

- [89] J. D. Van Hamme, A. Singh, and O. P. Ward, "Recent advances in petroleum microbiology," *Microbiology and Molecular Biology Reviews: MMBR*, vol. 67, no. 4, pp. 503–549, 2003.
- [90] H. C. A. Brandt, E. M. Hendriks, M. A. J. Michels, and F. Visser, "Thermodynamic modeling of asphaltene stacking," *Journal of Physical Chemistry*, vol. 99, no. 26, pp. 10430–10432, 1995.
- [91] J. H. Pacheco-Sánchez, I. P. Zaragoza, and J. M. Martínez-Magadán, "Asphaltene aggregation under vacuum at different temperatures by molecular dynamics," *Energy and Fuels*, vol. 17, no. 5, pp. 1346–1355, 2003.
- [92] J. H. Pacheco-Sánchez, F. Álvarez-Ramírez, and J. M. Martínez-Magadán, "Morphology of aggregated asphaltene structural models," *Energy and Fuels*, vol. 18, no. 6, pp. 1676–1686, 2004.
- [93] T. F. Yen, J. G. Erdman, and S. S. Pollack, "Investigation of the structure of petroleum asphaltene by X-ray diffraction," *Analytical Chemistry*, vol. 33, no. 11, pp. 1587–1594, 1961.
- [94] L. Artok, Y. Su, Y. Hirose, M. Hosokawa, S. Murata, and M. Nomura, "Structure and reactivity of petroleum-derived asphaltene," *Energy and Fuels*, vol. 13, no. 2, pp. 287–296, 1999.
- [95] H. Groenzin and O. C. Mullins, "Molecular size and structure of asphaltene from various sources," *Energy and Fuels*, vol. 14, no. 3, pp. 677–684, 2000.
- [96] T. F. Yen, "Present status of the structure of petroleum heavy ends and its significance to various technical applications," *American Chemical Society, Division of Petroleum Chemistry*, vol. 17, no. 1, pp. F102–F114, 1972.
- [97] M. Siskin, S. R. Kelemen, C. P. Eppig, L. D. B. And, and M. Afeworki, "Asphaltene molecular structure and chemical influences on the morphology of coke produced in delayed coking," *Energy and Fuels*, vol. 20, no. 3, pp. 1227–1234, 2006.
- [98] O. C. Mullins, "The modified Yen model," *Energy and Fuels*, vol. 24, no. 4, pp. 2179–2207, 2010.
- [99] D. D. Li and M. L. Greenfield, "Chemical compositions of improved model asphalt systems for molecular simulations," *Fuel*, vol. 115, pp. 347–356, 2014.
- [100] L. Zhang and M. L. Greenfield, "Relaxation time, diffusion, and viscosity analysis of model asphalt systems using molecular simulation," *Journal of Chemical Physics*, vol. 127, no. 19, article 194502, 2007.
- [101] L. Zhang and M. L. Greenfield, "Effects of polymer modification on properties and microstructures of model asphalt systems," *Energy and Fuels*, vol. 22, no. 5, pp. 3363–3375, 2008.
- [102] L. Zhang and M. L. Greenfield, "Analyzing properties of model asphalts using molecular simulation," *Energy and Fuels*, vol. 21, no. 3, pp. 1712–1716, 2007.
- [103] D. A. Storm, S. J. Decanio, M. M. Detar, and V. P. Nero, "Upper bound on number average molecular weight of asphaltene," *Fuel*, vol. 69, no. 6, pp. 735–738, 1990.
- [104] Y. Ding, B. Tang, Y. Zhang, J. Wei, and X. Cao, "Molecular dynamics simulation to investigate the influence of SBS on molecular agglomeration behavior of asphalt," *Journal of Materials in Civil Engineering*, vol. 27, no. 8, article C4014004, 2015.
- [105] A. Bhasin, R. Bommavaram, M. L. Greenfield, and D. N. Little, "Use of molecular dynamics to investigate self-healing mechanisms in asphalt binders," *Journal of Materials in Civil Engineering*, vol. 23, no. 4, pp. 485–492, 2011.
- [106] Y. Lu and L. Wang, "Nanoscale modeling of the mechanical properties of asphalt and aggregate," in *Proceedings of the Pavements and Materials*, pp. 43–53, Los Angeles, CA, USA, August 2010.
- [107] G. Xu and H. Wang, "Study of cohesion and adhesion properties of asphalt concrete with molecular dynamics simulation," *Computational Materials Science*, vol. 112, pp. 161–169, 2016.
- [108] G. Xu and H. Wang, "Molecular dynamics study of oxidative aging effect on asphalt binder properties," *Fuel*, vol. 188, pp. 1–10, 2017.
- [109] Y. Ding, B. Huang, X. Shu, Y. Zhang, and M. E. Woods, "Use of molecular dynamics to investigate diffusion between virgin and aged asphalt binders," *Fuel*, vol. 174, pp. 267–273, 2016.
- [110] H. Yao, Q. Dai, Z. You, A. Bick, M. Wang, and S. Guo, "Property analysis of exfoliated graphite nanoplatelets modified asphalt model using molecular dynamics (MD) method," *Applied Sciences*, vol. 7, no. 1, p. 43, 2017.
- [111] X. Zhou, X. Zhang, S. Xu, S. Wu, Q. Liu, and Z. Fan, "Evaluation of thermo-mechanical properties of graphene-carbon-nanotubes modified asphalt with molecular simulation," *Molecular Simulation*, vol. 43, no. 4, pp. 1–8, 2017.
- [112] M. Gonzalez, S. L. Tighe, J. B. Medley, and N. Muzzin, "Assessing friction response of nanoconcrete for rigid pavements using British pendulum tester and tribometer," in *Proceedings of the 94th Annual Meeting, Transportation Research Board*, Washington, DC, USA, 2015.
- [113] Y. Xiao, C. Li, M. Wan, X. Zhou, Y. Wang, and S. Wu, "Study of the diffusion of rejuvenators and its effect on aged bitumen binder," *Applied Sciences*, vol. 7, no. 4, p. 397, 2017.
- [114] H. Wang, Z. Dang, L. Li, and Z. You, "Analysis on fatigue crack growth laws for crumb rubber modified (CRM) asphalt mixture," *Construction and Building Materials*, vol. 47, no. 5, pp. 1342–1349, 2013.
- [115] F. Moreno-Navarro and M. C. Rubio-Gámez, "UGR-FACT test for the study of fatigue cracking in bituminous mixes," *Construction and Building Materials*, vol. 43, no. 2, pp. 184–190, 2013.
- [116] S. Zhi, W. W. Gun, L. X. Hui, and T. Bo, "Evaluation of fatigue crack behavior in asphalt concrete pavements with different polymer modifiers," *Construction and Building Materials*, vol. 27, no. 1, pp. 117–125, 2012.
- [117] Y. Zhang, R. Luo, and R. L. Lytton, "Characterizing permanent deformation and fracture of asphalt mixtures by using compressive dynamic modulus tests," *Journal of Materials in Civil Engineering*, vol. 24, no. 7, pp. 898–906, 2011.
- [118] Y. Zhang, X. Luo, R. Luo, and R. L. Lytton, "Crack initiation in asphalt mixtures under external compressive loads," *Construction and Building Materials*, vol. 72, pp. 94–103, 2014.
- [119] X. Luo, R. Luo, and R. Lytton, "Modified Paris's law to predict entire crack growth in asphalt mixtures," *Transportation Research Record: Journal of the Transportation Research Board*, vol. 2373, no. 1, pp. 54–62, 2013.
- [120] Z. Suo and W. G. Wong, "Analysis of fatigue crack growth behavior in asphalt concrete material in wearing course," *Construction and Building Materials*, vol. 23, no. 1, pp. 462–468, 2009.
- [121] K. Nishimura and N. Miyazaki, "Molecular dynamics simulation of crack growth under cyclic loading," *Computational Materials Science*, vol. 31, no. 3, pp. 269–278, 2004.
- [122] F. L. Shang and T. Kitamura, "Molecular dynamics simulation on crack initiation at bi-material interface edges," *Key Engineering Materials*, vol. 340–341, pp. 949–954, 2007.

- [123] P. Pödra and S. Andersson, "Simulating sliding wear with finite element method," *Tribology International*, vol. 32, no. 2, pp. 71–81, 1999.
- [124] T. Macginley and J. Monaghan, "Modelling the orthogonal machining process using coated cemented carbide cutting tools," *Journal of Materials Processing Technology*, vol. 118, no. 1–3, pp. 293–300, 2001.
- [125] Y. C. Yen, J. Söhner, B. Lilly, and T. Altan, "Estimation of tool wear in orthogonal cutting using the finite element analysis," *Journal of Materials Processing Technology*, vol. 146, no. 1, pp. 82–91, 2004.
- [126] N. Fillot, I. Iordanoff, and Y. Berthier, "A granular dynamic model for the degradation of material," *Journal of Tribology*, vol. 126, no. 3, pp. 606–614, 2003.
- [127] D. Y. Li, K. Elalem, M. J. Anderson, and S. Chiovelli, "A microscale dynamical model for wear simulation," *Wear*, vol. 225, no. 4, pp. 380–386, 1999.
- [128] G. K. Sfantos and M. H. Aliabadi, "Application of BEM and optimization technique to wear problems," *International Journal of Solids and Structures*, vol. 43, no. 11, pp. 3626–3642, 2006.
- [129] L. Rodríguez-Tembleque, R. Abascal, and M. H. Aliabadi, "A boundary element formulation for wear modeling on 3D contact and rolling-contact problems," *International Journal of Solids and Structures*, vol. 47, no. 18–19, pp. 2600–2612, 2010.
- [130] F. Sun, Y. Hou, L. Wang, L. Huang, and Z. Qian, "A molecular dynamics (MD) simulation on tire-aggregate friction," *International Journal of Pavement Research and Technology*, vol. 10, no. 4, pp. 343–351, 2017.
- [131] Y. Mo, K. T. Turner, and I. Szlufarska, "Friction laws at the nanoscale," *Nature*, vol. 457, no. 7233, pp. 1116–1119, 2009.
- [132] D. S. Grierson, E. E. Flater, and R. W. Carpick, "Accounting for the JKR–DMT transition in adhesion and friction measurements with atomic force microscopy," *Journal of Adhesion Science and Technology*, vol. 19, no. 3–5, pp. 291–311, 2005.
- [133] T. J. Colburn and G. J. Leggett, "Influence of solvent environment and tip chemistry on the contact mechanics of tip-sample interactions in friction force microscopy of self-assembled monolayers of mercaptoundecanoic acid and dodecanethiol," *Langmuir*, vol. 23, no. 9, pp. 4959–4964, 2007.
- [134] J. Gao, W. D. Luedtke, D. Gourdon, M. Ruths, J. N. Israelachvili, and U. Landman, "Frictional forces and Amontons' law: from the molecular to the macroscopic scale," *Journal of Physical Chemistry B*, vol. 108, no. 11, pp. 3410–3425, 2004.
- [135] Y. Hou, H. Zhang, J. Wu, L. Wang, and H. Xiong, "Study on the microscopic friction between tire and asphalt pavement based on molecular dynamics simulation," *International Journal of Pavement Research and Technology*, vol. 11, no. 2, pp. 205–212, 2017.
- [136] J. Shimizu, H. Eda, M. Yoritsune, and E. Ohmura, "Molecular dynamics simulation of friction on the atomic scale," *Nanotechnology*, vol. 9, no. 2, pp. 118–123, 1998.

## Research Article

# Moisture Susceptibility of Sustainable Warm Mix Asphalt

Amjad H. Albayati <sup>1</sup>, Hasan M. Al-Mosawe,<sup>2</sup> Abbas A. Allawi <sup>1</sup>, and Nazar Oukaili<sup>1</sup>

<sup>1</sup>Department of Civil Engineering, College of Engineering, University of Baghdad, 10070 Baghdad, Iraq

<sup>2</sup>Department of Civil Engineering, College of Engineering, Al-Nahrain University, 10070 Baghdad, Iraq

Correspondence should be addressed to Abbas A. Allawi; a.allawi@uobaghdad.edu.iq

Received 27 February 2018; Revised 4 June 2018; Accepted 3 July 2018; Published 19 August 2018

Academic Editor: Xue Luo

Copyright © 2018 Amjad H. Albayati et al. This is an open access article distributed under the Creative Commons Attribution License, which permits unrestricted use, distribution, and reproduction in any medium, provided the original work is properly cited.

Sustainable pavements are pavements that meet the requirements of present generation without influencing the capability of the future generation to meet their needs. One of the problems of the warm mix asphalt is that it has low resistance to moisture damage; therefore, the aim of this research paper is to study the possibility of producing more durable warm mixes against the moisture damage with the use of recycled concrete aggregate (RCA) which has not been studied before. Six replacement rates (0, 20, 40, 60, 80, and 100%) for the coarse version aggregate (VA) with RCA were studied. The Marshall mix design method was used to determine the optimum asphalt cement content for each replacement rate. Thereafter, specimens with the optimum asphalt cement content were prepared and tested in the indirect tension test to evaluate their moisture susceptibility. The results revealed that the mixes with higher percentage of RCA possess higher optimum asphalt content. Moreover, an improvement of 13 and 28% in Marshall stability and tensile strength ratio (TSR), respectively, was obtained in case that the VA was entirely replaced by the RCA.

## 1. Introduction and Background

Recently, the increase of construction prices coupled with the increase of the environmental regulations and awareness has driven a strong movement toward the adoption of sustainable technology in various construction projects including the asphalt concrete pavement. The sustainable pavement is the pavements that meet the requirements of the present generation without influencing the capability of the future generation to meet their needs. Examples of sustainable pavement include warm mix asphalt mixtures, mixes containing recycled products, and mixes containing waste products. The warm mix asphalt mixes are mixtures which could be produced and compacted approximately 15–40°C lower than that of hot mix asphalt (HMA) mixtures depending on the type of additives adopted to produce the warm mix [1].

Globally, the amount of construction and demolition waste generated each year has been estimated to be 1183 million tonnes [2]. In Iraq, annually, the generated waste solid is approximately 144 thousand tonnes and 68% of them is the construction and demolition waste. The concrete is the most significant component in the construction

and demolition waste. The management of these huge waste quantities is considered as a serious challenge due to the landfill shortage and transport costs. This leads to the introduction of the RCA concrete aggregate as an alternative sustainable material for asphalt mixes. Many research studies have performed to examine and evaluate the use of RCA in hot mix asphalt.

Wong et al. [3] studied the substitution of the granite filler/fines by the RCA in hot mix asphalt (HMA), and the mixes with percent of RCA satisfied the Marshall mix design criteria. They found that the higher percent of replaced RCA revealed a greater stiffness and rutting resistance. Mills-Beale and You [4] studied the behavior of hot mix asphalt (HMA) containing RCA based on the superpave mix design method. They concluded that the voids in mineral aggregates (VMA) and voids filled in asphalt (VFA) were decreased as the percent of RCA was increased in the mix.

A study has been performed to evaluate RCA as a hot mix aggregate by Bhusal and Wen [5] as a sustainable material in which six different percentages of RCA were used. Test results indicated that the optimum asphalt ratio increases due to the high absorption of RCA and a reduction in other properties of

TABLE 1: Physical properties of asphalt cement based on performance grade.

Binder	Parameters	Temperature measured	Measured parameters	Specification requirements, AASHTO M320-05
Original	Flash point (°C)	—	298	230°C, min
	Viscosity at 135°C (Pa s)	—	0.487	3 Pa s, max
	DSR, $G/\sin \delta$ at 10 rad/s (kPa)	58	3.3522	1.00 kPa, min
		64	2.020	
	70	0.889		
RTFO aged	Mass loss (%)	—	0.654	1%, max
	DSR, $G/\sin \delta$ at 10 rad/s (kPa)	58	4.1596	2.2 kPa, min
		64	3.1483	
		70	1.9809	
PAV aged	DSR, $G/\sin \delta$ at 10 rad/s (kPa)	28	4684	5000 kPa, max
		25	6477	
	BBR, creep stiffness (MPa)	−6	134.0	300 MPa, max

hot mixes (modulus, resistance to rutting, fatigue, thermal cracking, and resistance to moisture damage).

Rafi et al. [6] conducted a study to evaluate the results obtained from the use of RCA aggregate in hot asphalt mixtures as compared with reference mixtures made with RCA using the Marshall method. Their test results showed that the specific gravity, air voids, and voids in mixes made by adding RCA were less than the reference mixes, and the ratio of stability/flow remained similar for all the mixes.

Motter et al. [7] evaluated the use of fractions of RCA that were obtained from 30 MPa compressive strength concrete in hot mix asphalt instead of natural aggregate coarse with different ratios of replacement (0, 25, 50, 75, and 100%). Test results for permanent deformation and durability by the moisture-induced damage test were studied according to the Marshall mix design method. Test results indicated that it is possible to use RCA as an asphalt concrete surface layer on low-volume roads in spite of high absorption, higher Los Angeles abrasion, and lower density for RCA rather than the crushed stone aggregates.

Al-Bayati et al. [8] studied the effect of RCA on the volumetric properties of HMA in which different mix designs of the HMA mixture was performed for RCA with different percentage ratios of replacing and treatment methods. Test results showed that the treatment method is more successful for developing the physical properties of RCA. The replacement of natural aggregate by RCA concrete aggregate increases the optimum asphalt content for the mixtures, and the voids in mineral aggregates (VMA) is decreased. The use of treated RCA with 30% leads to an improvement in VMA and a little increase in void filled with asphalt VFA as compared with the same percent of untreated RCA. It was seen in general the treated RCA seems to have better performance than untreated RCA properties.

Perez et al. [9] studied the availability of using RCA in HMA. Two asphalt mixes of 50% containing RCA with additional two reference mixtures without recycled aggregate were prepared. It was observed that the mixtures with RCA had high water absorption level which results in open graded and had considerable potential for stripping, a characteristic and higher dynamic modulus. Also, a deterioration of the fatigue law was indicated as compared with

the reference mixtures. They concluded that it was possible to use RCA in the design of flexible pavements for roads with medium to low volume of traffic, and more research is required to cover the use of asphalt mixtures with different types of RCA. The aim of this paper is to establish the use and study the performance of RCA in warm mix asphalt aiming at more sustainable paving products.

## 2. Materials

The raw materials which shall be used in the preparation of warm asphalt concrete mixtures for this study, namely, asphalt cement, aggregate, and mineral filler, were characterized using routine type of tests, and the results were compared with specification requirement to evaluate their suitability for job mix.

**2.1. Asphalt Cement.** The asphalt cement which was supplied from the Doura refinery (south-west of Baghdad) was tested as per the Superpave performance grade requirement, and the results are shown in Table 1. It is obvious from the results that the asphalt cement has a performance grade of PG 64-16. Photographs for the tests are shown in Figure 1.

**2.2. Aggregate.** Two types of coarse aggregates were used in the preparation of asphalt concrete mixtures (VA and RCA). The VA was crushed quartz obtained from the Al-Nibaie quarry (north of Baghdad) whereas the RCA was supplied from the concrete recycling factory in Alrathwanya district (near Baghdad International Airport); this type of aggregate was originally obtained from crushing of Texas T-wall barriers (Figure 2) with a design compressive strength of 30 MPa. The properties of the VA and RCA aggregate are shown in Table 2 which also presents the version fine aggregate test results. The coarse and fine aggregates used in this work were sieved and recombined in the proper proportions to meet the wearing course gradation as required by Iraqi standard specification (State Corporation for Roads and Bridges (SCRB)) [10]. The gradation curve for the aggregate is presented in Figure 3.

**2.3. Filler.** Limestone dust was used as the mineral filler for the preparation of warm mix asphalt concrete mixtures.



FIGURE 1: Photograph for asphalt cement PG test.



FIGURE 2: Texas T-wall before and after crushing.

TABLE 2: Physical properties of aggregates.

Property	ASTM designation	Test results		SCRB specification
		VA	RCA	
<i>Coarse aggregate</i>				
1. Bulk specific gravity	C-127	2.632	2.331	—
2. Apparent specific gravity		2.636	2.501	—
3. Water absorption (%)		0.261	2.91	—
4. Percent wear by Los Angeles abrasion (%)	C-131	18	28	30 max
5. Soundness loss by sodium sulfate solution (%)	C-88	4.3	6.1	12 max
6. Fractured pieces (%)	D5821	97	100	90 min
<i>Fine aggregate</i>				
1. Bulk specific gravity	C-128		2.561	—
2. Apparent specific gravity			2.622	—
3. Water absorption (%)			0.809	—
4. Sand equivalent (%)	D-2419	59		45 min
5. Clay lumps and friable particles (%)	C142	1.2		3 max

The chemical and physical properties of the limestone dust are presented in Table 3.

2.4. *Aspha-min*. Aspha-min powder (shown in Figure 4) was used as an additive for the production of WMA; it is sodium

aluminosilicate hydrothermally crystallized into fine powder. Aspha-min (containing approximately 21% water by weight) was added at a rate of 0.3% (by the weight of total mix) to the heated aggregate blend. The physical and chemical properties of the Aspha-min are presented in Table 4.

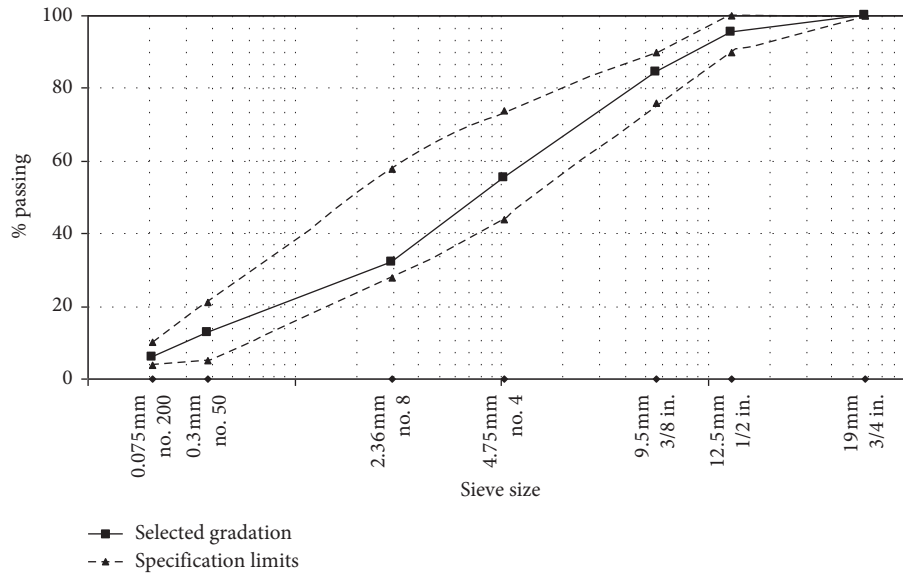


FIGURE 3: Selected aggregate gradation and specification limit.

TABLE 3: Properties of fillers.

Filler type	Chemical composition (%)							Physical properties		
	CaO	SiO <sub>2</sub>	Al <sub>2</sub> O <sub>3</sub>	MgO	Fe <sub>2</sub> O <sub>3</sub>	SO <sub>3</sub>	L.O.I	Specific gravity	Surface area* (m <sup>2</sup> /kg)	% passing sieve no. 200 (0.075)
Limestone	29	10	6	16	1	0.12	37	2.84	247	95

\*Blain air permeability method (ASTM C204).

### 3. Experimental Work and Specimen Preparation

Six replacement rates for the VA with RCA were investigated during laboratory works, and they are 0, 20, 40, 60, 80, and 100%. The specimens were labeled as WRU followed by the replacement percentage. The experimental work consists the use of the Marshall mix design method (ASTM D6926) to determine the optimum asphalt content for each replacement percentage. Then, the optimum asphalt content was used in the preparation of specimens for the indirect tension test to evaluate the moisture susceptibility of the warm mix asphalt.

According to the gradation requirements shown in Figure 3, the various fractions of aggregate (retained on each of the following sieve, 1/2, 3/8, no. 4, no. 8, no. 50, and no. 200) and the mineral filler were combined into a batch of 1150 gm on the mixing bowl and heated to a temperature of 120°C for 6 hours prior to mixing. Asphalt cement was also heated in a container to a temperature of 155°C (for 2 hours) which is corresponding to a viscosity of 170 cSt obtained from the viscosity-temperature relationship shown in Figure 5. Aspha-min was added to the heated aggregate with a rate of 0.3% (by the weight of total mix), the blend was thoroughly mixed for approximately 30 seconds, and then the exact amount of asphalt cement was poured to the mixing bowl and the bowl contents were thoroughly mixed for two minutes.



FIGURE 4: Aspha-min powder.

The mixing temperature was 125°C (30°C minus the HMA concrete temperature, 155°C). To bring the mixture to the compaction temperature 115°C (10°C minus mixing temperature), the bowl with its content was transferred to an oven and stored for 10 minutes in 115°C. In this period, the compaction mold (4 inches (101.6 mm) in diameter and 3 inches (76.5 mm) in height) which was preheated to 115°C is prepared, and then the mixture was poured into the compaction mold. For the Marshall mix design method, the compaction was achieved using 75 blows of the automatic

TABLE 4: Physical and chemical properties of WMA additive, Aspha-min.

Property	Result
Ingredients	Na <sub>2</sub> O.Al <sub>2</sub> O <sub>3</sub> .2SiO <sub>2</sub> (sodium aluminosilicate)
SiO <sub>2</sub>	32.8%
Al <sub>2</sub> O <sub>3</sub>	29.1%
Na <sub>2</sub> O	16.1%
LOI	21.2%
Physical state	Granular powder
Color	White
Odor	Odorless
Specific gravity	2.03

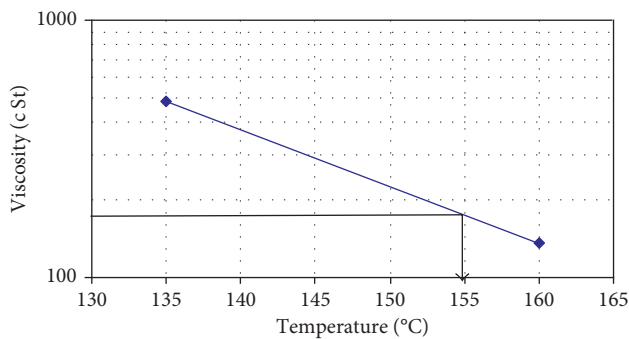


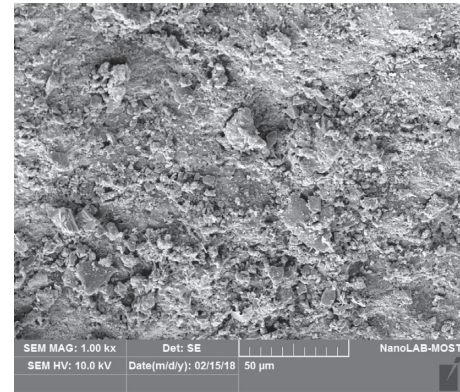
FIGURE 5: Viscosity-temperature chart of PG 64-16.

Marshall compactor on each side of the specimen, whereas for the indirect tension test purposes, according to the RCA replacement rate, different numbers of blows per each side (44 to 61) were used to produce specimens with target air voids of  $7 \pm 1\%$ .

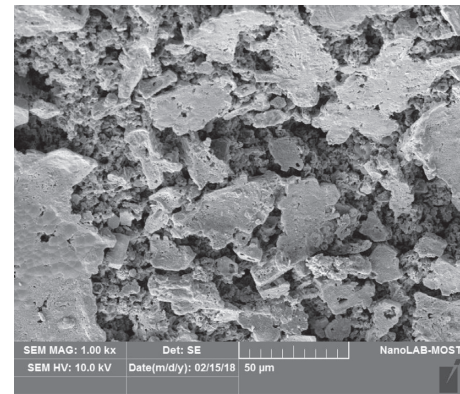
## 4. Results and Discussion

**4.1. Marshall Mix Design.** A complete mix design was conducted using the Marshall method as outlined in Asphalt Institute series no. 2 [11]. Based upon this method, the optimum content for the asphalt cement is obtained by averaging the three asphalt cement contents which yield the maximum stability, maximum unit weight, and 4% air voids.

For each percentage of RCA, five Marshall specimens were prepared starting from 4.4% with a constant increment rate in asphalt cement content of 0.3%. But for RCA replacement rate of 80 and 100%, it was noted after plotting the Marshall properties, the stability and bulk density of the WRU specimens continuously increase as the asphalt cement content increases; therefore, further specimens were prepared with extra asphalt cement content, 5.9% for WRU 80% and 5.9 as well as 6.2% for the WRU 100%. The increase in asphalt cement content was mainly because of the more porosity of the RCA than the VA due to the cement hydration reaction. SEM images were taken for the VA and RCA particles to prove the higher porosity of RCA, and this can be easily seen in Figure 6. The higher the porosity of the aggregate particles, the higher the content of the asphalt cement absorbed. The extended specimens showed a bend in stability as well as bulk density curves; hence, the optimum content for asphalt cement was well defined.



(a)



(b)

FIGURE 6: SEM images of the aggregates. (a) VA; (b) RCA.

The variation of Marshall properties with asphalt cement contents for each RCA replacement rate is exhibited in Figure 7. Examinations of the presented data suggest that the WRU specimens with the RCA content beyond 20% acquire higher asphalt cement content, stability peaks at 4.7% asphalt cement content for the specimens with RCA content of 0 and 20%, whereas for the remaining replacement rates, the asphalt cement content which yield the highest stability increased 0.3% for each 20% increase in the RCA content. This is attributed mainly to the higher absorption property for the RCA as compared to the VA (as shown previously in Table 2). This finding is in agreement with Mills–Beale and You [4], Motter et al. [7], and Al-Bayati et al. [8]. According to stability curves, the results indicate that all the WRU specimens satisfy the minimum stability requirements presented in the SCRBS specification of 8 kN. But an improvement of 13% was obtained in case that the VA entirely replaced by RCA. This could be attributed to the rough surface texture of RCA as compared to the VA. The results are in agreement with Wong et al. [3], Pérez et al. [9], and Zulkati et al. [12]. Based on the Marshall flow results, it is obvious that there is a tendency to increase the mixture Marshall flow as the asphalt cement content increases. However, at the asphalt cement content which yields the peak stability value, it is possible to note that the flow value for the WRU 100% was quite similar to WRU 0%, and it was 3.02 mm for the former and 3.05 mm for the latter. Also, as the asphalt cement content increases,

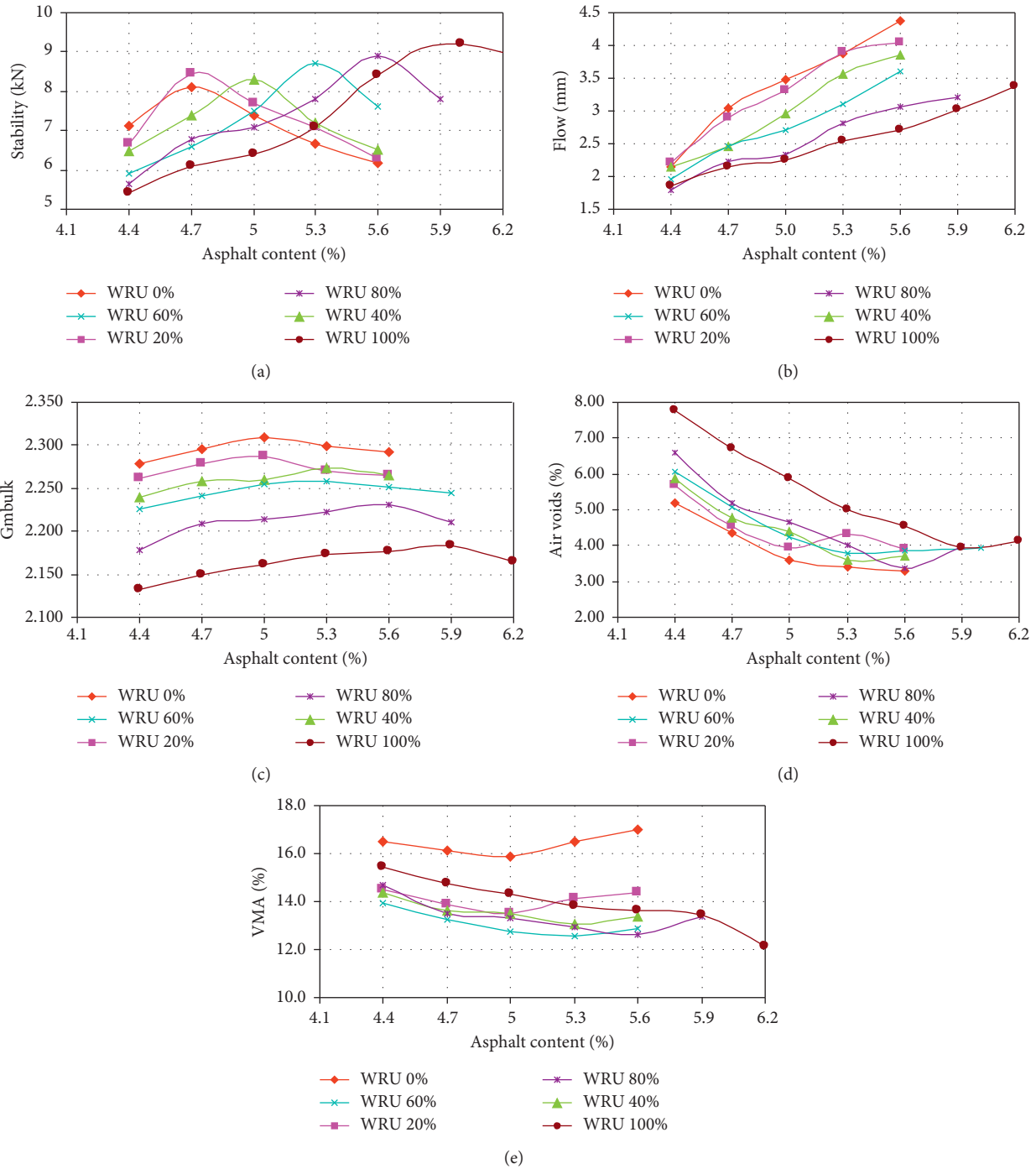


FIGURE 7: Marshall properties for WRU mixes.

the divergence in flow values becomes higher. All the flow values that belong to peak stability value satisfy the requirement for the SCRB specification flow requirement (2–4 mm). The flow value findings are in agreement with Pérez et al. [13] and Rafi et al. [6]. Regarding the bulk specific gravity results graphically shown in Figure 7, it is obvious that there is a trend of increasing bulk specific gravity as the asphalt cement content increases to a certain point, beyond which further increase in asphalt cement leads to reduction in the bulk specific gravity (Gmbulk).

Also, it could be observed that this relationship follows the same trend of that between the RCA content and Marshall stability. As the RCA replacement rate increases, the Gmbulk of the specimens decreases. The peak value of Gmbulk corresponding to WRU 100% (at 6.2% asphalt cement content) was lower than that of WRU 0% (at 5.0% asphalt cement content) by 5.45%. This could be attributed to the lower density of the RCA grain as compared to the VA (as presented in Table (2)). Comparable behavior that agrees with this finding was obtained by Motter et al. [7],

Rafi et al. [6], and Bhusal et al. [14]. The volumetric property, air voids (AV), results revealed that there is a trend of reduction in AV as the asphalt cement content increases. Also, the mixes with higher RCA content possess higher AV. At the asphalt contents which yield the peak Gmbulk values, the AV for the WRU 100% was higher than that of WRU 0% by approximately 10%. This was expected since the RCA grains have higher absorption than that of the VA. This finding is comparable with that obtained by Motter et al. [7] and Rafi et al. [6]. Nevertheless, all the AV values for the WRU mixes at the peak Gmbulk are within the range of the SCRBS specification requirement (3–5%). The voids in mineral aggregate (VMA) results as presented in Figure (7) showed that the mixes with VA have higher VMA values than those containing RCA. The average VMA for the WRU 0% over the entire asphalt cement content was 16.4 which is higher than that of WRU 100% by 17%. The inspection for the VMA expression which is given in (1) and reviewing the data presented in Table (2) and Figures (3) and (7) revealed that the rate of decrease in denominator is higher than that of the numerator, Therefore, it is possible to argue that the VMA decreases as the percentage of RCA replacement increases.

$$\text{VMA} = 100 - \left( \frac{P_a \times G_{mbulk}}{G_{abulk}} \right), \quad (1)$$

where  $P_a$  = aggregate percentage in mix (by mass),  $G_{mbulk}$  = specimen bulk density, and  $G_{abulk}$  = aggregate bulk density.

The optimum asphalt cement content for the WRU mixes with all the replacement rates which was calculated based on averaging the three asphalt cement contents which yield the maximum stability, maximum unit weight, and 4% air voids is shown in Table 5. These contents will be used for specimen preparation for the moisture susceptibility evaluation.

**4.2. Moisture Susceptibility.** The adopted procedure to evaluate the moisture susceptibility of WMA and HMA specimens is ASTM D 4867. For each mix type, six specimens were compacted; one subset of the specimens (three specimen) was tested at temperature of 25°C (unconditioned specimens) in the indirect tension test, whereas the other subset was subjected to one cycle of freezing and thawing (16 hrs in  $-18 \pm 2^\circ\text{C}$  and then, 24 hrs in  $60 \pm 1^\circ\text{C}$ ) and then tested the same as the first subset (conditioned specimens). During the indirect tension test, the specimen is loaded along the diameter and the splitting force is recorded (as shown in Figure 8). The test parameters are calculated as follow:

$$\text{ITS} = \frac{2P}{\pi t D}, \quad (2)$$

$$\text{TSR} = \frac{\text{C.ITS}}{\text{UC.ITS}}$$

where  $P$  = splitting load,  $t$  = specimen height (thickness),  $D$  = specimen diameter, C.ITS = conditioned indirect tensile stress, and UC.ITS = unconditioned indirect tensile stress.

Based on the results exhibited in Figures 9 and 10, it is obvious that there is a distinct trend for the increase of tensile

TABLE 5: Optimum asphalt content for WRU mixes.

RCA (%)	0	20	40	60	80	100
Optimum asphalt content (%)	4.83	4.88	5.15	5.23	5.5	5.88



FIGURE 8: Indirect tension test for the WRU specimen.

strength (unconditioned) as the RCA replacement rate increases. The tensile strength for the WRU 100% was higher than that of WRU 0% by 36.8%. This increase in tensile strength is mainly due to the surface texture of the aggregate, and this impacts the bond between asphalt and aggregate particle. It is clearly shown in Figure 11 that the failure occurs in the mastic zone of the WRU 0% while it breaks the RCA particles in the WRU 100% sample, which refers to a better bond.

It was observed that the WRU 100% specimen splitting surface included broken RCA, whereas the WRU 0% failure plane passes through the VA-asphalt cement interface; this reflects the increase in tensile strength of the RCA over the VA. Reminding that the minimum acceptable limit for the TSR is 80%, the replacement of the entire coarse aggregate with the RCA resulted in improvement of the TSR by 18%, and this was the only case which satisfies the TSR minimum limit. This finding was comparable with that obtained by Motter et al. [7] and Paranavithana and Mohajerani [15].

## 5. Conclusions

According to the presented works in this research and within the limitation of the test program and the materials used, the following salient conclusions can be drawn:

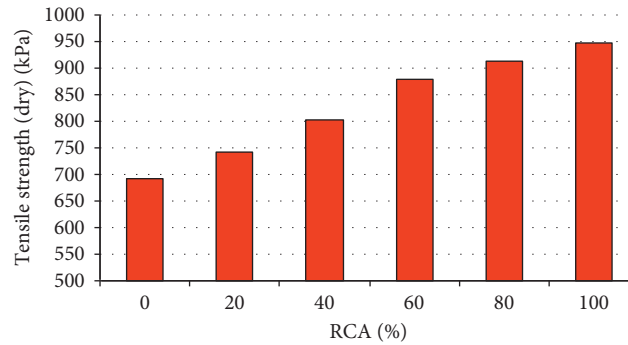


FIGURE 9: Unconditioned indirect tension test results specimen.

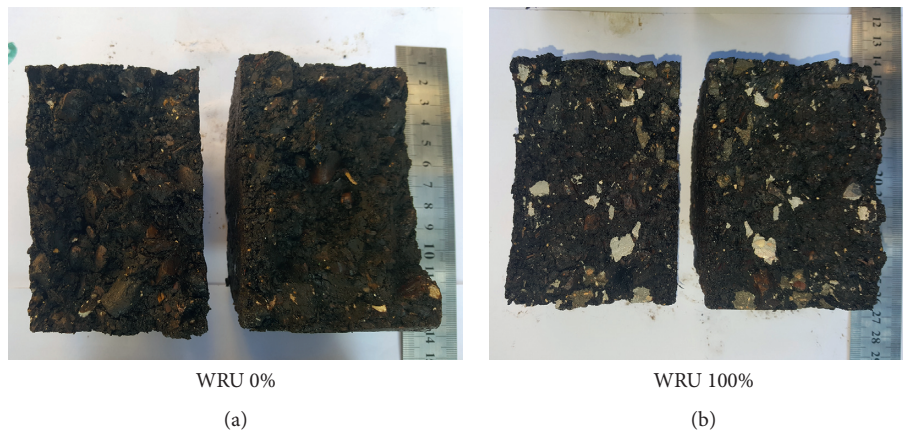


FIGURE 10: Tensile strength ratio results.

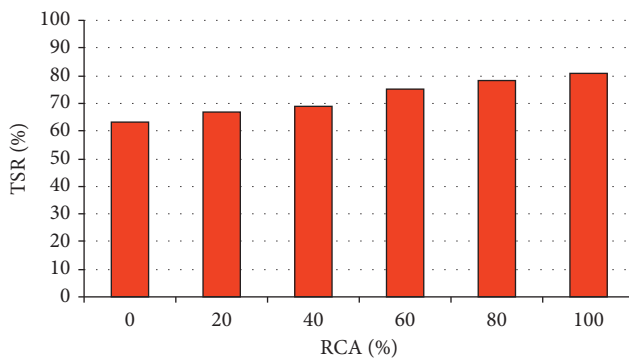


FIGURE 11: WRU unconditioned specimens after the indirect tension test. (a) WRU 0%; (b) WRU 100%.

(a) The use of different replacement rates for the RCA has a significant influence on the Marshall mix design properties, and some of the obtained results can be summarized as follows:

(1) The mixes with higher percentage of RCA possess higher optimum asphalt content, the highest optimum asphalt cement content (5.88%) belongs to WRU 100% indicating that for each 20% increase in RCA replacement percent beyond the 20%, the asphalt cement demand increases by 0.2%.

(2) An improvement of 13% in Marshall stability was obtained in case that the VA entirely replaced by the RCA, the Marshall stability for the WRU 100% was the highest (9.8 kN) in comparison with all other RCA replacement values.

(3) At the peak stability, the Marshall flow value for the WRU 100% was quite similar to WRU 0%, and it was 3.02 mm for the former and 3.05 mm for the latter.

(4) The air voids for the WRU 100% was higher than that of WRU 0% by approximately 10% at the peak Gmbulk, but both satisfied the specification requirements (3–5%).

(b) The replacement of the entire coarse aggregate in WRU mixes with the RCA resulted in improvement of the TSR by 28%, and the moisture susceptibility was for WRU 100% satisfied the TSR minimum limit (80%). Also, the unconditioned tensile strength for the WRU 100% was higher than that of WRU 0% by 36.8%.

(c) The use of RCA instead of VA has shown a significant improvement in moisture susceptibility of warm mix asphalt prepared using Aspha-min additive and has added to the local knowledge the possibility of producing more durable mixes against the moisture damage mode of failure.

## Data Availability

The data used to support the findings of this study are available from the corresponding author upon request.

## Conflicts of Interest

The authors declare that they have no conflicts of interest.

## References

- [1] A. R. Pasandín and I. Pérez, "Overview of bituminous mixtures made with recycled concrete aggregates," *Construction and Building Materials*, vol. 74, pp. 151–161, 2015.
- [2] R. Purushothaman, R. R. Amirthavalli, and L. Karan, "Influence of treatment methods on the strength and performance characteristics of recycled aggregate concrete," *Journal of Materials in Civil Engineering*, vol. 27, no. 5, article 04014168, 2014.
- [3] Y. D. Wong, D. D. Sun, and D. Lai, "Value-added utilisation of recycled concrete in hot-mix asphalt," *Waste Management*, vol. 27, no. 2, pp. 294–301, 2007.
- [4] J. Mills-Beale and Z. You, "The mechanical properties of asphalt mixtures with recycled concrete aggregates," *Construction and Building Materials*, vol. 24, no. 3, pp. 230–235, 2010.
- [5] S. Bhusal and H. Wen, "Evaluating recycled concrete aggregate as hot mix asphalt aggregate," *Advances in Civil Engineering Materials*, vol. 2, no. 1, pp. 252–265, 2013.
- [6] M. M. Rafi, A. Qadir, and S. H. Siddiqui, "Experimental testing of hot mix asphalt mixture made of recycled aggregates," *Waste Management & Research*, vol. 29, no. 12, pp. 1316–1326, 2011.
- [7] J. S. Motter, L. F. R. Miranda, and L. L. B. Bernucci, "Performance of hot mix asphalt concrete produced with coarse recycled concrete aggregate," *Journal of Materials in Civil Engineering*, vol. 27, no. 11, article 04015030, 2015.
- [8] H. K. A. Al-Bayati, S. L. Tighe, and J. Achebe, "Influence of recycled concrete aggregate on volumetric properties of hot mix asphalt," *Resources, Conservation and Recycling*, vol. 130, pp. 200–214, 2018.
- [9] I. Pérez, A. R. Pasandín, and L. Medina, "Hot mix asphalt using C&D waste as coarse aggregates," *Materials & Design (1980–2015)*, vol. 36, pp. 840–846, 2012.
- [10] SCRBR/9, "General specification for roads and bridges," in *Section R/9, Hot-mix asphalt concrete pavement, Revised Edition*, State Corporation of Roads and Bridges, Ministry of Housing and Construction, Republic of Iraq, 2003.
- [11] AI, *Thickness Design-Asphalt Pavements for Highways and Streets, Manual Series No. 1*, Asphalt Institute, College Park, MD, USA, 1981.
- [12] A. Zulkati, Y. D. Wong, and D. D. Sun, "Mechanistic performance of asphalt-concrete mixture incorporating coarse recycled concrete aggregate," *Journal of Materials in Civil Engineering*, vol. 25, no. 9, pp. 1299–1305, 2012.
- [13] I. Pérez, M. Toledano, J. Gallego, and J. Taibo, "Mechanical properties of hot mix asphalt made with recycled aggregates from reclaimed construction and demolition debris," *Materiales de Construcción*, vol. 57, no. 285, pp. 17–29, 2007.
- [14] S. Bhusal, X. Li, and H. Wen, "Evaluation of effects of recycled concrete aggregate on volumetrics of hot-mix asphalt," *Transportation Research Record: Journal of the Transportation Research Board*, vol. 2205, pp. 36–39, 2011.
- [15] S. Paranavithana and A. Mohajerani, "Effects of recycled concrete aggregates on properties of asphalt concrete," *Resources, Conservation and Recycling*, vol. 48, no. 1, pp. 1–12, 2006.

## Research Article

# Investigation of Thermal Cooling Effectiveness of RRVCS for Permafrost Protection under Wide Expressway Embankment

Tao Tang <sup>1</sup>, Tao Ma <sup>1</sup>, Xiaoming Huang <sup>1</sup>, Qiuming Xiao <sup>2</sup>, Hao Wang,<sup>3</sup>  
and Guangji Xu<sup>1</sup>

<sup>1</sup>School of Transportation, Southeast University, Nanjing 210096, China

<sup>2</sup>School of Traffic and Transportation Engineering, Changsha University of Science and Technology, Changsha 410004, China

<sup>3</sup>Department of Civil and Environmental Engineering, Rutgers, The State University of New Jersey, Newark, NJ 08854, USA

Correspondence should be addressed to Tao Ma; matao@seu.edu.cn and Qiuming Xiao; xiaoxiaoyu69@sina.com

Received 4 March 2018; Accepted 28 May 2018; Published 19 July 2018

Academic Editor: Jinchang Wang

Copyright © 2018 Tao Tang et al. This is an open access article distributed under the Creative Commons Attribution License, which permits unrestricted use, distribution, and reproduction in any medium, provided the original work is properly cited.

In order to improve the thermal stability of wide embankment for the Qinghai-Tibet Expressway (QTE) to be constructed in permafrost zones on Qinghai-Tibet plateau, a new kind of reflective-resistant-ventilated coupling structure (RRVCS) was proposed and designed. A numerical model was then developed through ABAQUS to investigate the influences of RRVCS on the thermal regime of wide embankment. The temperature field and thawing depth of normal wide embankment without protective measures, wide embankment with crushed stone layer, and wide embankment with RRVCS were compared to verify the cooling effectiveness of RRVCS based on numerical analysis. Vermiculite powder has great influences on the thermal property of asphalt mixture, and it can be reduced by 22.8%, 29.5%, 37.3%, and 50.6% after the addition of 4%, 6%, 8%, and 10% vermiculite powder, respectively. Under the same condition, the temperature of RRVCS embankment is the lowest and its thermal stability is the best. Setting crushed stone layer can improve the thermal stability of embankment. However, the improvement is limited for wide embankment with width exceeding 26 m. RRVCS has the best protective effects on the thermal stability of wide embankment and is recommended as a protective measure for wide embankment of expressway in permafrost regions of Qinghai-Tibet Plateau.

## 1. Introduction

As the first expressway connecting Tibet to other provinces in China, the Qinghai-Tibet Expressway (QTE) will be constructed on the Qinghai-Tibet Plateau in accordance with the China National Expressway Network Plan [1]. The construction of QTE is of great importance because it can eliminate traffic bottlenecks in Tibetan areas and promote China's social and economic development. However, it is quite difficult to build a high-quality expressway on the Qinghai-Tibet Plateau [2] due to its extreme conditions such as high altitude, low air temperature and pressure, and strong solar radiation [3]. Another difficulty is that the building of QTE, like the existing Qinghai-Tibet Highway (QTH), may have adverse effects on the fragile ecosystem of the Qinghai-Tibet Plateau [4]. More importantly, since QTE will pass through more than 500 km of continuous permafrost regions, a lot of technical barriers especially permafrost degradation have to be addressed [5].

Permafrost is very sensitive to climate change, and its strength decreases dramatically with rising temperature. Based on meteorological data available, it was predicted that air temperature over the Tibetan Plateau would increase 2.2°C to 2.6°C in the coming fifty years [6]. Because of climate warming and human activities, the permafrost in this area could thaw and lose its bearing capacity, leading to active-layer detachment failure, thaw subsidence, and failure of many other geohazards [7]. To address these issues, much effort has been exerted by researchers all over the world and a number of measures to cool down permafrost subgrade have been devised, including crushed stone embankment, thermosyphons, air-cooling ducts, awnings, insulating materials, raising the embankment height, and combinations of these methods [8–12]. While some are passive methods impeding the heat transferred to the frozen soil, others are proactive measures releasing the heat accumulated in permafrost embankment. Generally, all these methods are effective in

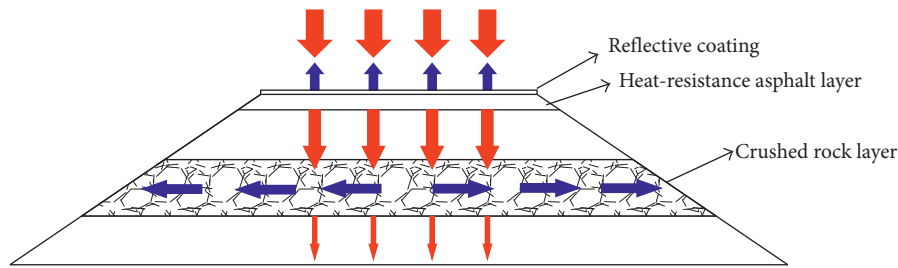


FIGURE 1: Schematic diagram of the reflective-resistant-ventilated coupling structure.

cooling current permafrost embankments according to engineering practices.

While most existing highways and railways in permafrost regions adopt narrow embankments whose widths are no more than 10 m, QTE is characterized by wide embankment with width more than 24.5 m, which is at least twice the width of current embankments. Due to the increased width of asphalt pavement, the heat-absorption intensity in wide embankment would be much higher compared with narrow embankment. Meanwhile, the heat at the embankment center is more difficult to dissipate outward due to the extended heat diffusion path, which can lead to faster permafrost degradation and more severe thaw settlement [12]. Therefore, striking differences exist between current narrow embankments and the new wide embankment of QTE. Since most of the existing cooling methods are based on narrow embankments, they may not be effective in cooling QTE's wide embankment.

Thus, this study aims to find effective cooling measurements for the wide embankment of QTE. To achieve this objective, a new kind of reflective-resistant-ventilated coupling structure (RRVCS) was proposed and designed. Based on the finite element software ABAQUS, a numerical model was built to simulate the temperature field of wide embankment and evaluate the effectiveness of RRVCS to improve the thermal stability of wide embankment. Another conventional cooling method, namely, crushed stone layer, was selected for comparison. The influences of different protective measures on the temperature field and thawing depth of underlying permafrost of wide embankment were investigated based on numerical analysis.

## 2. Design of RRVCS

To mitigate the thaw settlement of QTE and the degradation of its underlying permafrost, it is desired to explore strategies that make the pavement more heat resistant and the embankment more ventilated [13–15]. Among various possible strategies, pavements with high solar reflectance or low thermal conductivity might conduct less heat downward during heat-absorbing of summertime, while crushed stone embankment can cool permafrost by the air convective effect in the voids during heat-releasing of wintertime [16, 17]. The combined strategies of reflective heat-resistant pavement and ventilated embankment could be a potential practice for improving the stability of the expressway embankment in the permafrost areas.

Therefore, a reflective-resistant-ventilated coupling structure (RRVCS) was proposed in this study. It consists of three



FIGURE 2: Photo of the reflective coating.

parts: reflective coating, heat-resistant pavement, and crushed stone embankment. The cooling effect of RRVCS includes the following: (1) the reflective coating would increase the albedo of road surface and decrease the solar radiation absorbed by asphalt pavement; (2) the heat-resistant pavement could impede the heat transferring downward, thus reducing the heat conducted to the frozen soil; and (3) the crushed stone embankment can dramatically release heat accumulated in permafrost embankment according to the Rayleigh–Bernard convection mechanism [18]. While (3) is embankment technology which embodies the function of *ventilated*, (1) and (2) are the pavement measures which manifest the action of *reflective* and *resistant*, respectively. Figure 1 is the schematic diagram of RRVCS. (The red arrows represent heat flowing inward, and the blue arrows represent heat flowing outward).

**2.1. Reflective Coating.** As the dark surface of asphalt pavement has strong heat absorption ability, it is considered to be one of the major causes for permafrost degradation. In order to prevent heat entering into asphalt pavement, a lot of heat reflective materials have been developed. Generally, their global solar reflectance is within the range of 0.4 to 0.8 [19]. In this paper, a white-colored thin layer was used as the reflective coating of RRVCS, as shown in Figure 2. Its solar reflectance was back calculated as 0.5 according to temperature test results. Considering the fact that the reflectivity of the coating can be reduced rapidly by traffic load and environment, its reflectivity was set to be 0.3 for numerical analysis to simulate the long-term behavior of the reflective coating.



FIGURE 3: Photo of vermiculite powder.

**2.2. Heat-Resistant Pavement.** Vermiculite powder, as shown in Figure 3, is characterized as low thermal conductivity and excellent heat insulation. In this study, heat-resistant pavement was designed by adding vermiculite powder into asphalt mixture to lower its thermal conductivity. The maximum dosage was selected as 10% (by weight) of the aggregate to avoid its detrimental impacts on mixture's mechanical performances. Asphalt mixture of type AC-13 was designed, and its gradation is shown in Table 1. Here, SBS (styrene-butadiene-styrene) modified asphalt was used, and the asphalt content was 5.5%. The coarse aggregate was basalt, and the mineral filler was made from limestone.

Asphalt mixtures with 0%, 4%, 6%, 8%, and 10% of vermiculite were made according to China technical specification [20]. Thermal properties of the five types of asphalt mixtures, including heat capacity and thermal conductivity, were measured by a Mathis TCI thermal conductivity tester. The test results can be seen in Table 2.

It can be observed that the thermal conductivity of asphalt mixtures decreases with vermiculite content increasing. Compared with the specimens without vermiculite, the thermal conductivity can be reduced by 22.8%, 29.5%, 37.3%, and 50.6% after the addition of 4%, 6%, 8%, and 10% vermiculite powder, respectively. The test results also indicate that a higher vermiculite content results in a lower specific heat capacity. For example, the specific heat capacity decreases 14.4% when vermiculite dosage increases from 0% to 10%. In this study, asphalt mixture with 10% vermiculite was chosen as the heat-resistant pavement of RRVCS to prevent heat entering into the embankment as much as possible.

**2.3. Crushed Stone Embankment.** Crushed stone embankment is a common roadbed cooling method, which can lower the permafrost temperature based on the air convective effect in the crushed stone layer. It has been widely used in permafrost regions. It is proved that the cooling effects of crushed stone embankment are mainly influenced by the particle size and the thickness of the crushed stone layer [21]. Particles with diameters of 6~8 cm tend to have better cooling effect compared with others [22]. Although there exists an optimum thickness for the crushed stone layer, the thickness is too difficult to be determined because a lot of factors have to be considered. In this paper, a 1.5 m thick crushed stone layer with diameters of 6~8 cm was selected as the crushed stone embankment of RRVCS.

### 3. Finite Element Modeling

**3.1. Fundamental Theory and Equations.** The freezing and thawing of frozen soils are complex processes involving thermal transfer, moisture migration, deformation, and phase change. To simplify the numerical analysis, mass transfer and heat loss of vaporization were not considered in this study. Therefore, based on mass and energy conservation theory [23], two-dimensional heat-fluid coupling equations can be obtained as follows:

$$\begin{aligned} \left( c\rho_s + \rho_w \frac{\partial w_u}{\partial T} \right) \frac{\partial T}{\partial t} = \frac{\partial}{\partial x} \left[ \left( k_x + L\rho_w D_x \frac{\partial w_u}{\partial T} \right) \frac{\partial T}{\partial x} \right] \\ + \frac{\partial}{\partial y} \left[ \left( k_y + L\rho_w D_y \frac{\partial w_u}{\partial T} \right) \frac{\partial T}{\partial y} \right], \end{aligned} \quad (1)$$

where  $c$  is the soil specific heat capacity ( $\text{J}\cdot\text{kg}^{-1}\cdot\text{K}^{-1}$ ),  $\rho_s$  and  $\rho_w$  are the soil and water densities, respectively ( $\text{kg}\cdot\text{m}^{-3}$ ),  $w_u$  is the volumetric unfrozen soil moisture ( $\text{m}^3\cdot\text{m}^{-3}$ ),  $T$  is the temperature ( $^{\circ}\text{C}$ ),  $t$  is the time (s),  $k_x$  and  $k_y$  are the thermal conductivity components of soils at  $x$  and  $y$  directions, respectively ( $\text{W}\cdot\text{m}^{-1}\cdot\text{K}^{-1}$ ),  $D_x$  and  $D_y$  are the water diffusivity components at  $x$  and  $y$  directions, respectively ( $\text{m}^2\cdot\text{s}^{-1}$ ),  $L$  is the volumetric latent heat of thawing ( $\text{J}\cdot\text{m}^{-3}$ ), and  $x$  and  $y$  are the horizontal and vertical directions, respectively.

Based on the physical state (frozen or thawed) of soils and the thermal properties of their components, the equivalent thermal parameters can be obtained as follows:

$$\begin{aligned} c\rho_s + \rho_w \frac{\partial w_u}{\partial T} = \begin{cases} (c_{su} + w_0 c_w) \rho_d, & T \geq -\theta_f \\ \rho_d c_{sf} + \rho_d c_i w_0 + \rho_d (c_w - c_i) \cdot w_0 \theta_f^b (-T)^{-b} + L \cdot w_0 \theta_f^b \cdot b \cdot (-T)^{-(b+1)}, & T < -\theta_f, \end{cases} \\ k_x + L\rho_w D_x \frac{\partial w_u}{\partial T} = k_y + L\rho_w D_y \frac{\partial w_u}{\partial T} = \begin{cases} \lambda_u, & T \geq -\theta_f \\ \lambda_f + LD \cdot w_0 \theta_f^b \cdot b (-T)^{-(b+1)}, & T < -\theta_f, \end{cases} \end{aligned} \quad (2)$$

where  $c_{sf}$  and  $c_{su}$  are the specific heat capacities of soils at frozen and thawed states, respectively ( $\text{J}\cdot\text{kg}^{-1}\cdot\text{K}^{-1}$ ),  $w_0$  is the

volumetric unfrozen water content at the initial state ( $\text{m}^3\cdot\text{m}^{-3}$ ),  $c_i$  is the specific heat capacity of ice ( $\text{J}\cdot\text{kg}^{-1}\cdot\text{K}^{-1}$ ),

TABLE 1: Aggregate gradation for AC-13 mixture.

Sieve sizes (mm)	16.0	13.2	9.5	4.75	2.36	1.18	0.6	0.3	0.15	0.075
Passing (%)	100	96.6	70.1	43.2	32.5	23.7	17.2	12.0	8.5	6.8

TABLE 2: Test results of the thermal parameters of asphalt mixture.

Vermiculite dosage (%)	0	4	6	8	10
Thermal conductivity (W/m·K)	1.154	0.891	0.814	0.724	0.57
Specific heat capacity (J/kg·K)	716.24	691.68	657.44	633.62	613.24

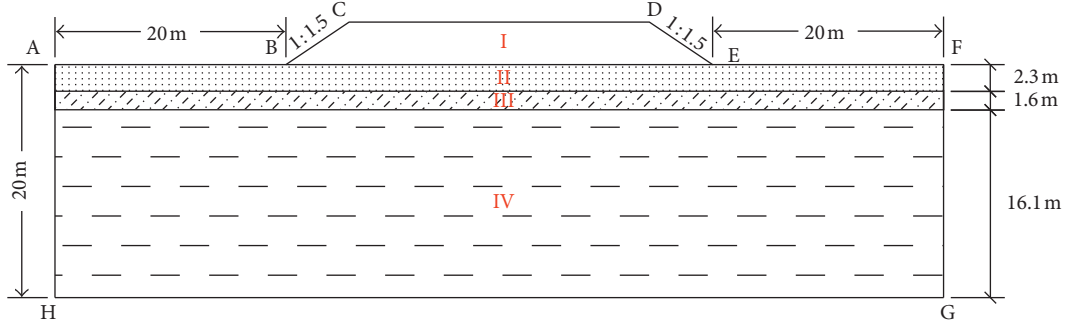


FIGURE 4: Geometric sketch of computational region.

$c_w$  is the specific heat capacity of water ( $\text{J}\cdot\text{kg}^{-1}\cdot\text{K}^{-1}$ ),  $\rho_d$  is the soil dry density ( $\text{kg}\cdot\text{m}^{-3}$ ),  $\theta_f$  is the absolute freezing temperature,  $b$  is a constant related to soil type,  $\lambda_f$  and  $\lambda_u$  are the soil thermal conductivities in the frozen and thawed states, respectively ( $\text{W}\cdot\text{m}^{-1}\cdot\text{K}^{-1}$ ), and  $D$  is the water diffusivity of soils ( $\text{m}^2\cdot\text{s}^{-1}$ ).

The crushed stone layer in highway embankment is a porous media, in which the heat convects unsteadily. Therefore, it is different from the other layers of the embankment. The governing equations for mass, momentum, and energy of the crushed stone layer are given as follows [24]:

Continuity:

$$\frac{\partial \rho}{\partial t} + \frac{\partial(\rho u)}{\partial t} + \frac{\partial(\rho v)}{\partial t}. \quad (3)$$

Momentum:

$$u = -\frac{K}{\mu} \frac{\partial \rho}{\partial x}, \quad (4)$$

$$v = \frac{K}{\mu} \left\{ \frac{\partial \rho}{\partial x} - \rho_0 [1 - \beta(T - T_0)g] \right\}.$$

Energy:

$$C_e \frac{\partial T}{\partial t} + C_a \left( u \frac{\partial T}{\partial x} + v \frac{\partial T}{\partial y} \right) = \frac{\partial}{\partial y} \left( k_y \frac{\partial T}{\partial y} \right) + \frac{\partial}{\partial x} \left( k_x \frac{\partial T}{\partial x} \right), \quad (5)$$

where  $\rho$  is the density of air in porous medium, which can be decided by air temperature ( $\rho = \rho_0 [1 - \beta(T - T_0)]$ );  $\rho_0$  and  $T_0$  are the reference air density and temperature, respectively;  $\beta$  is the air thermal expansion coefficient;  $u$  and  $v$  are the components of air velocities;  $K$  is the permeability of porous medium;  $\mu$  is the dynamic air viscosity;  $p$  is the air pressure;  $C_a$  is the air specific heat at constant pressure; and  $C_e$  is the effective volumetric heat capacity.

**3.2. Numerical Model and Parameters.** Figure 4 shows the geometric sketch of computational region for the numerical model. Part I represents the wide embankment which is 50 m in width, 3 m in height, and 1 : 1.5 for the side slope gradient. According to the monitoring section K3 + 016 of Qinghai-Tibet Highway, the natural ground consists of three layers represented by Parts II, III, and IV, respectively. To eliminate the influence of model size on the simulation results, the natural ground depth underlying embankment is chosen as 20 m while the flank fields are extended for 20 m from both slope toes of embankment. The specific material parameters for different soils are seen in Table 3. The pavement structure and corresponding material parameters are listed in Table 4. To analyze the influences of embankment width on the cooling effectiveness of different measures, the width of embankment in the numerical model is adjustable. DC2D8 (eight-node quadrilateral heat-transmitting element) was adopted in the numerical model. And user-defined subordinate program named as "UMATHT" was developed to calculate the equivalent thermal parameters of soils. During numerical modeling, the 1.5 m thick crushed stone layer was set at 0.5 m above the surface of the natural ground. Table 5 lists the thermal parameters of crushed stone layer.

TABLE 3: Material parameters for different soils.

Material parameters	Part I Gravel soil	Part II Pebbly clay	Part III Gravel loam	Part IV Strong erosion mudstone
$W_0$ (%)	25	30	30	30
$\rho_d$ ( $\text{kg}\cdot\text{m}^{-3}$ )	1800	1700	1300	1500
$c_{sf}$ ( $\text{kJ}\cdot\text{kg}^{-1}\cdot\text{K}^{-1}$ )	0.71	0.73	0.75	0.75
$c_{su}$ ( $\text{kJ}\cdot\text{kg}^{-1}\cdot\text{K}^{-1}$ )	0.79	0.84	0.84	0.84
$c_i$ ( $\text{kJ}\cdot\text{kg}^{-1}\cdot\text{K}^{-1}$ )	2.09	2.09	2.09	2.09
$c_w$ ( $\text{kJ}\cdot\text{kg}^{-1}\cdot\text{K}^{-1}$ )	4.182	4.182	4.182	4.182
$\lambda_f$ ( $\text{W}\cdot\text{m}^{-1}\cdot\text{K}^{-1}$ )	1.980	2.69	1.22	1.82
$\lambda_u$ ( $\text{W}\cdot\text{m}^{-1}\cdot\text{K}^{-1}$ )	1.919	1.95	0.87	1.47
$-\theta_f$ ( $^{\circ}\text{C}$ )	-0.20	-0.10	-0.19	-0.05
$D$ ( $\text{m}^2\cdot\text{s}^{-1}$ )	$9.35 \times 10^{-6}$	4.66	3.73	3.44
$B$	0.610	0.733	0.574	0.474
$L$ ( $\text{J}\cdot\text{m}^{-3}$ )	334.56	334.56	334.56	334.56

TABLE 4: Pavement structure and material parameters.

	Upper asphalt layer	Lower asphalt layer	Base	Subbase	Cushion
Material	AC13	AC20	ATP25	Cement stabilized macadam	Graded gravel
Thickness (m)	0.04	0.05	0.12	0.24	0.2
Density ( $\text{kg}\cdot\text{m}^{-3}$ )	2300	2320	2350	2200	2000
Specific capacity ( $\text{J}\cdot\text{kg}^{-1}\cdot\text{K}^{-1}$ )	1670	1670	1260	960	1100
Thermal conductivity ( $\text{W}\cdot\text{m}^{-1}\cdot\text{K}^{-1}$ )	1.15	1.20	0.81	1.56	1.68

TABLE 5: Thermal parameters for crushed stone layer.

Materials	Density ( $\text{kg}\cdot\text{m}^{-3}$ )	Specific capacity ( $\text{J}\cdot\text{kg}^{-1}\cdot\text{K}^{-1}$ )	Thermal conductivity ( $\text{W}\cdot\text{m}^{-1}\cdot\text{K}^{-1}$ )
Crushed stone	1490	839	0.40

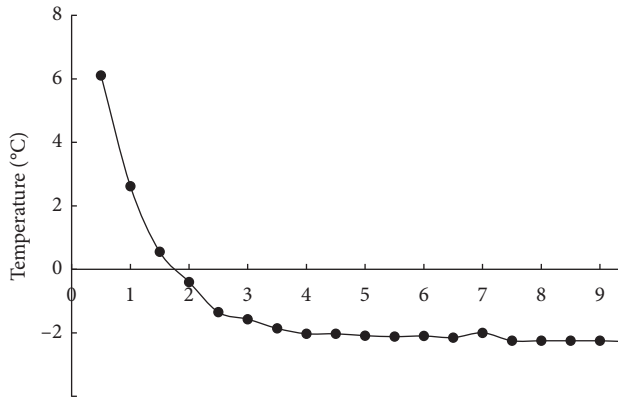


FIGURE 5: Initial ground temperature at different depths.

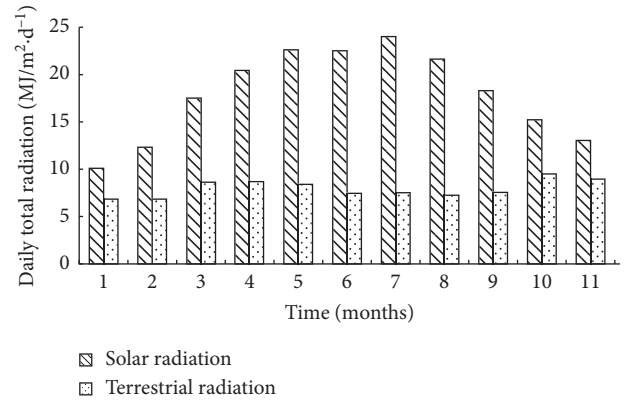


FIGURE 6: Field observed data for solar and ground radiation.

3.3. *Initial and Boundary Conditions.* The temperature field data at section K3 + 016 of QTH in August 2000 were used in this study as the initial ground temperatures of the model. Figure 5 shows the initial temperature at different depths from the natural ground surface (represented by line AF in Figure 4).

Most of the current temperature field models of permafrost embankments used the first thermal boundary condition. However, this kind of boundary condition is based on observed temperature data of narrow embankments and

cannot be simply applied to wide embankments. Therefore, in this study, the second and third thermal boundary conditions including solar radiation, terrestrial radiation, wind velocity, and air temperature were adopted in the model. The field observed data for solar and terrestrial radiation which are used in numerical analysis are given in Figure 6. The monthly average wind velocities are summarized in Table 6.

According to previous research [25], the air temperature increment after fifty years was predicted to be  $2.6^{\circ}\text{C}$ . During numerical analysis, the monthly average air temperature was

TABLE 6: Monthly average wind velocities.

Month	1	2	3	4	5	6	7	8	9	10	11	12
Wind velocities (m·s <sup>-1</sup> )	5.69	5.83	5.92	4.79	4.37	4.11	3.72	3.37	3.38	3.58	4.29	5.23

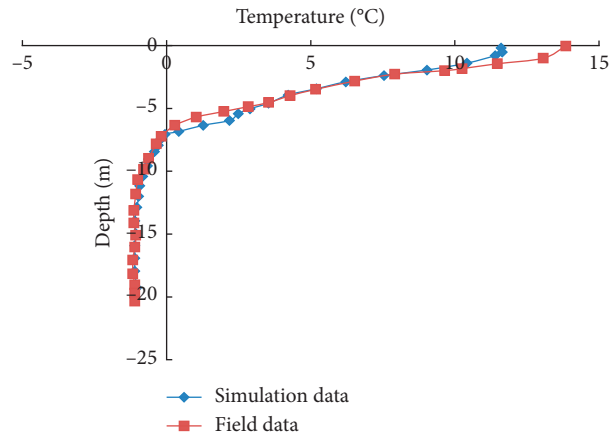


FIGURE 7: Comparison between calculated and measured temperature data in September.

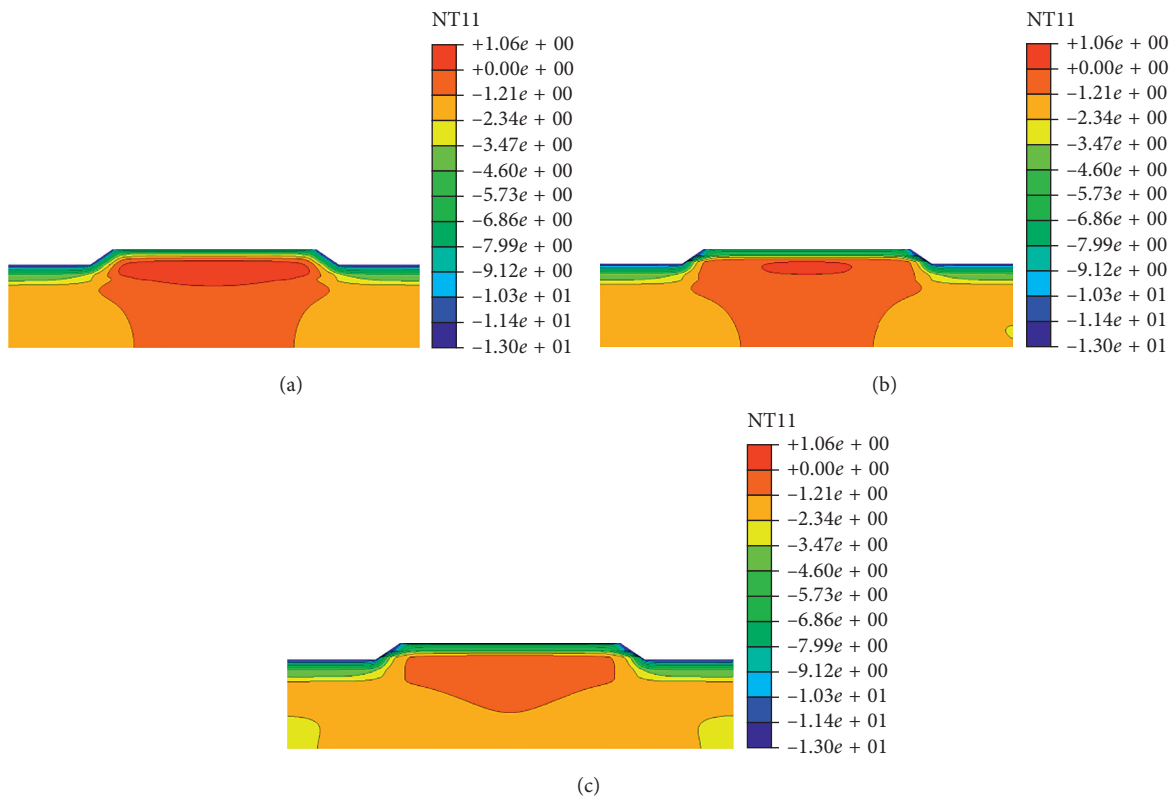


FIGURE 8: The tenth-year temperature fields in January for different embankments: (a) normal embankment, (b) CS embankment, and (c) RRVCS embankment.

described by sine function, as shown in (6). User-defined subordinate programs DFLUX and FILM were developed to define the second thermal boundary condition (solar

radiation and terrestrial radiation) and the third thermal boundary condition (wind velocity and air temperature), respectively:

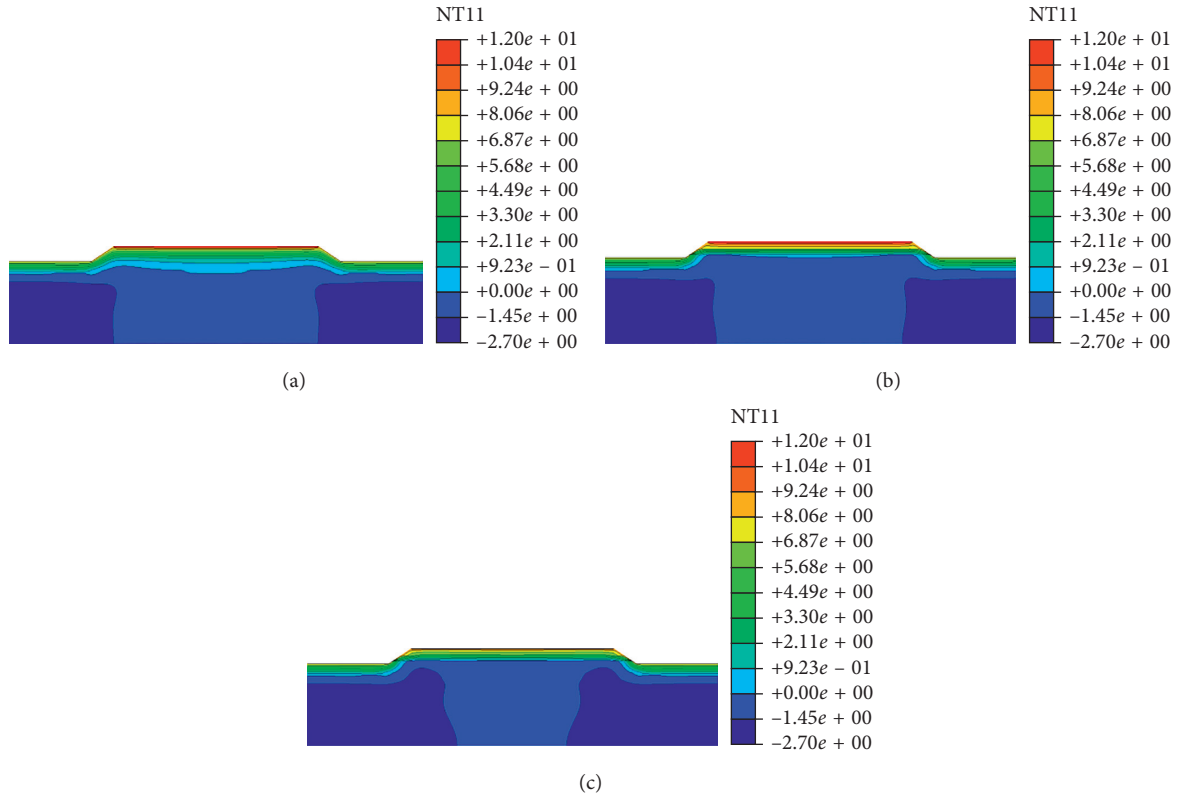


FIGURE 9: The tenth-year temperature fields in August for different embankments: (a) normal embankment, (b) CS embankment, (c) and RRVCS embankment.

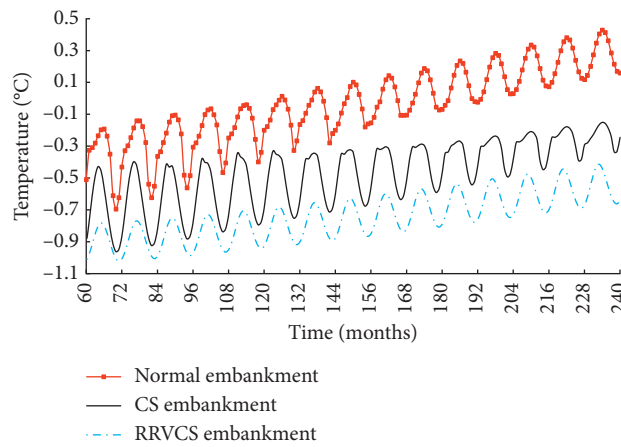


FIGURE 10: Temperature variations with service time for different embankments.

$$T = -5.2 + 11.3 \sin\left(\frac{2\pi}{12}t + \frac{5\pi}{9}\right) + \frac{2.6t}{600}, \quad (6)$$

where  $T$  is the monthly average air temperature ( $^{\circ}\text{C}$ ) and  $t$  is the time (month).

3.4. *Verification of Numerical Analysis.* To verify the validity of finite element modeling, the temperature field of section K3 + 016 of the Qinghai-Tibet Highway was calculated using

the numerical model. Figure 7 shows the field temperature data and the simulation data at different depths in September (along the embankment centerline). During numerical analysis, the calculation parameters are fixed and boundary conditions are simplified. Therefore, the simulation data and field data are not exactly the same. However, they are close to each other and present similar variation trend, which proves the feasibility of the numerical model.

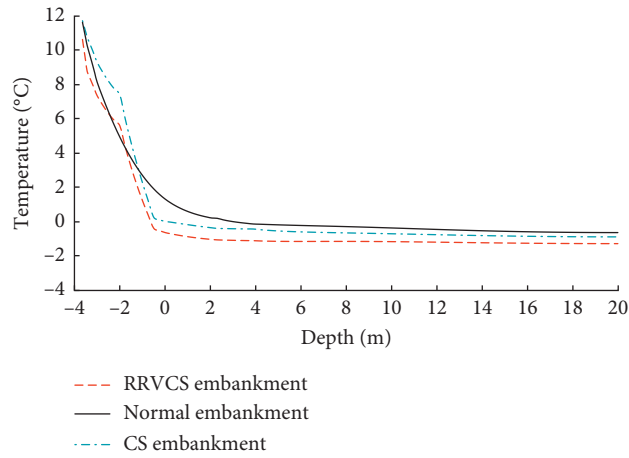


FIGURE 11: Temperature variations with depth at centerline of embankments.

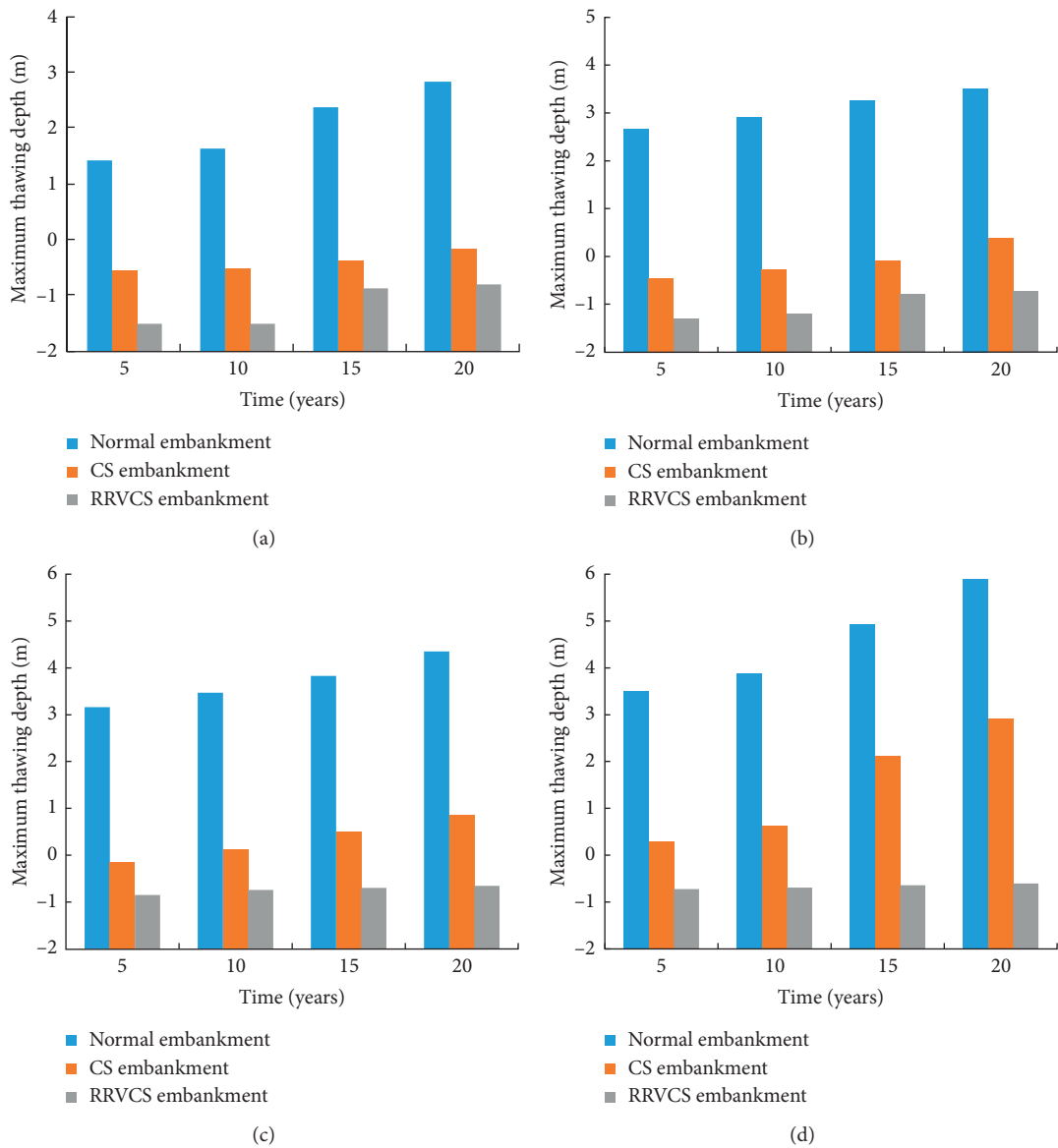


FIGURE 12: Continued.

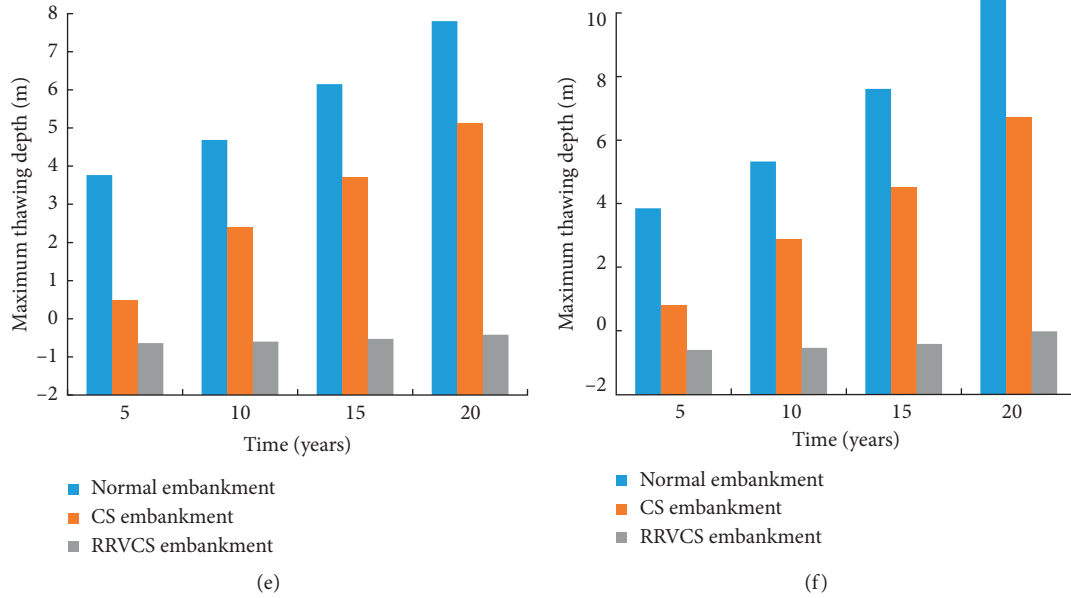


FIGURE 12: The maximum thawing depth versus service time for embankments with different widths: (a) 10 m, (b) 18 m, (c) 26 m, (d) 34 m, (e) 42 m, and (f) 50 m.

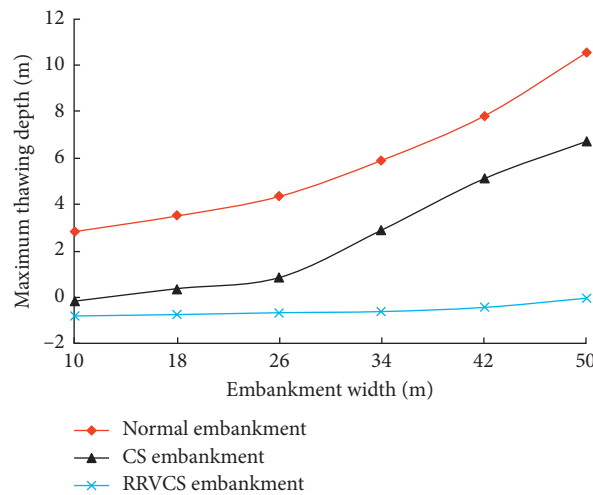


FIGURE 13: The maximum thawing depth versus embankment width for different embankments.

## 4. Results and Discussion

**4.1. Influences of RRVCS on the Temperature Field of Wide Embankment.** Numerical analysis was conducted to obtain the thermal regimes of normal embankment without protective measures, embankment with crushed stone layer (CS embankment), and embankment with RRVCS (RRVCS embankment). Here, the width of all the embankments was chosen as 50 m.

Figures 8 and 9 show the tenth-year temperature fields of the three different embankments in January and August, respectively (the temperature decreases gradually when the color changes from red to blue). From Figure 8, it can be seen that, even at the coldest season, obvious thawing core (represented by the dark red zone with temperature higher than 0°C) was found

within the normal embankment and the CS embankment. However, the thawing core within the normal embankment is much larger than that within the CS embankment. Meanwhile, there is no thawing core within the RRVCS embankment.

From Figure 9, it can be seen that the 0°C contour of the CS embankment is closer to the natural ground surface than that of the normal embankment. While the 0°C contours (shown as the edge of the blue zone with temperature lower than 0°C) of normal embankment and CS embankment are beneath the natural ground, the 0°C contour of RRVCS embankment is above the natural ground (within the embankment). It proves that both crushed stone layer and RRVCS can improve the thermal regime of wide embankment; however, RRVCS embankment has better improving effects.

**4.2. Influences of RRVCS on the Temperature Variations of Wide Embankment.** Figure 10 shows the temperature variations during two decades at the 5 m depth of centerline for different embankments. It can be seen from Figure 10 that all of the three embankments present similar trends: the temperature varies periodically over time but the annual average temperature keeps increasing. The temperature of normal embankment exceeds 0°C after the 10th year, which indicates that the thawing depth of normal embankment has been larger than 5 m since the 10th year. However, the temperature of CS embankment and RRVCS embankment is all less than 0°C during the two decades; hence, their thawing depths are less than 5 m. At the same time point, normal embankment has the highest temperature while RRVCS embankment has the lowest temperature. As a result, RRVCS embankment can slow down the degradation trend of permafrost and has the best thermal stability compared with the other two types of wide embankments.

**4.3. Influences of RRVCS on the Thawing Depth of Wide Embankment.** The temperature variations with depth at the centerline for different embankments are shown in Figure 11. It shows that the temperatures decrease with the depth increasing and 0°C appears at smaller depth for embankment with protective measures. Meanwhile, at the same depth of underlying permafrost, embankment with RRVCS has lowest temperature, which indicates that RRVCS embankment has the least disturbance on the underlying permafrost.

Figure 12 shows the variations of maximum thawing depth with service time for embankments with different widths. It is clearly indicated that, for the same embankment width and service time, the RRVCS embankment has the smallest thawing depth while the normal embankment has the biggest thawing depth. The thawing depth of CS embankment is smaller than that of normal embankment but larger than that of RRVCS embankment. The maximum thawing depth twenty years after embankment construction versus embankment width is shown in Figure 13. It can be seen that with the increase of the embankment width, the thawing depth of normal embankment keeps increasing rapidly while the thawing depth of RRVCS embankment increases slowly. For CS embankment, the thawing depth increases slowly with the embankment width increasing when the embankment width is less than 26 m but increases rapidly with the embankment width increasing after the embankment width exceeds 26 m. Therefore, the cooling effects of crushed stone layer can be obviously weakened by wide embankment with width exceeding 26 m. Meanwhile, the thawing depth differences between normal embankment and RRVCS embankment increase continuously with embankment width increasing. Thus, the RRVCS embankment has the best protective effects for the thermal regime of the wide embankment section.

## 5. Conclusions

- (1) Vermiculite powder has great influences on the thermal property of asphalt mixture. The thermal

conductivity can be reduced by 22.8%, 29.5%, 37.3%, and 50.6% after the addition of 4%, 6%, 8%, and 10% vermiculite powder.

- (2) The temperatures of normal embankment and embankments with protective measures all change periodically over time, but the mean temperatures rise. At the same time, the temperatures of RRVCS embankment are much lower and the time to reach the maximum temperature is obviously delayed compared with the other embankments.
- (3) Both crushed stone layer and RRVCS can improve the thermal regime of wide embankment. However, after the width of embankment exceeds 26 m, the protective effects of crushed stone layer are obviously weakened by increasing embankment width. Since the reflective coating and heat-resistant pavement are to provide heat resistance for permafrost ground in hot reason and crushed stone layer aims to facilitate the heat dissipation of permafrost ground during cold season, the RRVCS has the best protective effect for wide embankment.
- (4) The reflective-resistant-ventilated coupling structure proposed in this paper provides a promising way to protect the wide embankment of expressway in permafrost zones. It is proposed to be used in the construction of the Qinghai-Tibet Expressway.

## Data Availability

All of the data supporting the conclusions of the study are available in the article and the authors are willing to share the data underlying the findings of the article.

## Conflicts of Interest

The authors declare that there are no conflicts of interest regarding the publication of this paper.

## Acknowledgments

This study was financially supported by the Open Fund of State Engineering Laboratory of Highway Maintenance Technology (Changsha University of Science & Technology, kfj160104), Natural Science Foundation of Jiangsu (BK20161421), National Natural Science Foundation of 363 China (no. 51378006), and Fundamental Research Funds for the Central Universities (no. 2242015R30027).

## References

- [1] T. Wang, G. Q. Zhou, X. Jiang, and J. Z. Wang, "Assessment for the spatial variation characteristics of uncertain thermal parameters for warm frozen soil," *Applied Thermal Engineering*, vol. 134, pp. 484–489, 2018.
- [2] C. Yuan, Q. Yu, Y. You, and L. Guo, "Formation mechanism of longitudinal cracks in expressway embankments with inclined thermosyphons in warm and ice-rich permafrost regions," *Applied Thermal Engineering*, vol. 133, pp. 21–32, 2018.

- [3] S. J. Wang, J. B. Chen, J. Z. Zhang, and Z. L. Li, "Development of highway constructing technology in the permafrost region on the Qinghai-Tibet plateau," *Science in China Series E: Technological Sciences*, vol. 52, no. 2, pp. 497–506, 2009.
- [4] H. J. Jin, Q. H. Yu, S. L. Wang, and L. Z. Lü, "Changes in permafrost environments along the Qinghai-Tibet engineering corridor induced by anthropogenic activities and climate warming," *Cold Regions Science and Technology*, vol. 53, no. 3, pp. 317–333, 2008.
- [5] Y. Sheng, J. M. Zhang, Y. Z. Liu, and J. M. Wu, "Thermal regime in the embankment of Qinghai-Tibetan highway in permafrost regions," *Cold Regions Science and Technology*, vol. 35, no. 1, pp. 35–44, 2002.
- [6] G. D. Cheng, "A roadbed cooling approach for the construction of Qinghai-Tibet railway," *Cold Regions Science and Technology*, vol. 42, no. 2, pp. 169–176, 2005.
- [7] R. Fortier, A. M. Leblanc, and W. B. Yu, "Impacts of permafrost degradation on a road embankment at Umiujaq in Nunavik (Quebec), Canada," *Canadian Geotechnical Journal*, vol. 48, no. 5, pp. 720–740, 2011.
- [8] Q. B. Wu and F. J. Niu, "Permafrost changes and engineering stability in Qinghai-Xizang plateau," *Chinese Science Bulletin*, vol. 58, no. 10, pp. 1079–1094, 2013.
- [9] Q. B. Wu and T. J. Zhang, "Changes in active layer thickness over the Qinghai-Tibetan plateau from 1995 to 2007," *Journal of Geophysical Research*, vol. 115, no. 9, pp. 1–12, 2010.
- [10] Q. H. Yu, Y. Z. Liu, and C. J. Tong, "Analysis of the subgrade deformation of the Qinghai-Tibetan highway," *Journal of Glaciology and Geocryology*, vol. 24, no. 5, pp. 623–627, 2002.
- [11] C. Zhang, H. N. Wang, Z. P. You, and B. Ma, "Sensitivity analysis of longitudinal cracking on asphalt pavement using MEPDG in permafrost region," *Journal of Traffic and Transportation Engineering (English Edition)*, vol. 2, no. 1, pp. 40–47, 2015.
- [12] Q. H. Yu, X. C. Pan, G. D. Cheng, and Y. Bai, "Heat transfer process of roadway embankments with different type and width of road surface in permafrost regions," *Progress in Natural Science*, vol. 17, no. 3, pp. 314–319, 2007.
- [13] J. P. Li and Y. Sheng, "Analysis of the thermal stability of an embankment under different pavement types in high temperature permafrost regions," *Cold Regions Science and Technology*, vol. 54, no. 2, pp. 120–123, 2008.
- [14] Z. Wen, S. Yu, W. Ma, and J. L. Qi, "In situ experimental study on thermal protection effects of the insulation method on warm permafrost," *Cold Regions Science and Technology*, vol. 53, no. 3, pp. 369–381, 2008.
- [15] J. J. Wu, W. Ma, Z. Z. Sun, and Z. Wen, "In-situ study on cooling effect of the two-phase closed thermosyphon and insulation combinational embankment of the Qinghai-Tibet," *Cold Regions Science and Technology*, vol. 60, no. 3, pp. 234–244, 2010.
- [16] B. X. Sun, L. J. Yang, Q. Liu, W. Wang, and X. Z. Xu, "Experimental study on cooling enhancement of crushed rock layer with perforated ventilation pipe under airtight top surface," *Cold Regions Science and Technology*, vol. 68, no. 3, pp. 150–161, 2011.
- [17] J. W. Zhang, J. P. Li, and X. J. Quan, "Thermal stability analysis under embankment with asphalt pavement and cement pavement in permafrost regions," *Scientific World Journal*, vol. 2013, Article ID 549623, no. 12, pp. 1–12, 2013.
- [18] G. D. Cheng, Y. M. Lai, Z. Z. Sun, and F. Jiang, "The 'thermal semi-conductor' effect of crushed rocks," *Permafrost and Periglacial Processes*, vol. 18, no. 2, pp. 151–160, 2007.
- [19] Y. F. Du, Q. Shi, and S. Y. Wang, "Highly oriented heat-induced structure of asphalt pavement for reducing pavement temperature," *Energy and Buildings*, vol. 85, pp. 23–31, 2014.
- [20] JTG F40-2004, *Technical Specifications for Construction of Highway Asphalt Pavement*, China Communications Press, Beijing, China, 2004.
- [21] J. Qian, Q. H. Yu, Y. H. You, J. Hu, and L. Guo, "Analysis on the convection cooling process of crushed-rock embankment of high-grade highway in permafrost regions," *Cold Regions Science and Technology*, vol. 78, pp. 115–121, 2012.
- [22] B. X. Sun, X. Z. Xu, Y. M. Lai, S. J. Wang, and J. Z. Zhang, "Impact of ballast grain sizes on natural convection cooling effect of embankment in permafrost regions," *Chinese Journal of Geotechnical Engineering*, vol. 26, no. 6, pp. 809–814, 2004.
- [23] R. L. Harlan, "Analysis of coupled heat-fluid transport in partially frozen soil," *Journal of Water Resource Research*, vol. 9, no. 5, pp. 1314–1323, 1973.
- [24] S. J. Wang, "Study on highway subgrade stabilization and prediction technique in plateau permafrost region," Ph.D. thesis, Southeast University, Nanjing, China, 2005.
- [25] S. J. Wang, X. M. Huang, and S. G. Hou, "Numerical analyses of pavement deformation and stress in permafrost regions," *Journal of Glaciology and Geocryology*, vol. 28, no. 2, pp. 217–222, 2006.

## Research Article

# Measurement of Degree of Compaction of Fine-Grained Soil Subgrade Using Light Dynamic Penetrometer

Junhui Zhang <sup>1</sup>, Yongsheng Yao <sup>1</sup>, Jianlong Zheng,<sup>1</sup> Xiangqun Huang,<sup>1,2</sup> and Tian Lan<sup>1</sup>

<sup>1</sup>National Engineering Laboratory of Highway Maintenance Technology, Changsha University of Science & Technology, Changsha 410114, China

<sup>2</sup>Hunan Communications Research Institute, Changsha 410007, China

Correspondence should be addressed to Yongsheng Yao; yaoyongsheng23@163.com

Received 27 February 2018; Revised 29 April 2018; Accepted 26 May 2018; Published 12 July 2018

Academic Editor: Qiang Tang

Copyright © 2018 Junhui Zhang et al. This is an open access article distributed under the Creative Commons Attribution License, which permits unrestricted use, distribution, and reproduction in any medium, provided the original work is properly cited.

To determine the degree of compaction of subgrades filled with fine-grained soil, the compaction test and light dynamic penetrometer (LDP) test were carried out for low liquid-limit clay samples with different water contents in laboratory. Then, a prediction equation of the penetration ratio (PR) defined as the depth per drop of the hammer of LDP, degree of compaction ( $K$ ), and water content ( $\omega$ ) was built. After that, the existing fine-grained soil subgrades on LDP-based field tests were excavated. The on-site PR values, water contents, and degrees of compaction of slopes were obtained. The estimated degrees of compaction using the prediction equation were compared with measured values of the degree of compaction in field. The results show that there is good consistency between them, and an error within 3.5% was obtained. In addition, the water content should be determined firstly while using the prediction equation which is proposed in this study. Therefore, a numerical method of the water content of a subgrade was developed, and the predicted and measured water contents were compared, which shows a relatively high relativity. Then, the degree of compaction of fine-grained soil subgrades can be calculated according to the predicting equation, which involves the penetration ratio (PR) and the numerically calculated water content as input instead of the measured value in the field.

## 1. Introduction

In civil engineering, the investigation of the strength and integrity of every highway subgrade becomes necessary to optimize pavement structural performance and safety [1]. The degree of compaction is a significant index of investigation to achieve the goal of in situ quality control/quality assurance of granular pavement layers (subgrade, subbase, and base) [2–4]. If the results of investigation do not meet the requirements of compaction in design, the carrying capacity of the subgrade would be lower and then some distresses would occur such as the settlement of the subgrade and the cracking of pavement [5]. Traditionally, one of the activities during the subgrade investigation is determination of degree of compaction with different field and laboratory tests such as the sand-cone method [6] and cutting ring method [7, 8]. Although these evaluation methods are the best and reliable, they have

relatively complicated steps and take much time to have the end result [9]. In addition, the soil samples in these methods need to be cored or excavated on the subgrade which is destructive and can have significant impact on pavement performance [10]. To overcome these shortcomings, many nondestructive and time-saving determination methods and equipment have been developed [11–13].

As a nondestructive, effective, fast, and reliable testing method, the dynamic cone penetrometer (DCP) has been introduced as a criterion for testing the foundation capacity in specifications of American Association of State Highway and Transportation Officials (AASHTO) and South Africa [14]. This device provides continuous and uninterrupted stratigraphic data when its cone probe is driven into soil along the vertical depth. The data obtained from the DCP have got a strong theoretical acceptance and can be used to comprehensively assess the foundation soil. The application of the DCP

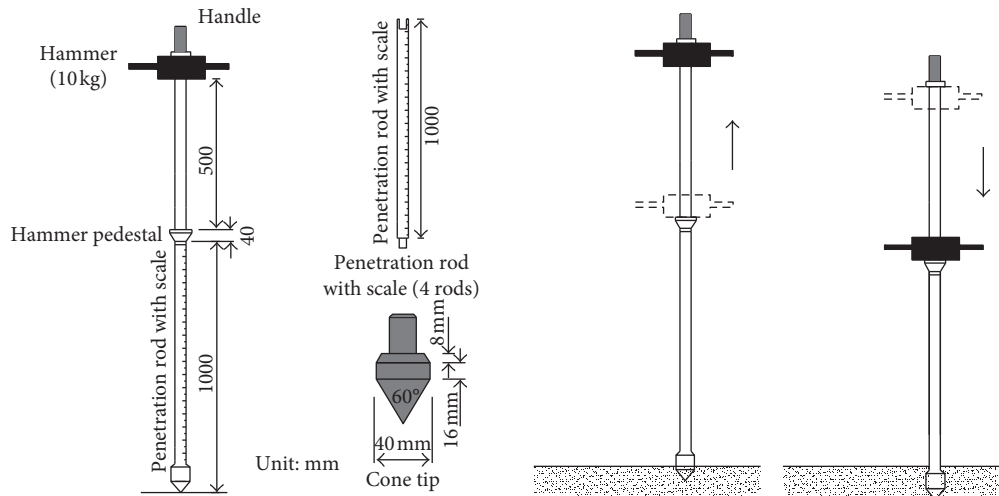


FIGURE 1: Diagram of the LDP device and principal.

was further investigated by previous researchers. Siekmeier et al. [15], George et al. [16], and Mukabi [17] built the empirical formula combining the penetration ratio (PR) of the DCP with the elasticity modulus and California bearing ratio (CBR). Mohammadi et al. [18], Alghamdi [19], Emre et al. [20], and Yang et al. [21] have gained some beneficial achievements to evaluate the subgrade compactness by the DCP, and the correlation between the degree of compaction, penetration ratio, and water content was established. The advantage of using the DCP is testing the soil properties in its natural density and moisture content state. These applications of the theory and method of the DCP have been accepted for different soils, and they provide a way to the empirical correlations based on the statistical analyses of field tests and soil properties.

The light dynamic penetrometer (LDP) is also a non-destructive method to evaluate the performance of the soil layer, which has a similar working principle to the DCP's. Compared to the DCP, its hammer is lighter and the drop distance is shorter, which is convenient and fast for the field testing of subgrade using the LDP instead of the DCP. Therefore, the objective of this paper is to test the degree of compaction of the fine-grained soil subgrade using the LDP. First, the principles and steps of the LDP-based test were introduced. The compaction and LDP tests of a typical low liquid-limit clay were conducted in the laboratory, and a quadratic predicting equation between the degree of compaction ( $K$ ), the penetration ratio (PR), and the water content ( $\omega$ ) was established. Then, the validity of this equation was verified by the field tests of fine-grained soil subgrades. Finally, a numerical method for calculating the water content of subgrades was put forward and verified. Thus, the degree of compaction of fine-grained soil subgrades can be calculated according to the quadratic predicting equation, which uses the penetration ratio (PR) and the numerically calculated water content instead of the measured value in the field.

## 2. Device and Testing Method of LDP

The light dynamic penetrometer (LDP), a small-sized portable foundation soil in situ test penetrometer, consists of

a hammer (10 kg in weight and 500 mm in drop distance), a penetration rod (1,000 mm long and a total of 4 rods), and a conical head (40 mm in diameter and  $60^\circ$  at the conical tip), as shown in Figure 1. When a field test is conducted using the LDP, the depth and drops of the hammer of the LDP are recorded when the cone tip is driven into soils by the hammer. The penetration ratio (PR), defined as the depth per drop of the hammer, can reflect the properties of soil layers.

When a test using the LDP is conducted, the following procedure should be carried out:

- (1) The testing site should be flat, and a record book also should be prepared.
- (2) Cone tip and penetration rod with scale should be assembled and connected. The penetration rod should always be perpendicular to the ground surface when the test is in progress.
- (3) When the test is in progress, the penetration rod should be held on by one tester. The hammer should be lifted and released along the penetration rod. At the same time, the penetration frequency and depth are needed to be recorded.

## 3. LDP-Based Lab Test and Prediction of Degree of Compaction

**3.1. LDP-Based Lab Test.** The soil samples were taken from the Nanchang-Zhangshu expressway widening project in Jiangxi Province. The liquid limit, plastic limit, optimum moisture content, maximum dry density, and particle size analysis were conducted for soil classification and basic properties. Their liquid limit and plastic limit are 35.8% and 22.8%, respectively. According to the compaction test, the optimum moisture content and maximum dry density are 13.0% and  $1.954 \text{ g/cm}^3$ , respectively. The particle size analysis shows that 0.075 mm passing percentage of the soil samples is 82.2%. Therefore, the soil sample was categorized as a low liquid-limit clay according to the standard of *Test*



FIGURE 2: LDP-based lab test.

*Methods of Soils for Highway Engineering* (JTG E40-2007) in China.

In order to study the influence of water content on the PR measured by the LDP, different soil specimens with 5 initial water contents and 5 dry densities were prepared. The water contents of soil samples were set to 9%, 13%, 16%, 19%, and 23%, covering the possible moisture content range of subgrade soils in China. The degrees of compaction of the subgrade are 96% and 93%, respectively, according to the requirements of the current specification in China. In order to improve the accuracy of the LDP-based test, the degrees of compaction of 82%, 86%, 90%, 94%, and 98% of soil samples were selected. The samples of 152 mm × 220 mm (diameter × height) were prepared by the static pressure method by 5 layers, as shown in Figure 2. The relationships between the water content and PR with different degrees of compaction were curved in Figure 3. It can be seen in Figure 3 that the minimum PR value is found nearby the optimum water content for the same degree of compaction, and the PR values decrease with the increasing degree of compaction values for the same water content. As mentioned above, the penetration ratio (PR) of the LDP can reflect the density properties of soil layers. Thus, the relationship between the PR, degree of compaction ( $K$ ), and water content ( $\omega$ ) of soils can be built according to the results of the LDP [18–21], as shown in the following equation:

$$K = 0.1538\omega^2 - 3.9713\omega - 1.1284PR + 121.3193 \quad (R^2 = 0.897), \quad (1)$$

where  $K$  is the degree of compaction of soil (%), PR is the penetration ratio (mm/drop), and  $\omega$  is the water content of soil (%).

**3.2. LDP-Based Field Test.** A typical section of K24 + 600, where the soil samples were taken from, was selected. The light dynamic penetrometer (LDP) tests were carried out

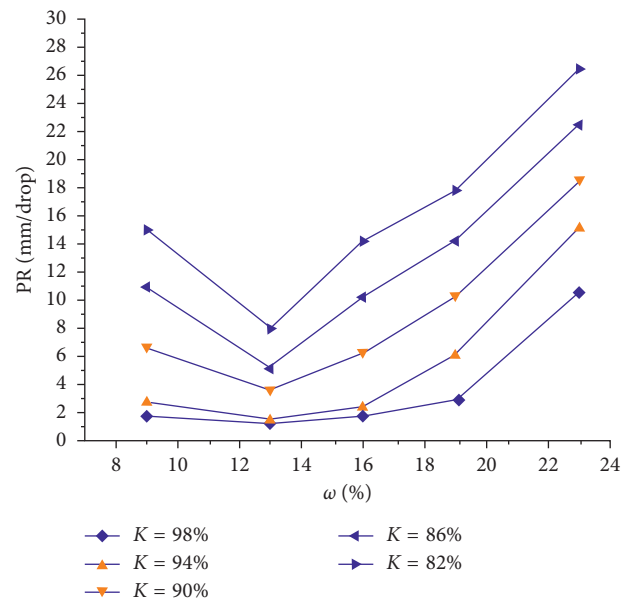


FIGURE 3: PR- $\omega$  under different compaction conditions.

from the top of 96 zone (i.e., the degree of compaction of 96%), 94 zone, and 93 zone of the existing subgrade, with a penetrating depth of 360 cm, as shown in Figure 4. The test data were recorded for every 20 cm penetration depth.

Figure 5 shows the PR values of different testing programs. It can be seen from Figure 5 that the PR values gradually increase with the increasing depth, which indicates that the degree of compaction of subgrades' slope soil gradually decreases with the increasing depth. The PR value is about 13 mm per stroke of the hammer within the depth of 100 cm of the subgrade slope and distributes relatively uniformly. The reason is that the LDP-based field test was conducted in summer, and the water contents of slope surface were relatively low. The PR values increase gradually and are 14 mm to 20 mm per hammering within the depth of

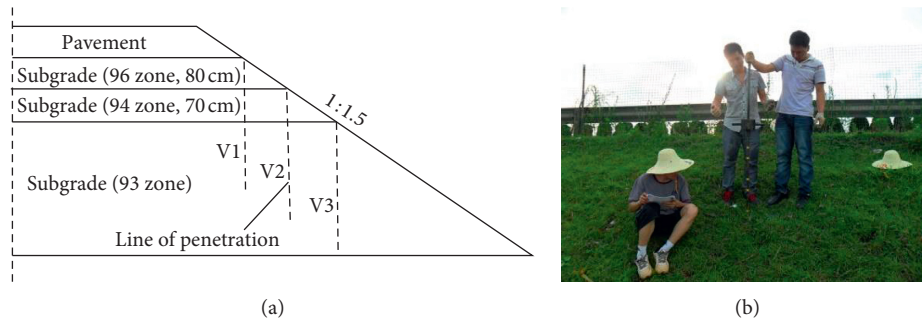


FIGURE 4: (a) Diagram of LDP-based test. (b) LDP-based field test.

100 cm to 360 cm. In addition, it can be seen from Figure 5 that though V1, V2, and V3 started from the top of different zones, their PR values are almost the same within the depth of 100 cm. It shows that there is no obvious difference in properties of the subgrade within this scope in spite of the fact that their initial degrees of compaction are different. Also, Figure 5 shows that the PR values of V3 section are larger than those of the other two sections, which indicates that the water contents of the bottom subgrade are larger than those of the top subgrade.

**3.3. Measurement of Degree of Compaction and Water Content of Subgrade Slope.** To investigate the changes of the degree of compaction and water content of the subgrade slope of K24 + 600, it was excavated manually to a ditch with a 50 cm width and a 510 cm depth along the V1 section. The degree of compaction and water content were measured by the cutting ring test method on the horizontal planes with a vertical distance of 20 cm. The lowest horizontal plane is on the bottom of the ditch. For every horizontal plane, two soil samples with a distance of 20 cm in the longitudinal direction (parallel to the traffic direction) were selected, as shown in Figure 6. Their average values were taken as the final values for this location.

Figure 7 shows the measured water contents and degrees of compaction. It can be seen in Figure 7(a) that the water content increases gradually with the increasing depth and becomes relatively stable below the depth of 200 cm. The water contents are between 18% and 27% within the depth of 200 cm and 21% to 27% below the depth of 200 cm. This is because the water content for the top depth is controlled by the climate and that for the bottom depth is controlled by the ground water. The former changes sharply for different seasons, while the latter is stable with seasonal changes. It can be seen in Figure 7(b) that the degree of compaction changes sharply from 80% to 93% within the depth of 200 cm. For the depth below 200 cm, the degrees of compaction are relatively stable, changing from 82% to 88%.

**3.4. Comparison of Predicted and Measured Degrees of Compaction.** The estimated degrees of compaction using (1) and the measured values are shown in Figure 8. It can be seen in Figure 8 that they are relatively consistent. The root mean square errors between the estimated and measured

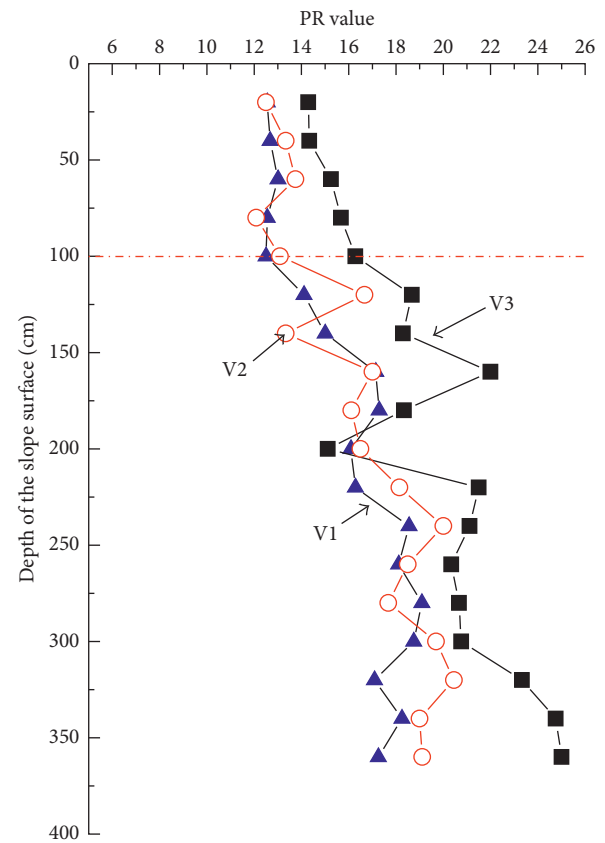


FIGURE 5: PR values for different sections.

degrees of compaction at V1, V2, and V3 vertical sections are 3.44%, 3.24%, and 3.31%, respectively, and the average of root mean square errors is 3.33%. Therefore, the differences between the estimated and measured degrees of compaction are acceptable, which means that the predicting equation of degrees of compaction based on the PR and water content has a satisfactory accuracy.

#### 4. Degree of Compaction according to Numerical Moisture Content

According to the above research, the degree of compaction of subgrade slope soil at different depths can be calculated based on the PR value and the measured water content. The former can be gained quickly using the LDP, and the latter is



FIGURE 6: Locations of soil samples.

time consuming. Therefore, a rapid method to determine the water content is the key to calculate the degree of compaction using (1). The water content of subgrade slope soil can be calculated using the numerical simulation, which is proved to be rational by some researchers using the Geo-Studio software [22–25].

**4.1. Test Parameters.** This simulation needs some parameters including the hydraulic properties, thermodynamic properties, physiological parameters, and meteorological parameters of soils. All the needed parameters are shown in Table 1. Their values can be referred to the literature [22].

**4.2. Calculated and Measured Water Content Values.** Then, a numerical modelling of the subgrade slope of K24 + 600 was completed according to the method of the literature [22, 26, 27]. Water content was calculated using the parameters mentioned above, and the results of calculated water content values of soil are shown in Figure 9. The measured values for the section of K24 + 600 are also drawn in Figure 9. It can be seen in Figure 9 that the calculated and measured water contents of V1, V2, and V3 sections show a good coincidence in general. Due to the inhomogeneity of the subgrade and the measured errors, some data are scattered. Besides the discrete points, the root mean square errors between the measured and calculated water contents of V1, V2, and V3 sections are 1.19%, 1.53%, and 1.34%, respectively, and their average value is 1.35%. It shows a relatively high accuracy for engineering practices. Therefore, the water content of the subgrade in different depths can be calculated using the numerical method.

**4.3. Degree of Compaction Based on Calculated and Measured Water Contents.** Furthermore, to investigate the accuracy of the degrees of compaction from (1) using the calculated and

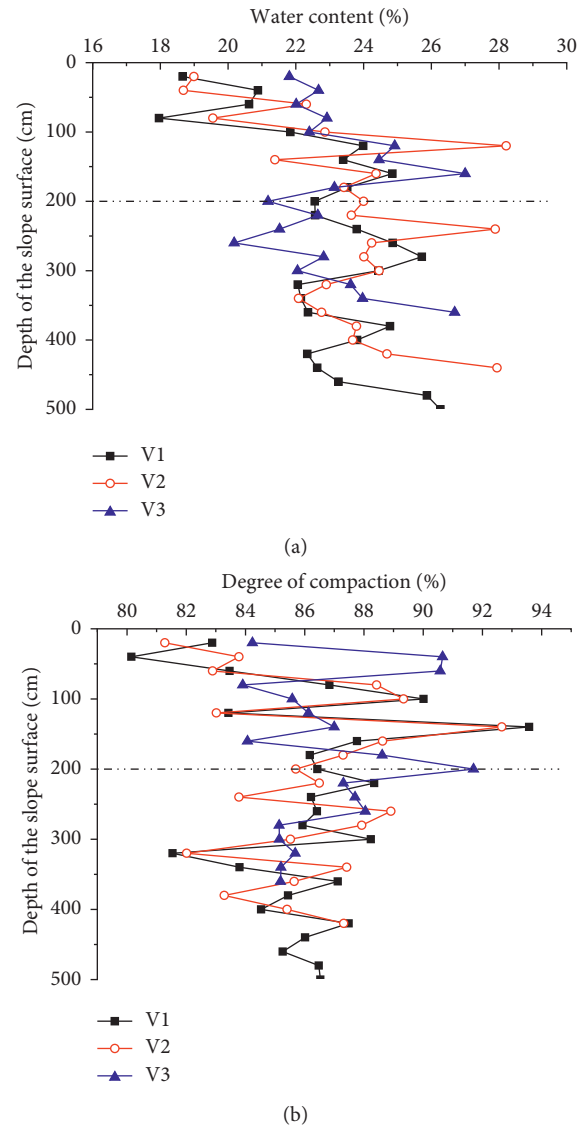


FIGURE 7: Water contents (a) and degrees of compaction (b) for the existing subgrade.

measured water contents, they are shown in Figure 10. It can be seen from Figure 10 that the estimated degrees of compaction of the subgrade based on the numerical water content, in general, do not deviate from the measured values significantly. Due to the inhomogeneity of the subgrade and the measured errors, some test points are scattered. Besides three discrete points, the root mean square errors between the estimated and measured degrees of compaction are 2.80%, 3.53%, and 2.46% for V1, V2, and V3 sections, respectively, and their average value is 2.93%. It shows that, for an existing subgrade, these degrees of compaction estimated by (1) according to the numerical and measured water contents are almost equivalent. Since the water content of any depth in subgrades can be determined using the numerical method in this study without excavating the subgrade slopes, which is much more time-saving than the measurement in the field, the PR and numerical water content can be used to predict the degree of compaction using (1) quickly.

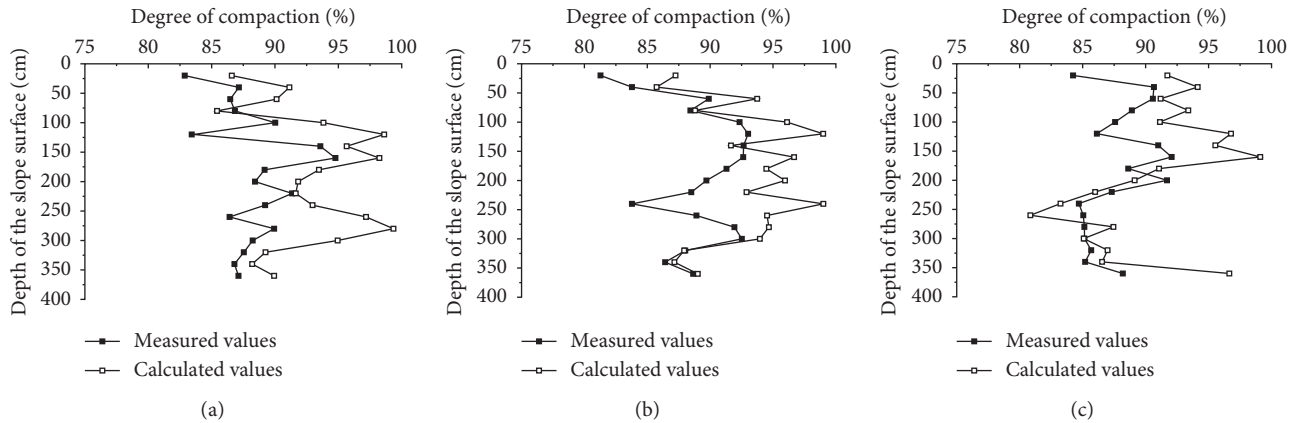


FIGURE 8: Estimated and measured degrees of compaction. Comparison of section: (a) V1; (b) V2; (c) V3.

TABLE 1: Parameters required for the numerical simulation [22].

Parameter category	Relevant parameter	Symbol	Unit
Hydraulic properties	Soil-water characteristic curve	SWCC	—
	Saturated infiltration coefficient	$k_{ws}$	m/s
Thermodynamic properties	Heat conductivity coefficient	$\lambda_t$	—
	Specific heat per unit volume	$\lambda_v$	J/(m <sup>3</sup> ·°C)
Physiological parameters of vegetations	Leaf area index	LAI	—
	Root depth index	$L_R$	M
Meteorological parameters	Daily average temperature	$T$	°C
	Daily relative moisture	RH	%
	Daily relative wind speed	$U$	m/s
	Daily average rainfall	$P_r$	mm

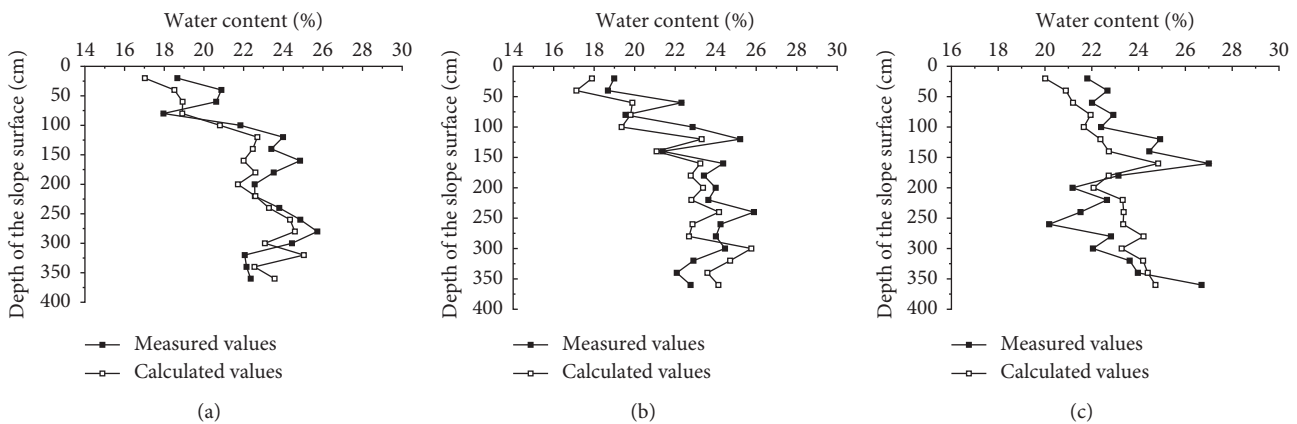


FIGURE 9: Calculated and measured water content values of soil at each vertical section. Comparison of vertical section: (a) V1; (b) V2; (c) V3.

## 5. Conclusions

The compaction test and light dynamic penetrometer (LDP) tests were carried out for low liquid-limit clay samples with different water contents in laboratory. The water content and degree of compaction were measured for a typical subgrade slope of K24 + 600 by the LDP test in field. Then, a prediction equation of the penetration ratio (PR), degree of compaction (K), and water content ( $\omega$ ) was built and verified. In order to

avoid excavating the subgrade slope to measure its water content, a numerical method to determine the water content of a subgrade slope was put forward. It can be utilized to substitute the measured water content. Some major conclusions may be drawn as follows:

- (1) A quadratic function between the degree of compaction, PR, and water content measured of low liquid-limit clay was established and verified. The root mean square error between the estimated and

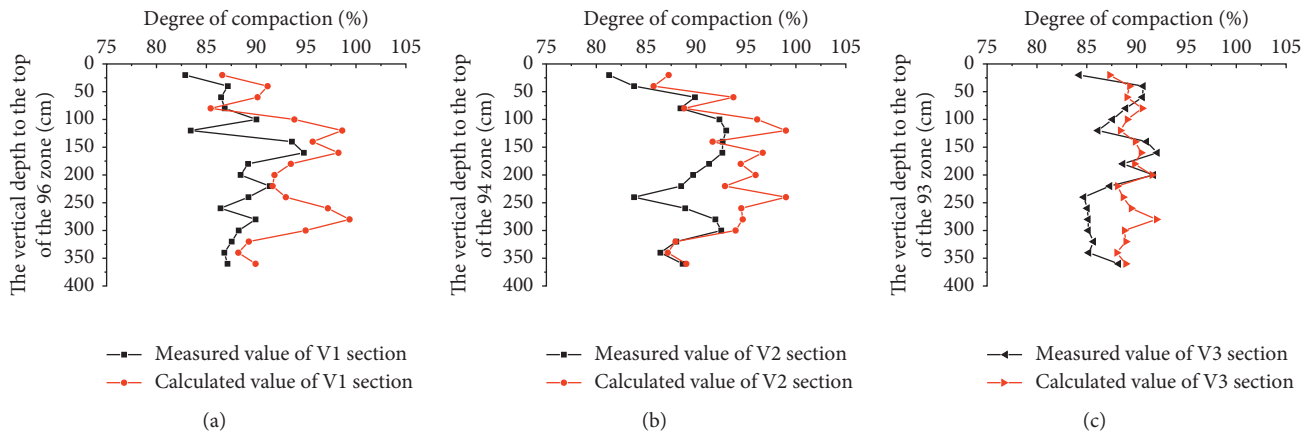


FIGURE 10: Degrees of compaction calculated according to different water contents. Comparison of section: (a) V1; (b) V2; (c) V3.

measured degrees of compaction was within 3.5%, which proves the validity of the relationship proposed in this study.

- (2) It is difficult to measure the water content without excavating the subgrade slopes. A numerical method of water content for subgrade slope soils was proposed and verified. The results show that they have a relatively satisfactory accuracy. Therefore, this numerical method can be utilized to calculate the water content in subgrades, which is much more time saving than the on-site measurement.
- (3) According to the numerical water content, the PR value obtained by the LDP-based field test, and the relationship between the degree of compaction, PR, and water content built in this study, the degree of compaction can be determined quickly. This method was proved to be rational by comparing the calculated and measured water contents.

## Data Availability

The data used to support the findings of this study are available from the corresponding author upon request.

## Conflicts of Interest

The authors declare that they have no conflicts of interest.

## Acknowledgments

The authors gratefully acknowledge the financial support by the National Key Research and Development Program of China (2017YFC0805307), National Natural Science Foundation of China (51478054), Excellent Youth Foundation of Natural Science Foundation of Hunan Province (2018JJ1026), Key Project of Education Department of Hunan Province (17A008), Jiangxi Communications Department Program (2013C0011), and Open Research Fund of State Engineering Laboratory of Highway Maintenance Technology, Changsha University of Science and Technology (kfj150103).

## References

- [1] B. T. Nguyen and A. Mohajerani, "Determination of CBR for fine-grained soils using a dynamic lightweight cone penetrometer," *International Journal of Pavement Engineering*, vol. 16, no. 2, pp. 180–189, 2015.
- [2] M. Kłos, Z. Waszczyszyn, and M. J. Sulewska, "Neural identification of compaction characteristics for granular soils," *Nucleic Acids Research*, vol. 30, no. 1, pp. 395–397, 2017.
- [3] J. H. Zhang, J. H. Peng, J. L. Zheng, and Y. S. Yao, "Characterisation of stress and moisture dependent resilient behaviour for compacted clays in South China," *Road Materials and Pavement Design*, pp. 1–14, 2018.
- [4] A. U. Rehman, K. Farooq, H. Mujtaba et al., "Prediction of California bearing ratio (CBR) and compaction characteristics of granular soils," *Acta Geotechnica Slovenica*, vol. 14, no. 1, pp. 63–72, 2017.
- [5] A. M. Shaban and P. J. Cosentino, "Modeling long-term deformations of unbound pavement materials using the miniaturized pressure meter creep data," *Geotechnical Testing Journal*, vol. 39, no. 5, article 20150273, 2016.
- [6] S. S. Park, "Evaluation of the sand-cone method for determination of the in-situ density of soil," *Geotechnique*, vol. 60, no. 9, pp. 701–707, 2010.
- [7] J. W. Park and J. L. Ferracane, "Measuring the residual stress in dental composites using a ring slitting method," *Dental Materials*, vol. 21, no. 9, pp. 882–889, 2005.
- [8] J. W. Park and J. L. Ferracane, "Evaluation of residual stress in self-adhesive resin cement by the thin ring cutting method," *Dental Materials*, vol. 27, no. S1, p. e58, 2011.
- [9] G. Zhan, "Old and new embankment splicing technology in highway reconstruction project," *Applied Mechanics and Materials*, vol. 587–589, pp. 1190–1193, 2014.
- [10] W. Liu, S. Qu, Z. Nie, and J. Zhang, "Effects of density and moisture variation on dynamic deformation properties of compacted lateritic soil," *Advances in Materials Science and Engineering*, vol. 2016, Article ID 5951832, 11 pages, 2016.
- [11] J. H. Zhang, Q. P. Jiang, Y. Q. Zhang, L. L. Dai, and H. X. Wu, "Nondestructive measurement of water content and moisture migration of unsaturated red clays in South China," *Advances in Materials Science and Engineering*, vol. 2015, Article ID 542538, 7 pages, 2015.
- [12] J. E. Herrick and T. L. Jones, "A dynamic cone penetrometer for measuring soil penetration resistance," *Soil Science Society of America Journal*, vol. 66, no. 4, pp. 1320–1324, 2002.

- [13] L. David Suits, T. C. Sheahan, D. H. Chen, D. F. Lin, P. H. Liau, and J. Bilyeu, "A correlation between dynamic cone penetrometer values and pavement layer moduli," *Geotechnical Testing Journal*, vol. 28, no. 1, pp. 42–49, 2005.
- [14] S. A. Khedr, C. K. David, and L. James, "Automated cone penetrometer: a nondestructive field test for subgrade evaluation," *International Journal of Rock Mechanics and Mining Sciences & Geomechanics Abstracts*, vol. 23, no. 3, p. 94, 1985.
- [15] J. A. Siekmeier, D. Young, and D. Beberg, "Comparison of the dynamic cone penetrometer with other tests during subgrade and granular base characterization in Minnesota," in *Nondestructive Testing of Pavements and Backcalculation of Moduli: Third Volume*, ASTM International, West Conshohocken, PA, USA, 2000.
- [16] V. George, N. C. Rao, and R. Shivashankar, "PFWD, DCP and CBR correlations for evaluation of lateritic subgrades," *International Journal of Pavement Engineering*, vol. 10, no. 3, pp. 189–199, 2009.
- [17] J. N. Mukabi, "Review of DCP Based CBR-UCS and resilient modulus models for applications in highway and airport pavement design," *US Army*, vol. 10, p. 1, 2016.
- [18] S. D. Mohammadi, M. R. Nikoudel, H. Rahimi, and M. Khamehchiyan, "Application of the dynamic cone penetrometer (DCP) for determination of the engineering parameters of sandy soils," *Engineering Geology*, vol. 101, no. 3-4, pp. 195–203, 2008.
- [19] H. A. Alghamdi, *Dynamic Cone Penetrometer (DCP) Based Evaluation of Sustainable Low Volume Road Rehabilitation Techniques*, Ohio University, Columbus, OH, USA, 2016.
- [20] U. Z. V. Emre, S. Mehmet, and İ. Gökalp, "Comparison of DCP, CBR, and RLT test results for granular pavement materials and subgrade with structural perspective," in *Proceedings of the International Symposium Non-Destructive Testing in Civil Engineering (NDT-CE)*, vol. 2, pp. 158–176, Berlin, Germany, September 2015.
- [21] B. Yang, R. Zhang, X. D. Zha, C. Liu, and Q. Pan, "Improved testing method of dynamic cone penetrometer in laboratory for evaluating compaction properties of soil subgrade," *Road Materials and Pavement Design*, vol. 17, no. 2, pp. 487–498, 2015.
- [22] Y. S. Yao, J. L. Zheng, Z. S. Chen, J. H. Zhang, and Y. Li, "Field measurements and numerical simulations of temperature and moisture in highway engineering using a frequency domain reflectometry sensor," *Sensors*, vol. 16, no. 6, p. 857, 2016.
- [23] F. Niu, A. Li, J. Luo et al., "Soil moisture, ground temperatures, and deformation of a high-speed railway embankment in Northeast China," *Cold Regions Science and Technology*, vol. 133, pp. 7–14, 2017.
- [24] N. An, S. Hemmati, and Y. Cui, "Numerical analysis of soil volumetric water content and temperature variations in an embankment due to soil-atmosphere interaction," *Computers and Geotechnics*, vol. 83, pp. 40–51, 2017.
- [25] J. R. Philip and D. A. V. Deries, "Moisture movement in porous materials under temperature gradients," *Transactions American Geophysical Union*, vol. 38, no. 2, pp. 222–232, 1957.
- [26] N. Lu, M. Kaya, and J. W. Godt, "Interrelations among the soil-water retention, hydraulic conductivity, and suction-stress characteristic curves," *Journal of Geotechnical and Environmental Engineering*, vol. 140, no. 5, article 04014007, 2014.
- [27] C. W. W. Ng, C. Zhou, and A. K. Leung, "Comparisons of different suction control techniques by water retention curves: theoretical and experimental studies," *Vadose Zone Journal*, vol. 14, no. 9, 2015.

## Research Article

# Investigating the Pavement Vibration Response for Roadway Service Condition Evaluation

Zhoujing Ye <sup>1</sup>, Yang Lu <sup>2</sup>, and Linbing Wang <sup>3,4</sup>

<sup>1</sup>National Center for Materials Service Safety, University of Science and Technology Beijing, Beijing 100083, China

<sup>2</sup>Civil Engineering Department, Boise State University, Boise, ID 83725-2060, USA

<sup>3</sup>Joint USTB-Virginia Tech Lab on Multifunctional Materials, USTB, Beijing 100083, China

<sup>4</sup>Virginia Tech, Blacksburg, VA 24061, USA

Correspondence should be addressed to Linbing Wang; wangl@vt.edu

Received 24 February 2018; Accepted 28 May 2018; Published 8 July 2018

Academic Editor: Yuqing Zhang

Copyright © 2018 Zhoujing Ye et al. This is an open access article distributed under the Creative Commons Attribution License, which permits unrestricted use, distribution, and reproduction in any medium, provided the original work is properly cited.

Dynamic response of pavement provides service condition information and helps with damage prediction, while limited research is available with the simulation of pavement vibration response for evaluating roadway service condition. This paper presents a numerical model for the analysis of the pavement vibration due to the dynamic load created by a passing vehicle. A quarter vehicle model was used for the determination of the vehicle moving load. Both random and spatial characteristics of the load were considered. The random nonuniform moving load was then introduced in a 3D finite element model for the determination of the traffic-induced pavement vibration. The validated numerical model was used to assess the effects of dynamic load, material properties, and pavement structures on pavement vibration response. Numerical analyses showed that the vibration modes changed considerably for the different roadway service conditions. The vibration signals reflect the level of road roughness, the stiffness of the pavement materials, and the integrity of pavement structure. The acceleration extrema, the time-domain signal waveform, the frequency distribution, and the sum of squares of Fourier amplitude can be potential indexes for evaluating roadway service condition. This provides recommendations for the application of pavement vibration response in early-warning and timely maintenance of road.

## 1. Introduction

Pavement, the important transportation infrastructure, provides a smooth riding surface and basic load-bearing capacity for vehicles to travel on. Pavement structure will deteriorate under cyclic traffic loading and environmental factors. Early repair and maintenance scheduling increase the safe operation and in-service performance of pavement. This can be achieved through an accurate and consistent monitoring of dynamic response of pavement. Because the signal pattern can be analyzed to distinguish between deteriorated or cracked pavement section from the intact ones [1].

Stress-strain, displacement, and acceleration are the important monitoring parameters for the dynamic response of pavement. Due to the substantial improvement of acceleration sensing technologies, the microelectromechanical system (MEMS)-based acceleration sensors have been used

in the monitoring of pavement vibration. The acceleration signals caused by the moving vehicle load were processed to obtain traffic information including vehicle speed, axle weight, and traffic volume [2–5]. Moreover, by detecting the acceleration of pavement under specific wheel loadings and analyzing the vibration modes, it is possible to evaluate the pavement service condition.

Over the past several years, experimental studies have analyzed the pavement vibrations generated by vehicles to evaluate pavement service condition. Arraigada et al. [6] used accelerometers to measure pavement deflections due to traffic loads. Levenberg [7] inferred the pavement layer properties by using an integral electronic piezoelectric accelerometer. Yu and Yu [8] developed a cost-effective vibration-based system for preliminary evaluation of pavement conditions. Zhang et al. [9] analyzed time and frequency spectrums of vertical acceleration for the HMA

slabs under different loading scenarios. However, the application of pavement vibration response in roadway service condition is still in the experimental stage.

On the contrary, theoretical and numerical studies have also been conducted. This can save large amount of laboratory efforts and time. The analyses considering the pavement vibration under dynamic vehicle load are widely adopted by many studies for various research purposes. Ju [10] developed a finite element (FE) model to investigate the characteristics of the building vibrations induced by adjacent moving trucks. Xu and Hong [11] investigated the effects of both a single heavy truck flow and a two-way traffic flow on building vibration. The results showed that traffic-induced ground vibrations disrupted high-tech facilities. Mhanna et al. [12] investigated the effect of the vehicle speed, the road unevenness, and the vehicle suspension system on the traffic-induced vibrations. Some recommendations were suggested for the reduction of these vibrations. Lak et al. [13] studied the relation between road unevenness, the dynamic vehicle response, and ground-borne vibrations. The influence of road unevenness on the free field vibrations was investigated. Wang et al. [14] tested four trackbed materials for their relative vibration attenuation capacities and studied the effect of different speed and weight of the passing train on the performance of the paving materials. Their purpose is to reduce the adverse effects of pavement vibration on the surrounding structures and vehicles, rather than to analyze the pavement vibration signals for evaluating the pavement service condition.

However, there are few studies to evaluate the pavement service condition through vibration simulation analysis. The assessment of roadway service condition is mainly reflected by the monitoring of stress, strain, and displacement. Saad et al. [15] examined the dynamic response of the fatigue strain at the bottom of the asphalt concrete layer and rutting strain at the top of the subgrade material by 3D FE analyses. Alavi et al. [16] compared the dynamic strain data of intact and damaged FE model under moving tire loading. Features extracted from the dynamic strain data were used to detect the damage progression. Xue et al. [17] simulated the loading process by using finite-element analysis. The ratio between vertical stress and longitudinal horizontal strain was demonstrated to be related to the strength of pavements and can be used for the back-calculation of pavement modulus. Wu et al. [18] investigated the dynamic responses of stress and deflection at the critical load position by changing thickness, modulus of isolating layer, and the combination between the isolating layer and concrete slab. Patil et al. [19] studied the effects of vehicle-pavement interaction, pavement thickness, and soil parameters on the dynamic response of pavement to reveal their influences on pavement dynamic performances, including the effects of subbase module on maximum deflection.

Due to the improved MEMS-accelerometer technology, pavement vibration response can be used not only for traffic information monitoring but also has the potential to be used for evaluating the roadway service condition. This paper

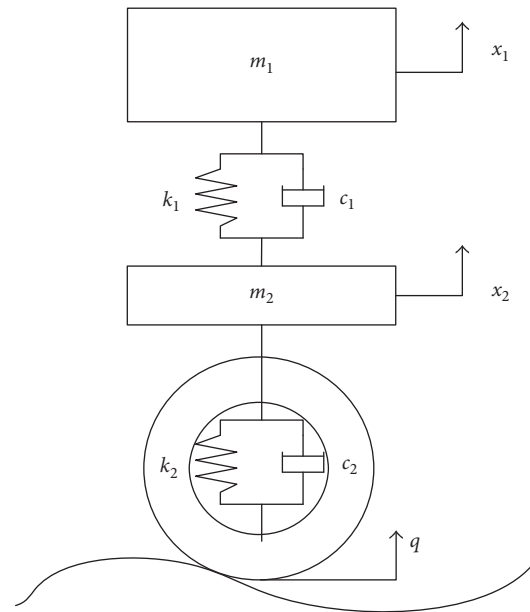


FIGURE 1: The quarter vehicle model.

presents a numerical model for the analyses in the time-frequency domain of the traffic-induced vibrations. The numerical modeling includes two stages. In the first stage, a quarter vehicle model is used for the determination in the time domain of the load due to road roughness. Both random and spatial characteristics of the load were considered. In the second stage, a 3D FE model of road is used to determine the pavement vibrations due to the load, which is calculated in the first stage. Then, the validated road model is used to evaluate the effects of dynamic load, pavement materials, and structure on pavement vibration response, so as to determine the potential evaluation index of roadway service condition.

## 2. Numerical Model

In the case of vehicle-road interaction, the prediction of the dynamic axle loads can be uncoupled from the solution of the road-pavement interaction problem due to the high stiffness of the road compared to the vehicle's suspension system or tire [20–23]. Therefore, the numerical modeling includes two stages: Firstly, the dynamic axle load resulting from pavement roughness was calculated by establishing a moving vehicle model composed of springs, dampers, and lumped mass. Then, the resulting axle dynamic load is used in a 3D numerical modeling for the determination of the pavement vibrations.

### 2.1. Random Nonuniform Moving Load

**2.1.1. Time History.** The quarter vehicle model, the half vehicle model, and the 3D vehicle model are the common vehicle models. But the quarter vehicle model is a widely used model because it can easily be used with personal computers to predict ride quality and pavement loading

TABLE 1: The parameters of medium truck.

Vehicle parameters	Value
$m_1$ (kg)	4450
$m_2$ (kg)	550
$k_1$ (N·m <sup>-1</sup> )	1000000
$c_1$ (N·s·m <sup>-1</sup> )	15000
$k_2$ (N·m <sup>-1</sup> )	1750000
$c_2$ (N·s·m <sup>-1</sup> )	2000

[24]. Although the quarter vehicle model does not allow to model pitch and roll effect on tire forces, the stochastic load can be simulated efficiently by using the quarter vehicle model when vehicle moves straight at a constant speed. Figure 1 shows the quarter vehicle model [25].

In this model, the suspension and nonsuspension masses corresponding to the one corner of the vehicle are denoted by  $m_1$  and  $m_2$ , respectively. The suspension system is represented by a linear spring of stiffness  $k_1$  and a linear damper of damping rate  $c_1$ . The tire is modeled by a linear spring of stiffness  $k_2$  and a linear damper of damping rate  $c_2$ . The vertical displacements of suspension mass and nonsuspension mass are  $x_1$  and  $x_2$ , respectively. The parameter values chosen for this study are shown in Table 1 [26].

According to the D'Alembert's principle, the motion differential equations of this vibration system are written as

$$M\ddot{X} + C\dot{X} + KX = P, \quad (1)$$

where  $M$ ,  $C$ ,  $K$ ,  $X$ , and  $P$  are mass matrix, damping matrix, stiffness matrix, displacement matrix, and excitement matrix, respectively. They are written as

$$M = \begin{pmatrix} m_1 & 0 \\ 0 & m_2 \end{pmatrix}, \quad (2)$$

$$K = \begin{pmatrix} k_1 & -k_1 \\ -k_1 & k_1 + k_2 \end{pmatrix}, \quad (3)$$

$$C = \begin{pmatrix} c_1 & -c_1 \\ -c_1 & c_1 + c_2 \end{pmatrix}, \quad (4)$$

$$P = \begin{pmatrix} 0 \\ k_2q + c_2\dot{q} \end{pmatrix}, \quad (5)$$

$$X = \begin{pmatrix} x_1 \\ x_2 \end{pmatrix}, \quad (6)$$

where  $q$  is the displacement excited by road roughness, which can be calculated as [27]

$$\dot{q}(t) = 2\pi n_0 \sqrt{G_q(n_0)} v \cdot w(t) - \omega_0 q(t), \quad (7)$$

where  $w(t)$  is the time domain signal of Gaussian white noise with mean zero;  $G_q$  is the road roughness coefficient;  $v$  is the vehicle speed (m/s); and  $n_0$  is the reference space frequency and  $n_0 = 0.1 \text{ m}^{-1}$ . According to (1)–(7), the

vehicle random dynamic load forcing on the pavement can be calculated as

$$\begin{aligned} F_t &= F_d + G, \\ G &= (m_1 + m_2)g, \\ F_d &= k_2(x_2 - q) + c_2(\dot{x}_2 - \dot{q}), \end{aligned} \quad (8)$$

where  $F_t$  is the vehicle random dynamic load;  $G$  is the vehicle static load;  $g$  is the acceleration of gravity; and  $F_d$  is the dynamic load applied by tires on pavement.

The quarter vehicle model was established in Matlab/Simulink. The speed was set to 10 m/s. According to the ISO 8608, the classes A, B, and C of road were obtained by adjusting the geometric mean of road roughness coefficient. The geometric mean of road roughness coefficient was set as 16 (i.e.,  $G_q = 16$ ) when the road was a class A road [28]. Class A road represents high grade road, such as the highway, indicating that the surface of road is smoothness.

The sampling frequency of stochastic load was set as 1000 Hz. Figure 2 shows the random dynamic load when the vehicle speed is 10 m/s and road is class A road.

When the vehicle travels on the class A road, the value of vehicle dynamic load is not constant due to the effect of road roughness, vehicle suspension system, vehicle speed, weight, and other factors. The value of vehicle dynamic load is random and fluctuates around 48 kN.

**2.1.2. Spatial Distribution.** In order to obtain the more actual pavement dynamic response, it is necessary to consider both random and spatial characteristics of the load. The actual tire-to-pavement contact is surface to surface contact. Once the total tire force is known, the actual or more rational contact pressure distribution can be used by considering the actual configurations of the tires [29]. The actual tire-to-pavement contact is simplified as a rectangular area [30]. The rectangular area is affected by the tire pattern and the load value which varies with the space. Figure 3 shows a common style of tire pattern. The size of the rectangular area is 20 cm × 18 cm. There are five rib areas caused by the tire pattern [31].

When the vehicle moves straight at a constant speed, the ratio of load amplitude is about 1 : 0.9 : 0.5 in center rib (R3), intermediate rib (R2, R4), and edge rib (R1, R5). Moreover, the spatial distribution of the vertical load can be simplified as a half-sine function in each rib area along the traffic direction [31, 32].

**2.1.3. Moving Load.** In order to simulate the movement of vehicle load, the secondary development of DLOAD subroutine was carried out based on FE software, ABAQUS, to simulate the random nonuniform moving load. A specified coordinate function COORDS(\*) and a time function TIME(1) were used to define the loading area and implement the moving load. Equation (9) means the loading area moves at a constant velocity along the  $X$  axis which is defined as traffic direction.

$$X = \text{COORDS}(1) - V \times \text{TIME}(1) - X_0, \quad (9)$$

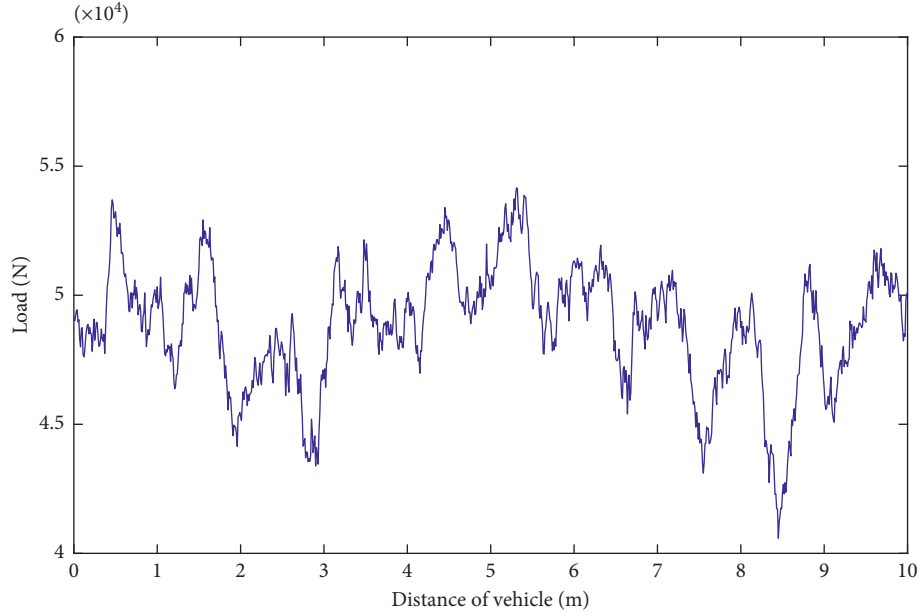


FIGURE 2: The random dynamic load when the vehicle speed is 10 m/s and road is class A road.



FIGURE 3: The actual tire-to-pavement contact.

where COORDS(1) is an array containing the  $X$  coordinates of the load integration point;  $X_0$  is initial coordinate  $X$  value of load;  $V$  is the vehicle speed; and TIME(1) is the current value of step time. Therefore,  $X$  is an array containing the  $X$  coordinates of the load integration point corresponding to the moving coordinate system.

Then the load in each rib by considering random and spatial characteristics was defined. Equation (11) means the spatial distribution of load at time  $t$ .

$$Y = \text{COORDS}(2) - Y_0, \quad (10)$$

$$\begin{aligned} &\text{if } \text{abs}(X) \leq \frac{b}{2} \text{ and } \text{abs}(Y) \leq \frac{c}{2}, \\ &\text{then } P(t) = a * \frac{F(t)}{S} \times \sin\left(\frac{\pi}{b} \times X + \frac{\pi}{2}\right), \end{aligned} \quad (11)$$

where COORDS(2) is an array containing the  $Y$  coordinates of the load integration point; the direction of  $Y$  axis is perpendicular to the traffic direction;  $Y_0$  is initial coordinate  $Y$  value of load;  $\text{abs}(X) \leq (b/2)$  defines the length of the loading area;  $\text{abs}(Y) \leq (c/2)$  defines the width of the loading area;  $a$  is the ratio of load amplitude, which is set as 1 for R3, 0.9 for R2 and R4, and 0.5 for R1 and R5;  $b$  is the length of the load distribution along the traffic direction, which is set as 18 cm for R3, 16 cm for R1, R2, R4, and R5;  $c$  is the width of the load distribution perpendicular to the traffic direction, which is set as 3 cm for each rib;  $S$  is the actual contact area that is the sum of the areas from R1 to R5;  $P(t)$  is the set of the surface pressure on the load integration point at TIME(1); and  $F(t)$  is the random load produced by the quarter vehicle model at TIME(1).

The random nonuniform moving load is achieved by (9) and (11). The vehicle speed was set as 10 m/s, and the length of loading area was set as 3 m. Therefore, the total time period was 0.3 s. The increment time was set as 0.001 s, which was consistent with the sampling frequency (1000 Hz) of stochastic load. Thus, the applied load can be assumed a continuous moving load if loading time is short enough.

**2.2. Finite Element Model of Road.** With the increased computational capabilities, the dynamic FE analysis of a pavement structure is a technique of considerable reduction in computation cost than before. A 3D FE model was developed to analyze the dynamic response of pavement under a moving truck tire loading.

**2.2.1. Calculation Parameters.** A model geometry of  $9.0 \text{ m} \times 6.5 \text{ m} \times 4 \text{ m}$  block was created to represent a typical four-layer roadway structure that referred to the structure of

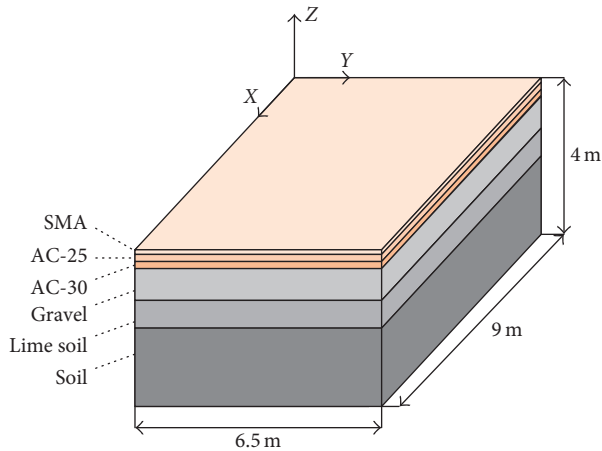


FIGURE 4: The 3D FE model of road.

TABLE 2: The material parameters of asphalt concrete pavement.

Material	Thickness (cm)	Elastic modulus (MPa)	Poisson's ratio	Density ( $\text{kg/m}^3$ )	Damping ratio
SMA16	4	1400	0.35	2400	0.05
AC25	5	1200	0.35	2400	0.05
AC30	7	1000	0.35	2400	0.05
Gravel	38	1300	0.25	2100	0.05
Lime soil	36	600	0.3	1900	0.05
Soil	200	50	0.4	1800	0.05

Beijing 6th ring road. The information of this structure came from Dong's research [31]. Figure 4 shows the road model. The surface layer includes SMA, AC25, and AC30. The axes of X, Y, and Z were set align with the longitudinal, transverse, and vertical direction, respectively. The driving direction was along the positive direction of X axis.

Material parameters of each structure layer were determined by reference to the Specifications for Design of Highway Asphalt Pavement (Appendix E) [33], as shown in Table 2. The material parameters of AC30 were estimated by referring to the lower limit value of material parameters of AC25. The material viscosity was considered using Rayleigh damping for the energy dissipation through the medium. The damping ratio of pavement structure is generally between 0.02 and 0.2 and is set as 0.05 [34].

**2.2.2. Constrain Condition and Mesh Generation.** The three direction movements and rotations were restrained at the bottom of the subgrade on the model. The normal directions were restrained corresponding to the four sides of the model. In order to decrease the number of elements and reduce the cost of computation, the interface between subbase and subgrade was set as Tie constraint because of the small deformation on the subgrade. A Tie constraint ties two separate surfaces together so that there is no relative motion between them. The central area of the model surface was set as the loading area, so as to reduce the effect of boundary constraint on the simulation results.

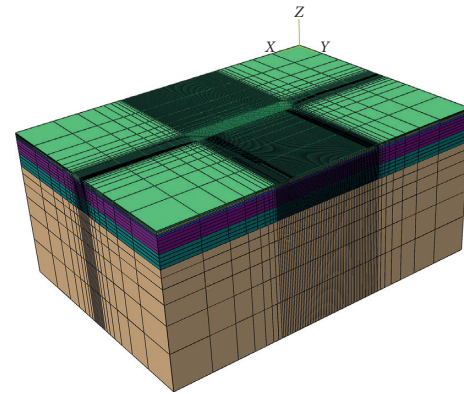


FIGURE 5: Mesh of the 3D FE model.



FIGURE 6: The field test on G320 road at Kunming.

Finer meshes were used in the loading area. The coarser meshes were used for the area far away from the loading area not only to ensure accuracy but also to improve calculation efficiency, as shown in Figure 5.

The road model was idealized with linear hexahedral element of type (C3D8R). The length and width of elements were  $2\text{ cm} \times 2\text{ cm}$  in the loading area. The heights of elements were 2 cm, 2.5 cm, and 3.5 cm for SMA, AC25, and AC30 layers, respectively.

**2.3. Model Validation.** In order to verify the road model, the simulation results were compared with the experimental data. The measured strain data came from Dong's research [31]. Dong et al. embedded the fiber Bragg grating (FBG) sensors on the Beijing Liuhuan Expressway. The FBG sensors were used to measure the vertical, transversal, and longitudinal strains of the pavement under the vehicle moving load. The measured vibration data came from our field test. The self-developed acceleration sensing nodes were embedded on G320 road at Kunming to acquire the pavement vibration signal generated by vehicle moving load. The medium truck with a total weight of 25t passed the monitoring area at a speed of 35 km/h. The depth of the accelerometer from the surface of road is 8 cm. The pavement vibration signal excited by the front axle of this truck was chosen to compare with the simulated data, as shown in Figure 6.

Figure 7 shows the monitoring points. The point #A was selected for strain and vibration response analysis. The point

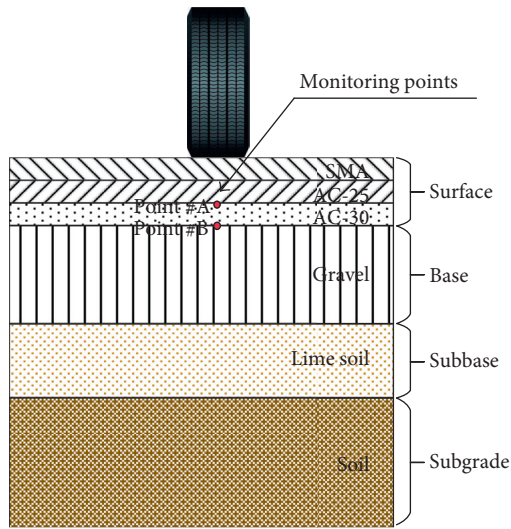


FIGURE 7: The monitoring points on the transverse section of the model center.

#B was selected for strain response analysis. Figure 8 shows the comparison between simulated data and measured data.

In Figures 8(a)–8(c), the strain curves of simulation rebounded rapidly and did not have hysteresis after loading because the viscoelasticity of the asphalt pavement was not considered. However, the difference of maximum values between the simulated and measured data is just around 15%. And the trend of strain curves matches well. The reasons for the deviations of strain curves were attributed to difference in the material parameters and random vehicle load adopted in real situation. However, the comparison still exhibits consistency between simulated and measured data and verifies that the numerical model used for FE simulation is coherent.

Figure 8(d) shows only one peak for the vibration because of one-wheel loading. The waveform initially falls and rises rapidly to form a significant peak and then falls again. Finally, it levels off. These characteristics are consistent with the measured data trend. However, the magnitude of simulated data is 10 times larger than the experimental data. This is because the simulated acceleration data can only be extracted from nodes of element by using ABAQUS program, and the nodes have a mass close to zero. However, the sensor node for pavement vibration monitoring has real mass. According to Newton's second law, the magnitude of the acceleration of an object is inversely proportional to the mass of the object. Therefore, the measured data were used as a reference, and the mass scaling factor was set to 10. The mass-scaled simulation data match well with measured data. This model can be used to analyze road vibration response qualitatively under multiple conditions.

### 3. Results and Discussions

The validated FE model was adopted for various simulations to provide additional information on dynamic pavement performance, which might prove costly via laboratory tests only. The factors that would influence the dynamic

responses of pavement under moving vehicle load are typically related with the external excitation from vehicle load, material properties, and geometric properties of pavement.

**3.1. Influence of Dynamic Load.** Vehicle parameters, speed, weight, and road roughness have influence on dynamic load of tire to pavement [25, 29, 35]. Therefore, the dynamic load coefficient (DLC) was used to represent the variation of the dynamic load, which can be calculated as

$$\text{DLC} = \frac{1}{F_s} \sqrt{\frac{\sum_{i=1}^N (F_i - F_s)^2}{N - 1}} \times 100\%, \quad (12)$$

where  $F_i$  is the vehicle random dynamic load at the  $i$ th time step;  $F_s$  is the static load produced by vehicles; and  $N$  is the total time step. The time step is 0.001 s and the total time is 0.3 s.

The random dynamic load corresponding to different DLC was obtained by the quarter vehicle model, as shown in Figure 9. A larger value of DLC indicates the load fluctuates more dramatically.

By considering the actual tire-to-pavement contact, the random nonuniform load was applied to the road model to acquire pavement vibration response. The monitoring area was the surface of SMA layer below the tire center line, as shown in Figure 10.

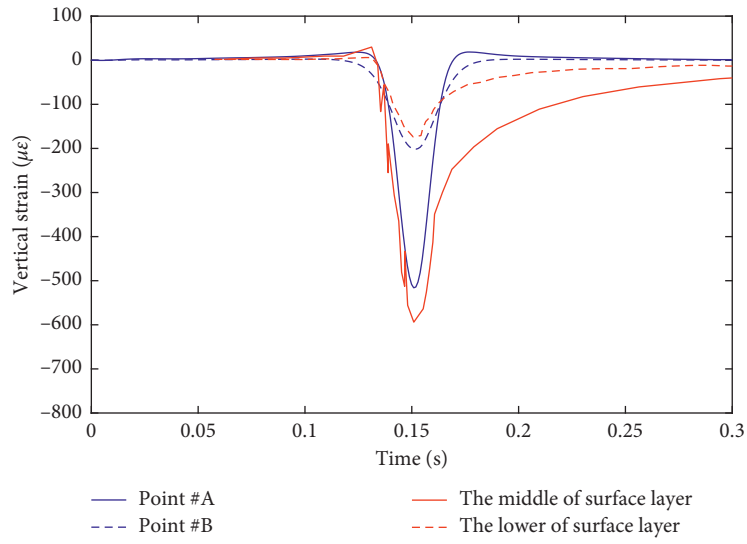
Figure 11 shows the acceleration extrema of each node in the monitoring area. The acceleration extrema are the difference value between the maximum and the minimum acceleration in a loading time period.

In Figure 11, the variation of the acceleration extrema is random. The distribution range of acceleration extrema is larger when DLC is higher. The median values significantly increase with an increase in DLC, which is from 0.8 g to 1.33 g, indicating that the number of larger acceleration extrema will grow if the dynamic load fluctuates more dramatically.

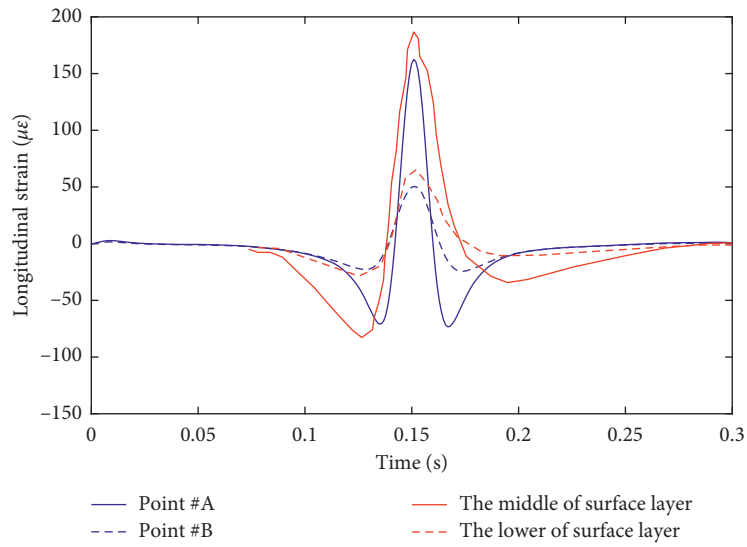
DLC increases when the surface condition of pavement declines. DLC increases with the increase of vehicle speed and the decrease of vehicle weight [29, 35]. When the experimental vehicle passes the test road at the same speed, the vehicle weight and speed can remain the same. The distribution range of acceleration extrema is larger when DLC is higher. Therefore, the wider distribution range of acceleration extrema indicates the worst condition of road surface.

**3.2. Influence of Surface Materials.** Asphalt and cement concrete are the common materials of the pavement surface layer, and their material properties are different. Asphalt concrete is a flexible material while cement concrete is a rigid one. Therefore, the influence of material properties on the pavement vibration was analyzed by comparing asphalt and cement concrete. Table 3 shows the material parameters of the cement concrete [18]:

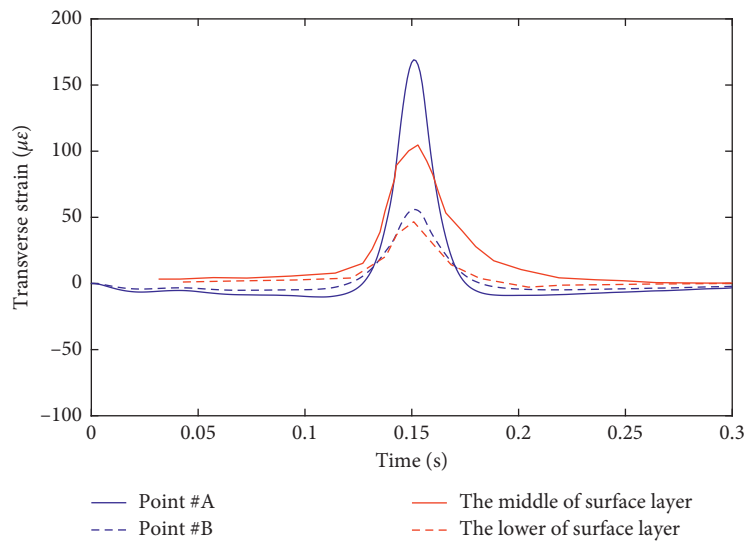
The vibration response was compared between asphalt and cement concrete pavements. The monitoring points #1, #2, and #3 of asphalt concrete pavement were placed below



(a)



(b)



(c)

FIGURE 8: Continued.

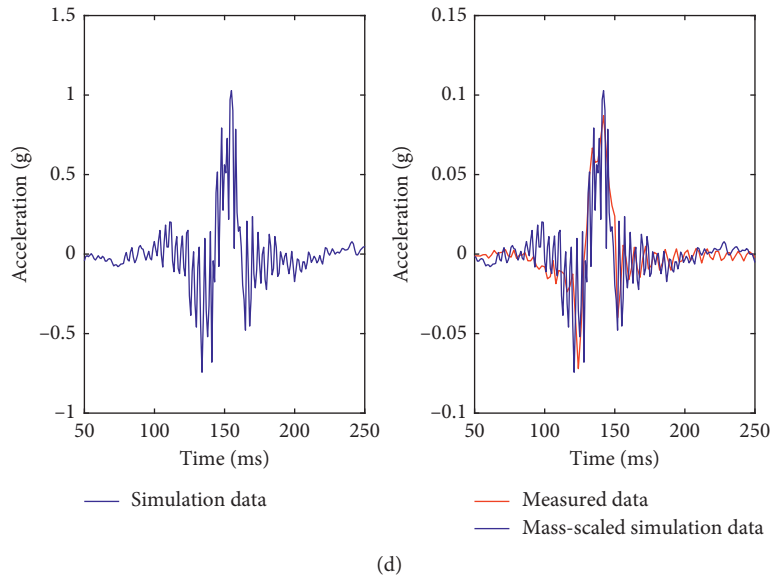


FIGURE 8: The comparison between simulated data and measured data (blue curves are simulated data and red curves are measured data). (a) The comparison of vertical strain. (b) The comparison of longitudinal strain. (c) The comparison of transverse strain. (d) The comparison of vertical acceleration.

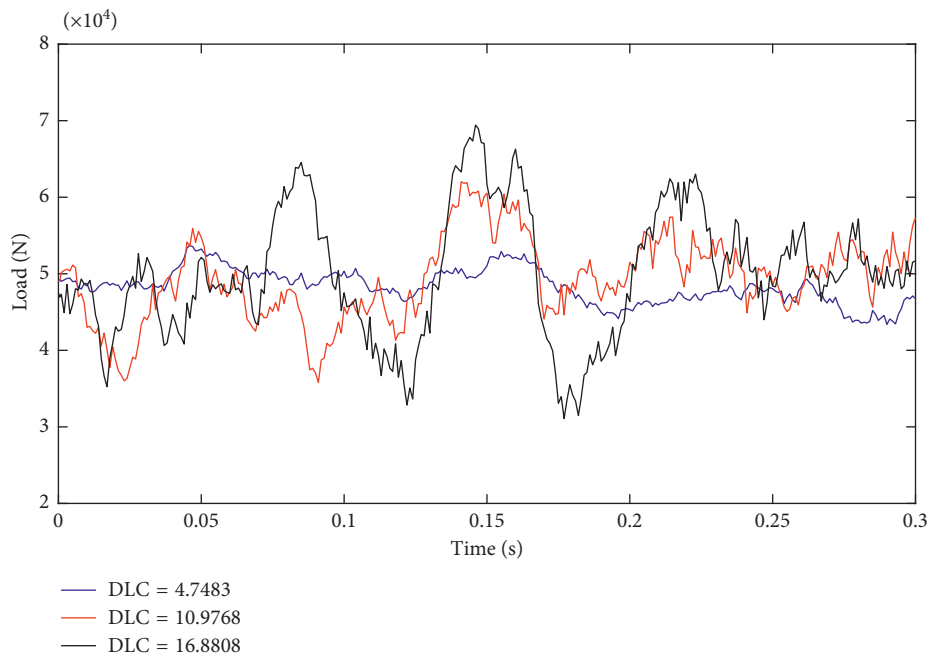


FIGURE 9: The random dynamic load corresponding to different DLC.

the tire, at the top of the SMA layer, the AC25 layer, and the AC30 layer, respectively. The coordinate of monitoring points in the model of cement concrete pavement was kept the same, as shown in Figure 12.

The dynamic load was applied to the road model when the road was class A road and the vehicle speed was 10 m/s. The vertical acceleration signals of different materials were compared at each monitoring point, as shown in Figure 13.

In Figures 13(a) and 13(b), the time-domain signal waveform can reflect information about the properties of the

pavement materials, such as the degrees of flexibility and rigidity. For the asphalt concrete pavement, the vertical acceleration amplitude decreases significantly with an increase in the depth. The waveform tends to vibrate upward, which is due to the flexibility and integrity of the asphalt concrete pavement. The energy of downward vibration is absorbed by the flexible structures. On the contrary, for the cement concrete pavement, the waveform is almost symmetric, and the vertical acceleration amplitude has no obvious change at each point. This is due to a high strength of

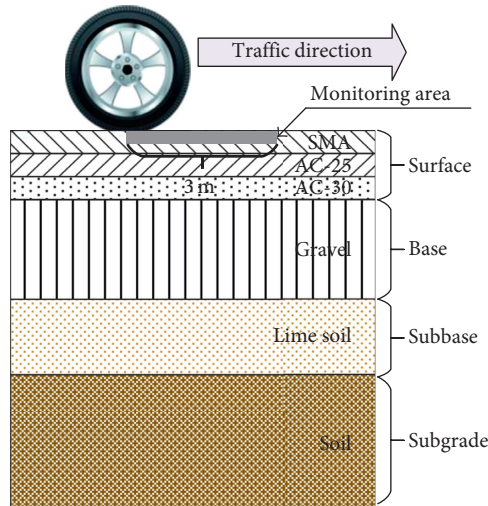
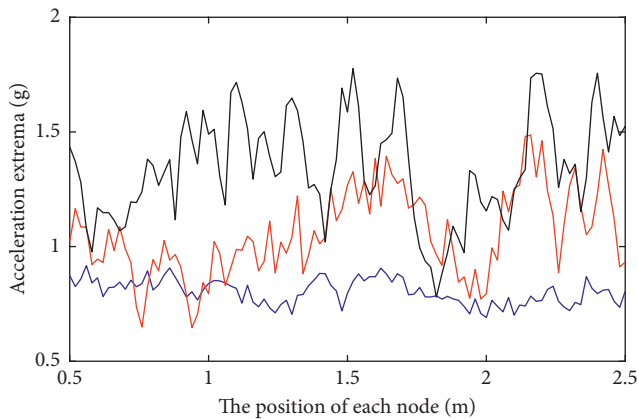
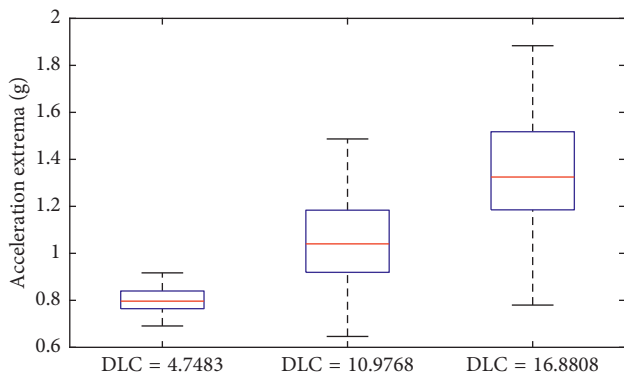


FIGURE 10: The monitoring area.



— DLC = 4.7483  
 — DLC = 10.9768  
 — DLC = 16.8808

(a)

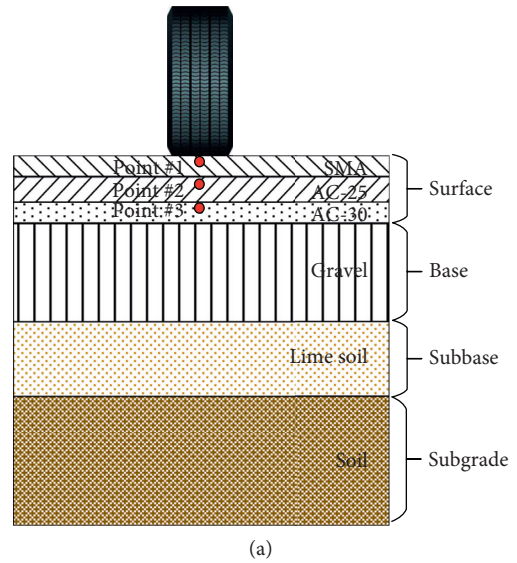


(b)

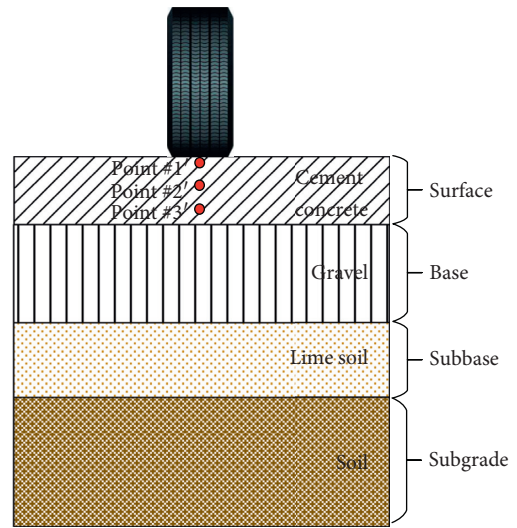
FIGURE 11: The distribution of acceleration extrema under different dynamic load. (a) The acceleration extrema of each node in the monitoring area. (b) The distribution box of acceleration extrema.

TABLE 3: The material parameters of cement concrete pavement.

Material	Thickness (cm)	Elastic modulus (MPa)	Poisson's ratio	Density (kg/m <sup>3</sup> )	Damping ratio
Cement concrete	16	31000	0.15	2400	0.05
Gravel	38	1300	0.25	2100	0.05
Lime soil	36	600	0.3	1900	0.05
Soil	200	50	0.4	1800	0.05



(a)



(b)

FIGURE 12: The monitoring points on the transverse section of the model center between asphalt and cement concrete pavements. (a) Asphalt concrete pavement. (b) Cement concrete pavement.

the cement concrete pavement. When the vehicle load acts on the surface layer of cement concrete pavement, it acts like a rigid plate body.

In Figures 13(c) and 13(d), the vibration frequency of asphalt concrete pavement is mainly within 50 Hz.

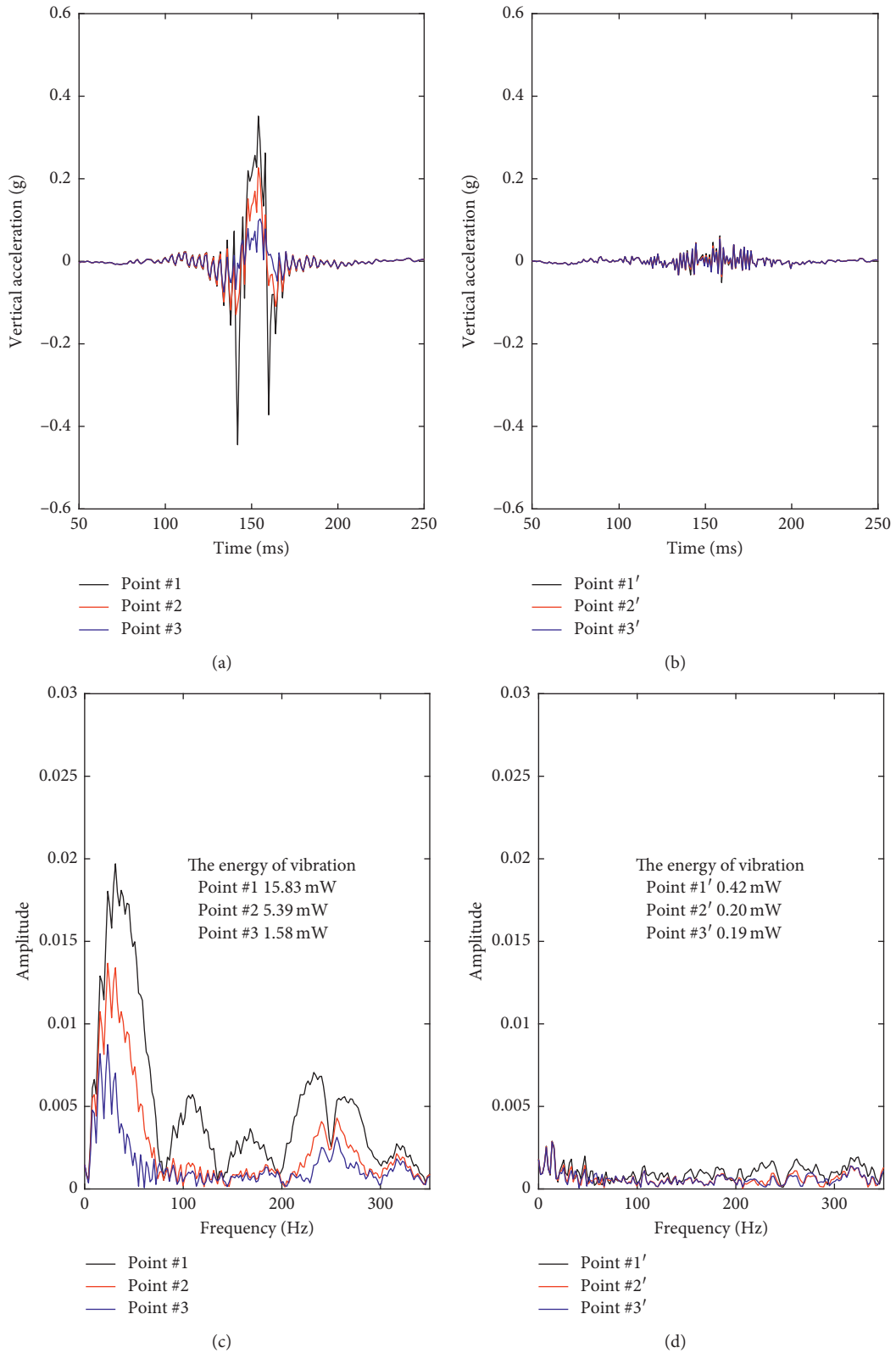


FIGURE 13: Comparison of vertical acceleration signals between asphalt and cement concrete pavements. (a) Time-domain vertical acceleration signals of asphalt concrete pavement. (b) Time-domain vertical acceleration signals of cement concrete pavement. (c) Frequency-domain vertical acceleration signals of asphalt concrete pavement. (d) Frequency-domain vertical acceleration signals of cement concrete pavement.

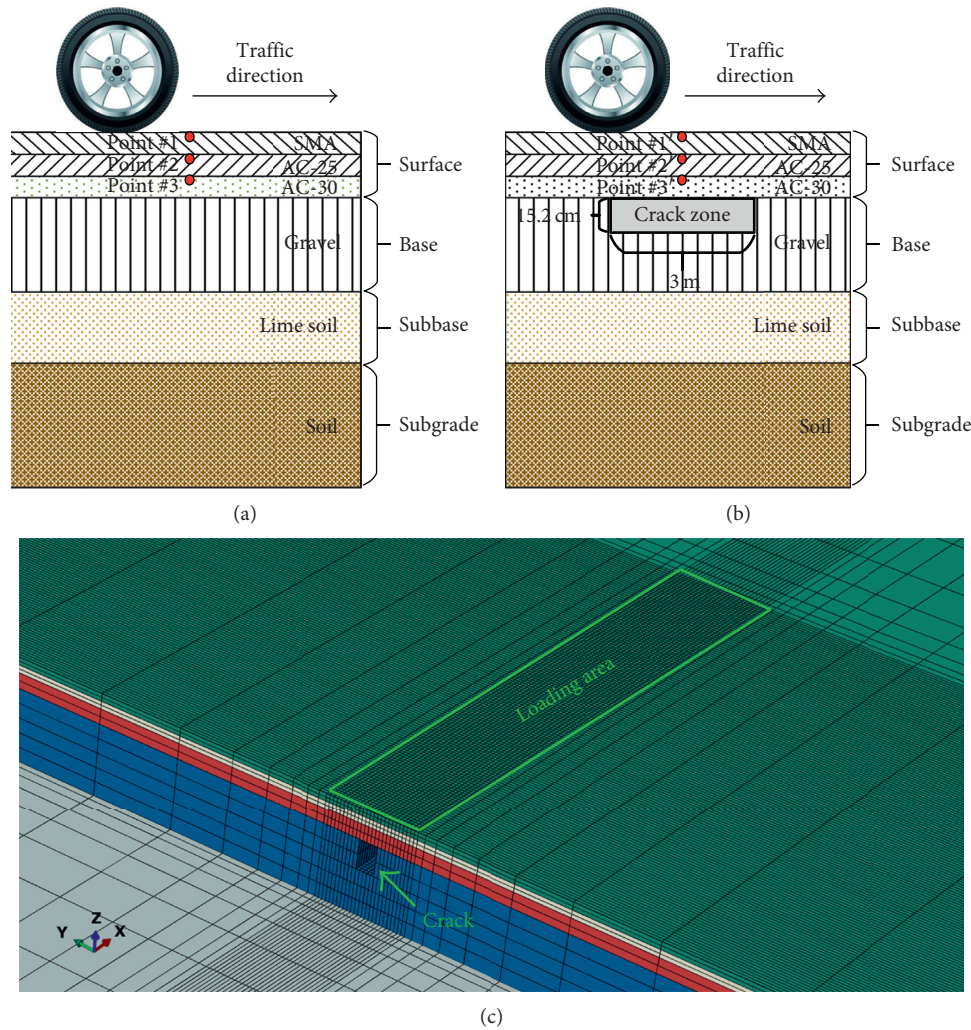


FIGURE 14: The monitoring points on the longitudinal section below the tire center line. (a) Intact pavement. (b) Damaged pavement. (c) Crack zone and loading area.

According to the Parseval's theorem, the energy of vibration can be identified as the sum of squares of Fourier amplitude. The energy of vibration becomes smaller with an increase in the depth. The energy is 15.83 mW at point #1, while it is only 1.58 mW at point #3. On the contrary, the vibration frequency of the cement concrete pavement distributes normally. The energy of vibration is 0.42 mW at point #1' and 0.20 mW at point #2, which is far less than that of asphalt concrete pavement. The energy becomes smaller with an increase in the depth, but the decrease of energy is small. This is due to the good integer property of the surface layer of the cement concrete pavement. According to the law of conservation of energy, when the vehicle drives on the cement concrete pavement, the vehicle suspension system absorbs more energy, which results in the bumpiness of vehicle. But, the driving experience is good when the vehicle drives on the asphalt concrete pavement. However, the asphalt concrete pavement is susceptible to damage as it absorbs more energy.

**3.3. Influence of the Structure Integrity.** The pavement vibration response was compared between two cases: one with a road model that has no crack and the other with 3 m-long and 10 cm-wide by 15.2 cm-deep crack located in the base layer, as shown in Figure 14. The crack area of the base layer was hollowed out according to the set size. The crack area was no need to mesh and define material parameter.

The vertical acceleration signals of different structure integrity were compared at each monitoring point, as shown in Figure 15.

In Figures 15(a) and 15(b), the vertical acceleration amplitude decreases as the depth increases for the noncracked model. However, for the cracked model, the vertical acceleration amplitude first decreases and then increases as the depth increases. The vertical acceleration amplitude of cracked model is maximum at point #3'. Moreover, the vertical acceleration signals of cracked model have more prominent fluctuation characteristics under moving load, which is especially evident at point #3' near the crack zone. This is because the crack decreases the bearing capacity and stability of pavement structure.

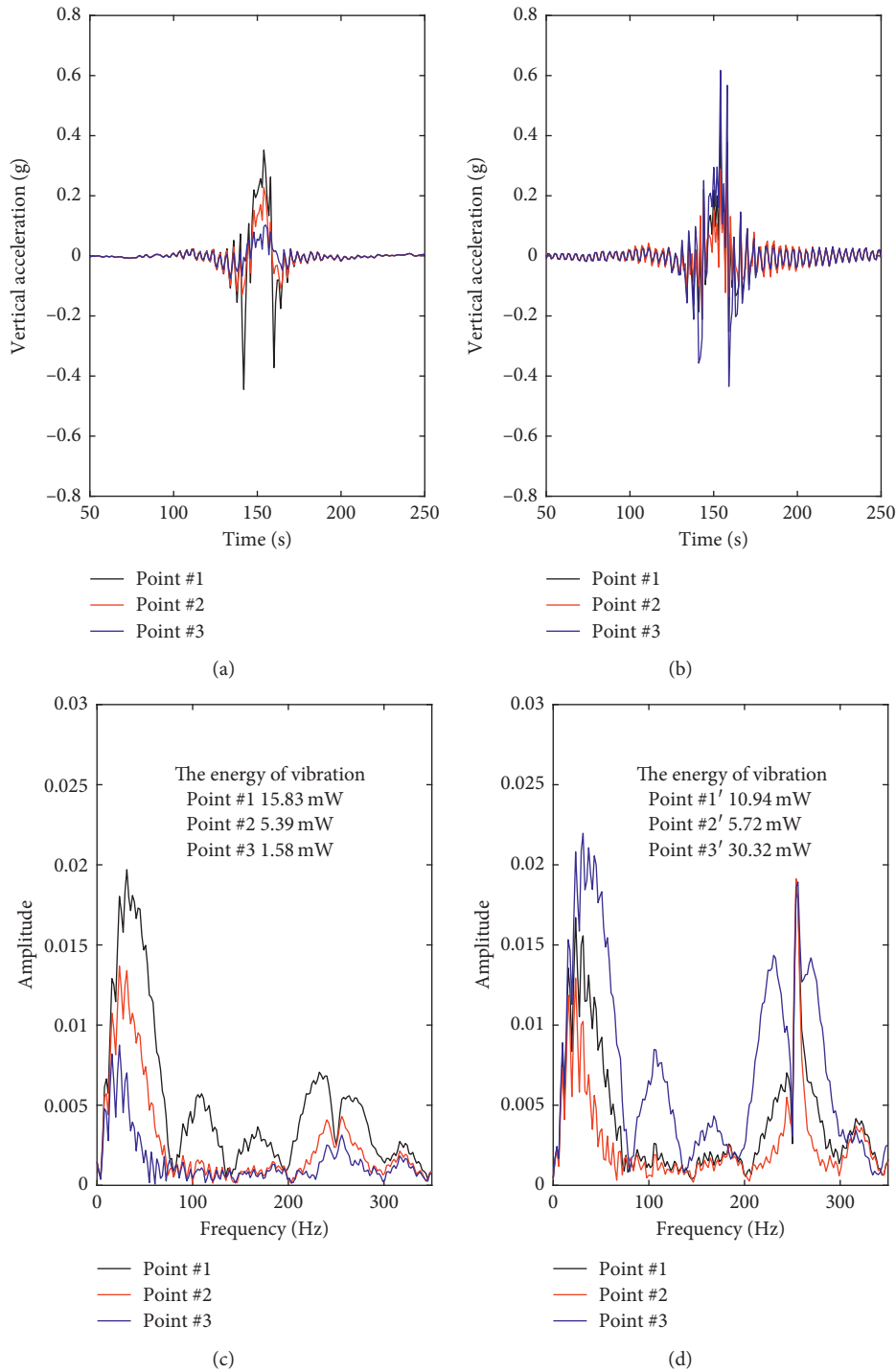


FIGURE 15: Comparison of the vertical acceleration signals of different structure integrity. (a) Time-domain vertical acceleration signals of asphalt concrete pavement with no crack. (b) Time-domain vertical acceleration signals of asphalt concrete pavement with crack. (c) Frequency-domain vertical acceleration signals of asphalt concrete pavement with no crack. (d) Frequency-domain vertical acceleration signals of asphalt concrete pavement with crack.

In Figures 15(c) and 15(d), the frequency distribution can reflect the information about the structure integrity of pavement. For the noncracked model, the vibration frequency of asphalt concrete pavement is mainly within 50 Hz. However, when the cracking is present, the vibration frequency is not only below 50 Hz but also at 250 Hz. This is due

to the cracks that change the natural frequency of pavement structure. In addition, the energy of vibration becomes smaller with an increase in the depth for the noncrack model. However, for the cracked model, the damage areas have larger vibration energy compared with the intact areas. The energy of vibration is maximum at point #3' which

reaches 30.32 mW. This leads to further expansion of the crack and material failure. Under the same moving vehicle load, the total energy absorbed by damaged pavement, that is, 46.98 mW, is higher than the total energy absorbed by intact pavement, that is, 22.80 mW. This leads to a shorter service life of the damaged pavement.

#### 4. Conclusions

This paper presented a numerical model for the analysis of the pavement vibrations resulting from vehicle moving load. The quarter vehicle model was used to determine the random load due to the road roughness. The random and spatial characteristics of the load were considered. Then the random nonuniform moving load was applied to the 3D FE model of the road, so as to acquire pavement vibration response. The vertical acceleration signals of various simulations were analyzed to find out the potential evaluation index of roadway service condition.

Numerical analyses showed that the vibration modes changed considerably for the different roadway service conditions. The vibration signals reflect the level of road roughness, the stiffness of the pavement materials, and the integrity of pavement structure. The acceleration extrema, the time-domain signal waveform, the frequency distribution, and the sum of squares of Fourier amplitude can be the potential index for roadway service condition evaluation. This provides recommendations for the application of pavement vibration response in early-warning and efficient maintenance of the road.

The numerical model can be used for analysis of the traffic-induced pavement vibration under different conditions, which is helpful for the evaluation of pavement service condition. However, there are still some improvements in a future study. The road model can be improved by considering the effect of ambient temperature and viscoelasticity of asphalt. And a further analysis could be done by doing the field test.

#### Data Availability

The data used to support the findings of this study are included within the supplementary information files.

#### Conflicts of Interest

The authors declare no conflicts of interest.

#### Acknowledgments

The research performed in this paper was supported by the National Key Research and Development Plan (no. 2017YFF0205602).

#### Supplementary Materials

The data file includes the data of Figure 2, Figure 8, Figure 9, Figure 11, Figure 13, and Figure 15. The references file includes important references that are written in Chinese

and a software for reading CAJ documents. (*Supplementary Materials*)

#### References

- [1] N. D. Beskou and D. D. Theodorakopoulos, "Dynamic effects of moving loads on road pavements: a review," *Soil Dynamics and Earthquake Engineering*, vol. 31, no. 4, pp. 547–567, 2011.
- [2] Z. J. Ye, L. B. Wang, W. Xu, Z. Gao, and G. Yan, "Monitoring traffic information with a developed acceleration sensing node," *Sensors*, vol. 17, no. 12, p. 2817, 2017.
- [3] R. Bajwa, R. Rajagopal, P. Varaiya et al., "In-pavement wireless sensor network for vehicle classification," in *Proceedings of the 10th International Conference of Information Processing in Sensor Networks*, pp. 85–96, IEEE, Chicago, IL, USA, April 2011.
- [4] W. Ma, D. Xing, A. Mckee et al., "A wireless accelerometer-based automatic vehicle classification prototype system," *IEEE Transactions on Intelligent Transportation Systems*, vol. 15, no. 1, pp. 104–111, 2014.
- [5] M. Stocker, P. Silvonen, M. Rönkkö, and M. Kolehmainen, "Detection and classification of vehicles by measurement of road-pavement vibration and by means of supervised machine learning," *Journal of Intelligent Transportation Systems*, vol. 20, no. 2, pp. 125–137, 2016.
- [6] M. Arraigada, M. N. Partl, S. M. Angelone, and F. Martinez, "Evaluation of accelerometers to determine pavement deflections under traffic loads," *Materials and Structures*, vol. 42, no. 6, pp. 779–790, 2009.
- [7] E. Levenberg, "Inferring pavement properties using an embedded accelerometer," *International Journal of Transportation Science and Technology*, vol. 1, no. 3, pp. 229–246, 2012.
- [8] B. X. Yu and X. Yu, "Vibration-based system for pavement condition evaluation," in *Proceedings of the 9th International Conference on Applications of Advanced Technology in Transportation*, pp. 183–189, ASCE, Chicago, IL, USA, August 2006.
- [9] Y. Zhang, C. Druta, L. Wang, H. Xiong, and W. Zhang, "Dynamic responses of asphalt concrete slab under cyclic wheel loading using acceleration spectrum analysis," *Construction and Building Materials*, vol. 152, pp. 134–144, 2017.
- [10] S. H. Ju, "Finite element investigation of traffic induced vibrations," *Journal of Sound and Vibration*, vol. 321, no. 3–5, pp. 837–853, 2009.
- [11] Y. L. Xu and X. J. Hong, "Stochastic modeling of traffic-induced building vibration," *Journal of Sound and Vibration*, vol. 313, no. 1–2, pp. 149–170, 2008.
- [12] M. Mhanna, M. Sadek, and I. Shahrour, "Numerical modeling of traffic-induced ground vibration," *Computers and Geotechnics*, vol. 39, pp. 116–123, 2012.
- [13] M. A. Lak, G. Degrande, and G. Lombaert, "The effect of road unevenness on the dynamic vehicle response and ground-borne vibrations due to road traffic," *Soil Dynamics and Earthquake Engineering*, vol. 31, no. 10, pp. 1357–1377, 2011.
- [14] J. C. Wang, X. Zeng, and R. L. Mullen, "Three-dimensional finite element simulations of ground vibration generated by high-speed trains and engineering countermeasures," *Journal of Vibration and Control*, vol. 11, no. 12, pp. 1437–1453, 2005.
- [15] B. Saad, H. Mitri, and H. Poorooshasb, "Three-dimensional dynamic analysis of flexible conventional pavement foundation," *Journal of Transportation Engineering*, vol. 131, no. 6, pp. 460–469, 2005.
- [16] A. H. Alavi, H. Hasni, N. Lajnef, and K. Chatti, "Continuous health monitoring of pavement systems using smart sensing

- technology,” *Construction and Building Materials*, vol. 114, pp. 719–736, 2016.
- [17] W. Xue, L. Wang, D. Wang, and C. Druta, “Pavement health monitoring system based on an embedded sensing network,” *Journal of Materials in Civil Engineering*, vol. 26, no. 10, article 04014072, 2014.
- [18] J. Wu, J. Liang, and S. Adhikari, “Dynamic response of concrete pavement structure with asphalt isolating layer under moving loads,” *Journal of Traffic and Transportation Engineering*, vol. 1, no. 6, pp. 439–447, 2014.
- [19] V. A. Patil, V. A. Sawant, and K. Deb, “3D finite-element dynamic analysis of rigid pavement using infinite elements,” *International Journal of Geomechanics*, vol. 13, no. 5, pp. 533–544, 2013.
- [20] M. J. Markow, J. K. Hedrick, B. D. Brademeyer et al., “Analyzing the interaction between dynamic vehicle loads and highway pavements,” *Transportation Research Record*, no. 1196, pp. 161–169, 1998, <http://onlinepubs.trb.org/Onlinepubs/trr/1988/1196/1196-016.pdf>.
- [21] D. Cebon, *Interaction between Heavy Vehicles and Roads*, Society of Automotive Engineers, Warrendale, PA, USA, 1993, ISBN: 1-56091-336-3.
- [22] T. D. Gillespie, S. M. Karamihas, M. W. Sayers et al., “Effects of heavy-vehicle characteristics on pavement response and performance,” Technical Report 353, National Cooperative Highway Research Program, Transportation Research Board, Washington, DC, USA, 1992, <http://deepblue.lib.umich.edu/bitstream/2027.42/996/2/58749.0001.001.pdf>.
- [23] M. S. Mamlouk, “General outlook of pavement and vehicle dynamics,” *Journal of Transportation Engineering*, vol. 123, no. 6, pp. 515–517, 1997.
- [24] K. B. Todd and B. T. Kulakowski, “Simple computer models for predicting ride quality and pavement loading for heavy trucks,” *Transportation Research Record: Journal of the Transportation Research Board*, vol. 147, no. 3, pp. 137–150, 1989, <http://onlinepubs.trb.org/Onlinepubs/trr/1989/1215/1215-016.pdf>.
- [25] L. Sun and T. W. Kennedy, “Spectral analysis and parametric study of stochastic pavement loads,” *Journal of Engineering Mechanics*, vol. 128, no. 3, pp. 318–327, 2002.
- [26] Z. Lu, Z. Hu, H. Yao, J. Liu, and Y. Zhan, “An analytical method for evaluating highway embankment responses with consideration of dynamic wheel-pavement interactions,” *Soil Dynamics and Earthquake Engineering*, vol. 83, pp. 135–147, 2016.
- [27] Y. J. Lu, S. P. Yang, S. H. Li, and L. Chen, “Numerical and experimental investigation on stochastic dynamic load of a heavy duty vehicle,” *Applied Mathematical Modelling*, vol. 34, no. 10, pp. 2698–2710, 2010.
- [28] ISO, *Mechanical Vibration—Road Surface Profiles—Reporting of Measured Data*, ISO 8608, International Organization for Standardization, Geneva, Switzerland, 1995.
- [29] X. M. Shi and C. S. Cai, “Simulation of dynamic effects of vehicles on pavement using a 3D interaction model,” *Journal of Transportation Engineering*, vol. 135, no. 10, pp. 736–744, 2009.
- [30] M. N. S. Hadi and B. C. Bodhinayake, “Non-linear finite element analysis of flexible pavements,” *Advances in Engineering Software*, vol. 34, no. 11-12, pp. 657–662, 2003.
- [31] Z. J. Dong, Y. Q. Tan, and J. P. Ou, “Dynamic response analysis of asphalt pavement under three-directional non-uniform moving load,” *China Civil Engineering Journal*, vol. 46, no. 6, pp. 122–130, 2013.
- [32] H. Wang, I. L. Al-Qadi, and I. Stanculescu, “Simulation of tyre-pavement interaction for predicting contact stresses at static and various rolling conditions,” *International Journal of Pavement Engineering*, vol. 13, no. 4, pp. 310–321, 2012.
- [33] JTG, *Specifications for Design of Highway Asphalt Pavement, JTG D50*, Bureau of Chinese Standard, Beijing, China, 2006.
- [34] H. Y. Li, *Research on dynamics of pavement structure due to vehicle and pavement interaction*, Ph.D. thesis, Beijing Jiaotong University, Beijing, China, 2011.
- [35] Y. Q. Zhao, L. Bai, L. A. Liu et al., “Measurement and analysis of dynamic loading of trucks,” *Journal of Hunan University*, vol. 41, no. 11, pp. 129–132, 2014.

## Research Article

# Estimation of Soil-Water Characteristic Curve for Cohesive Soils with Methylene Blue Value

Junhui Zhang <sup>1</sup>, Junhui Peng <sup>1</sup>, Yejuan Chen,<sup>2</sup> Jue Li,<sup>1</sup> and Feng Li<sup>1</sup>

<sup>1</sup>National Engineering Laboratory of Highway Maintenance Technology, Changsha University of Science and Technology, Changsha 410114, China

<sup>2</sup>Changsha Commerce and Tourism College, Changsha 410001, China

Correspondence should be addressed to Junhui Peng; [q376689004@163.com](mailto:q376689004@163.com)

Received 1 March 2018; Accepted 10 June 2018; Published 5 July 2018

Academic Editor: Qiang Tang

Copyright © 2018 Junhui Zhang et al. This is an open access article distributed under the Creative Commons Attribution License, which permits unrestricted use, distribution, and reproduction in any medium, provided the original work is properly cited.

This study described a new methylene blue test to measure the methylene blue value (MBV) for 15 cohesive soils and established the relationship between MBV and plasticity index (PI) and between MBV and percent passing No. 200 sieve ( $P_{200}$ ), respectively. Thereafter, the soil-water characteristic curves (SWCCs) for 15 cohesive soils based on Fredlund and Xing's model were generated by the pressure plate test. Then, regression equations for determining the four fitting parameters in a previously developed SWCC equation by using the measured MBV were utilized to generate the SWCC for the cohesive soils. At the same time, the slope parameter,  $b_f$ , in the SWCC equations was found to be associated with the moisture susceptibility of cohesive soils. A higher  $b_f$  value indicates that the material is more moisture susceptible. In addition, a lower MBV/PI/ $P_{200}$  shows a lower suction at the same degree of saturation; on the other hand, a higher MBV/PI/ $P_{200}$  presents a higher suction. Therefore, the moisture-holding capacity of cohesive soils increases with increasing MBV, PI, and  $P_{200}$ . Finally, the proposed estimation method was validated by a comparison between the four determined fitting parameters from MBV and the pressure plate test.

## 1. Introduction

The soil-water characteristic curve (SWCC) is a graphical relationship between the matric suction and the water content. It is one of the basic characteristics of partially unsaturated soils, and as such, it is useful for estimating the other properties of soil, when solving engineering problems in these three classic areas: fluid flow, compressibility, and shear strength [1]. For example, when modeling unsaturated moisture flow beneath a highway pavement, the hydraulic conductivity of the base course and subgrade materials, as a function of moisture content, must be known. Since the experimental procedures, in which a filter paper or pressure plate test, adopted for determining the matric suction-water content relationship, is time-consuming and cost-intensive [2, 3], recent research has placed a major focus on an estimation method to predict the SWCC using some mathematical functions [1, 4, 5]. However, the shape of the curve depends on many basic soil properties, such as the percent

passing No. 200 sieve ( $P_{200}$ ), plasticity index (PI), and environmentally induced factors that determine the stress state, compaction level, and temperature. It is difficult to find a valid and convenient mathematical expression to describe it. However, several analytical functions for predicting the SWCC can be found in some literatures [6–9]. The predicting variables, including sieve analysis and index properties, display extensive variability in those literatures [10]. Some time-consuming and material-consuming experiments are still necessary, including sieve analysis and Atterberg limits. Under this circumstance, Hakan Sahin et al. proposed a new estimation method to determine SWCC for unbound aggregate mixtures based on the methylene blue value (MBV) and percent fines content (PFC) [11–13].

The methylene blue has a large polar organic molecule  $C_{16}H_{18}N_3S^+$  that can be adsorbed onto the negatively charged surfaces of clay minerals. The amount of adsorbed methylene blue depends on the amount of the surface area of the clay particles. The more the methylene blue adsorbed by

the clay particles, the brighter the methylene blue solution will be. The adsorbed methylene blue is able to be quantified by assessing the color change of the methylene blue solution. At the same time, SWCCs for cohesive soils reveal their water-holding capacity which depends on the specific surface area of the clay particles [9,14–18]. Based on the above description about the methylene test, MBV reflects the specific surface area of soil particles. Therefore, SWCCs for cohesive soils can be predicted using the methylene blue value. Once the relationship between the four fitting coefficients of Fredlund and Xing's model, which are shown in (1), and the MBV is built, SWCCs for cohesive soils will be determined:

$$\theta_{\omega} = C(h) \times \frac{\theta_s}{\left\{ \ln \left[ \exp(1) + (h/a_f)^{b_f} \right] \right\}^{c_f}}, \quad (1)$$

$$C(h) = 1 - \frac{\ln(1 + (h/h_r))}{\ln(1 + (10^6/h_r))},$$

where  $\theta_{\omega}$  is the volumetric water content;  $\theta_s$  is the saturated volumetric water content;  $h$  is the matric suction; and  $a_f$ ,  $b_f$ ,  $c_f$ , and  $h_r$  are fitting coefficients, which are primarily a function of the air entry value, rate of water extraction from the soil, residual water content, and suction at which the residual water content occurs, respectively. Once these four fitting parameters are determined, the SWCC for a specific soil can be established automatically.

This study is organized as follows: The forthcoming section introduces a new methylene blue test method, and the methylene blue tests of 15 cohesive soils were completed. Subsequently, the correlation between PI and MBV and between  $P_{200}$  and MBV was proposed and analyzed, respectively. The next section builds the correlations between the four fitting parameters of Fredlund and Xing's model and the MBV, which were validated subsequently. The final section summarizes the major findings of this study.

## 2. Experiments and Materials

Based on the preceding discussions, this section presents the laboratory experiments and materials required to develop the fitting models for the SWCCs.

**2.1. Laboratory Experiments.** The sieve test and Atterberg limit test were employed to determine the particle distribution and plasticity index, respectively. At the same time, the maximum dry density and optimum moisture content, which were utilized to mold the soil samples for the pressure plate test, were gained according to the Proctor test. Thereafter, the pressure plate test was used to measure the matric suction for different moisture contents. In addition, the methylene blue test was used to detect the amount of fine particles in 15 cohesive soils. The pressure plate test and methylene blue test are briefly introduced in the following sections.

**2.2. New Methylene Blue Test.** A traditional methylene blue test, specified in ASTM C837 [19], was used to determine the

active clay content in fine materials by measuring the methylene blue dye content adsorbed by clay particles. This traditional test method contains an empirical check criterion, in which the test procedures need to be repeated until a light blue ring is found. It is time-consuming and requires experienced personnel to operate the test, which is similar to the method of the current specification of *Test Methods of Aggregate for Highway Engineering* in China. Recently, a new test method, which measures the MBV of soils by using the methylene blue solution with a colorimeter, was proposed by W.R. Grace Inc. The advantage of this new test method is that it is relatively simple, inexpensive, and repeatable. Figure 1 shows the apparatus which consists of a colorimeter, a 150  $\mu$ L pipette with a resolution of 1  $\mu$ L, a dropper, a 3 mL syringe, two 50 mL plastic bottles, two sample bottles, methylene blue solution, and distilled water. In addition, a 0.20  $\mu$ m filter of the syringe, a portable balance with a resolution of 0.01 g, a standard sieve, and a small glass tube are also needed.

Firstly, the sample was passed through a 2 mm sieve, and 20.00 g sample was taken as the initial amount. The sample was added to a plastic bottle with 30.00 mL calibrated methylene blue solution. The mixture was shaken for 1 min, rested for 3 min, and shaken again for 1 more min. Thereafter, the mixture was filtered through a 2.0  $\mu$ m filter by using a syringe. And the mixture passing the filter was used for the rest of the experiment. Subsequently, 30.00 mL of the filtered solution was added to a plastic bottle and filled with distilled water until a total of 45.00 g is collected. The newly mixed solution was put into a small glass tube plugged into the colorimeter, and the MBV can be measured by using the colorimeter. It is considered that 20.00 g is a valid sample amount, and the value of reading is valid, if the MBV reading is smaller than 7.50 mg/g. The sample size must be halved to 10.00 g, and the test procedure should be repeated, if the MBV is higher than 7.50 mg/g. It is worth mentioning that the total test time for a measurement is less than 10 min. The methylene blue value (mg/g) can be calculated by (2) after the methylene blue tests were completed:

$$\text{MBV} = \frac{(C_i - C_f) \times M_{\text{MB}}}{M_{\text{FM}}} \times 1000 \text{ mg/g}, \quad (2)$$

where  $C_i$  is the initial concentration of the methylene blue solution;  $C_f$  is the final concentration of the methylene blue solution;  $M_{\text{MB}}$  is the weight of the methylene blue solution; and  $M_{\text{FM}}$  is the weight of the soil samples. The average value of three tests for one soil is selected as the final MBV.

Table 1 shows the soil amount and the corresponding valid MBV range. It should be noted that the method using the methylene blue solution with a colorimeter is not suitable for soils in the case that the MBV is larger than 60 mg/g. For this case, the traditional method to measure the MBV should be adopted [19, 20].

**2.3. Pressure Plate Test.** The pressure plate consists of a high-pressure nitrogen gas bottle, a reducing valve, a pressure cooker, a ceramic plate, and so on, which is used to measure both matric and total suction with respect to the moisture

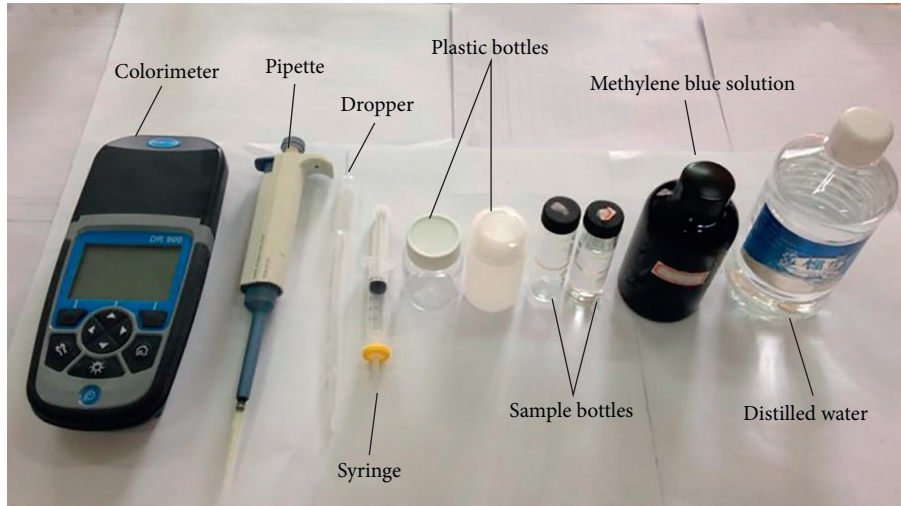


FIGURE 1: Apparatus.

TABLE 1: Soil amount and corresponding valid MBV range.

Soil weight (g)	MBV range (mg/g)
20	$0 < \text{MBV} < 7.5$
10	$7.5 \leq \text{MBV} < 15$
5	$15 \leq \text{MBV} < 30$
2.5	$30 \leq \text{MBV} < 60$

content of the sample. For this test, soil samples of 618 mm diameter and 100 mm height were made by a cutting ring at compacted degree of 90% and at the optimum moisture content. Then, the samples were put into a vacuum saturator and were taken out 48 hours later for equilibrating the internal moisture content. Thereafter, the mass was recorded when there is no water on the surface of samples. Subsequently, the ceramic plate was put into the pressure cooker and saturated. The following step was to put the saturated sample into the pressure plate and add air pressure until reaching a balanced state. After that, the moisture content of the sample was measured and the pressure was read. By repeating the above steps, the SWCC for the soil sample can be developed.

**2.4. Materials.** Fifteen cohesive soils were taken from different field sites of Hunan Province in this study, which is located in South China [21]. Table 2 summarizes the results for laboratory testing. Since the MBV of the soil samples S13 and S14 is larger than 60 mg/g, it was measured by the traditional method [19, 20].

### 3. Correlations between MBV and PI and between $P_{200}$ and MBV

The four fitting coefficients of Fredlund and Xing's model can be predicted by  $P_{200}$  and PI, based on the available database. Thus, it is necessary to analyze the relationship between the MBV and PI and between MBV and  $P_{200}$ , respectively. Figure 2 presents the relationship between the MBV and PI for the selected cohesive soils and the solid line

represents a trend line. A correlation equation is observed between PI and MBV, as shown in (3). Witczak et al. [22, 23] suggested subjective criteria for goodness predictions based on the coefficient of determination ( $R^2$ ) values. An excellent fit can be defined as  $R^2 \geq 0.9$ , a good fit covers the  $R^2$  range of 0.7–0.89, and a fair fit is defined as  $0.4 \leq R^2 \leq 0.69$ . Therefore, (3) is a good fit for selected cohesive soils and can provide a relatively satisfactory correlation. This equation indicates that the MBV also has the ability to classify the plasticity of cohesive soils and the positive correlation with PI:

$$\text{PI} = e^{(2.525+0.008 \text{ MBV})} \quad (R^2 = 0.72). \quad (3)$$

Simultaneously, the relationship between the  $P_{200}$  and MBV was gained according to Figure 3. The data of S2, S11, and S12 were not considered because of their large variability. Equation (4) shows their mathematical formula, which is a good fit:

$$P_{200} = 44.66 \ln(\text{MBV} + 21.73) - 115.52 \quad (R^2 = 0.79). \quad (4)$$

Many studies have reported that the clay mineral is a key factor that affects the suction variation of a soil, and clay minerals are known to have a much higher  $P_{200}$  than other small mineral particles. Thus, as can be seen from the above, MBV and  $P_{200}$  are positively correlated. It indicates that the higher clay mineral content corresponds to higher MBV for soil sample, since the MBV is positively correlated with  $P_{200}$ .

## 4. Regression Analysis and Validation

**4.1. Regression Analysis.** The SWCCs for 15 cohesive soils were measured by the pressure plate test, which are presented in Figure 4. The slope of the SWCC in the middle stage represented the suction loss ratio with increasing moisture content in this figure. The steeper suction slopes represent that soil sample is more moisture susceptible. "Moisture susceptibility" describes the rate of loss of subgrade strength, stiffness, and resistance to permanent

TABLE 2: Testing results.

Soil sample	Liquid limit (%)	Plastic limit (%)	PI (%)	Optimum moisture content (%)	Maximum dry density (g/cm <sup>3</sup> )	P <sub>200</sub> (%)	MBV (mg/g)	Classification
S1	43.30	26.10	17.20	11.20	1.84	52.14	18.98	ML
S2	36.10	22.70	13.40	14.00	1.88	66.80	20.18	CLS
S3	33.60	19.80	13.80	11.90	1.93	54.00	22.38	MLS
S4	35.90	19.10	16.80	11.20	1.84	51.60	27.33	CLS
S5	36.60	21.50	15.10	18.90	1.68	56.50	31.87	CLS
S6	42.50	25.00	17.50	17.20	1.75	79.10	34.64	CL
S7	44.70	28.50	16.20	15.50	1.85	73.10	37.12	CLS
S8	42.30	22.00	20.30	14.00	1.86	59.80	38.27	CLS
S9	35.80	19.30	16.50	16.00	1.92	68.70	40.45	CLS
S10	39.80	26.80	13.00	18.00	1.80	72.30	44.13	CLS
S11	35.70	16.00	19.70	11.40	1.98	64.30	54.11	CLS
S12	35.80	17.00	18.80	15.50	1.84	94.20	57.34	CL
S13	46.10	22.10	24.00	17.00	1.84	93.10	80.33	CLS
S14	56.50	30.10	26.40	23.50	1.56	95.08	94.00	CH
S15	40.90	21.60	19.30	14.80	1.87	64.30	39.97	CLS

Note. M denotes silt; C denotes clay; S denotes soils with sand; L and H denote soils with a low liquid limit (no more than 50%) and a high liquid limit (larger than 50%).

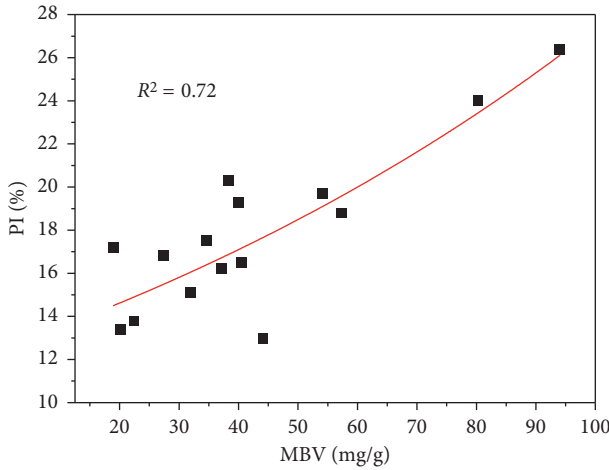


FIGURE 2: Correlation between MBV and PI.

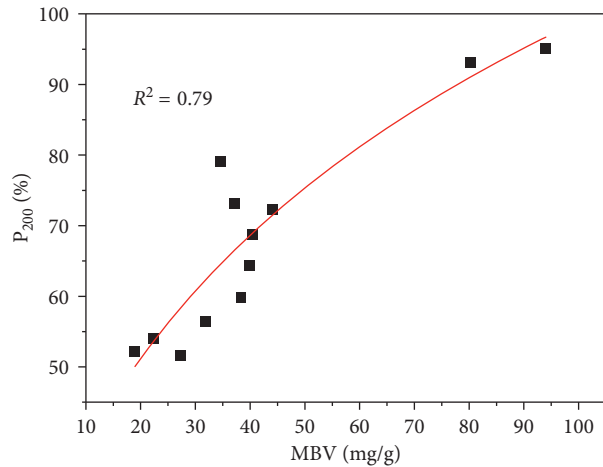


FIGURE 3: Correlation between MBV and P<sub>200</sub>.

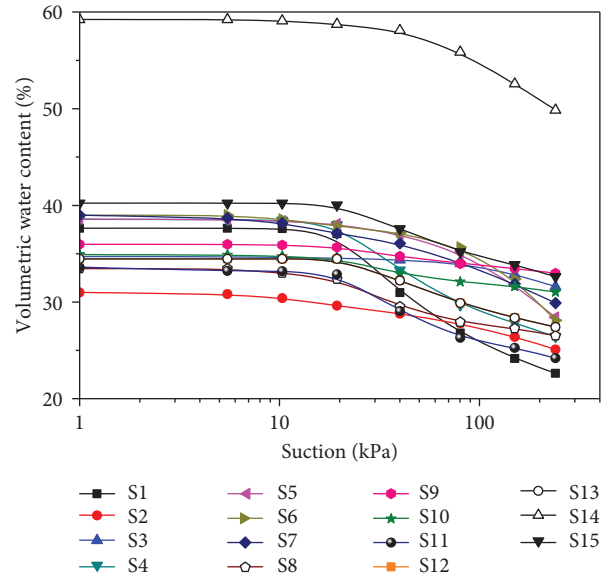


FIGURE 4: SWCCs of cohesive soils.

of the selected soils is ranked as follows: S1 > S2 > S3 > S4 > S5 > S6 > S7 > S8 > S15 > S9 > S10 > S11 > S12 > S13 > S14, according to the comparison of the slope values of SWCCs, as shown in Figure 4.

The four coefficients of Fredlund and Xing's model were gained, according to the results of the pressure plate test, as shown in Table 3.

To investigate the correlation between the four fitting parameters and the MBV, the regression analysis was performed for soil samples S1~S14. In addition, the soil sample S15 was used to validate the rationality of the correlations. Each fitting parameter had a unique equation to describe its relationship with the MBV, as presented in (5)–(8). The air entry value of soil,  $a_f$  is formulated in (5). The rate of water extraction of the soil exceeding the air entry value,  $b_f$  is formulated based on the MBV given in (6). The mathematical relationship describing the residual

deformation with increasing moisture. Therefore, the slope of the SWCCs can also be used to evaluate the moisture susceptibility of subgrade soils. The moisture susceptibility

TABLE 3: Fitting coefficients of Fredlund and Xing's model.

Soil sample	$a_f$ (kPa)	$b_f$	$c_f$	$h_r$ (kPa)
S1	28.55	1.28	2.72	941.39
S2	30.86	1.26	2.67	1097.66
S3	34.78	1.22	2.58	1361.42
S4	42.33	1.13	2.4	1870.75
S5	48.15	1.06	2.24	2262.48
S6	51.30	1.01	2.15	2474.93
S7	53.91	0.98	2.07	2651.18
S8	55.07	0.96	2.04	2728.95
S9	57.16	0.93	1.97	2870.17
S10	60.46	0.88	1.86	3092.12
S11	68.17	0.76	1.60	3611.81
S12	70.36	0.72	1.53	3759.60
S13	83.11	0.51	1.08	4618.98
S14	89.05	0.42	0.88	5019.56
S15	56.71	0.94	1.98	2839.74

water content of the soil,  $c_f$  is given in (7). The mathematical formula describing the suction value at the residual water content,  $h_r$ , is given in (8):

$$a_f = 27.4 \ln(\text{MBV} - 9.9) - 34.7 \quad (R^2 = 0.90), \quad (5)$$

$$b_f = 1.66e^{(-0.014 \text{MBV})} \quad (R^2 = 0.72), \quad (6)$$

$$c_f = 0.729e^{(-0.057 \text{MBV})} + 0.12 \quad (R^2 = 0.73), \quad (7)$$

$$h_r = 2221.59 \ln(\text{MBV} - 4.78) - 5024 \quad (R^2 = 0.90). \quad (8)$$

According to the above description, (5) and (8) are excellent fits and (6) and (7) are good fits according to the research results of Witczak et al. Those equations can provide a relatively satisfactory correlation. In addition,  $a_f$  and  $h_r$  have a positive relationship with the MBV, which increase with the increasing MBV. On the other hand,  $b_f$  and  $c_f$  have a negative relationship with the MBV, which mean that these two fitting coefficients decrease with the increasing MBV. Among the four parameters,  $b_f$  is a special one. It represents not only the moisture susceptibility but also the slope of the SWCC.

**4.2. Validation.** In order to verify the rationality of the prediction method for cohesive soils in this study, the four fitting coefficients of SWCC from the pressure plate test and MBV measured for soil sample S15 were compared, as shown in Table 4. For soil sample S15, the MBV was 39.97 mg/g and the four fitting coefficients  $a_f$ ,  $b_f$ ,  $c_f$ , and  $h_r$  gained from (5)–(8) are 51.06, 0.94, 0.20, and 2839.74, respectively, and they are 51.34, 0.95, 0.25, and 2736.15 according to the pressure plate test. Therefore, the difference is negligible for the fitting coefficients between the pressure plate test and new prediction method by the methylene blue test, except the residual suction value  $h_r$ . However, this difference in the residual suction values will not affect the whole curve of the SWCCs, as shown in Figure 5. It can be seen from Figure 5 that there is a little difference for the initial stage with a low suction, and subsequently, two curves

TABLE 4: Fitting parameters from test and estimation using MBV.

Soil sample S15	MBV (mg/g)	$a_f$ (kPa)	$b_f$	$c_f$	$h_r$ (kPa)
Parameters from MBV		51.06	0.94	0.20	2839.74
Parameters from the pressure plate test	39.97	51.34	0.95	0.25	2736.15

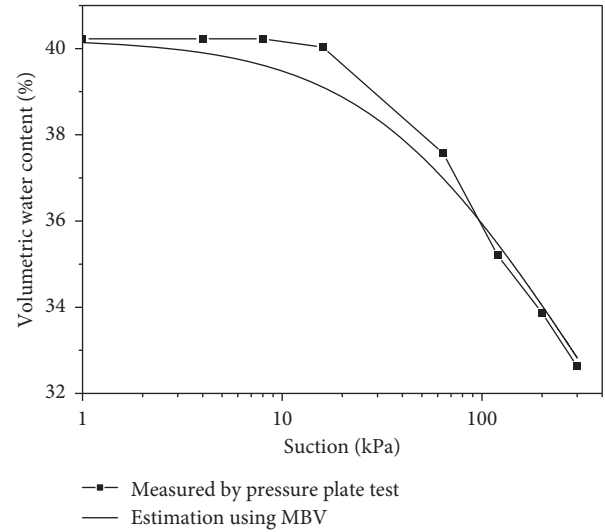


FIGURE 5: SWCCs from test and estimation methods.

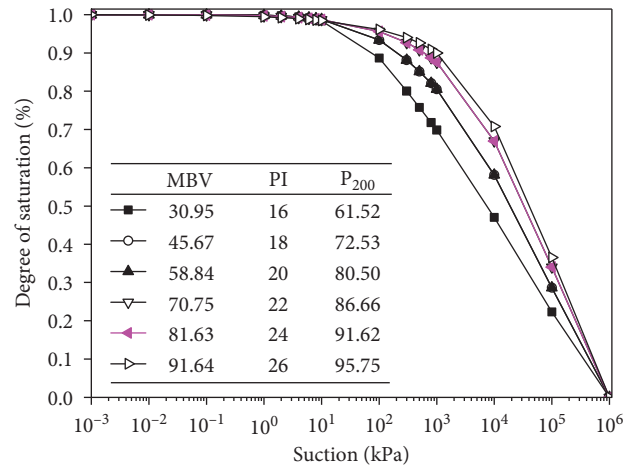


FIGURE 6: SWCCs with different methylene blue values.

are almost consistent with the increasing suctions. Thus, the accuracy of the prediction method for cohesive soils based on the MBV is acceptable.

## 5. SWCCs Predicted Using the Methylene Blue Test

Figure 6 shows the suction change with the degree of saturation under six different methylene blue values. It is noted that the suction decreases with decreasing MBV under the same degree of saturation; on the other hand, a higher MBV shows a higher suction under the same degree of saturation,

which means a high moisture-holding capacity. Therefore, the moisture-holding capacity of cohesive soils increases with the increasing MBV.

And at the same time, the four fitting parameters can be expressed in terms of PI and  $P_{200}$ , by substituting (3) and (4) into (5)–(8). The PI and  $P_{200}$  values and the corresponding MBV are also given in Figure 6. Since the MBV has a positive correlation with them, the moisture-holding capacity of cohesive soils increases with the increasing PI and  $P_{200}$ . As mentioned above, lower PI or  $P_{200}$  values correspond to lower plasticity soils and higher PI or  $P_{200}$  values are associated with higher plasticity soils, which has the same law reflected in Figure 6.

This study indicates that there is a relationship between the four fitting parameters of Fredlund and Xing's model and the MBV for cohesive soils. The MBV is easy to be measured in a practical engineering. However, the pressure plate test or filter paper, adopted for determining the SWCC, is time-consuming and cost-intensive. Therefore, the four parameters of Fredlund and Xing's model can be predicted by MBV in a very short time compared to other experimental procedures. And this method can generate the SWCCs for cohesive soils far more efficiently with an acceptable accuracy. Meanwhile, it can even be used in field investigations since the methylene blue test only requires limited portable test equipment.

## 6. Conclusions and Discussions

In order to more effectively determine the MBV for 15 cohesive soils, a new methylene blue test was proved. Then, the mathematical formulations between the four fitting coefficients of Fredlund and Xing's model and the MBV were developed and verified. The major conclusions are drawn as follows:

- (1) Compared to other experimental procedures, the new methylene blue test with a colorimeter required fewer experimental tools and soil samples. At the same time, the colorimeter provided an objective way to assess the color change of the methylene blue solution. It greatly reduces the subjective error.
- (2)  $P_{200}$  and PI were positively related to MBV, which indicates that the higher clay mineral content corresponds to higher PI or MBV for soil sample.
- (3) The fitting parameters  $a_f$  and  $h_f$  were directly proportional to the MBV, which increase with the increasing MBV, and  $b_f$  and  $c_f$  were negatively related to the MBV, which means that these two fitting coefficients decrease with the increasing MBV. When the MBV was measured, the four fitting parameters can be calculated using (5)–(8), and its accuracy was proved to be acceptable. It was more efficient to describe the SWCC based on Fredlund and Xing's model by the methylene blue test compared to other experimental procedures.
- (4) The slope parameter  $b_f$  was suitable to evaluate the moisture susceptibility of cohesive soils. Therefore,

the MBV can also be used to describe the moisture susceptibility of cohesive soils, which can be gained much more easily and quickly than  $b_f$ .

- (5) It was seen that the correlation coefficients of the mathematical formulations between the four fitting coefficients and the MBV were not high enough. More cohesive soils need to be selected to modify the formulations in the future research. In spite of this, the difference in the results of the pressure plate test and the prediction method using MBV was acceptable.

## Data Availability

The data used to support the findings of this study are available from the corresponding author upon request.

## Conflicts of Interest

The authors declare that there are no conflicts of interest regarding the publication of this paper.

## Acknowledgments

The authors gratefully acknowledge the financial support of the National Natural Science Foundation of China (51478054), National Key Research and Development Program of China (2017YFC0805307), Excellent Youth Foundation of Natural Science Foundation of Hunan Province of China (2018JJ1026), Key Project of Education Department of Hunan Province (17A008), and Jiangxi Communications Department Program (2013C0011). The study was also supported by the Open Research Fund of Science and Technology Innovation Platform of State Engineering Laboratory of Highway Maintenance Technology, Changsha University of Science & Technology (kfj150103).

## References

- [1] S. Nazari, M. Hassanlourad, E. Chavoshi, and A. Mirzaii, "Experimental investigation of unsaturated silt-sand soil permeability," *Advances in Civil Engineering*, vol. 2018, Article ID 4946956, 12 pages, 2018.
- [2] R. Zhang and J.-L. Zheng, "Study on moisture equilibrium of highway expansive soil embankment," *Journal of Highway and Transportation Research and Development*, vol. 30, no. 11, pp. 24–32, 2013, in Chinese.
- [3] C. W. W. Ng, C. Zhou, Q. Yuan, and J. Xu, "Resilient modulus of unsaturated subgrade soil: Experimental and theoretical investigations," *Canadian Geotechnical Journal*, vol. 50, no. 2, pp. 223–232, 2013.
- [4] M. T. V. Genuchten, "A closed-form equation for predicting the hydraulic conductivity of unsaturated soils," *Soil Science Society of America Journal*, vol. 44, no. 5, pp. 892–898, 1980.
- [5] H. J. Vereecken, J. Maes, J. Feyen, and P. Darius, "Estimating the soil moisture retention characteristic from texture, bulk density, and carbon content," *Soil Science*, vol. 148, no. 6, pp. 389–403, 1989.

- [6] D. G. Fredlund and A. Xing, "Equations for the soil-water characteristic curve," *Canadian Geotechnical Journal*, vol. 31, no. 4, pp. 521–532, 1994.
- [7] C. E. Zapata, "Uncertainty in soil-water-characteristic curve and impacts on unsaturated shear strength predictions," Ph.D. thesis, Arizona State University, Tempe, AZ, USA, 1999.
- [8] Y. Y. Perera, C. E. Zapata, W. N. Houston, and S. L. Houston, "Long-term moisture conditions under highway pavements," in *Proceedings of the Geotechnical Engineering for Transportation Projects*, pp. 1132–1143, Los Angeles, CA, USA, July 2004.
- [9] Y. Y. Perera, C. E. Zapata, W. N. Houston, and S. L. Houston, "Prediction of the soil-water characteristic curve based on grain-size-distribution and index properties," in *Proceedings of the Geo-Frontiers Congress*, pp. 1–12, Austin, TX, USA, January 2005.
- [10] J. Epps, S. Sebesta, B. Hewes, H. Sahin, R. Luo, and J. Button, "Development of a specification for flexible base construction," Tech. Rep. no. FHWA/TX-13/0-6621, 2014.
- [11] H. Sahin, F. Gu, and R. L. Lytton, "Development of soil-water characteristic curve for flexible base materials using the methylene blue test," *Journal of Materials in Civil Engineering*, vol. 27, no. 5, article 04014175, 2015.
- [12] H. Sahin, "Nondestructive test methods for rapid assessment of flexible base performance in transportation infrastructures," Ph.D. thesis, Texas A&M University, College Station, TX, USA, 2014.
- [13] W. N. Houston, H. B. Dye, C. E. Zapata, Y. Y. Perera, and A. Harraz, "Determination of SWCC using one point suction measurement and standard curves," in *Proceedings of the Fourth International Conference on Unsaturated Soils*, pp. 1482–1493, Carefree, AZ, USA, April 2006.
- [14] F. Gu, H. Sahin, X. Luo, R. Luo, and R. L. Lytton, "Estimation of resilient modulus of unbound aggregates using performance-related base course properties," *Journal of Materials in Civil Engineering*, vol. 27, no. 6, article 04014188, 2014.
- [15] M. D. Fredlund, G. W. Wilson, and D. G. Fredlund, "Use of the grain-size distribution for estimation of the soil-water characteristic curve," *Canadian Geotechnical Journal*, vol. 39, no. 5, pp. 1103–1117, 2002.
- [16] Y. Yukselen and A. Kaya, "Suitability of the methylene blue test for surface area, cation exchange capacity and swell potential determination of clayey soils," *Engineering Geology*, vol. 102, no. 2, pp. 38–45, 2008.
- [17] C. Khengboon, L. Engchoon, and H. Rahardjo, "A simplified method to estimate the soil-water characteristic curve," *Canadian Geotechnical Journal*, vol. 47, no. 12, pp. 1382–1400, 2010.
- [18] X. Li, J. H. Li, and L. M. Zhang, "Predicting bimodal soil-water characteristic curves and permeability functions using physically based parameters," *Computers & Geotechnics*, vol. 57, no. 4, pp. 85–96, 2014.
- [19] ASTM, *Standard Test Method for Methylene Blue Index of Clay*, ASTM, West Conshohocken, PA, USA, 2009.
- [20] J. Xiao, H.-P. Yang, J.-H. Zhang, and X.-Y. Tang, "Surficial failure of expansive soil cutting slope and its flexible support treatment technology," *Advances in Civil Engineering*, vol. 2018, Article ID 1609608, 13 pages, 2018.
- [21] J.-H. Zhang, Q.-P. Jiang, Y.-Q. Zhang, L.-L. Dai, and H.-X. Wu, "Nondestructive measurement of water content and moisture migration of unsaturated red clays in South China," *Advances in Materials Science & Engineering*, vol. 2015, Article ID 542538, 7 pages, 2015.
- [22] M. W. Witczak, T. K. Pellinen, and M. M. Elbasyouny, "Pursuit of the simple performance test for asphalt concrete fracture/cracking," *Journal of the Association of Asphalt Paving Technologists*, vol. 71, pp. 767–778, 2002.
- [23] A. G. Seferoğlu, M. T. Seferoğlu, and M. V. Akpınar, "Investigation of the effect of recycled asphalt pavement material on permeability and bearing capacity in the base layer," *Advances in Civil Engineering*, vol. 2018, Article ID 2860213, 6 pages, 2018.

## Research Article

# Application of the Bipotential Theory to a Nonassociated Drucker–Prager Model

Yang-Jing Zhou,<sup>1</sup> Zhi-Qiang Feng ,<sup>1,2</sup> Juan Antonio Rojas Quintero,<sup>3</sup> Jian-Bo Zhou,<sup>1</sup> and Hui-Jian Chen<sup>1</sup>

<sup>1</sup>School of Mechanics and Engineering, Southwest Jiaotong University, Chengdu, China

<sup>2</sup>LMEE Univ-Evry, Université Paris-Saclay, Evry, France

<sup>3</sup>CONACYT, Instituto Tecnológico de Ensenada, Ensenada, BC, Mexico

Correspondence should be addressed to Zhi-Qiang Feng; [zhiqiang.feng@univ-evry.fr](mailto:zhiqiang.feng@univ-evry.fr)

Received 14 December 2017; Accepted 1 March 2018; Published 21 May 2018

Academic Editor: Qiang Tang

Copyright © 2018 Yang-Jing Zhou et al. This is an open access article distributed under the Creative Commons Attribution License, which permits unrestricted use, distribution, and reproduction in any medium, provided the original work is properly cited.

The bipotential theory allows us to describe nonassociated material laws. In this paper, we propose its application to the Drucker–Prager model. With a new description of the implicit flow rules, we propose dual constitutive cones as well as five forms of the bipotential function: the elastic stage in rate form, the plastic stage in rate form, the elastic stage in incremental form, the plastic stage in incremental form, and the elastoplastic stage in incremental form. By combining these with the finite element method, a numerical strategy that deals with the nonassociated Drucker–Prager model is obtained. Two examples are simulated to verify the accuracy, the stability, and the practicability of the algorithm in civil engineering.

## 1. Introduction

The exploration of the material constitutive laws plays an important role in its numerical modeling. Much work has been done in dealing with associated plastic materials such as metals. A return mapping algorithm was proposed by Simo and Taylor to simulate the behavior of associated elastoplastic materials [1]. On the basis of the return mapping algorithm, many other algorithms were proposed to study different associated constitutive laws of materials [2, 3, 4]. However, as we know, most rock-soil materials belong to the nonassociated materials category, and their behavior is more complex [5] because the plastic flow direction is not orthogonal to the yield surface. Typical methods dealing with nonassociated rock-soils consist in generating two potential functions: a yield function which delimits the zone of plasticity, and the flow potential which defines the plastic flow direction. The use of these two potentials to describe nonassociated rock-soils breaks the frame of orthogonality between stress and plastic strain, which is a classical property in solid mechanics. However, it is desirable to

obtain a unique potential which can express both the yield and the flow rules. The bipotential method put forward by De Saxcé and Feng [6] achieves this goal. More recently, Sun et al. proposed the fractional plasticity which brings some new ideas to the study of nonassociated plasticity [7, 8].

On the basis of the Legendre transformations, the Fenchel inequality with respect to two conjugate variables was established [9]. According to whether the free energy could be separated into two convex potential functions or not, materials were divided into the generalized standard materials (GSMs) and implicit standard materials (ISMs) [10]. De Saxcé et al. have shown that the bipotential algorithm could not only satisfy the constitutive laws of ISMs but also meet the implicit flow requirements of material conjugated variables [11, 12]. Nowadays, the bipotential method can be used to solve constitutive laws of ISMs, including frictional contact, nonassociated metal materials, or even nonassociated rock-soils among other examples.

Feng proposed a bipotential method combining both the Signorini and Coulomb conditions to solve the frictional contact [13]. De Saxcé and Feng summarized the main

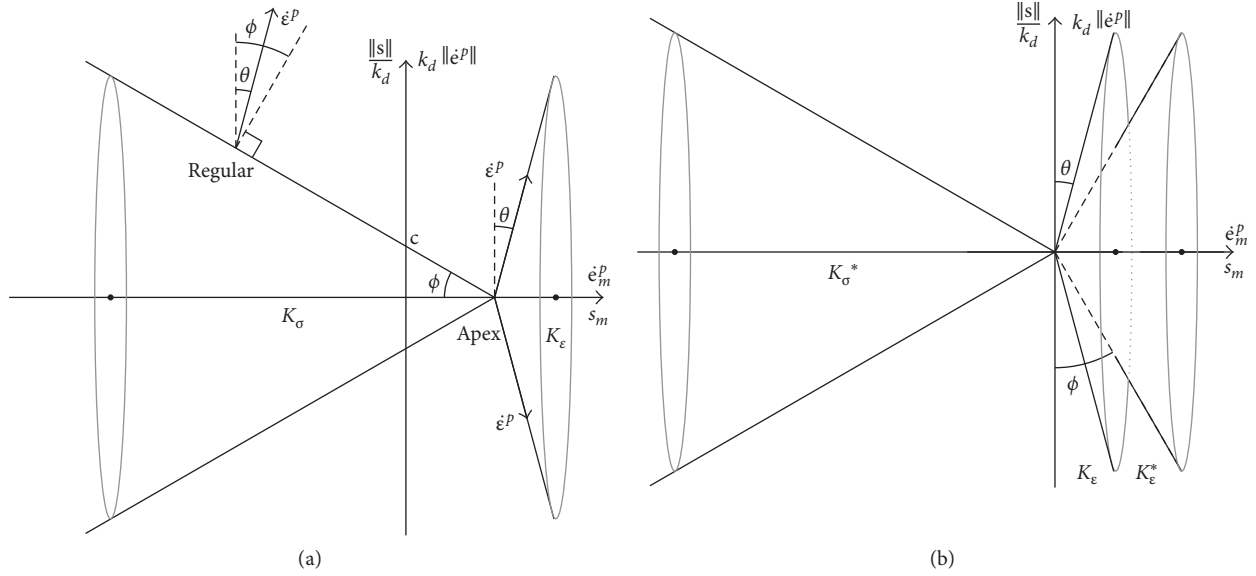


FIGURE 1: Cones of the nonassociated Drucker–Prager model. (a) Constitutive cones. (b) Dual cones.

process of the bipotential algorithm and proved that the algorithm had a high efficiency in dealing with contact issues [14]. The Uzawa algorithm was used to replace the Newton–Raphson algorithm to solve the nonlinear equations. This improved the speed of the solving strategy [15]. Others have also developed the algorithm in frictional contact considering large deformations [16], anisotropy [17], and impact dynamics [18].

The bipotential method is also applied to solve the constitutive laws of materials. On the basis of De Saxcé’s work, Bodovillé succeeded in applying the bipotential method in kinematic hardening models [19]. Bouby et al. conducted a shakedown analysis, by comparing different models with the linear unlimited, the linear limited, and the nonlinear kinematic hardening [20]. Chaaba et al. stated the superiority of combining the bipotential method with sequential limit analysis in disposing the nonassociated nonlinear hardening models [21]. Zhou et al. compared the accuracy and stability of the return mapping algorithm against the bipotential algorithm in two typical non-associated models [22]. Cheng et al. simulated the behaviors of a hollow sphere modeled with a nonassociated material under an isotropic loading [23]. Aiming at ductile porous materials, the bipotential method was applied to limit analysis and a stress-based variational model was developed. In addition, some homogenization problems were also studied. Bousshine et al. derived the bipotential function of nonassociated rock-soils in detail [24]. Hjiiaj et al. discussed the singular point on the nonassociated model, keeping the integrity of the bipotential algorithm [25]. Berga aimed at the nonassociated plasticity of rock-soils, giving a detailed process in establishing its bipotential function [26]. Furthermore, he proposed a numerical process and simulated some basic examples [27]. On the basis of Berga’s work, Zhou et al. applied the bipotential algorithm in the geotechnical context [28].

The abovementioned investigations show some advantages provided by the bipotential method in dealing with ISMs. However, regarding the expression of the dual cone of the Drucker–Prager model, further detail is needed to explain how the new transmission meets the implicit flow requirements. This paper focuses on the implicit flow laws of the perfect elastoplastic Drucker–Prager model, detailing the derivation process of the incremental elastoplastic bipotential of the Drucker–Prager model. When applying the bipotential algorithm into the finite element method, a large time increment is used to conduct the numerical implementation of the nonassociated Drucker–Prager model of the whole structure.

This paper is structured as follows. The cones of the nonassociated Drucker–Prager model are introduced in detail in Section 2. Combining them with the bipotential theory, in Section 3, we establish the incremental bipotential function of the nonassociated Drucker–Prager model by a deriving strategy. Two numerical examples are proposed in Section 4, verifying the accuracy, the stability, and the practicability of the bipotential Drucker–Prager model implementation. Finally, Section 5 gives some conclusions of the presented work.

## 2. Nonassociated Drucker–Prager Model

The nonassociated Drucker–Prager model is a classic three-parameter model: the cohesion  $c$ , the internal friction angle  $\phi$ , and the dilatancy angle  $\theta$  [29]. The relations of stress and plastic strain rate can be expressed by a Drucker–Prager constitutive cone, which consists of the hydrostatic part and the deviatoric part. They are  $\boldsymbol{\sigma} = (s_m, \mathbf{s})$  and  $\dot{\boldsymbol{\epsilon}}^p = (\dot{\epsilon}_m^p, \dot{\boldsymbol{\epsilon}}^p)$ , where  $s_m = Tr(\boldsymbol{\sigma})/3$ ,  $\mathbf{s} = \boldsymbol{\sigma} - s_m \mathbf{1}$ ,  $\dot{\epsilon}_m^p = Tr(\dot{\boldsymbol{\epsilon}}^p)$ , and  $\dot{\boldsymbol{\epsilon}}^p = \dot{\boldsymbol{\epsilon}} - \dot{\epsilon}_m^p \mathbf{1}/3$ , where  $\mathbf{1}$  is the second-order unit tensor. In the elastic state, the stress variable  $\boldsymbol{\sigma} = (s_m, \mathbf{s})$  belongs to the constitutive stress cones  $K_\sigma$ , as shown in Figure 1(a). The expression of these stress cones is as follows.

$$K_{\sigma} = \left\{ (s_m, \mathbf{s}) \left| \frac{\|\mathbf{s}\|}{k_d} + s_m \tan \phi \leq c \right. \right\}, \quad (1)$$

where  $\|\cdot\|$  stands for the Euclidean norm and the  $k_d$  parameter is a function of the internal friction angle  $\phi$  as  $k_d = 3\sqrt{2}/\sqrt{9 + 12 \tan^2 \phi}$ . In the principal stress space, the Drucker–Prager cone is the inscribed compressive meridian of the Mohr–Coulomb pyramid. Due to the nonassociated flow rules of the Drucker–Prager model, the dual plastic rate cone  $K_{\epsilon}$  is obtained as shown in Figure 1(a). The regular and the apex points on the stress cone have different flow expressions. At a regular point, namely, ( $s_m \neq c/\tan \phi$  and  $\|\mathbf{s}\| \neq 0$ ),  $K_{\sigma}$  is differentiable, and the flow direction  $K_{\epsilon^P}$  can be expressed as

$$K_{\epsilon^P} \in \left\{ (\dot{\epsilon}_m^P, \dot{\epsilon}^P) \mid \dot{\epsilon}_m^P = k_d \tan \theta \|\dot{\epsilon}^P\| \right\}. \quad (2)$$

At the apex point, namely, ( $s_m = c/\tan \phi$  and  $\|\mathbf{s}\| = 0$ ),  $K_{\sigma}$  is nondifferentiable, and the flow direction cannot be determined. A convex set is used here. There exists a cone  $K_{\epsilon^a}$  such that

$$K_{\epsilon^a} \in \left\{ (\dot{\epsilon}_m^P, \dot{\epsilon}^P) \mid \dot{\epsilon}_m^P > k_d \tan \theta \|\dot{\epsilon}^P\| \right\}. \quad (3)$$

So, associating (2) with (3), the plastic rate cone  $K_{\epsilon}$  is unified as follows:

$$K_{\epsilon} \in \left\{ (\dot{\epsilon}_m^P, \dot{\epsilon}^P) \mid \dot{\epsilon}_m^P \geq k_d \tan \theta \|\dot{\epsilon}^P\| \right\}. \quad (4)$$

The implicit flow laws of the nonassociated Drucker–Prager model can be written as follows:

$$\begin{aligned} \sigma &\in \partial \Psi K_{\epsilon}(\dot{\epsilon}^P), \\ \dot{\epsilon}^P &\in \partial \Psi K_{\sigma}(\sigma), \end{aligned} \quad (5)$$

where  $\Psi K_{\sigma}(\sigma)$  and  $\Psi K_{\epsilon}(\dot{\epsilon}^P)$  are indicator functions.

Equation (5) can also be written with the hydrostatic part and the deviatoric part:

$$\begin{aligned} s_m &\in \partial_{\dot{\epsilon}_m^P} \Psi K_{\epsilon}(\dot{\epsilon}^P) \\ \mathbf{s} &\in \partial_{\dot{\epsilon}^P} \Psi K_{\epsilon}(\dot{\epsilon}^P), \\ \dot{\epsilon}_m^P &\in \partial_{s_m} \Psi K_{\sigma}(\sigma) \\ \dot{\epsilon}^P &\in \partial_{\mathbf{s}} \Psi K_{\sigma}(\sigma). \end{aligned} \quad (6)$$

From Figure 1(a), it can be noted that when  $\theta = \phi$ ,  $K_{\epsilon}$  and  $K_{\sigma}$  are dual cones, the material is associated, and the flow direction is normal to its yield surface. If  $\theta \neq \phi$ , the material is nonassociated, and there exists an angle  $\phi - \theta$  between the plastic flow direction and the yield surface, as shown in Figure 1(a). So, the implicit flow laws between stress and plastic strain are therefore not met. There is a new expression which not only satisfies the nonassociated flow rules but also meets the constitutive requirements. Moving the stress cone along the negative  $s_m$  direction by a distance  $c/\tan \phi$ , the cone translates from the location  $(s_m, \|\mathbf{s}\|)$  to  $(0, 0)$ , as shown in Figure 1(b). A new stress cone  $K_{\sigma}^*$  can be defined as

$$K_{\sigma}^* = \left\{ (s_m, \mathbf{s}) \left| \frac{\|\mathbf{s}\|}{k_d} + s_m \tan \phi \leq 0 \right. \right\}, \quad (7)$$

with  $K_{\epsilon}^*$  being the dual cone of  $K_{\sigma}^*$  and is defined as

$$K_{\epsilon}^* = \left\{ (\dot{\epsilon}_m^P, \dot{\epsilon}^P) \mid \dot{\epsilon}_m^P \geq k_d \tan \phi \|\dot{\epsilon}^P\| \right\}. \quad (8)$$

According to the geometric features of  $K_{\epsilon}(\dot{\epsilon}^P)$ ,  $K_{\epsilon}^*(\dot{\epsilon}^P)$ ,  $K_{\sigma}(\sigma)$ , and  $K_{\sigma}^*(\sigma)$  and combining them with (6), while setting  $c_{\phi} = c/\tan \phi$ , the implicit flow laws of the nonassociated Drucker–Prager model under new constitutive cones can be stated as

$$\begin{aligned} \sigma &\in \partial \Psi K_{\epsilon}(\dot{\epsilon}^P) = \partial \Psi K_{\epsilon}^*(\dot{\epsilon}^P) + (c_{\phi}, \mathbf{s}), \\ \dot{\epsilon}^P &\in \partial \Psi K_{\sigma}(\sigma) = \partial \Psi K_{\sigma}^*(\sigma) + (k_d (\tan \theta - \tan \phi) \dot{\epsilon}^P, \mathbf{s}). \end{aligned} \quad (9)$$

Equation (9) is divided into a hydrostatic part and a deviatoric part:

$$\begin{aligned} s_m &\in \partial_{\dot{\epsilon}_m^P} \Psi K_{\epsilon}^*(\dot{\epsilon}^P) + c_{\phi} \\ \mathbf{s} &\in \partial_{\dot{\epsilon}^P} \Psi K_{\epsilon}^*(\dot{\epsilon}^P), \\ \dot{\epsilon}_m^P &\in \partial_{s_m} \Psi K_{\sigma}^*(\sigma) + k_d (\tan \theta - \tan \phi) \|\dot{\epsilon}^P\| \\ \dot{\epsilon}^P &\in \partial_{\mathbf{s}} \Psi K_{\sigma}^*(\sigma). \end{aligned} \quad (10)$$

Equation (10) is the new expression of the implicit flow laws based on the dual cone of the Drucker–Prager model. On the basis of the bipotential theory, we try to find a bipotential function  $b(\sigma, \dot{\epsilon}^P)$ , which satisfies the constitutive laws of the nonassociated Drucker–Prager model and meets the requirements of implicit flow laws.

### 3. Bipotential of the Nonassociated Drucker–Prager Model

In solid mechanics, many materials can be represented by a relationship of a set of coupled variables  $(\sigma, \dot{\epsilon})$ . According to their free energy, materials are divided into generalized standard materials (GSMs) and implicit standard materials (ISMs) [12], where GSMs are similar to associated materials, whose plastic flow directions are normal to their yield surfaces. ISMs have the same characteristics of nonassociated materials, whose plastic flow directions and yield surfaces are not orthogonal. Under the traditional plastic mechanics, the expressions of their free energy are different. However, in the framework of the bipotential theory, the materials potential can be unified. The energy potential of the ISM cannot be separated. A bipotential was promoted by De Saxcé and Feng in [6], which describes the materials free energy by dual potentials. The bipotential  $b(\sigma, \dot{\epsilon})$  is convex with respect to  $\sigma$  when  $\dot{\epsilon}$  remains constant and convex with respect to  $\dot{\epsilon}$  when  $\sigma$  remains constant [26]. So, there exists

$$\begin{aligned} \text{GSM: } &\forall (\sigma, \dot{\epsilon}) \quad W(\sigma) + V(\dot{\epsilon}) \geq \sigma : \dot{\epsilon}, \\ \text{ISM: } &\forall (\sigma, \dot{\epsilon}) \quad b(\sigma, \dot{\epsilon}) \geq \sigma : \dot{\epsilon}. \end{aligned} \quad (11)$$

The flow rules are therefore expressed by subdifferential mappings:

$$\begin{aligned} \text{GSM: } &\sigma \in \partial V(\dot{\epsilon}), \quad \dot{\epsilon} \in \partial W(\sigma), \\ \text{ISM: } &\sigma \in \partial_{\dot{\epsilon}} b(\sigma, \dot{\epsilon}), \quad \dot{\epsilon} \in \partial_{\sigma} b(\sigma, \dot{\epsilon}). \end{aligned} \quad (12)$$

As shown in the section above, in the elastic state, the bipotential of the Drucker–Prager model conforms to the characteristics of GSMs. And, in the plastic state, the model satisfies the features of ISMs. So, in order to establish the

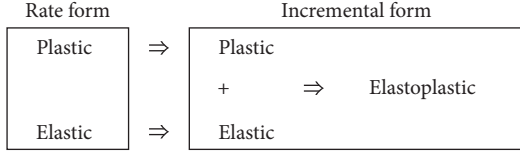


FIGURE 2: Incremental form of the elastoplastic bipotential deriving strategy.

incremental bipotential function of the nonassociated Drucker–Prager model  $\Delta b^{eP}(\Delta\sigma, \Delta\epsilon)$ , a deriving strategy from the rate form to an incremental one is applied, as shown in Figure 2.

**3.1. The Rate Form.** In the elastic state, the bipotential consists of two convex potentials:  $V^e(\dot{\epsilon}^e)$  which is the strain energy density and  $W^e(\sigma)$  which is the complementary energy density. The superscript “e” stands for the elastic state. Due to (11), the elastic bipotential of the Drucker–Prager model in the rate form can be expressed as

$$b^e(\sigma, \dot{\epsilon}^e) = V^e(\dot{\epsilon}^e) + W^e(\sigma) \geq \sigma : \dot{\epsilon}. \quad (13)$$

What is more, under the plastic state, the Drucker–Prager model falls into the category of ISMs. According to (11), the rate form of the plastic bipotential is

$$b^P(\sigma, \dot{\epsilon}^P) \geq \sigma : \dot{\epsilon} + \Psi K_\sigma^*(\sigma) + \Psi K_\epsilon^*(\dot{\epsilon}^P). \quad (14)$$

Separating  $\sigma : \dot{\epsilon}^P$  into a hydrostatic and a deviatoric part, there is

$$\sigma : \dot{\epsilon} = s_m \cdot \dot{e}_m^P + s \cdot \dot{e}^P + \Psi K_\sigma^*(\sigma) + \Psi K_\epsilon^*(\dot{\epsilon}^P), \quad (15)$$

where in the hydrostatic part,

$$s_m \cdot \dot{e}_m^P = c_\phi \dot{e}_m^P + (s_m - c_\phi) \dot{e}_m^P. \quad (16)$$

Considering (1) and (4), (16) becomes

$$s_m \cdot \dot{e}_m^P \leq c_\phi \dot{e}_m^P + k_d \tan \theta (s_m - c_\phi) \|\dot{e}_m^P\|. \quad (17)$$

The Cauchy–Schwarz inequality is used to deal with the deviatoric part. By combining it with (1), the following inequality arises:

$$s \cdot \dot{e}^P \leq \|s\| \cdot \|\dot{e}^P\| \leq -k_d \tan \phi (s_m - c_\phi) \|\dot{e}^P\|. \quad (18)$$

Then, from (14), (15), (17), and (18), the rate form of plastic bipotential can be expressed as

$$b^P(\sigma, \dot{\epsilon}^P) = c_\phi \dot{e}_m^P + k_d (\tan \theta - \tan \phi) (s_m - c_\phi) \|\dot{e}_m^P\| + \Psi K_\sigma^*(\sigma) + \Psi K_\epsilon^*(\dot{\epsilon}^P). \quad (19)$$

Taking  $\sigma = (s_m, s)$  and  $\dot{\epsilon}^P = (\dot{e}_m^P, \dot{e}^P)$  as partial derivatives to (19), it is proved that the implicit flow laws can be expressed.

**3.2. The Incremental Form.** Assume the plastic strain rate is constant, namely,  $\Delta\epsilon = \Delta t \cdot \dot{\epsilon}$ . The incremental elastic bipotential is written as follows.

$$\Delta b^e(\Delta\sigma, \Delta\epsilon^e) = \Delta V^e(\Delta\epsilon^e) + \Delta W^e(\Delta\sigma) \geq \sigma : \dot{\epsilon}. \quad (20)$$

Due to the definitions of  $\Delta V^e(\Delta\epsilon^e)$  and  $\Delta W^e(\Delta\sigma)$ ,

$$\begin{aligned} \Delta V^e(\Delta\epsilon^e) &= \frac{\Delta\sigma : \Delta\epsilon^e}{2} = \frac{(\Delta s_m \cdot \Delta e_m^e + \Delta s : \Delta\epsilon^e)}{2} \\ &= \frac{K_c (\Delta e_m^e)^2}{2} + \mu \|\Delta\epsilon^e\|^2, \\ \Delta W^e(\Delta\sigma) &= \frac{\Delta\sigma : \Delta\epsilon^e}{2} = \frac{(\Delta s_m \cdot \Delta e_m^e + \Delta s : \Delta\epsilon^e)}{2} \\ &= \frac{(\Delta s_m)^2}{2K_c} + \frac{4\mu \|\Delta s\|^2}{2K_c}. \end{aligned} \quad (21)$$

The elastic incremental bipotential of the Drucker–Prager model is

$$\Delta b^e(\Delta\sigma, \Delta\epsilon^e) = \frac{K_c (\Delta e_m^e)^2}{2} + \mu \|\Delta\epsilon^e\|^2 + \frac{(\Delta s_m)^2}{2K_c} + \frac{\|\Delta s\|^2}{4\mu}. \quad (22)$$

The incremental stress is written as  $\Delta\sigma = \sigma_1 - \sigma_0$ , where the subscript 0 means the initial value of an increment step and the subscript 1 stands for the final value. From the implicit flow laws of (12), there exists

$$\begin{aligned} \Delta\epsilon^P &\in \partial_\sigma b^P(\sigma_0 + \Delta\sigma, \Delta\epsilon^P), \\ \Delta\sigma + \sigma_0 &\in \partial_{\Delta\epsilon^P} b^P(\sigma_0 + \Delta\sigma, \Delta\epsilon^P). \end{aligned} \quad (23)$$

The incremental plastic bipotential is written as

$$(\sigma_0 + \Delta\sigma) : \Delta\epsilon^P \leq b^P(\sigma_0 + \Delta\sigma, \Delta\epsilon^P). \quad (24)$$

Then,

$$\Delta\sigma : \Delta\epsilon^P \leq b^P(\sigma_0 + \Delta\sigma, \Delta\epsilon^P) - \sigma_0 : \Delta\epsilon^P. \quad (25)$$

Due to (11), it can be also obtained that

$$\Delta\sigma : \Delta\epsilon^P \leq b^P(\Delta\sigma, \Delta\epsilon^P). \quad (26)$$

From (24) to (25), the incremental plastic bipotential can be expressed as the following inequality:

$$\Delta b^P(\Delta\sigma, \Delta\epsilon^P) \geq b^P(\sigma_0 + \Delta\sigma, \Delta\epsilon^P) - \sigma_0 : \Delta\epsilon^P. \quad (27)$$

In addition, combining (19) and (27), the bipotential is

$$\begin{aligned} \Delta b^P(\Delta\sigma, \Delta\epsilon^P) &= c_\phi \Delta e_m^P + k_d (\tan \theta - \tan \phi) (s_{m0} + \Delta s_m - c_\phi) \\ &\quad \cdot \|\Delta\epsilon^P\| - s_{m0} \Delta e_m^P - s_0 : \Delta\epsilon^P + \Psi K_\sigma^*(\sigma) \\ &\quad + \Psi K_\epsilon^*(\dot{\epsilon}^P). \end{aligned} \quad (28)$$

In order to combine the incremental elastic bipotential and the incremental plastic one, a new function is proposed as follows:

$$b(\mathbf{x}, \mathbf{y}) = b_1(\mathbf{x}, \mathbf{y} - \mathbf{y}') \circledast_{\mathbf{y}} b_2(\mathbf{x}, \mathbf{y}'). \quad (29)$$

The symbol  $\circledast_{\mathbf{y}}$  in (29) is called the inf-convolution of  $b_1(\mathbf{x}, \mathbf{y} - \mathbf{y}')$  and  $b_2(\mathbf{x}, \mathbf{y}')$  with respect to the space of  $\mathbf{y}$ . It is defined by the following.

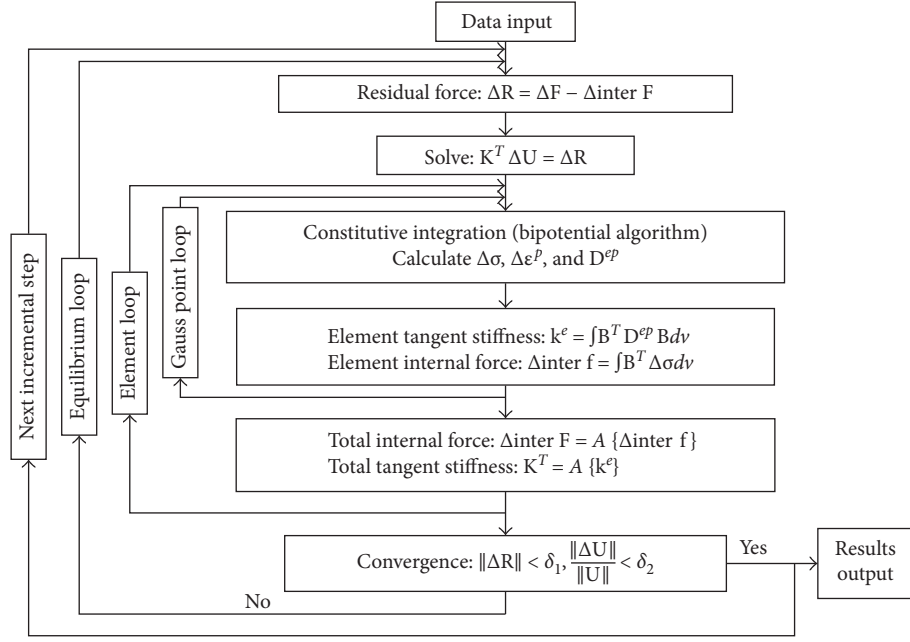


FIGURE 3: Process of the Newton–Raphson strategy.

$$b_1(\mathbf{x}, \mathbf{y} - \mathbf{y}') \odot_{\mathbf{y}} b_2(\mathbf{x}, \mathbf{y}') = \inf_{\mathbf{y}'} [b_1(\mathbf{x}, \mathbf{y} - \mathbf{y}') + b_2(\mathbf{x}, \mathbf{y}')]. \quad (30)$$

Considering the strain decomposition  $\Delta \boldsymbol{\varepsilon}^e = \Delta \boldsymbol{\varepsilon} - \Delta \boldsymbol{\varepsilon}^p$ , the incremental elastoplastic bipotential can be expressed as

$$\Delta b^{ep}(\Delta \boldsymbol{\sigma}, \Delta \boldsymbol{\varepsilon}) = \Delta b^e(\Delta \boldsymbol{\sigma}, \Delta \boldsymbol{\varepsilon} - \Delta \boldsymbol{\varepsilon}^p) \odot_{\Delta \boldsymbol{\varepsilon}^p} \Delta b^p(\Delta \boldsymbol{\sigma}, \Delta \boldsymbol{\varepsilon}^p). \quad (31)$$

We could also state that

$$\Delta b^{ep}(\Delta \boldsymbol{\sigma}, \Delta \boldsymbol{\varepsilon}) = \inf_{\Delta \boldsymbol{\varepsilon}^p} [\Delta b^e(\Delta \boldsymbol{\sigma}, \Delta \boldsymbol{\varepsilon} - \Delta \boldsymbol{\varepsilon}^p) + \Delta b^p(\Delta \boldsymbol{\sigma}, \Delta \boldsymbol{\varepsilon}^p)]. \quad (32)$$

And finally, from (22), (28), and (32), the expression of the incremental elastoplastic bipotential is

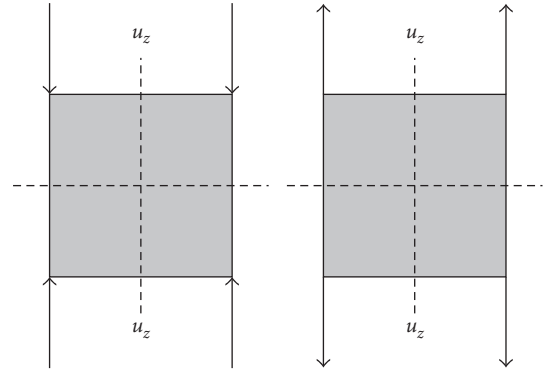


FIGURE 4: Uniaxial compression/tension of the Drucker–Prager model example.

$$\begin{aligned} \Delta b^{ep}(\Delta \boldsymbol{\sigma}, \Delta \boldsymbol{\varepsilon}) = & \inf_{\Delta e_m^p \geq k_d \tan \theta \|\Delta \boldsymbol{\varepsilon}^p\|} \left\{ \frac{K_c (\Delta e_m - \Delta e_m^p)^2}{2} + \mu \|\Delta \boldsymbol{\varepsilon} - \Delta \boldsymbol{\varepsilon}^p\| + c_\phi \Delta e_m^p + k_d (\tan \theta - \tan \phi) (s_{m0} + \Delta s_m - c_\phi) \|\Delta \boldsymbol{\varepsilon}^p\| \right. \\ & \left. - s_{m0} : \Delta e_m^p - s_0 : \Delta \boldsymbol{\varepsilon}^p \right\} + \frac{\|\Delta \boldsymbol{s}\|^2}{4\mu} + \frac{(\Delta s_m)^2}{2K_c} + \Psi K_\sigma^*(\sigma) + \Psi K_\varepsilon^*(\dot{\boldsymbol{\varepsilon}}^p). \end{aligned} \quad (33)$$

#### 4. Numerical Examples

With the incremental elastoplastic bipotential of the non-associated Drucker–Prager model, a finite element method is applied to conduct the numerical implementation. We apply the Newton–Raphson method to solve nonlinear equations. The process of the strategy is demonstrated in Figure 3. At the Gauss point level,  $\Delta \boldsymbol{\sigma}$  and  $\Delta \boldsymbol{\varepsilon}^p$  represent the incremental

stress and strain tensors.  $\mathbf{D}^{ep}$  is the local tangent matrix. At the element level,  $\Delta \text{inter } \mathbf{f}$  is the element internal force and  $\mathbf{k}^T$  is the element tangent stiffness.  $\mathbf{B}$  stands for the strain matrix, depending on the element shape function. In the global level,  $\Delta \mathbf{R}$ ,  $\Delta \mathbf{F}$ , and  $\Delta \text{inter } \mathbf{F}$  stand for the incremental residual, external, and internal force vector.  $\mathbf{U}$  and  $\Delta \mathbf{U}$  represent the total and incremental displacement vector.  $\mathbf{K}^T$  is the total tangent stiffness matrix. The symbol  $\mathcal{A}()$

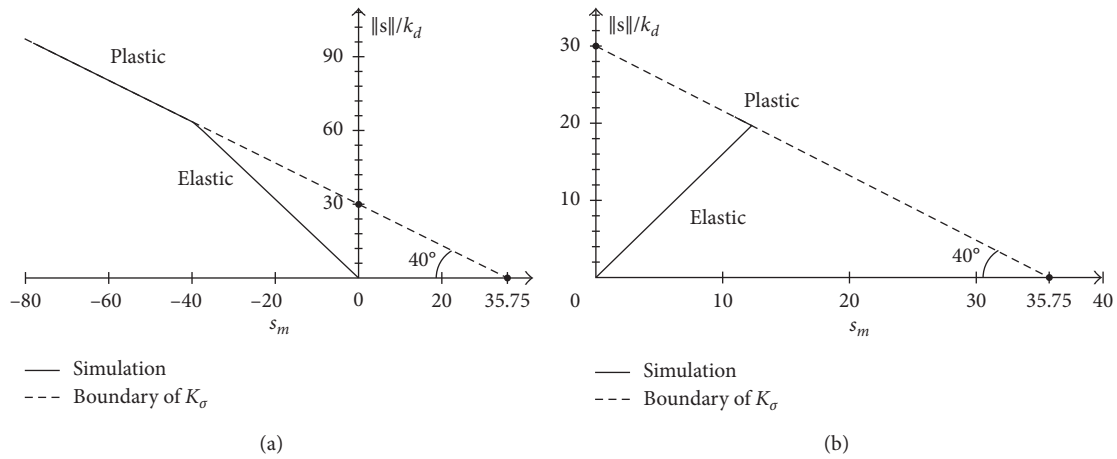


FIGURE 5: Comparison of the simulated constitutive law versus the theoretical one: (a) compression; (b) tension.

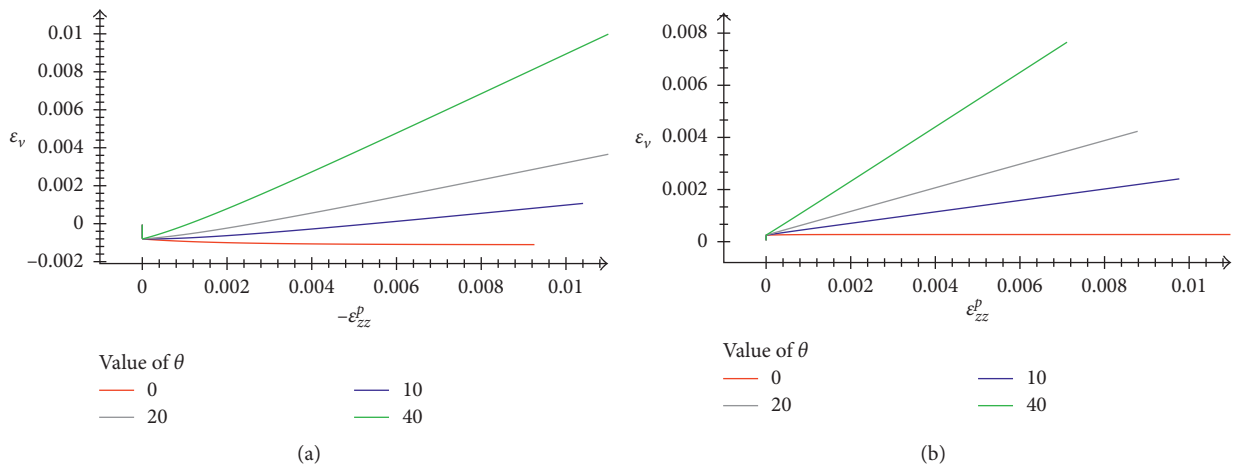


FIGURE 6: Volume expansion under different dilatancy angles: (a) compression; (b) tension.

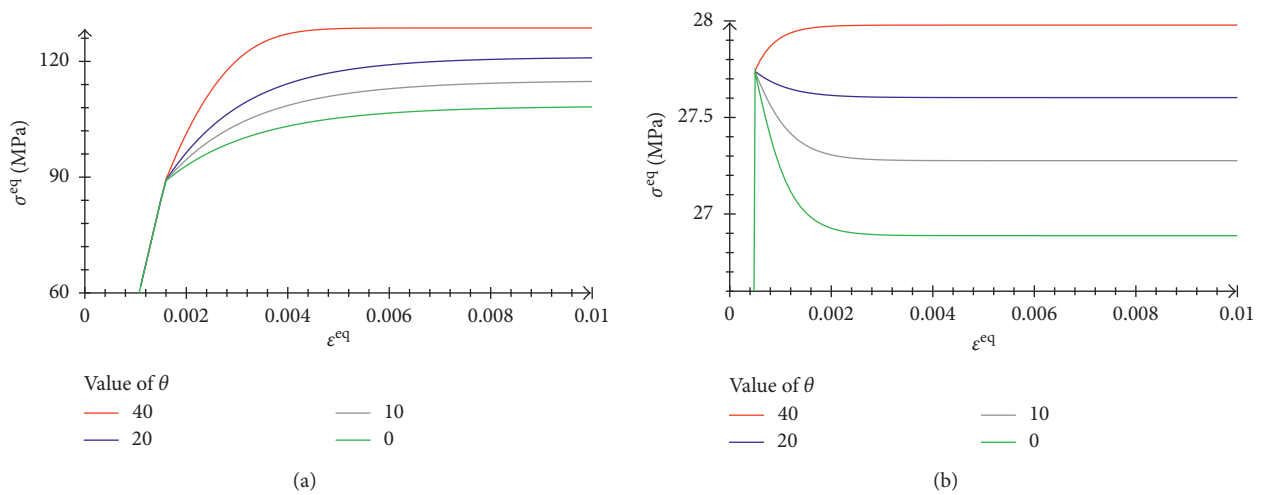


FIGURE 7: Equivalent stress-strain curves for various dilatancy angles: (a) compression; (b) tension.

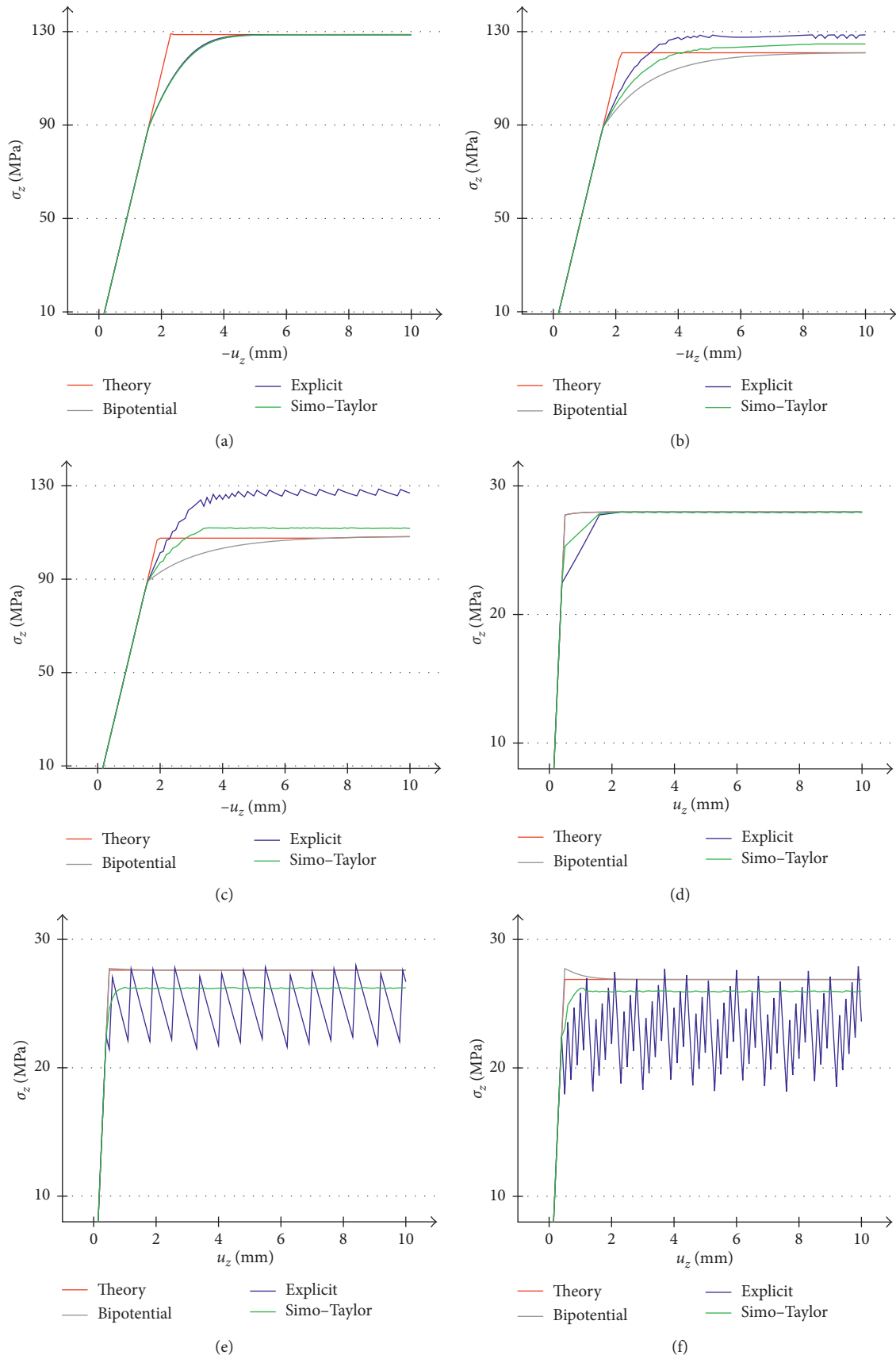


FIGURE 8: Comparison of different algorithms associated with various dilatancy angles based on stress-displacement curves. Compression at (a)  $\theta = 40^\circ$ , (b)  $\theta = 20^\circ$ , and (c)  $\theta = 20^\circ$ . Tension at (d)  $\theta = 40^\circ$ , (e)  $\theta = 20^\circ$ , and (f)  $\theta = 0^\circ$ .

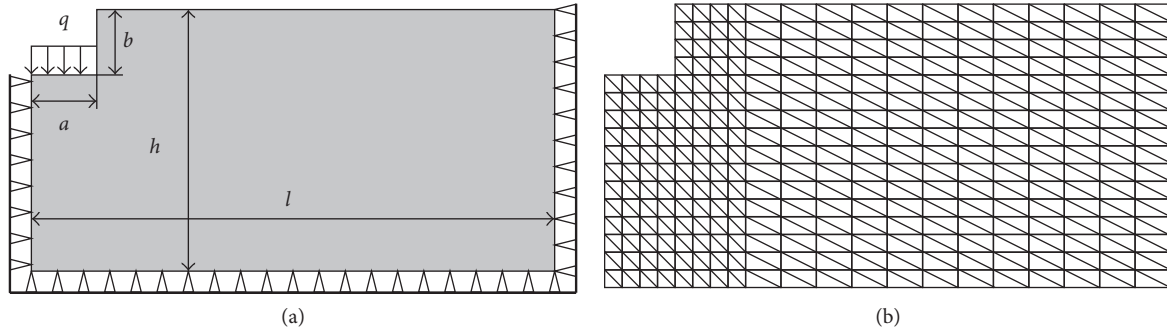


FIGURE 9: Geometry (a) and mesh (b) of the soil under a deep rigid strip footing.

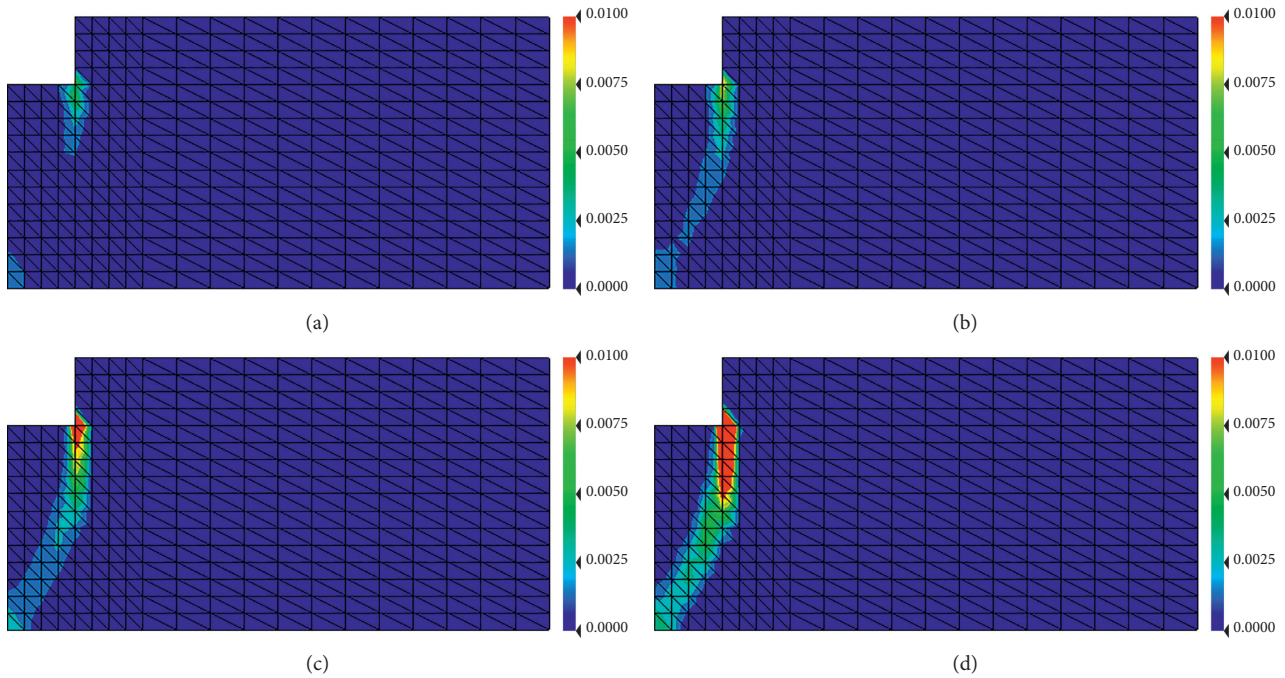


FIGURE 10: Comparing the slip bands for various dilatancy angles while locking the maximum plastic strain: (a)  $\theta = \phi = 30^\circ$ ; (b)  $\theta = 20^\circ$ ; (c)  $\theta = 10^\circ$ ; (d)  $\theta = 0^\circ$ .

denotes the assembling operation, and  $\delta_1$  and  $\delta_2$  are tolerances of the convergence.

For the numerical implementation, a program was developed in C++. In this section, two numerical examples are simulated to verify the accuracy, stability, and practicability of the proposed approach.

**4.1. Example 1: Uniaxial Tension and Compression.** Simple uniaxial tension and compression examples are simulated to verify the accuracy of the constitutive laws. Because of the perfect elastoplasticity of the nonassociated Drucker–Prager model, we apply a displacement  $u_z$  on the body to avoid nonconvergence, as shown in Figure 4. A kind of dolomite is chosen in the example. The material parameters are Young's modulus  $E = 0.5 \times 10^5$  MPa, Poisson's ratio  $\nu = 0.33$ , cohesion  $c = 30$  MPa, internal friction angle  $\phi = 40^\circ$ , and dilatancy angle  $\theta = 20^\circ$ .

**4.1.1. Constitutive Curves.** The constitutive cone of the nonassociated Drucker–Prager model has been introduced in Section 2, and the theoretical cone  $K_\sigma$  is shown in Figure 1(a). In Figure 5, the solid line stands for the simulated results and the dashed line represents the boundary of the stress cone. At the coordinate  $\|s\|/k_d - s_m$ , the simulation curves of compression and tension are shown in Figure 5. By comparing the numerical curve with the theoretical one, it appears obvious that the elastic parts are both in the cone  $K_\sigma$  and that the plastic parts are on the boundary of  $K_\sigma$ . This shows that the simulation satisfies the constitutive law of the nonassociated Drucker–Prager model.

Furthermore, dilatancy is a special property in rock-soils. Associated flow rule leads to a nonnegligible volume expansion after the model enters a plastic stage. However, using a nonassociated flow rule is suitable to control the dilated value. Figure 6 shows the volume expansion under compression/tension with different dilatancy angles. The

constitutive simulation reveals the requirements of soil dilatancy.

Dilatancy angle influences the constitutive curves. Figure 7 shows the results for different dilatancy angles at the equivalent stress  $\sigma^{eq}$  and the equivalent strain  $\varepsilon^{eq}$ . From Figure 7(a), the trends of the curves conform to the characteristic of perfect elastoplasticity. Maximum stress value increases as the dilatancy angle escalates. From Figure 7(b), we can see that the limit stress also increases slightly with a greater dilatancy angle. What is more, a softening phenomenon can be observed when the loading begins. The results satisfy the consequence in [24].

**4.1.2. Limit Stress Analysis.** In numerical fields, the explicit algorithm introduced in [30] is a typical method for simulating the nonassociated models. The return mapping algorithm is widely used in the simulation of materials constitutive laws [1]. Both methods need the detailed expressions of the yield and the plastic potential functions. In this work, the two potential functions are defined by the yield potential  $F = (\sin \phi / \sqrt{3} \sqrt{3 + \sin^2 \phi_1}) I_1 + \sqrt{J_2} - (\sqrt{3} \cos \phi / \sqrt{3 + \sin^2 \phi})$  and the plastic potential  $Q = (\sin \phi / \sqrt{3} \sqrt{3 + \sin^2 \phi_2}) I_1 + \sqrt{J_2} - (\sqrt{3} \cos \theta / \sqrt{3 + \sin^2 \theta})$ . When  $\phi = \theta$ , the plastic potential  $Q$  equals  $F$ . Therefore, the model is associated. What is more, the literature [31] gives us the analytical equivalent stress under uniaxial compression and tension loadings. Therefore, Figure 8 gives the comparison between the bipotential, explicit, Simo–Taylor, and the theoretical value.

Figure 8 displays the comparison of 4 algorithms on the compression and tension example for various dilatancy angles for stress-displacement. We limit such curves to 100 steps. As shown in Figure 8(a), if the material is associated and if the transition parts from elasticity to plasticity are neglected, theoretical results are properly satisfied by three methods. As illustrated in Figure 8(b) and Figure 8(c), when the dilatancy angle decreases to 0 degrees, the bipotential results are still satisfying. The error between the return mapping algorithm and the analytical result is smaller than 3.04%. The explicit simulation has a slight oscillation. In Figure 8(d), we note that the peak stress for the three methods is nearly the same as those of the analytical results when the material is associated. From Figures 8(e) and 8(f), we remark that the peak stress calculated by the bipotential method satisfies the theoretical value when the dilatancy angle decreases. The peak value that the return mapping algorithm returns is 5.03% smaller than the analytical one. The result of the explicit algorithm displays oscillations and nonconvergence. From the analysis above, the bipotential algorithm is more accurate and stable in dealing with the nonassociated Drucker–Prager model.

**4.2. Example 2: The Effect of Deep Footing.** Deep footing is a kind of structure foundation that is widely used in civil engineering. A plane strain model is used in this example. The geometry of soils under deep footing is shown in Figure 9(a), where  $l = 100$  m,  $h = 50$  m,  $a = 12.5$  m, and  $b = 12.5$  m. The mesh contains 1289 nodes and 608 6-node triangle elements,

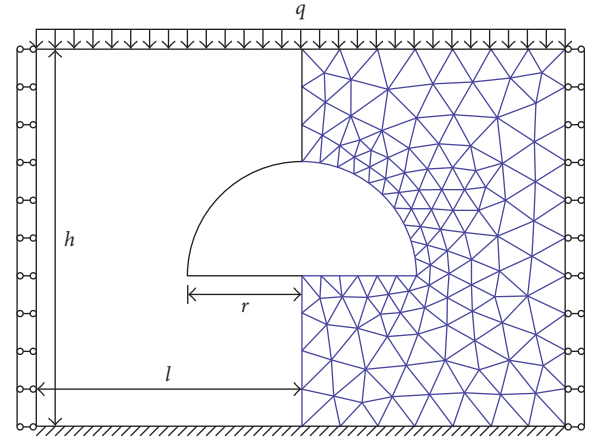


FIGURE 11: Geometry and mesh for the tunnel example.

as shown in Figure 9(b). A uniform pressure  $q = 16.0$  kN/m<sup>2</sup> is applied on the surface of the foundation trench to equivalently represent the loading of the deep footing. Soil parameters are Young's modulus  $E = 2.5 \times 10^6$  kPa, Poisson's ratio  $\nu = 0.33$ , soil cohesion  $c = 2$  kPa, internal friction angle  $\phi = 30^\circ$ , and a dilatancy angle of  $\theta = 20^\circ$ .

Soil mass failure happens when the plastic band generates. Although, in this example, only a small deformation case is considered, the slip bands can still be observed. Here, we study the influence of different dilatancy angles for the slip bands. By locking the maximum plastic strain at  $\varepsilon^p = 0.01\%$ , the slip bands can be expressed by the contour plot of the plastic strain. Under the same value of pressure  $q = 10.24$  kN, the slip band zones for varying dilatancy angles are illustrated in Figure 10. We note that with the increase of the nonassociated property, the slip band becomes more distinct, which means that the phenomenon of soil mass failure becomes more evident. In other words, when the dilatancy angle decreases, the soil around the deep footing slides easier. This satisfies the results from the typical landslide theory of soils mechanics [5].

**4.3. Example 3: Modeling of the Ground Surrounding a Tunnel.** This example is concerned by modeling the ground surrounding a tunnel in its cross section. The mesh contains 498 nodes and 225 6-node triangle elements. Both the geometry and the mesh are shown in Figure 11. In Figure 11,  $l = 14$  m,  $h = 20$  m, and  $r = 6$  m. The parameters of the ground are  $E = 30,000$  kN/m<sup>2</sup>,  $\nu = 0.3$ ,  $c = 10$  kN/m<sup>2</sup>, and  $\phi = 20^\circ$ . A uniform pressure  $q = 10$  kN/m<sup>2</sup> is given on the surface of the ground. The von Mises stress distribution is plotted in Figure 12.

Comparing for different dilatancy angles, Figure 13 gives the vertical displacement  $U_y$  curves for the top of the tunnel, and the horizontal displacement  $U_x$  curves for the bottom edge of the tunnel.

It can be observed that when the dilatancy angle increases,  $U_x$  increases slightly as well, and  $U_y$  decreases accordingly. In other words, the larger the  $\theta$  is, the stiffer the ground is. This is in accordance with what happens in reality for tunnel engineering [32]. Therefore, it is possible to apply the proposed numerical strategy in civil engineering.

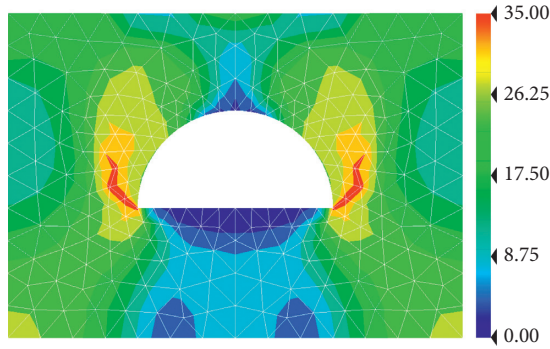
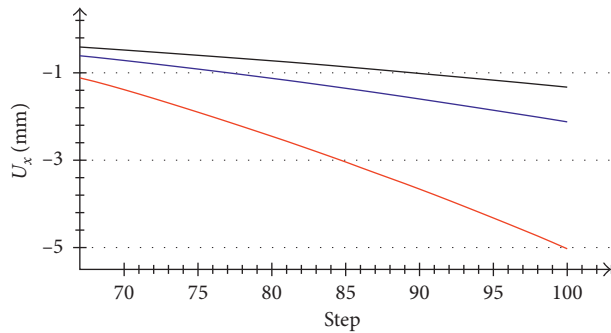
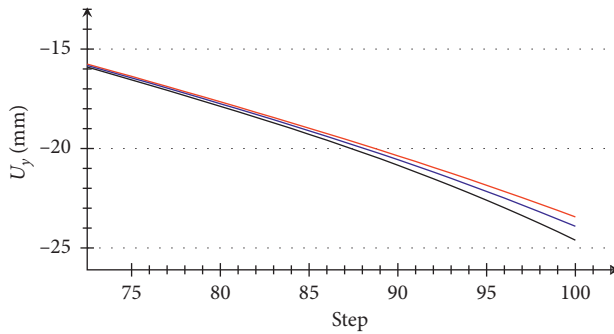


FIGURE 12: von Mises stress.



Value of  $\theta$   
 — 20  
 — 10  
 — 0

(a)



Value of  $\theta$   
 — 20  
 — 10  
 — 0

(b)

FIGURE 13: Displacements of the tunnel with different dilatancy angles: (a) vertical displacement  $U_y$  at the top of the tunnel; (b) horizontal displacement  $U_x$  at the bottom edge of the tunnel.

## 5. Conclusion

In this paper, we have proposed a numerical strategy to simulate the behavior of nonassociated materials. From numerical experiments, we have found the following:

- (i) In the simple uniaxial tensile/compressive loading example, the simulated constitutive cones coincide

with the theoretical ones as well as the constitutive curves.

- (ii) The volume expansion of the material after plasticification can be controlled by dilatancy angles.
- (iii) From the comparisons of stress-displacement curves calculated with different algorithms, the bipotential method proved to be more stable and more accurate.
- (iv) In the deep footing example, slip bands with varying dilatancy angles are compared. When the dilatancy angle decreases, the soil around the deep footing slides easier. The practicability of the bipotential algorithm in civil engineering was therefore verified.
- (v) The von Mises stress and displacements of the ground surrounding a tunnel were properly predicted.

As a conclusion, the proposed strategy is well suited to study the nonassociated Drucker–Prager model, and the developed program is possible to be applied in civil engineering.

## Conflicts of Interest

The authors declare that all funding programmes do not lead to any conflict of interests regarding the publication of the paper.

## Acknowledgments

The authors gratefully acknowledge the financial support of the National Natural Science Foundation of China (Grant no. 11772274) and the National Key R&D Program of China (Grant no. 2017YFB0703200).

## References

- [1] J. C. Simo and R. L. Taylor, “Consistent tangent operators for rate-independent elastoplasticity,” *Computer Methods in Applied Mechanics and Engineering*, vol. 48, no. 1, pp. 101–118, 1985.
- [2] R. I. Borja, *Plasticity: Modeling & Computation*, Springer Science & Business Media, Berlin, Germany, 2013.
- [3] J. L. Chaboche, “A review of some plasticity and viscoplasticity constitutive theories,” *International Journal of Plasticity*, vol. 24, no. 10, pp. 1642–1693, 2008.
- [4] J. C. Simo and T. J. R. Hughes, *Computational Inelasticity*, Springer-Verlag, Berlin, Germany, 2008.
- [5] K. Terzaghi, R. B. Peck, and G. Mesri, *Soil Mechanics in Engineering Practice*, John Wiley & Sons, Hoboken, NJ, USA, 1996.
- [6] G. de Saxcé and Z. Q. Feng, “New inequality and functional for contact with friction: the implicit standard material approach,” *Mechanics of Structures and Machines*, vol. 19, no. 3, pp. 301–325, 1991.
- [7] Y. Sun, Y. Gao, and Q. Zhu, “Fractional order plasticity modelling of state-dependent behaviour of granular soils without using plastic potential,” *International Journal of Plasticity*, vol. 102, pp. 53–69, 2018.
- [8] Y. Sun and Y. Shen, “Constitutive model of granular soils using fractional-order plastic-flow rule,” *International Journal of Geomechanics*, vol. 17, no. 8, p. 4017025, 2017.

- [9] W. Fenchel and D. W. Blackett, *Convex Cones, Sets, and Functions, Logistics Research Project*, Princeton University, Department of Mathematics, Princeton, NJ, USA, 1953.
- [10] G. de Saxcé, "A generalization of Fenchels inequality and its applications to the constitutive laws," *Comptes Rendus de l'Academie des Sciences Serie I*, vol. 314, no. 2, pp. 125–129, 1992.
- [11] G. de Saxcé, "The bipotential method, a new variational and numerical treatment of the dissipative laws of materials," in *Proceedings of 10th International Conference on Mathematical and Computer Modelling and Scientific Computing*, Boston, MA, USA, 1995.
- [12] G. de Saxcé and L. Bousshine, "Limit analysis theorems for implicit standard materials: application to the unilateral contact with dry friction and the non-associated flow rules in soils and rocks," *International Journal of Mechanical Sciences*, vol. 40, no. 4, pp. 387–398, 1998.
- [13] Z. Q. Feng, "2D or 3D frictional contact algorithms and applications in a large deformation context," *Communications in Numerical Methods in Engineering*, vol. 11, no. 5, pp. 409–416, 1995.
- [14] G. de Saxcé and Z. Q. Feng, "The bipotential method: a constructive approach to design the complete contact law with friction and improved numerical algorithms," *Mathematical and Computer Modelling*, vol. 28, no. 4–8, pp. 225–245, 1998.
- [15] P. Joli and Z. Q. Feng, "Uzawa and Newton algorithms to solve frictional contact problems within the bipotential framework," *International Journal for Numerical Methods in Engineering*, vol. 73, no. 3, pp. 317–330, 2008.
- [16] Z. Q. Feng, F. Peyraut, and Q. C. He, "Finite deformations of Ogden's materials under impact loading," *International Journal of Non-Linear Mechanics*, vol. 41, no. 4, pp. 575–585, 2006.
- [17] M. Hjjaj, Z. Q. Feng, G. de Saxcé, and Z. Mroz, "On the modelling of complex anisotropic frictional contact laws," *International Journal of Engineering Science*, vol. 42, no. 10, pp. 1013–1034, 2004.
- [18] Z. Q. Feng, C. Vallée, D. Fortuné, and F. Peyraut, "The 3é hyperelastic model applied to the modeling of 3d impact problems," *Finite Elements in Analysis and Design*, vol. 43, no. 1, pp. 51–58, 2006.
- [19] G. Bodovillé and G. de Saxcé, "Plasticity with non-linear kinematic hardening: modelling and shakedown analysis by the bipotential approach," *European Journal of Mechanics-A/Solids*, vol. 20, no. 1, pp. 99–112, 2001.
- [20] C. Bouby, G. de Saxcé, and J. B. Tritsch, "A comparison between analytical calculations of the shakedown load by the bipotential approach and step-by-step computations for elastoplastic materials with nonlinear kinematic hardening," *International Journal of Solids and Structures*, vol. 43, no. 9, pp. 2670–2692, 2006.
- [21] A. Chaaba, L. Bousshine, and G. de Saxcé, "Kinematic limit analysis of nonassociated perfectly plastic material by the bipotential approach and finite element method," *Journal of Applied Mechanics*, vol. 77, no. 3, p. 031016, 2010.
- [22] Y. J. Zhou, Z. Q. Feng, and P. Ning, "The bi-potential theory applied to non-associated constitutive laws," *Applied Mathematics and Mechanics*, vol. 36, no. 8, pp. 787–804, 2015, in Chinese.
- [23] L. Cheng, Y. Jia, A. Oueslati, and G. de Saxcé, "Plastic limit state of the hollow sphere model with non-associated Drucker–Prager material under isotropic loading," *Computational Materials Science*, vol. 62, pp. 210–215, 2012.
- [24] L. Bousshine, A. Chaaba, and G. de Saxcé, "Softening in stress–strain curve for Drucker–Prager non-associated plasticity," *International Journal of Plasticity*, vol. 17, no. 1, pp. 21–46, 2001.
- [25] M. Hjjaj, J. Fortin, and G. de Saxcé, "A complete stress update algorithm for the non-associated Drucker–Prager model including treatment of the apex," *International Journal of Engineering Science*, vol. 41, no. 10, pp. 1109–1143, 2003.
- [26] A. Berga, "Mathematical and numerical modeling of the non-associated plasticity of soils—part 1: the boundary value problem," *International Journal of Non-Linear Mechanics*, vol. 47, no. 1, pp. 26–35, 2012.
- [27] A. Berga, "Mathematical and numerical modeling of the non-associated plasticity of soils—part 2: finite element analysis," *International Journal of Non-Linear Mechanics*, vol. 47, no. 1, pp. 36–45, 2012.
- [28] Y. J. Zhou, Z. Q. Feng, and W. Y. Xu, "Non-associated constitutive law of soils and its simulation based on the bi-potential theory," *International Journal of Structural Analysis & Design*, vol. 1, no. 4, pp. 1–6, 2014.
- [29] D. C. Drucker and W. Prager, "Soil mechanics and plasticity analysis of limit design," *Quarterly of Applied Mathematics*, vol. 10, no. 2, pp. 157–165, 1952.
- [30] M. Ortiz and E. P. Popov, "Accuracy and stability of integration algorithms for elastoplastic constitutive relations," *International Journal for Numerical Methods in Engineering*, vol. 21, no. 9, pp. 1561–1576, 1985.
- [31] O. Kristensson and A. Ahadi, "Numerical study of localization in soil systems," *Communications in Numerical Methods in Engineering*, vol. 32, no. 8, pp. 600–612, 2005.
- [32] N. Barton, R. Lien, and J. Lunde, "Engineering classification of rock masses for the design of tunnel support," *Rock Mechanics*, vol. 6, no. 4, pp. 189–236, 1974.

## Research Article

# Pavement Analysis and Design by Multiphysics Reconstructing Algorithm for the Virtual Asphalt Mixture Based on the Discrete-Element Method

Danhua Wang,<sup>1</sup> Xunhao Ding<sup>1</sup>,<sup>2</sup> Tao Ma<sup>1</sup>,<sup>2</sup> Weiguang Zhang,<sup>2</sup> and Deyu Zhang<sup>3</sup>

<sup>1</sup>School of Computer Engineering, Nanjing Institute of Technology, Nanjing, Jiangsu 211167, China

<sup>2</sup>School of Transportation, Southeast University, 2 Sipailou, Nanjing, Jiangsu 210096, China

<sup>3</sup>School of Engineering and Architecture, Nanjing Institute of Technology, Nanjing, Jiangsu 211167, China

Correspondence should be addressed to Tao Ma; [matao@seu.edu.cn](mailto:matao@seu.edu.cn)

Received 26 February 2018; Accepted 8 April 2018; Published 7 May 2018

Academic Editor: Fan Gu

Copyright © 2018 Danhua Wang et al. This is an open access article distributed under the Creative Commons Attribution License, which permits unrestricted use, distribution, and reproduction in any medium, provided the original work is properly cited.

Based on the Particle Flow Code in Two dimensions (PFC2D), an algorithm for modeling the two-dimensional virtual asphalt mixture was proposed in this study. By combining the AIMS scanning technology (Aggregate Imaging Measurement System) with the designed stochastic algorithm, the virtual coarse aggregates could be generated rapidly and precisely. Different from the conventional methods, the contour shapes of the coarse aggregates were rebuilt only to balance the shape modeling precision and simulation efficiency. Then by distributing the coarse particles within container, virtual skeletons were formed firstly. An innovate algorithm was proposed afterwards to distinguish the external and internal area of the coarse aggregates and then model the mastic part by filling the irregular hollow shape with uniformly arranged balls. By deleting the mastic balls randomly, the voids were reconstructed consistent with the actual ratio. In the end, the virtual uniaxial compressive tests of AC-16 were simulated within PFC2D and the dynamic modulus at different load frequencies was predicted. The results indicated that the proposed algorithm could not only model the asphalt mixture precisely but also characterized its mechanical behavior as well.

## 1. Introduction

Asphalt mixtures are three-phase structures consisting of aggregates, asphalt binder, and air voids. It has been highlighted by many researchers that the mechanical performance of asphalt mixture was influenced by its heterogeneous components significantly [1–7]. Tests conducted by Liu and Dai [8] focused on the gradation influence on the rut resistance of the asphalt mixtures. The results showed that based on the Superpave Gyrotory Compactors (SGC), the optimum asphalt content is lower 0.2%~0.5% than the one by the Marshall method. As the aggregate size increased, the mixtures could have larger resistance compared to the smaller particles. Similar results were also concluded based on the studies of Coleri et al. [9] and Gokhale et al., respectively [10]. Focusing on the aggregate degradation during compaction, several designed tests were carried out

by Airey et al. [11] to reveal the inner mechanism. In their tests, two asphalt mixtures including a continuous and gap-graded gradation were compacted and compared. The results indicated that gap-graded asphalt mixture was degraded more easily compared to the continuously grade mixture. Isailović et al. [12] pointed out that asphalt ageing played an important role in reducing the effects of material recovery based on fatigue tests. In addition, the mixtures prepared with additionally 0.5% of bitumen by mass showed the best recovery characteristics compared to others. The void effects on fatigue life of asphalt mixture were analyzed by Hasan and Ahmad in early 1973 [13]. The voids within mixtures were varied by the changes of asphalt content and aggregate gradation. The fatigue response of different mixtures was investigated showing the important roles the voids played in. Apart from the fatigue performance, the rutting-resistance, moisture damage-resistance, and strength of asphalt mixture

would also be influenced by air void, which was founded by some researchers [14, 15]. Current design methods for asphalt mixtures mostly focused on the volumetric properties (aggregate gradation, asphalt content, and void) and paid little attention on the morphological characteristics of the components which were really hard to investigate just by laboratory apparatus. It is believed that, apart from the volumetric properties, the shapes of the inner components, especially the aggregates, indeed have impact on the properties of asphalt mixtures as well [16–18].

As an effective numerical technology, the Discrete-Element Method (DEM) was proposed by Cundall [19], and then a software named as Particle Flow Code (PFC) was developed to help the mechanical calculation of heterogeneous materials, which has been widely used in many fields [20, 21]. Not only the macromechanical behavior but also the microresponse of the asphalt mixtures could be predicted based on the PFC, and many virtual tests were conducted under complex conditions for various goals by some researchers [22–24]. However, prior to simulations, it is significantly important to develop the precise virtual models based on their volumetric and shape property which is a guarantee for the results validations [25]. Thus, many methods were proposed for heterogeneous component reconstitution within asphalt mixtures which fell into two categories in general. One is the random model and another is the image-based models. The random models tended to develop the virtual particles by some designed stochastic algorithm. By changing the control parameters related to shapes and sizes, a large number of the simplified virtual shapes could be developed rapidly. Such methods were proposed by Lu and Mcdowell [25], Das et al. [26], and Zhang et al. [27]. In Lu and Mcdowell's studies, the virtual particles were modeled by the overlapping balls [25], and the modeling algorithm was optimized further by Das et al. [26]. Coarse aggregates were assumed to be hexahedrons, pentahedrons, and tetrahedrons by Zhang et al. [27]. By cutting the particle clumps randomly with the help of three variables, the irregular shape was rebuilt preliminarily which was roughly consistent with the realistic ones. The random models for virtual particles could be generated in larger amounts quickly without preparing specimens in laboratory. Although it was performed with better efficiency compared to the image-based models, the shape modeling was not precise enough with excessive simplifications. The image-based models are mostly generated with the help of the X-ray computed tomography (CT) scanning technology [28]. By processing the component images from the scanning, the heterogeneous materials could be reconstructed within PFC precisely. Such methods were introduced and utilized in some studies [29–33]. However, the use of the image-based models are limited by the test environments and conditions which is a barrier preventing the virtual modeling to be conducted efficiently. First, a scanning device is must which provides the fundamental images. Second, when rebuilding image-based models, test specimens should be developed for scanning in advance. Therefore, it is time-consuming and cannot meet the needs of large amount simulation tasks. Thus, further studies are needed to optimize the particle

modeling which can be generated in quantities rapidly and maintain the realistic shapes at the same time.

## 2. Objective and Scope

The objective of this study is to rebuild the virtual asphalt mixtures rapidly and precisely based on the Discrete-Element Method (DEM). To achieve this, with the help of AIMS scanning technology, an algorithm was designed for modeling coarse aggregates, asphalt mastic, and voids. The relevant issues include the shape and size measurements through AIMS, irregular particle reconstitution derived from the standard virtual aggregates, asphalt mastic generation by irregular area judgments, random voids modeling, and the mechanical behavior prediction.

## 3. Shape Measurement through Scanning

The AIMS apparatus was utilized to record the particle shapes including the angularity index and size index. While scanning the samples, coarse aggregates should be put into slots of designed trays. With the trays rotated slowly, each particle would go through the scanning area, and a digital camera was set to capture their features. Shape properties of particles were calculated and stored and could be output for the virtual modeling within PFC2D. The related shape measurements are introduced as follows.

**3.1. Angularity Index.** Angularity index applies to coarse aggregate sizes and describes variations at the particle boundary that influence the overall shape. The angularity index quantifies changes along a particle boundary with higher gradient values indicating a more angular shape. Angularity index has a relative scale of 0 to 10000 with a perfect circle having a small nonzero value as shown in Figure 1. The angularity index is analyzed by quantifying the change in the gradient on a particle boundary and is related to the sharpness of the corners of 2-dimensional images of aggregate particles as shown in the following equation:

$$GA = \frac{1}{(n/3) - 1} \sum_{i=1}^{n-3} |\theta_i - \theta_{i+3}|, \quad (1)$$

where  $\theta$  is the angle of orientation of the edge points;  $n$  is the total number of points; and subscript  $i$  denotes the  $i$ th point on the edge of the particle.

**3.2. Size Index.** The particle's shortest, intermediate, and longest lengths are measured to describe the size characteristics as shown in Figure 2. The value  $L$  is the particle's longest length representing the largest size in all the directions. And the particle's intermediate length  $w$  is the largest size in the planes perpendicular to the particle's longest length. The particle's shortest length  $t$  is the largest size of the planes perpendicular to the particle's longest and intermediate lengths at the same time.

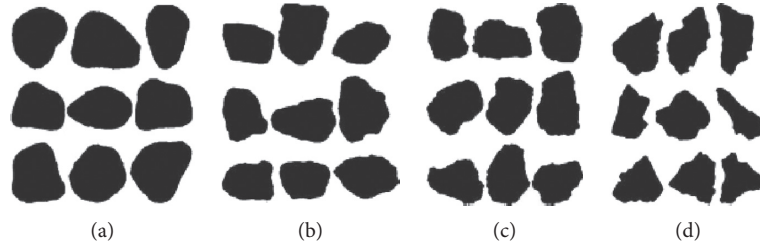


FIGURE 1: Angularity index for various shapes. (a)  $0 \leq \text{low} \leq 2100$ ; (b)  $2100 < \text{moderate} \leq 3975$ ; (c)  $3975 < \text{high} \leq 5400$ ; (d)  $5400 < \text{extreme} \leq 10000$ .

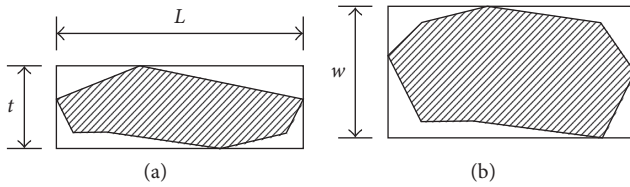


FIGURE 2: Size index for aggregate particles. (a) Side view; (b) top view.

#### 4. Algorithm for Developing Virtual Coarse Aggregates

**4.1. Standard Particles Generations.** The virtual coarse aggregates were rebuilt within PFC2D as shown in Figure 3. It is noted that with the goal of developing virtual specimen rapidly and randomly, not all the particles in actual mixtures should be scanned which would consume excessive time. It is meaningful to conduct simulations by generating representative virtual particles with enough irregular shapes. Thus, as an effective mean, when conducting other simulations, the representative virtual particles can be generated rapidly without scanning the components again.

As shown in (1), it is known that the angularity index quantifies changes along a particle boundary regardless of its size. Thus, shapes were modeled firstly without size variations. Enough coarse aggregates were selected firstly for rebuilding the standard particles with their intermediate lengths  $w$  (defined as the minimum sieve size that the particle is able to pass) converted to 19 mm compulsively. And the areas of all the adjusted particles were measured. Then, the particles of other sizes were derived from the standard ones by size adjustments. While generating the standard particles, the selected samples for particle reconstitution should have a large angularity index range from 1000 to 6500 which most realistic aggregates are distributed in. Then, the shape images were processed by filtering the redundant black pixels. Only some key black pixels in the shape contour were retained and then were imported to the PFC2D. The key black pixels could describe the boundary changes and capture the main properties of the irregular shapes. By generating balls in the positions of the retained pixels, the virtual particles could be developed as a rigid body through the input Fish command “clump,” as shown in Figure 3. 27 particles with various angular shapes were rebuilt by the proposed

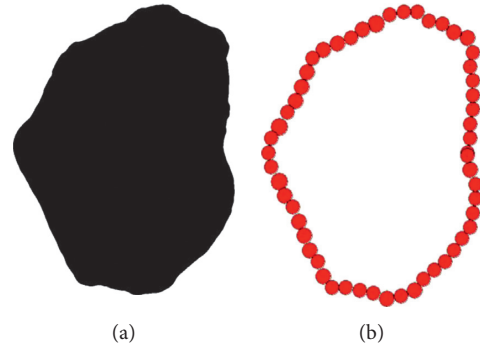


FIGURE 3: Rebuilding virtual particles by filling contours with balls.

methods. More angular shapes could also be modeled in the same way depending on the simulation needs but were not included here. Since it is very time-consuming to rebuild each particle in reality, the representative shape modeling, as a more efficient mean, could save time and develop virtual mixtures rapidly. In this study, the following proposed algorithm was introduced emphatically.

Assumptions were made that there was no fracture or break of virtual particles; thus, the inner balls of the virtual particles could be released which could conduct the simulations more effectively. The particle surfaces would bear the contact force and were simulated by the contour balls as shown in Figure 3. Compared to the solid virtual particles, the mass of the proposed methods was smaller than the reality and should be calibrated for all virtual particles as in the following equation.

$$p_2 = p_1 \times \frac{m \times \pi \times r^2}{n \times \pi \times (0.5/k)^2} = p_1 \times 4 \times \frac{m \times (rk)^2}{n}, \quad (2)$$

where  $p_2$  is the calibrated density ( $\text{g}/\text{cm}^3$ ),  $p_1$  is the initial density ( $\text{g}/\text{cm}^3$ ),  $m$  is the number of retained pixels,  $n$  is the number of all the pixels in Figure 1(a),  $k$  is the scaling ratio in image processing, and  $r$  is the radius of the ball located in the contour (mm).

**4.2. Particle Size Adjustments.** Each standard particle was coded and saved as an executable file. When generations started, corresponding code files were evoked and executed by PFC2D. To model the size variations, a designed controls parameter known as  $S_r$  were embedded in the code files, as shown in Table 1. As shown, the size ratio is defined as the intermediate length ratio between the other grade aggregates

TABLE 1: Size adjustments for simulations.

Size (mm)	Size ratio	Controls parameter	Size (mm)	Size ratio	Controls parameter
19	1	1	13.2–16	$\left(\frac{13.2}{19}, \frac{16}{19}\right)$	$\frac{13.2}{19} + \left(\frac{16}{19} - \frac{13.2}{19}\right) \times \text{urand}$
19–25	$\left(1, \frac{25}{19}\right)$	$1 + \left(\frac{25}{19} - 1\right) \times \text{urand}$	9.5–13.2	$\left(\frac{9.5}{19}, \frac{13.2}{19}\right)$	$\frac{9.5}{19} + \left(\frac{13.2}{19} - \frac{9.5}{19}\right) \times \text{urand}$
16–19	$\left(\frac{16}{19}, 1\right)$	$\frac{16}{19} + \left(1 - \frac{16}{19}\right) \times \text{urand}$	4.75–9.5	$\left(\frac{4.75}{19}, \frac{9.5}{19}\right)$	$\frac{4.75}{19} + \left(\frac{9.5}{19} - \frac{4.75}{19}\right) \times \text{urand}$

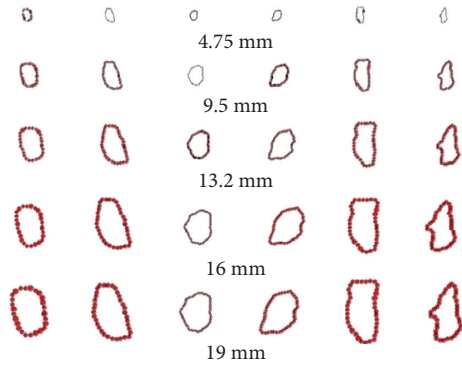


FIGURE 4: Virtual size reconstitutions based on standard particles.

and the standard ones. And the size ratios of each grade aggregates were coded with the help of the input “urand” value which was drawn from the uniform distribution  $U(0, 1)$  within PFC2D. Before the code files were evoked, the  $S_r$  was determined randomly by the system leading to the size generations. Moreover, the areas of different grades were adjusted together by multiplying the standard particle area with their size ratio squared.

Figure 4 shows the virtual size reconstitutions based on standard particles. As shown, the standard particles with 19 mm intermediate lengths were developed firstly, and then the others were derived from the standard ones with same angular shapes. By this way, 135 virtual particles with 27 angular shapes of 5 different grades were developed rapidly.

**4.3. Coarse Particles Distribution within Mixture.** The virtual asphalt mixtures were developed in 3 steps: the coarse aggregate generation, the asphalt mastic filling, and the voids modeling. It is unpractical to rebuild all the particles' shapes especially the numerous finer aggregates, which will exceed the computer capacity limitations. On the other side, the shape influences of the finer aggregates are not obvious to some extent compared to the coarse parts. So the major assumptions are made that the aggregates finer than 4.75 mm are regarded as the part of the asphalt mastic and are modeled by round balls directly within PFC2D.

Coarse aggregates were distributed randomly within the container area. The gradations of particles and the asphalt content were calculated and converted to mapping area in two dimensions. The mapping area of different grades particles were taken as control values which determined the end time of coarse aggregate generations. The coarse aggregates distributions were conducted as follows:

- (1) Determine the size of the virtual container and develop corresponding walls to model the boundary conditions.
- (2) Start the coarse particles generation with the size ranging from 16 mm to 19 mm. The virtual particles are generated one by one and the shape is selected randomly by executing the particle code files.
- (3) Develop three variables known as  $x^1$ ,  $y^1$ , and  $\text{rot}$  which is calculated as shown in (3). These three variables are all drawn from the uniform distribution with different ranges. Before a virtual particle is generated,  $x^1$ ,  $y^1$ , and  $\text{rot}$  embedded in the code files are determined randomly. And then the local coordinate system (coordinate system of particles) is converted to a global coordinate system (coordinate system of container). By using the random values of  $x^1$ ,  $y^1$ , and  $\text{rot}$ , the coarse particles can be generated at a random position within the container area.

$$\begin{aligned}
 x^1 &= U(0, x^w), \\
 y^1 &= U(0, y^h), \\
 \text{rot} &= U(0, 2\pi),
 \end{aligned} \tag{3}$$

where  $x^1$  and  $y^1$  are the random  $x$ - and  $y$ -coordinates of the initial positions, respectively;  $\text{rot}$  is the random angle of the generated particles.  $x^w$  and  $y^h$  are the width and height of the virtual containers.

- (4) Check the overlap of the generated particles. Since the particles are generated within container area one by one. So when a particle has been generated at a random position, it is necessary to check if it is overlapped with the others. If there is no overlap, the particle can be generated, else, change  $x^1$ ,  $y^1$ , and  $\text{rot}$  until the particle can be generated correctly;
- (5) Start to generate the next particle by cycling from step 2 to 4 until reach the required mapping area of 16–19 mm particles.

By the steps from 1 to 5, the virtual particles with the size ranging from 16 mm to 19 mm could be developed successfully. Then similar processes were carried out for the particles of other grades as shown in Figure 5. To distribute the different grades particles correctly, the particles with largest sizes should be generated first and then the smaller ones. For example, start the particle generation of 16–19 mm firstly, and then followed by 13.2–16 mm, 9.5–13.2 mm, and 4.75–9.5 mm in turns.

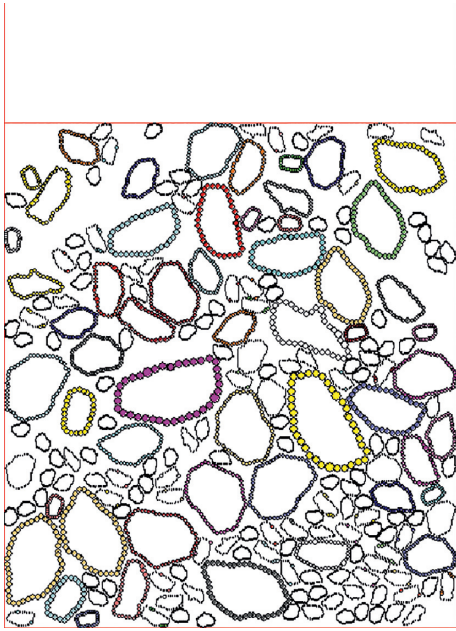


FIGURE 5: Coarse particles distributions within the virtual container.

### 5. Algorithm for Developing Asphalt Mixture

5.1. *Asphalt Mastic Modeling.* The asphalt mastic was modeled by the uniform arranged balls with a diameter of 0.001 m. As common practices, the conventional methods tended to fill the particle external area with finer balls (mastic part) by judging if there are balls already [27]. Because the virtual particles in conventional methods were filled with balls (solid shape), the external and internal areas of the particle could be distinguished easily by balls judgments. However, it is hard in the mastic balls directly when it comes to the coarse aggregate skeleton developed in this study, as shown in Figure 5. The differences were not obvious between the external and internal particle areas which were all irregular in shape. To fill the irregular hollow shape (particle external area) with balls and ignore the particle internal area, the algorithm for the asphalt mastic was introduced as followed.

- (1) Measure the size of total specimens to get all the coordinate values which are prepared for filling judgments.
- (2) Develop two parameters known as  $k_{right}$  and  $k_{left}$  to record the position properties. They are all set zero initially. Then check all the coordinate values from left to right and bottom to top in turns. The positions will fall into four categories as shown in Figures 6–9. Before a group of coordinate values is checked, two parallel control lines are utilized with a 0.001 m interval (diameter of the mastic ball). Check the two sides of the position and find the nearest entities (walls and particle balls without mastic balls generated already) between two control lines as follows. The control lines were not real lines plotted in the images but a designed routine coded in MATLAB to help the distance judgments.

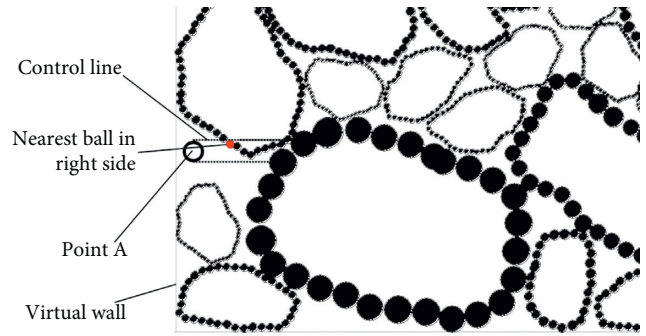


FIGURE 6: Distinguishing the position of mastic balls between the particle clump and the wall on the left side.

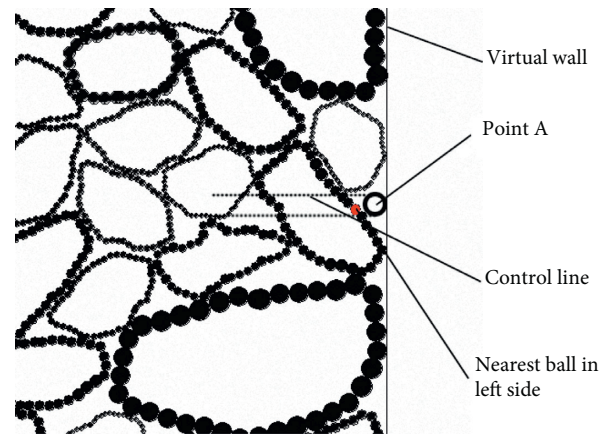


FIGURE 7: Distinguishing the position of mastic balls between the particle clump and the wall on the right side.

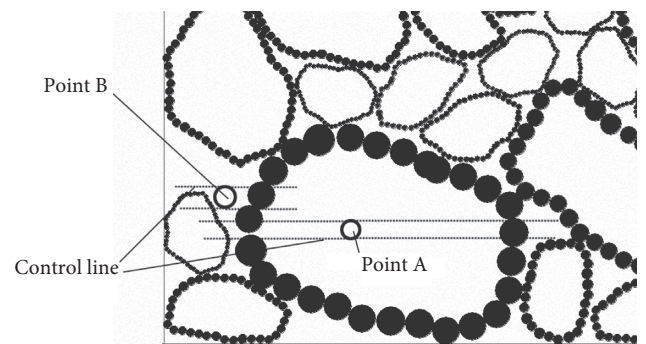


FIGURE 8: Distinguishing the position of mastic balls between two particle clumps (inside or outside the aggregates).

- (1) If there is a nearest particle ball in the right side, convert  $k_{right}$  from 0 to 1, else,  $k_{right}$  is still equal to 0.
- (2) If there is a nearest particle ball in left side, convert  $k_{left}$  from 0 to 1, else,  $k_{left}$  is still equal to 0.

Then the external and internal area of the particles can be distinguished by the combination of  $k_{right}$  and  $k_{left}$ . If  $k_{right}$  and  $k_{left}$  are equal to 1 and 0, respectively, the position is between the particle clump and the left wall as shown in

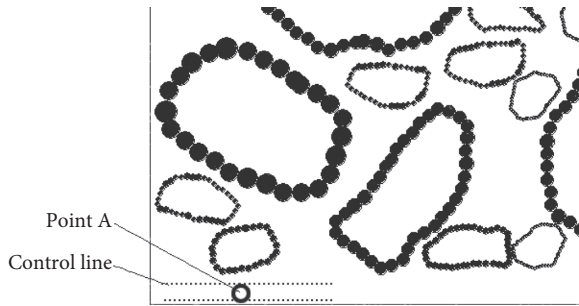


FIGURE 9: Distinguishing the position of mastic balls without any entities nearby in two sides.

Figure 6. Then the coordinate value is effective, and a mastic ball with the diameter of 0.001 m is generated here.

If  $k_{\text{right}}$  and  $k_{\text{left}}$  are equal to 0 and 1, respectively, the position is between the particle clump and the right wall as shown in Figure 7. Then the coordinate value is effective, and a mastic ball with the diameter of 0.001 m is generated here as well.

If  $k_{\text{right}}$  and  $k_{\text{left}}$  are equal to 1 and 1, respectively, two conditions should be analyzed, as shown in Figure 8. As shown, the points A and B are between two particle clumps with same  $k_{\text{right}}$  and  $k_{\text{left}}$ . The point A is inside the aggregates while B is outside the model between two different particles. In this condition, the nearest particle balls on both sides were analyzed further. With the help of the command pointer, the clump id of all the balls can be read and recognized. So comparing the clump id of the nearest balls, it is easy to determine whether the nearest balls belong to a same clump. If the clump id of two balls is equal, they come from the same particle clump. Otherwise, they belong to a different particle clump. Thus, if the nearest balls on left and right sides belong to a same particle clump, as the point A shown in Figure 8, the coordinate value is noneffective without any mastic balls generated here. When the nearest balls belong to different clumps, a mastic ball should be generated.

A specific condition should also be included as shown in Figure 9 due to the space between coarse aggregates.  $k_{\text{right}}$  and  $k_{\text{left}}$  are 0 and 0, respectively, when the space is enough among particles. When comes to this condition, mastic balls should also be generated. Following the proposed rules and coded it within PFC2D, the virtual asphalt mastic could be rebuilt successfully as shown in Figure 10. As shown, the uniform arranged balls were filled in the external particle area to model the mastic while the coarse aggregates kept same shapes and positions all the time.

**5.2. Escaped Balls Deletion and Voids Modeling.** Prior to modeling the voids, enough calculation steps should be done within PFC2D to make the ball system stable. The mastic balls would move continuously until reach the equilibrium state. However, due to the initial overlaps among balls (Figure 10), some of the mastic balls would go through the particle boundary and then escaped. So after the ball system reached the equilibrium state, an initial upward velocity was assigned to all balls and then simulated for a very short time.

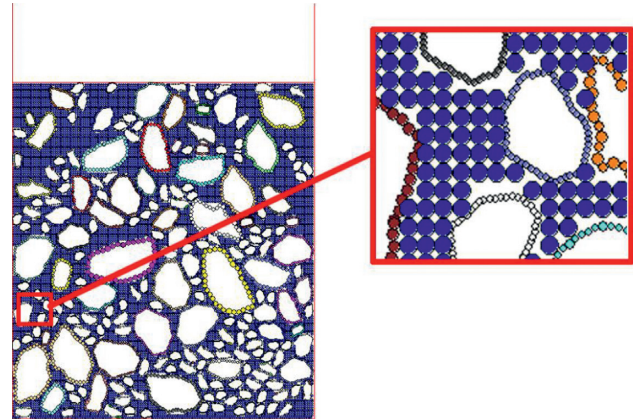


FIGURE 10: Filling the irregular area with balls to model the asphalt mastic.

The balls without any contact force during the short-time simulation were identified as the escaped balls and should be deleted as shown in Figure 11.

The void content in three dimensions was converted to mapping area in two dimensions which was the same with the coarse aggregates and asphalt mastic. Since the diameters of the mastic balls have been known, the number of the void balls could be determined. By deleting the mastic balls randomly until the number of the void balls reached requirements, the virtual void could be modeled well as shown in Figure 12(d).

**5.3. Example of Generating a Virtual Specimen.** The asphalt mixture of AC-16 was developed for simulation. The gradation of the AC-16 is shown in Table 2. Based on the gradation, the mapping areas of three-phase structures including the coarse aggregates, asphalt mastic, and the void content were calculated using (4) and (5). And the results of the AC-16 were summarized in Table 3.

$$M = \rho \times \frac{\pi \times D^2}{4} \times h, \quad (4)$$

Where  $M$  is the total mass of the specimen in three dimensions, g;  $\rho$  is the density of the specimen, g/cm<sup>3</sup>;  $D$  is the diameter of the specimen, cm; and  $h$  is the height of the specimen, cm.

When it comes to the two-dimensional specimen, the mass can be converted as following:

$$m = \frac{M}{V} \times S = \frac{V \times \rho}{V} \times D \times h = Dh\rho, \quad (5)$$

where  $m$  is the converted mass of specimen in two dimensions (g),  $V$  is the total volume of the specimen in three dimensions (cm<sup>3</sup>),  $S$  is the area of the specimen in two dimensions (cm<sup>2</sup>), and the others are the same as those of three dimensions.

The void content was 4% and the asphalt content was 4.5% in mixtures. Assumptions were made that the air void is distributed uniformly in mixtures so the void contents in two dimensions and three dimensions can be set as a same

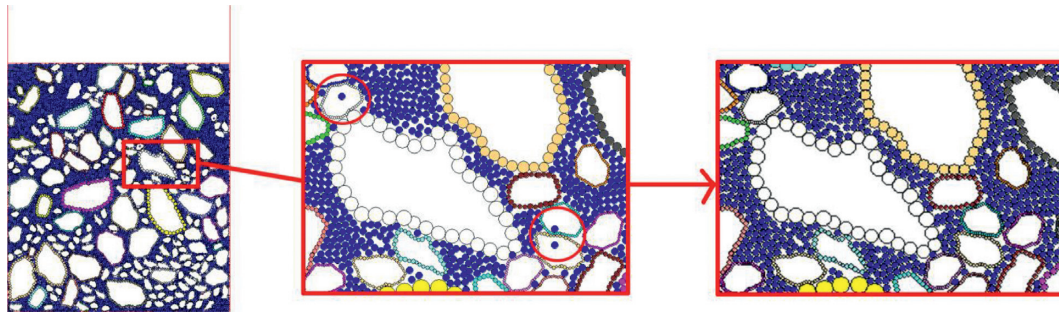


FIGURE 11: Escaped balls deletion before random voids modelling.

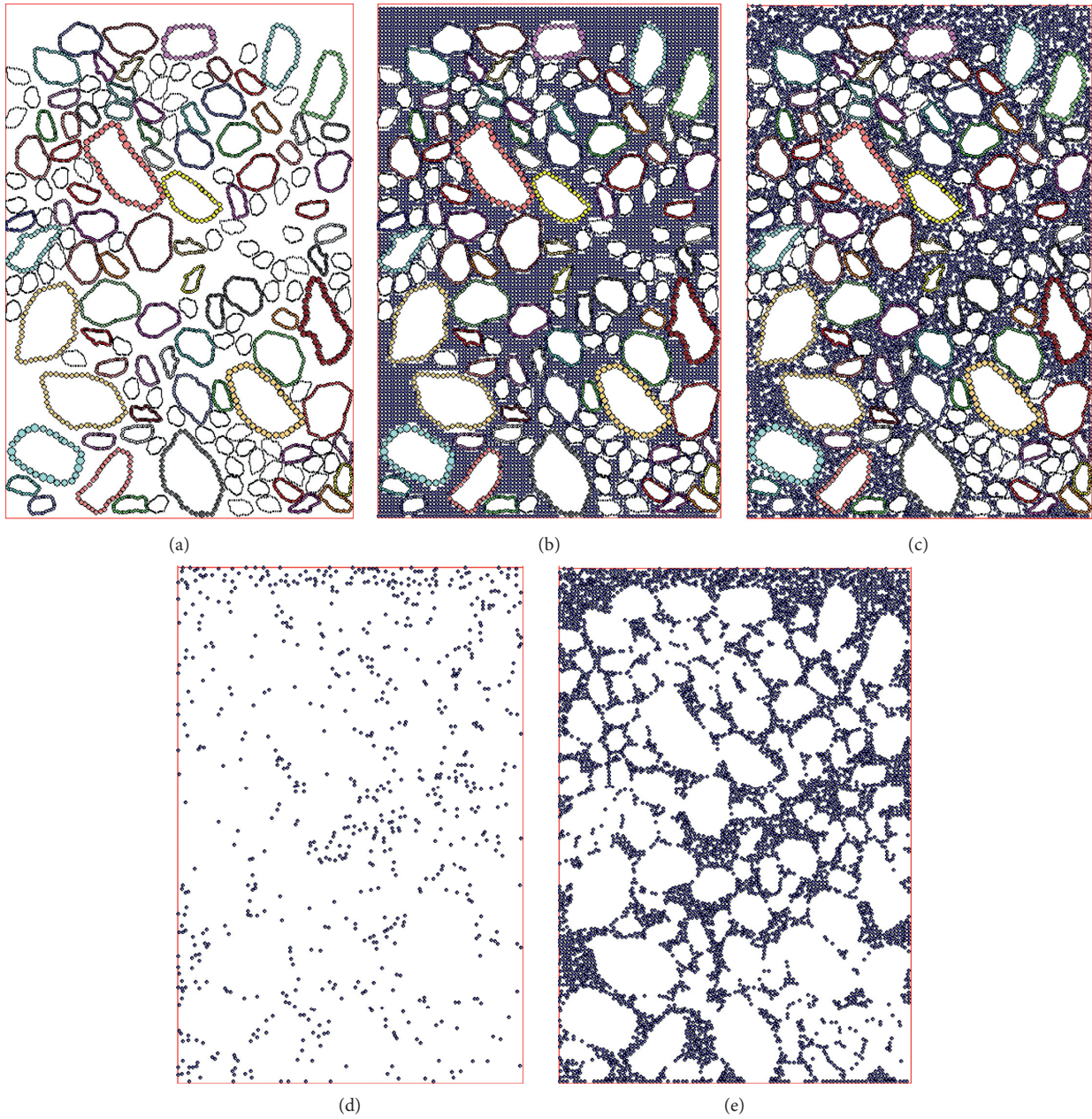


FIGURE 12: Modeling process of virtual asphalt mixtures: (a) aggregate skeleton; (b) uniform balls filling; (c) virtual asphalt mixture; (d) voids modeling; (e) asphalt mastic modelling.

TABLE 2: Gradations for AC-16.

Gradation	Passing ratio (%) for different sieving size (mm)											
	19	16	13.2	9.5	4.75	2.36	1.18	0.6	0.3	0.15	0.075	
AC-16	100	95	84	70	48	34	24.5	17.5	12.5	9.5	6.0	

TABLE 3: Mapping area calculations for three-phase structures.

Container area (m <sup>2</sup> )	Total mapping area for void (m <sup>2</sup> )	Total mapping area for coarse aggregates (m <sup>2</sup> )	Total mapping area for asphalt mastic (m <sup>2</sup> )
0.015	0.0006	0.0071	0.0073

TABLE 4: Summaries of the coarse aggregates.

Size (mm)	16	13.2	9.5	4.75
Required mapping area (m <sup>2</sup> )	$6.83e-4$	$1.50e-3$	$1.91e-3$	$3.01e-3$
Generated area (m <sup>2</sup> )	$7.18e-4$	$1.57e-3$	$1.95e-3$	$3.06e-3$
Error (%)	5.1	4.7	2.1	1.7

TABLE 5: Summaries of the asphalt mastic and voids.

A	B	C	D	E	F	Error (%)
$7.3e-3$	$7.301e-3$	9300	10076	764	12	0.014

A: required mapping area for asphalt mastic (m<sup>2</sup>); B: generated mapping area for asphalt mastic (m<sup>2</sup>); C: required number of balls within asphalt mastic; D: actual number of balls within asphalt mastic before void modeling; E: number of the deleted balls for modeling voids; F: number of the deleted balls which have been escaped.

value of 4%. Moreover, the densities of the coarse aggregates and asphalt mastic were  $2.7 \text{ g/cm}^3$  and  $2.0 \text{ g/cm}^3$ , respectively. By the proposed algorithm, the virtual container with a height of 150 mm and a width of 100 mm were developed firstly, then followed by the coarse aggregate, mastic and void generation, respectively, within PFC2D as shown in Figure 12.

To verify the precision of the inner components modeling, the final generated area of coarse aggregates, asphalt mastic, and voids were measured afterwards by the user-defined routine within PFC2D. The results were summarized in Tables 4 and 5. As shown, the error is 5.1%, 4.7%, 2.1%, and 1.7% for the 16 mm, 13.2 mm, 9.5 mm, and 4.75 mm aggregates, respectively. The modeling error decreased as the size decreased. This is due to the overflow of the lastly generated coarse particles of each grade and it is inevitable. When comes to the asphalt mastic, the modeling is significantly precise with 0.014% error only. The sole difference between the realistic and virtual mastic content was caused by the rounding error in mapping area calculations.

## 6. Performance Prediction of the Rebuilt Models

**6.1. Experiments.** Based on the Chinese test standards [34], uniaxial compressive test was conducted to evaluate the dynamic modulus of asphalt mixture in laboratory. The gradations of mixtures were shown in Table 2. And the

TABLE 6: Microparameters of selected constitutive models for particles and walls.

	Normal stiffness, $k_n$ (N/m)	Shear stiffness, $k_s$ (N/m)	Friction coefficient
4.75	$2.2e6$	$1.5e6$	0.6
9.5	$2.5e6$	$2.5e6$	0.55
13.2	$1.2e6$	$1.2e6$	0.5
16	$1.8e6$	$1.8e6$	0.4
Wall	$1e10$	$1e10$	0.35

mixtures were formed in a cylinder container with a height of 150 mm and a width of 100 mm. A Superpave gyratory compactor was utilized to compact the asphalt mixture to a targeted void level of 4% at the 4.5% asphalt content. The specimens were tested at 0°C and 138 kPa confining pressure and the loading frequencies are 0.1, 1, 5, 10, and 25 Hz, respectively.

**6.2. Simulations for Dynamic Modulus Prediction.** The virtual asphalt mixtures were developed as shown in Figure 12(c). When simulated, the top and bottom walls were modeled as a sine load while the walls on left and right sides kept a constant confining stress based on the numerical servo-mechanism within PFC2D. During the simulation, the axial deviatoric stress and axial strain were recorded together for the dynamic modulus calculations.

According to the PFC2D manuals [35], several constitutive models were used for characterizing the mechanical behavior of the heterogeneous materials including the contact-stiffness models, sliding models, and Burger's models. The contact force in normal and shear direction between two entities was determined by the key microparameters in contact-stiffness models, known as the normal stiffness  $k_n$  and shear stiffness  $k_s$ . The sliding models were used for sliding movements by the frictional coefficient while Burger's models characterized the viscoelasticity of asphalt part. To reduce the error of the selected microparameters, the parameter calibrations were conducted separately for the coarse aggregates and asphalt mastic. According to the Chinese test standards [36], the penetration tests of the 4.75 mm, 9.5 mm, 13.2 mm, and 16 mm particles were carried out to get the force-displacement curves. Then virtual simulations for corresponding penetration tests were developed within PFC2D and were conducted for virtual results. By adjusting the microparameters of different size particles continuously until the simulation curves match the realistic, the best group of normal stiffness  $k_n$ , shear stiffness  $k_s$ , and frictional coefficient could be determined as shown in Table 6. Two kinds of contact points were defined by Burger's models. One is the contact point within asphalt, and another is between the asphalt mastic and aggregates.

TABLE 7: Microparameters at contacts within asphalt mastic.

$K_{mn}$ (Pa·m)	$K_{kn}$ (Pa·m)	$C_{mn}$ (Pa·m·s)	$C_{kn}$ (Pa·m·s)	$K_{ms}$ (Pa·m)	$K_{ks}$ (Pa·m)	$C_{ms}$ (Pa·m·s)	$C_{ks}$ (Pa·m·s)
1.14e3	7.92e2	1.95e6	5.58e4	3.79e2	2.64e1	6.49e5	1.86e4

TABLE 8: Microparameters at contacts between asphalt mastic and aggregates.

$K'_{mn}$ (Pa·m)	$K'_{kn}$ (Pa·m)	$C'_{mn}$ (Pa·m·s)	$C'_{kn}$ (Pa·m·s)	$K'_{ms}$ (Pa·m)	$K'_{ks}$ (Pa·m)	$C'_{ms}$ (Pa·m·s)	$C'_{ks}$ (Pa·m·s)
2.27e3	1.58e3	3.89e6	1.12e5	1.51e3	5.28e5	1.30e6	3.72e4

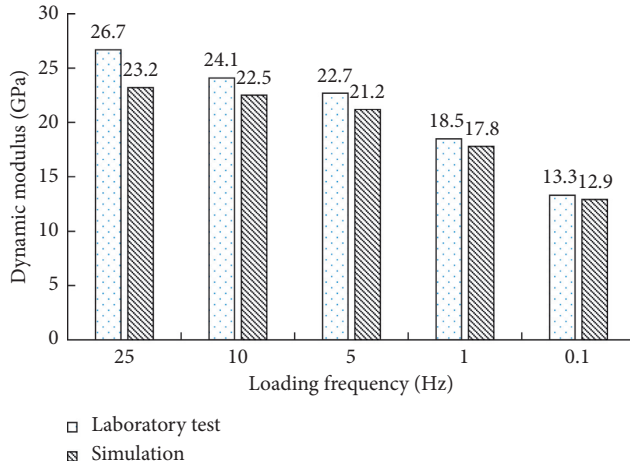


FIGURE 13: Dynamic modulus prediction based on the proposed models.

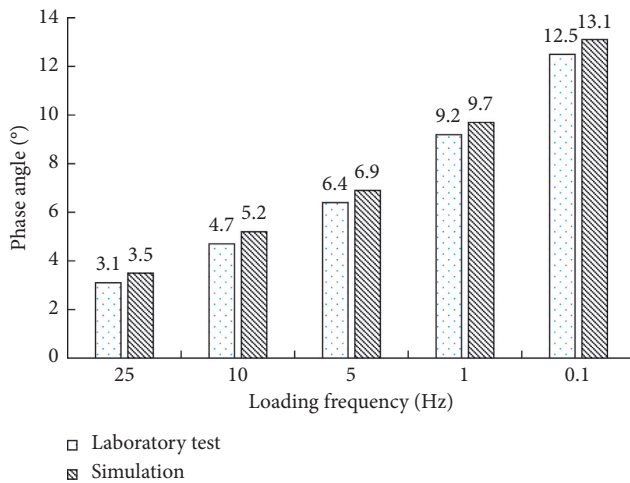


FIGURE 14: Phase angle prediction based on the proposed models.

Based on the previous studies [37], the microparameters of Burger's models at different contacts were shown in Tables 7 and 8.

Figure 13 shows the simulation results compared to the laboratory tests at the test temperature of 0°C. As shown, the virtual results have a good accordance with the truth. The prediction error of dynamic modulus is 12.7%, 6.7%, 6.6%, 3.8%, and 3.0% for the 25 Hz, 10 Hz, 5 Hz, 1 Hz, and 0.1 Hz, respectively. As shown in Figure 14, the predictions of phase angle is also effective with the minor error of 12.9%, 10.6%,

7.8%, 5.4% and 4.8% for the 25 Hz, 10 Hz, 5 Hz, 1 Hz, and 0.1 Hz, respectively. As the loading frequency decreased, the error decreased obviously. This is because the microparameters for simulations were all calibrated and determined by tests under the static loading rather than the cyclic loading. So when the load frequency is low in simulations, the cyclic loading could be taken as the static loading to some extent. When the load frequency increased, the difference between the static and cyclic loading grew leading to the error shown in the Figures 13 and 14. In summaries, the developed models can well predict the dynamic modulus of asphalt mixture, especially at low frequency, which verified the correctness of the proposed algorithm.

## 7. Conclusions

This paper proposed an algorithm for the reconstitution of the virtual asphalt mixture based on the DEM methods. By filling the shape contours with balls, the virtual coarse aggregates were developed precisely. Based on the algorithm for distinguishing the external and internal area of irregular particles, the asphalt mastic was generated properly by the designed rules. In the end, the validation of the proposed algorithm was verified by the virtual uniaxial compressive test. The main conclusions drawn from the study are as follows:

- (1) Virtual shapes were rebuilt precisely based on the AIMS scanning. By the random control parameters, numerous virtual particles derived from the standard ones were developed rapidly with various shapes and sizes. By combining the scanning technology with the stochastic algorithm, this method can well meet the DEM simulation needs.
- (2) The virtual asphalt mixtures were rebuilt in three steps. Firstly, the virtual coarse aggregates were distributed randomly to form the skeletons. Then an innovate algorithm was proposed to distinguish the external and internal area of the coarse particles. At last, by filling the designed area with uniform arranged balls and deleting mastic balls randomly, the asphalt mastic and void could be generated successfully. The results shows that the proposed algorithm can well model the inner components consistent to the actual gradations, asphalt content, and voids.
- (3) The validation of the developed models was verified by the virtual uniaxial compressive test. The error of

dynamic modulus is 12.7%, 6.7%, 6.6%, 3.8%, 3.0%, and the error of phase angle is 12.9%, 10.6%, 7.8%, 5.4%, and 4.8% for the 25 Hz, 10 Hz, 15 Hz, 1 Hz, and 0.1 Hz, respectively. It is indicated that the dynamic modulus of the asphalt mixtures can be well predicted based on the proposed algorithm, especially at low frequency.

## Conflicts of Interest

The authors declare that they have no conflicts of interest.

## Acknowledgments

The study is financially supported by the Science Foundations of Nanjing Institute of Technology, China (YKJ201423), National Natural Science Foundation of China (no. 51378006), and Natural Science Foundation of Jiangsu Province, China (BK20161421).

## References

- [1] B. Lira, D. Jelagin, and B. Birgisson, "Gradation-based framework for asphalt mixture," *Materials and Structures*, vol. 46, no. 8, pp. 1401–1414, 2013.
- [2] I. A. Johan, "The effect of different filler materials and gradation on rutting and cracking of bituminous mixture," *Journal of Fluid Mechanics*, vol. 599, no. 599, pp. 441–464, 2008.
- [3] O. Xu, Z. Wang, and R. Wang, "Effects of aggregate gradations and binder contents on engineering properties of cement emulsified asphalt mixtures," *Construction and Building Materials*, vol. 135, pp. 632–640, 2017.
- [4] D. H. Shen, M. F. Kuo, and J. C. Du, "Properties of gap-aggregate gradation asphalt mixture and permanent deformation," *Construction and Building Materials*, vol. 19, no. 2, pp. 147–153, 2005.
- [5] J. Zhang, H. Liu, P. Wang, J. Pei, D. Bao, and L. Jin, "Evaluation of aggregate gradation and distributing homogeneity based on the images of asphalt mixture," *Road Materials and Pavement Design*, vol. 18, no. S3, pp. 119–129, 2017.
- [6] H. Shi, T. Xu, and R. Jiang, "Combustion mechanism of four components separated from asphalt binder," *Fuel*, vol. 192, pp. 18–26, 2017.
- [7] J. Zhang, G. Liu, C. Zhu, and J. Pei, "Evaluation indices of asphalt–filler interaction ability and the filler critical volume fraction based on the complex modulus," *Road Materials and Pavement Design*, vol. 18, no. 6, pp. 1338–1352, 2017.
- [8] H. Y. Liu and J. L. Dai, "Effect of different gradations on asphalt mixture resistance to rut," *Journal of Chang'an University*, vol. 24, no. 5, pp. 11–15, 2004.
- [9] E. Coleri, R. Wu, J. M. Signore, and J. Harvey, "Rutting of rubberized gap-graded and polymer-modified dense-graded asphalt overlays in composite pavements," *Transportation Research Record: Journal of the Transportation Research Board*, vol. 2304, no. 1, pp. 195–204, 2012.
- [10] S. Gokhale, B. Choubane, T. Byron, and M. Tia, "Rut initiation mechanisms in asphalt mixtures as generated under accelerated pavement testing," *Transportation Research Record: Journal of the Transportation Research Board*, vol. 1940, no. 1, pp. 136–145, 2005.
- [11] G. D. Airey, A. E. Hunter, and A. C. Collop, "The effect of asphalt mixture gradation and compaction energy on aggregate degradation," *Construction and Building Materials*, vol. 22, no. 5, pp. 972–980, 2008.
- [12] I. Isailović, M. P. Wistuba, and A. C. Falchetto, "Investigation on mixture recovery properties in fatigue tests," *Road Materials and Pavement Design*, pp. 1–11, 2017.
- [13] A. Hasan, *Void Effects on Fatigue Life Asphaltic Concrete*, 1973, [http://arizona.openrepository.com/arizona/bitstream/10150/554485/1/AZU\\_TD\\_BOX101\\_E9791\\_1973\\_160.pdf](http://arizona.openrepository.com/arizona/bitstream/10150/554485/1/AZU_TD_BOX101_E9791_1973_160.pdf).
- [14] L. Li, L. Cao, and Y. Guo, "Influence of initial air void on performance of asphalt mixtures," *Journal of Tongji University*, vol. 34, no. 6, p. 757, 2006.
- [15] J. Hinrichsen and J. Heggen, "Minimum voids in mineral aggregate in hot-mix asphalt based on gradation and volumetric properties," *Transportation Research Record: Journal of the Transportation Research Board*, vol. 1545, no. 1, pp. 75–79, 1996.
- [16] C. G. Rocco and M. Elices, "Effect of aggregate shape on the mechanical properties of a simple concrete," *Engineering Fracture Mechanics*, vol. 76, no. 2, pp. 286–298, 2009.
- [17] L. Liu, D. Shen, H. Chen, and W. Xu, "Aggregate shape effect on the diffusivity of mortar: a 3D numerical investigation by random packing models of ellipsoidal particles and of convex polyhedral particles," *Computers and Structures*, vol. 144, pp. 40–51, 2014.
- [18] M. C. Li and I. Kett, "Influence of coarse aggregate shape on the strength of asphalt concrete mixtures," *Highway Research Record*, vol. 6, pp. 1062–1075, 2005.
- [19] P. A. Cundall, *Ball-A Program to Model Granular Media using the Distinct Element Method*, Technical Note, Advanced Technology Group, Dames & Moore, London, UK, 1978.
- [20] B. K. Mishra, "A review of computer simulation of tumbling mills by the discrete element method: part II—practical applications," *International Journal of Mineral Processing*, vol. 71, no. 1–4, pp. 73–93, 2003.
- [21] K. Huang, T. Xu, and G. Li, "Heating effects of asphalt pavement during hot in-place recycling using DEM," *Construction and Building Materials*, vol. 115, pp. 62–69, 2016.
- [22] A. R. Abbas, *Simulation of the Micromechanical Behavior of Asphalt Mixtures using the Discrete Element Method*, Washington State University, Pullman, WA, USA, 2004.
- [23] H. Yu and S. Shen, "Impact of aggregate packing on dynamic modulus of hot mix asphalt mixtures using three-dimensional discrete element method," *Construction and Building Materials*, vol. 26, no. 1, pp. 302–309, 2012.
- [24] J. Chen, B. Huang, and X. Shu, "Air-void distribution analysis of asphalt mixture using discrete element method," *Journal of Materials in Civil Engineering*, vol. 25, no. 10, pp. 1375–1385, 2013.
- [25] M. Lu and G. R. McDowell, "The importance of modelling ballast particle shape in the discrete element method," *Granular Matter*, vol. 9, no. 1–2, pp. 69–80, 2007.
- [26] N. Das, S. Thomas, J. Kopmann et al., "Modeling granular particle shape using discrete element method," *Monthly Notices of the Royal Astronomical Society*, vol. 420, no. 4, pp. 3368–3380, 2012.
- [27] D. Zhang, X. Huang, and Y. Zhao, "Algorithms for generating three-dimensional aggregates and asphalt mixture samples by the discrete-element method," *Journal of Computing in Civil Engineering*, vol. 27, no. 2, pp. 111–117, 2013.
- [28] E. Masad, "X-ray computed tomography of aggregates and asphalt mixes," *Materials Evaluation*, vol. 62, no. 7, pp. 775–783, 2004.
- [29] Z. Zhou, X. Gu, Q. Li, F. Ni, and R. Yuan, "Use of rejuvenator, styrene-butadiene rubber latex, and warm-mix asphalt technology to achieve conventional mixture performance with 50% reclaimed asphalt pavement," *Transportation*

- Research Record: Journal of the Transportation Research Board*, vol. 2575, pp. 160–167, 2016.
- [30] Q. Li, H. Yang, X. Ma, and F. Ni, “Evaluation of micro-structure and damage evolution for asphalt pavements in an advanced repeated load permanent deformation test using X-ray computed tomography,” *Road Materials and Pavement Design*, vol. 18, no. 5, pp. 1135–1158, 2017.
- [31] Y. Fu, L. Wang, M. T. Tumay, and Q. Li, “Quantification and simulation of particle kinematics and local strains in granular materials using X-ray tomography imaging and discrete-element method,” *Journal of Engineering Mechanics*, vol. 134, no. 2, pp. 143–154, 2008.
- [32] C. Jin, X. Yang, and Z. You, “Automated real aggregate modelling approach in discrete element method based on X-ray computed tomography images,” *International Journal of Pavement Engineering*, vol. 18, no. 9, pp. 837–850, 2015.
- [33] Ł. Skarżyński, M. Nitka, and J. Tejchman, “Modelling of concrete fracture at aggregate level using FEM and DEM based on X-ray  $\mu$ CT images of internal structure,” *Engineering Fracture Mechanics*, vol. 147, pp. 13–35, 2015.
- [34] Ministry of Transport of the People’s Republic of China, *Standard Test Methods of Bitumen and Bituminous Mixtures for Highway Engineering*, Ministry of Transport of the People’s Republic of China, Beijing, China, 2010.
- [35] Itasca Consulting Group, *PFC2D Manual Version 4.0*, Itasca Consulting Group, Minneapolis, MN, USA, 2008.
- [36] Ministry of Transport of the People’s Republic of China, *Test Methods of Soils for Highway Engineering*, Ministry of Transport of the People’s Republic of China, Beijing, China, 2007.
- [37] T. Ma, D. Zhang, Y. Zhang, Y. Zhao, and X. Huang, “Effect of air voids on the high-temperature creep behavior of asphalt mixture based on three-dimensional discrete element modeling,” *Materials and Design*, vol. 89, pp. 304–313, 2016.

## Research Article

# An Equal-Strain Analytical Solution for the Radial Consolidation of Unsaturated Soils by Vertical Drains considering Drain Resistance

Feng Zhou <sup>1</sup>, Zheng Chen <sup>2,3</sup> and Xudong Wang<sup>1</sup>

<sup>1</sup>College of Transportation Science & Engineering, Nanjing Tech University, Nanjing 210009, China

<sup>2</sup>State Key Laboratory of Water Resources and Hydropower Engineering Science, Wuhan University, Wuhan 430072, China

<sup>3</sup>Key Laboratory of Rock Mechanics in Hydraulic Structural Engineering, Ministry of Education, Wuhan University, Wuhan 430072, China

Correspondence should be addressed to Zheng Chen; [johnchan@whu.edu.cn](mailto:johnchan@whu.edu.cn)

Received 6 November 2017; Revised 27 January 2018; Accepted 6 February 2018; Published 12 April 2018

Academic Editor: Fan Gu

Copyright © 2018 Feng Zhou et al. This is an open access article distributed under the Creative Commons Attribution License, which permits unrestricted use, distribution, and reproduction in any medium, provided the original work is properly cited.

Developing an analytical solution for the consolidation of unsaturated soils remains a challenging task due to the complexity of coupled governing equations for air and water phases. This paper presents an equal-strain model for the radial consolidation of unsaturated soils by vertical drains, and the effect of drain resistance is also considered. Simplified governing equations are established, and an analytical solution to calculate the excess pore-air and pore-water pressures is derived by using the methods of matrix analysis and eigenfunction expansion. The average degrees of consolidation for air and water phases and the ground surface settlement are also given. The solutions of the equal-strain model are verified by comparing the proposed free-strain model with the equal-strain model, and reasonably good agreement is obtained. Moreover, parametric studies regarding the drain resistance effect are graphically presented.

## 1. Introduction

As a common phenomenon of civil engineering, consolidation is a process of decreasing soil volume when soil is subjected to an increased stress. Understanding of this phenomenon is vital to designs of soft soil foundations, pavements, and other engineering structures. Therefore, Terzaghi [1] established a classical theory for the analysis of consolidation in saturated soft soil foundation, which is well known in geotechnical engineering. Based on Terzaghi's theory, solutions of one-dimensional consolidation have been derived for multilayered soils [2, 3], non-Darcy flow [4, 5], time-dependent loading [6, 7], arbitrary boundary [8, 9], and nonlinear deformation [10, 11]. In practice, soft soils related to engineering are usually in a state of unsaturation. With the great progress made, some well-developed consolidation theories for unsaturated soft soils have been available [12–15]. Among these theories, Fredlund and Rahardjo's [15] consolidation

theory is well accepted for the consolidation of unsaturated soft soils.

Since the inception of the one-dimensional (1D) consolidation theory of unsaturated soft soils proposed by Fredlund and Hasan [16], the investigations for 1D consolidation have been significantly progressed. By assuming constant soil parameters during consolidation, Qin et al. [17, 18] adopted the Laplace transform and Cayley–Hamilton methods to obtain an analytical solution. Shan et al. [19] and Zhou et al. [20] converted the nonlinear governing flow equations into traditional diffusion equations and proposed alternative solutions satisfying those converted equations. Ho et al. [21], on the other hand, introduced exact solutions using the eigenfunction expansion and Laplace transform techniques. In addition, some general solutions that consider various boundary conditions [9, 19, 20, 22], initial pore-water and -air pressure distributions [9, 20], and complex time-dependent loadings [9, 19, 20, 22–24] were also obtained in a single soil layer. However, the soft soil foundation in practice

is not always singly layered. For this reason, Shan [25] presented an analytical solution of unsaturated multilayered soil with typical boundary conditions.

In subgrade and pavement engineering, vertical drains are one of the most commonly used techniques to accelerate the consolidation process and increase the bearing capacity of the subgrade. It is essential to expand the consolidation theory of unsaturated soft soils from one-dimensional vertical consolidation to radial consolidation. For this purpose, Conte [26] developed a general formulation that can be advantageously used to analyze consolidation under plane-strain conditions. Ho et al. [27] discussed the excess pore-air and pore-water pressure dissipations in the plane-strain consolidation of unsaturated soft soils using eigenfunction expansion and Laplace transform techniques. Shortly afterwards, the solutions of unsaturated soft soils subjected to different time-dependent loadings were also obtained by Ho [28].

However, a lot of attempts have been made to solve the axisymmetric consolidation model of unsaturated soft soils particularly with analytical approaches. Among the pioneered studies, Conte [26] introduced the finite element technique to obtain a solution for the coupled consolidation under the axisymmetric conditions. Qin et al. [29] dealt with the vertical drain consolidation problem in unsaturated soft soils using the modified Bessel functions and the Laplace transformation. On the other hand, Zhou and Tu [30] and Zhou [31] presented the differential quadrature method (DQM) to estimate the axisymmetric consolidation behavior in the unsaturated soft soils. Ho et al. [32] gave an analytical solution for the axisymmetric consolidation of unsaturated soft soils subjected to constant external loading. The analytical procedure employs the variable separation and Laplace transformation techniques while capturing the uniform and linear initial excess pore pressure distributions with depth.

Most of the models mentioned above were obtained based on the free-strain assumption. However, the solutions of the free-strain model are complex and inconvenient to use in practice. In the research of saturated soft soils, Barron [33] firstly proposed the consolidation model for vertical drains under free-strain and equal-strain models. The mathematical expressions are as follows:

$$c_r \left( \frac{\partial^2 u}{\partial r^2} + \frac{1}{r} \cdot \frac{\partial u}{\partial r} \right) + c_v \frac{\partial^2 u}{\partial z^2} = \frac{\partial u}{\partial t} \quad (\text{free-strain model}),$$

$$c_r \left( \frac{\partial^2 u}{\partial r^2} + \frac{1}{r} \cdot \frac{\partial u}{\partial r} \right) + c_v \frac{\partial^2 \bar{u}}{\partial z^2} = \frac{\partial \bar{u}}{\partial t} \quad (\text{equal-strain model}),$$

(1)

where  $u$  and  $\bar{u}$  are the excess pore-water pressure and average excess pore-water pressure, respectively;  $c_r$  and  $c_v$  are the coefficients of consolidation in the radial and vertical directions, respectively;  $r$  is the distance from the origin of the vertical drain in the radial direction;  $z$  is the distance from the surface of the foundation in the vertical direction; and  $t$  is the time. Barron [33] pointed out that there is negligible difference between the free-strain and equal-strain models. After this, equal-strain assumption is frequently used in most consolidation theories for vertical drains [34–36].

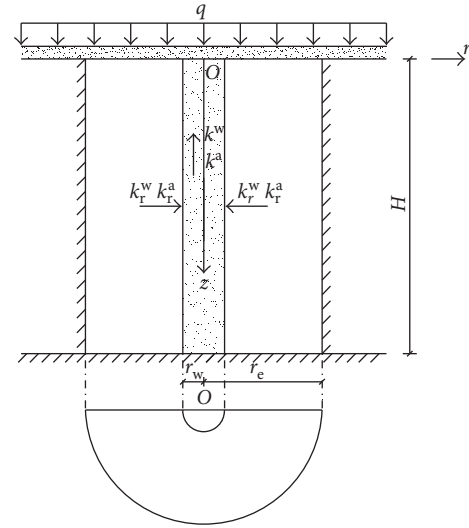


FIGURE 1: Calculation diagram of vertical drain in an unsaturated soil stratum.

At present, there is no reference about the equal-strain model in the research of unsaturated soft soils. The objective of this paper is to propose an equal-strain consolidation model to investigate the consolidation behavior of unsaturated soft soils. In addition, drain resistance will also be considered in this study, and the accuracy of the equal-strain model will be verified by comparing with the free-strain model proposed by Qin et al. [29]. Moreover, parametric studies regarding the drain resistance effect are also presented in this paper.

## 2. Problem Statements

**2.1. Model Description.** Figure 1 describes the details of the representative vertical drain within an unsaturated soft soil foundation. Dimensions of the soil system include the depth  $H$  and the radius of the influence zone  $r_e$ .  $k_r^w$  and  $k_r^a$  are the coefficients of water and air permeability of the foundation in the radial direction, respectively. The circular vertical drain with the radius  $r_w$  is installed at the center of the influence zone.  $k_v^w$  and  $k_v^a$  are the coefficients of water and air permeability of the vertical drain in the vertical direction, respectively. A constant surcharge  $q$  is instantaneously applied on the top surface of soft soil foundation.

**2.2. Basic Assumptions.** The basic assumptions are the same as those of Fredlund's consolidation theory for unsaturated soft soils and Barron's [33] consolidation theory for vertical drains. The other three assumptions are listed as follows:

- (1) All the soil parameters are constants during consolidation.
- (2) The strains at the same depth of the foundation are equal (equal-strain assumption).
- (3) The distribution of excess pore-air pressure in unsaturated soft soils is uniform.

**2.3. Derivation of Consolidation Governing Equations.** The governing equations for the consolidation of unsaturated soft soils with vertical drains consist of water phase and air phase equations under equal-strain conditions. In the polar coordinate system, considering a representative element of unsaturated soft soil foundation, with water and air flow in and out in the radial direction during consolidation, the derivation process is given as follows.

**2.3.1. Water Phase.** The net flux of water through the element is computed from the volume of water entering and leaving the element within a period of time. By utilizing Darcy's law, the net flux of water per unit volume of the soil can be expressed in the polar coordinate system as

$$\frac{\partial(V_w/V_0)}{\partial t} = \frac{k_r^w}{\gamma_w} \left( \frac{\partial^2 u_w}{\partial r^2} + \frac{1}{r} \cdot \frac{\partial u_w}{\partial r} \right), \quad (2)$$

where  $V_0$  is the initial total volume of the soil element,  $V_w$  is the volume of water in the soil element,  $\gamma_w$  is the unit weight of water, and  $u_w$  is the excess pore-water pressure.

The net flux of water per unit volume of the soil can be obtained by differentiating the water phase constitutive relation with respect to time:

$$\frac{\partial(V_w/V_0)}{\partial t} = m_{1k}^w \frac{\partial(q - \bar{u}_a)}{\partial t} + m_2^w \frac{\partial(\bar{u}_a - \bar{u}_w)}{\partial t}, \quad (3)$$

where  $m_{1k}^w$  and  $m_2^w$  describe the coefficients of water volume change with respect to a change in the net normal stress  $d(q - \bar{u}_a)$  and matric suction  $d(\bar{u}_a - \bar{u}_w)$ , respectively; and  $\bar{u}_w$  and  $\bar{u}_a$  are the average excess pore-water and pore-air pressures throughout the entire soil mass, respectively, which can be expressed as

$$\begin{aligned} \bar{u}_w &= \frac{1}{\pi(r_e^2 - r_w^2)} \int_{r_w}^{r_e} 2\pi r u_w dr, \\ \bar{u}_a &= \frac{1}{\pi(r_e^2 - r_w^2)} \int_{r_w}^{r_e} 2\pi r u_a dr, \end{aligned} \quad (4)$$

where  $u_a$  is the excess pore-air pressure.

Substituting (2) into (3), the governing equation for the water phase can be expressed as

$$\frac{\partial \bar{u}_w}{\partial t} + C_a^w \frac{\partial \bar{u}_a}{\partial t} + C_r^w \left( \frac{\partial^2 u_w}{\partial r^2} + \frac{1}{r} \cdot \frac{\partial u_w}{\partial r} \right) = 0, \quad (5)$$

where  $C_r^w$  is the coefficient of consolidation with respect to the water phase in the radial direction (i.e.,  $k_r^w/(\gamma_w m_2^w)$ ) and  $C_a^w$  is the interactive constant associated with the water phase (i.e.,  $(m_{1k}^w - m_2^w)/m_2^w$ ).

**2.3.2. Air Phase.** The net flux of air through the element is computed from the volume of air entering and leaving the element within a period of time. The flux of air per unit volume of the soil can be obtained by Fick's law as

$$\frac{\partial(\rho_a V_a/V_0)}{\partial t} = \frac{k_r^a}{g} \left( \frac{\partial^2 u_a}{\partial r^2} + \frac{1}{r} \cdot \frac{\partial u_a}{\partial r} \right), \quad (6)$$

where  $\rho_a$  is the density of air,  $g$  is the gravitational acceleration, and  $V_a$  is the volume of air phase.

Based on assumption 3, the distribution of excess pore-air pressure in unsaturated soft soils is uniform. The density of air is a function of air pressure in accordance with the ideal gas law. It can be expressed as

$$\rho_a = \frac{\omega_a}{RT_{at}} \bar{u}_a, \quad (7)$$

where  $\omega_a$  is the molecular mass of air,  $R$  is the molar gas constant,  $T_{at}$  is the absolute temperature,  $\bar{u}_a$  is the absolute excess pore-air pressure (i.e.,  $\bar{u}_a + u_{atm}$ ), and  $u_{atm}$  is the atmospheric pressure.

Replacing the air density,  $\rho_a$ , in (6) with (7) gives

$$\frac{\partial(V_a/V_0)}{\partial t} = \frac{k_r^a RT_{at}}{\bar{u}_a \omega_a g} \left( \frac{\partial^2 u_a}{\partial r^2} + \frac{1}{r} \cdot \frac{\partial u_a}{\partial r} \right) - \frac{(1 - S_s)n_s}{\bar{u}_a} \cdot \frac{\partial \bar{u}_a}{\partial t}, \quad (8)$$

where  $S_s$  is the degree of saturation and  $n_s$  is the porosity.

The flux of air per unit volume of the soil due to changes in the net normal stress,  $d(q - \bar{u}_a)$ , and the matric suction,  $d(\bar{u}_a - \bar{u}_w)$ , can be expressed by the following equation:

$$\frac{\partial(V_a/V_0)}{\partial t} = m_{1k}^a \frac{\partial(q - \bar{u}_a)}{\partial t} + m_2^a \frac{\partial(\bar{u}_a - \bar{u}_w)}{\partial t}, \quad (9)$$

where  $m_{1k}^a$  and  $m_2^a$  describe the coefficients of air volume change with respect to a change in the net normal stress  $d(q - \bar{u}_a)$  and matric suction  $d(\bar{u}_a - \bar{u}_w)$ , respectively.

By substituting (8) into (9), the governing equation for the air phase can be given as

$$C_w^a \frac{\partial \bar{u}_w}{\partial t} + \frac{\partial \bar{u}_a}{\partial t} + C_r^a \left( \frac{\partial^2 u_a}{\partial r^2} + \frac{1}{r} \cdot \frac{\partial u_a}{\partial r} \right) = 0, \quad (10)$$

where  $C_r^a$  is the coefficient of consolidation with respect to the air phase in the radial direction (i.e.,  $k_r^a RT_{at}/\{\omega_a g [\bar{u}_a (m_{1k}^a - m_2^a) - (1 - S_s)n_s]\}$ ) and  $C_w^a$  is the interactive constant associated with the air phase (i.e.,  $m_2^a \bar{u}_a / [\bar{u}_a (m_{1k}^a - m_2^a) - (1 - S_s)n_s]$ ).

By rearranging the governing equations of water and air phases, the consolidation equations for water and air phases can be written in matrix form as

$$\mathbf{K}_r \left( \mathbf{u}_{,rr} + \frac{1}{r} \mathbf{u}_{,r} \right) + \mathbf{C} \bar{\mathbf{u}}_{,t} = 0, \quad (11)$$

where  $\bar{\mathbf{u}} = \begin{Bmatrix} \bar{u}_w \\ \bar{u}_a \end{Bmatrix}$ ,  $\mathbf{u} = \begin{Bmatrix} u_w \\ u_a \end{Bmatrix}$ ,  $\mathbf{C} = \begin{bmatrix} 1 & C_w^a \\ C_a^w & 1 \end{bmatrix}$ ,  $\mathbf{K}_r = \begin{bmatrix} C_r^w & 0 \\ 0 & C_r^a \end{bmatrix}$ , and  $(\cdot)_{,r}$  and  $(\cdot)_{,t}$  denote the derivatives with respect to  $r$  and  $t$ , respectively.

**2.4. Initial and Boundary Conditions.** The external radius,  $r_e$ , is impervious or, because of symmetry, no water and air flow passes this boundary; that is,

$$\mathbf{u}_{,r} \Big|_{r=r_e} = 0. \quad (12)$$

Excess pore pressures at the interface of soil stratum and vertical drain satisfy flow continuity condition. The following boundary condition is considered:

$$\left( \mathbf{u}_{,r} + \frac{r_w}{2} \mathbf{B} \mathbf{u}_{,zz} \right) \Big|_{r=r_w} = 0, \quad (13)$$

$$\text{where } \mathbf{B} = \begin{bmatrix} k^w/k_r^w & 0 \\ 0 & k^a/k_r^a \end{bmatrix}.$$

The vertical boundary conditions are

$$\begin{aligned} \mathbf{u}|_{z=0} &= 0, \\ \mathbf{u}_{,z}|_{z=H} &= 0, \end{aligned} \quad (14)$$

which indicate that the top surface of the soft soil foundation is permeable to water and air, while the bottom surface is impermeable to water and air.

The initial excess pore pressures are uniform throughout the soil mass when  $t = 0$ . They can be calculated according to the method given by Fredlund and Rahardjo [15]. The initial condition is given as follows:

$$\bar{\mathbf{u}}|_{t=0} = \mathbf{u}_0, \quad (15)$$

$$\text{where } \mathbf{u}_0 = \begin{Bmatrix} u_0^w \\ u_0^a \end{Bmatrix}.$$

### 3. Solution of the Problem

**3.1. General Solution.** According to the boundary condition (12),  $\mathbf{u}_{,r}$  has to vanish as  $r$  goes to  $r_e$ . An integration of (11) with respect to  $r$  from  $r$  to  $r_e$  gives

$$\mathbf{u}_{,r} = \varphi(r) \mathbf{K}_r^{-1} \mathbf{C} \bar{\mathbf{u}}_{,t}, \quad (16)$$

where  $\varphi(r) = 1/2((r_e^2/r) - r)$ .

Then, an integration of (16) with respect to  $r$  in interval  $[r_w, r]$  results in

$$\mathbf{u} = \mathbf{u}|_{r=r_w} + \phi(r) \mathbf{K}_r^{-1} \mathbf{C} \bar{\mathbf{u}}_{,t}, \quad (17)$$

where  $\phi(r) = [(1/2)r_e^2 \ln(r/r_w)] - [(1/4)(r^2 - r_w^2)]$ .

Incorporating (17) into (4) to replace  $\mathbf{u}$  for  $\bar{\mathbf{u}}$ , we have

$$\bar{\mathbf{u}} = \mathbf{u}|_{r=r_w} + \psi \mathbf{K}_r^{-1} \mathbf{C} \bar{\mathbf{u}}_{,t}, \quad (18)$$

where  $\psi = (r_w^2/n^2 - 1)((1/2)n^4 \ln n - (3/8)n^4 + (1/2)n^2 - (1/8))$ .

The boundary condition of  $\mathbf{u}_{,zz}$  at  $r_w$  can be expressed as follows by combining (13) and (16):

$$\mathbf{u}_{,zz}|_{r=r_w} = -\frac{2\varphi(r_w)}{r_w} \mathbf{B}^{-1} \mathbf{K}_r^{-1} \mathbf{C} \bar{\mathbf{u}}_{,t}. \quad (19)$$

Substituting (19) into (18) results in

$$\mathbf{u}_{,zz}|_{r=r_w} = \frac{1}{\kappa^2} \mathbf{B}^{-1} (\mathbf{u}|_{r=r_w} - \bar{\mathbf{u}}), \quad (20)$$

where  $\kappa = (r_w/n^2 - 1)\sqrt{(1/2)n^4 \ln n - (3/8)n^4 + (1/2)n^2 - (1/8)}$ .

General solution for  $\mathbf{u}|_{r=r_w}$  can be written as products of functions with respect to dimensions  $z$  and time  $t$ . In addition, based on the homogeneous boundary conditions for the depth given in (14), the eigenfunction of  $\mathbf{u}|_{r=r_w}$  is  $\sin(Mz/H)$ . Hence,

$$\mathbf{u}|_{r=r_w} = \sum_{m=1}^{\infty} \frac{2}{M} \sin \frac{Mz}{H} \left[ \left( \frac{\kappa M}{H} \right)^2 \mathbf{B} + \mathbf{I} \right]^{-1} \mathbf{T}, \quad (21)$$

where  $\mathbf{I}$  is the identity matrix and  $M = [(2m-1)/2]\pi$ .

The average excess pore pressure  $\bar{\mathbf{u}}$  can be written as follows by substituting (21) into (20):

$$\bar{\mathbf{u}} = \sum_{m=1}^{\infty} \frac{2}{M} \sin \frac{Mz}{H} \mathbf{T}. \quad (22)$$

By substituting (21) and (22) into (18), the characteristic equation can be obtained using the orthogonality of sine function, as shown below:

$$\mathbf{T}_{,t} = \frac{1}{\psi} \mathbf{C}^{-1} \mathbf{K}_r \left\{ \mathbf{I} - \left[ \left( \frac{\kappa M}{H} \right)^2 \mathbf{B} + \mathbf{I} \right]^{-1} \right\} \mathbf{T}. \quad (23)$$

Based on the orthogonality of the sine function, the initial condition of  $\mathbf{T}$  can be obtained by the initial condition of  $\bar{\mathbf{u}}$  as

$$\mathbf{T}|_{t=0} = \mathbf{u}_0. \quad (24)$$

According to the initial condition (24), (23) can be solved as

$$\mathbf{T} = e^{-\mathbf{D}t} \mathbf{u}_0, \quad (25)$$

where  $\mathbf{D} = (1/\psi) \mathbf{C}^{-1} \mathbf{K}_r \left\{ \left[ \left( \frac{\kappa M}{H} \right)^2 \mathbf{B} + \mathbf{I} \right]^{-1} - \mathbf{I} \right\}$ .

Combining (21), (22), and (25) and substituting (21) and (22) into (17) give the solutions of  $\bar{\mathbf{u}}$  and  $\mathbf{u}$  as shown below:

$$\bar{\mathbf{u}} = \sum_{m=1}^{\infty} \frac{2}{M} \sin \frac{Mz}{H} e^{-\mathbf{D}t} \mathbf{u}_0, \quad (26)$$

$$\begin{aligned} \mathbf{u} &= \sum_{m=1}^{\infty} \frac{2}{M} \sin \frac{Mz}{H} \\ &\times \left\{ \left[ 1 - \frac{\phi(r)}{\psi} \right] \left[ \left( \frac{\kappa M}{H} \right)^2 \mathbf{B} + \mathbf{I} \right]^{-1} + \frac{\phi(r)}{\psi} \mathbf{I} \right\} e^{-\mathbf{D}t} \mathbf{u}_0. \end{aligned} \quad (27)$$

After solving  $\bar{\mathbf{u}}$ , the average degree of consolidation for water and air phases (i.e.,  $\mathbf{U}_e = \begin{pmatrix} U_{we} \\ U_{ae} \end{pmatrix}$ ) can be obtained as follows:

$$\mathbf{U}_e = \mathbf{F} - \frac{1}{H} \mathbf{E}^{-1} \int_0^H \bar{\mathbf{u}} dz = \mathbf{F} - \mathbf{E}^{-1} \sum_{m=1}^{\infty} \frac{2}{M^2} e^{-\mathbf{D}t} \mathbf{u}_0, \quad (28)$$

where  $\mathbf{E} = \begin{bmatrix} u_0^w & 0 \\ 0 & u_0^a \end{bmatrix}$  and  $\mathbf{F} = \begin{bmatrix} 1 \\ 1 \end{bmatrix}$ .

Based on Fredlund's theory, the volume change is given by the following constitutive equation for unsaturated soft soils [15]:

$$\frac{\partial \varepsilon_v}{\partial t} = m_{1k}^s \frac{\partial (q - \bar{u}_a)}{\partial t} + m_2^s \frac{\partial (\bar{u}_a - \bar{u}_w)}{\partial t}, \quad (29)$$

where  $\varepsilon_v$  is the volumetric strain,  $m_{1k}^s = m_{1k}^w + m_{1k}^a$  is the coefficient of volume change with respect to a change in net normal stress, and  $m_2^s = m_2^w + m_2^a$  is the coefficient of volume change with respect to a change in matric suction.

The ground surface settlement  $S_e$  of the unsaturated soft soil can be computed as

$$S_e = \int_0^H \int_0^t \frac{\partial \varepsilon_v}{\partial t} dt dz = HG \left( \mathbf{I} - \sum_{m=1}^{\infty} \frac{2}{M^2} e^{-Dt} \right) \mathbf{u}_0, \quad (30)$$

where  $\mathbf{G} = \{m_2^s \quad m_{1k}^s - m_2^s\}$ .

The normalized settlement, denoted as  $S_{ne}$ , can be determined based on the volumetric strain  $\varepsilon_v$  provided in (30):

$$S_{ne} = \frac{S_e}{S_e^{\infty}} = \frac{1}{\mathbf{G}\mathbf{u}_0} \mathbf{G} \left( \mathbf{I} - \sum_{m=1}^{\infty} \frac{2}{M^2} e^{-Dt} \right) \mathbf{u}_0, \quad (31)$$

where  $S_e^{\infty}$  is the ultimate ground surface settlement when the pore pressures dissipated entirely (i.e.,  $S_e^{\infty} = H[m_{1k}^s u_0^a + m_2^s (u_0^w - u_0^a)]$ ). As can be seen from (31),  $S_{ne}$  is also the total degree of consolidation which is dominated by both air and water phases.

**3.2. A Special Case.** When the effect of drain resistance is neglected, the permeability of drain well is endless, videlicet  $k^w$  and  $k^a$  tend towards infinity, which yields  $[(\kappa M/H)^2 \mathbf{B} + \mathbf{I}]^{-1} \rightarrow 0$ . Parameter  $\mathbf{D}$  can be rewritten as

$$\mathbf{D} = -\frac{1}{\psi} \mathbf{C}^{-1} \mathbf{K}_r. \quad (32)$$

Based on the theory of series, the following can be obtained:

$$\sum_{m=1}^{\infty} \frac{2}{M} \sin \frac{Mz}{H} = \sum_{m=1}^{\infty} \frac{2}{M^2} = 1 \quad (0 < z \leq H). \quad (33)$$

By substituting (32) and (33) into (26–28) and (30) and (31), the solutions can be simplified to

$$\bar{\mathbf{u}} = e^{(1/\psi)\mathbf{C}^{-1}\mathbf{K}_r t} \mathbf{u}_0, \quad (34)$$

$$\mathbf{u} = \frac{\phi(r)}{\psi} e^{(1/\psi)\mathbf{C}^{-1}\mathbf{K}_r t} \mathbf{u}_0, \quad (35)$$

$$\mathbf{U}_e = \mathbf{F} - \mathbf{E}^{-1} e^{(1/\psi)\mathbf{C}^{-1}\mathbf{K}_r t} \mathbf{u}_0, \quad (36)$$

$$S_e = HG \left( \mathbf{I} - e^{(1/\psi)\mathbf{C}^{-1}\mathbf{K}_r t} \right) \mathbf{u}_0, \quad (37)$$

$$S_{ne} = \frac{1}{\mathbf{G}\mathbf{u}_0} \mathbf{G} \left( \mathbf{I} - e^{(1/\psi)\mathbf{C}^{-1}\mathbf{K}_r t} \right) \mathbf{u}_0. \quad (38)$$

The equations from (34) to (38) are the simplified solutions in which the effect of drain resistance is neglected.

#### 4. Analysis of Consolidation Behavior

In this study, the accuracy of the proposed equal-strain consolidation model in the unsaturated soft soils is

investigated by comparing with the free-strain model. The consolidation behavior and influence factors are also discussed in this section. Following Fredlund and Rahardjo [15] and Conte [26], the consolidation parameters adopted in this study are listed as follows:

(i) Mechanical parameters

$$n_s = 0.5, S_s = 0.8, m_{1k}^w = -5 \times 10^{-8} \cdot \text{Pa}^{-1}, m_2^w = -2 \times 10^{-7} \cdot \text{Pa}^{-1}, m_{1k}^a = -2 \times 10^{-7} \cdot \text{Pa}^{-1}, m_2^a = 10^{-7} \cdot \text{Pa}^{-1}, k_r^w = 10^{-10} \text{ m/s}, k_r^a = 10^{-7} \text{ m/s}, k^w = 10^{-7} \text{ m/s}, \text{ and } k^a = 10^{-4} \text{ m/s}.$$

(ii) Fundamental constants of physics

$$T_{at} = 298.15 \text{ K}, R = 8.314 \text{ J/mol} \cdot \text{K}, u_{atm} = 101.3 \text{ kPa}, \omega_a = 29 \text{ g/mol}, g = 9.8 \text{ m/s}^2, \text{ and } \gamma_w = 10^4 \text{ N/m}^3.$$

(iii) Geometrical parameters

$$r_w = 0.2 \text{ m}, r_e = 1.8 \text{ m}, \text{ and } H = 10 \text{ m}.$$

(iv) Other parameters

$$q = 100 \text{ kPa}, u_0^w = 40 \text{ kPa}, \text{ and } u_0^a = 20 \text{ kPa}.$$

The above parameters are assumed to be constant during the consolidation process. An instantaneous compression induced by the external applied load  $q$  generates initial excess pore-water and pore-air pressures (i.e.,  $u_0^w$  and  $u_0^a$ , resp.). Considering that the soil is loaded three-dimensionally under isotropic conditions, changes in excess pore pressures can be determined using a method given by Fredlund and Hasan [16].

**4.1. Verification.** The validity of the equal-strain model had been verified in the saturated soft soils. In this section, the validity of the proposed equal-strain model in the unsaturated soft soils will be verified as well. For this purpose, the special consolidation case without considering drain resistance is analyzed by using the proposed equal-strain solution and one available free-strain solution [29].

Figures 2(a) and 2(b), respectively, demonstrate changes in the average degrees of consolidation of air and water phases with different ratios of  $k_r^a/k_r^w$  under the equal-strain and free-strain conditions. It is worth noting that the air permeability  $k_r^a$  is varying while the water permeability  $k_r^w$  is kept constant at  $10^{-10}$  m/s. In addition, the time factor is defined as  $T = C_r^w t/H^2$ . It can be observed from the figures that the results obtained from these two different models are in good agreement with each other. The slightly large difference between the two models is mainly found at the earlier stage of the consolidation process. Moreover, it can be seen that with an increase of  $k_r^a/k_r^w$ , the average degrees of consolidation increase gradually for both air phase and water phase. With an increase of consolidation time  $T$ , the curve of average degree of consolidation for water phase gradually tends to be consistent. This is because the pore-air pressure almost completely dissipates at the early stage of consolidation.

Figures 3(a) and 3(b) represent the difference of average consolidation degree between equal-strain model and free-strain model varying with  $T$  in different  $k_r^a/k_r^w$  values. As observed from Figure 3(a), the maximum difference (slightly more than 3%) between two models for air phase is mainly at

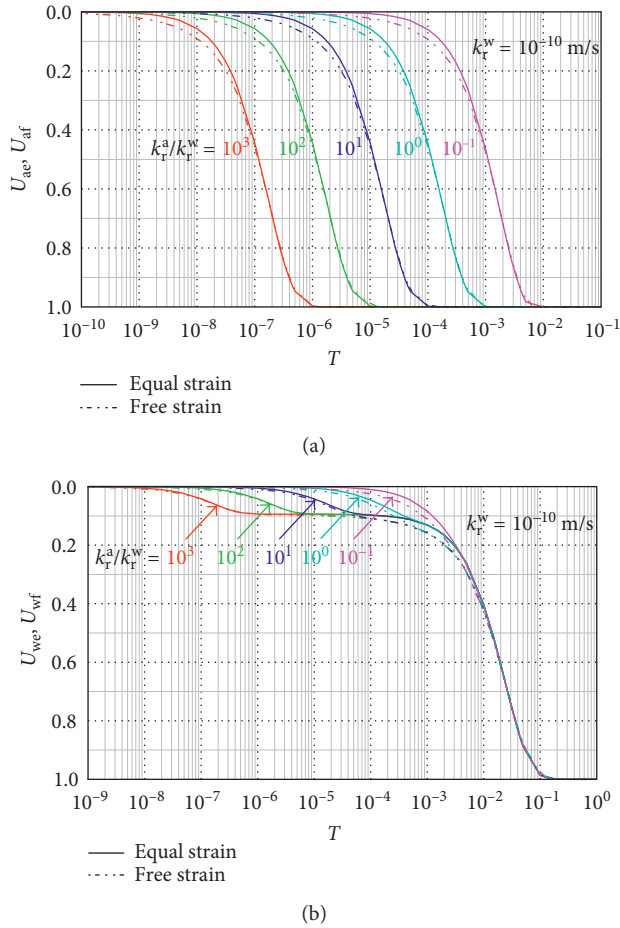


FIGURE 2: Average degrees of consolidation of (a) air phase and (b) water phase varying with different ratios of  $k_r^a/k_r^w$ .

the earlier stage of consolidation before the excess pore-water pressure begins to dissipate. Inversely, the maximum difference in the water phase is mainly near the end of the air dissipation, as shown in Figure 3(b). In brief, there is negligible influence on the difference between equal-strain condition and free-strain condition with different ratios of  $k_r^a/k_r^w$ . It shows that the equal-strain model is efficient in solving the unsaturated soil consolidation problem. Also, the solution is convenient for engineering application.

**4.2. Influence of Drain Resistance.** Figure 4 represents the degrees of consolidation of air and water phases and normalized settlement varying with  $T$  under different values of  $r_w$ . The influence radius  $r_e = 1.8$  m is adopted in this investigation. Figure 4(a) shows the degrees of consolidation of air phase varying with different values of  $r_w$  as time elapses. It is obvious that the consolidation proceeds more quickly with the increase of  $r_w$ . As the radius of vertical drain increases, the radial drainage area will be indirectly increased, which accelerates the process of consolidation. Figure 4(b) shows the degrees of consolidation of the water phase with different values of  $r_w$ . As observed, the rate of consolidation of water phase at the initial stage proceeds more quickly because of increasing  $r_w$ . After the excess pore-air pressure

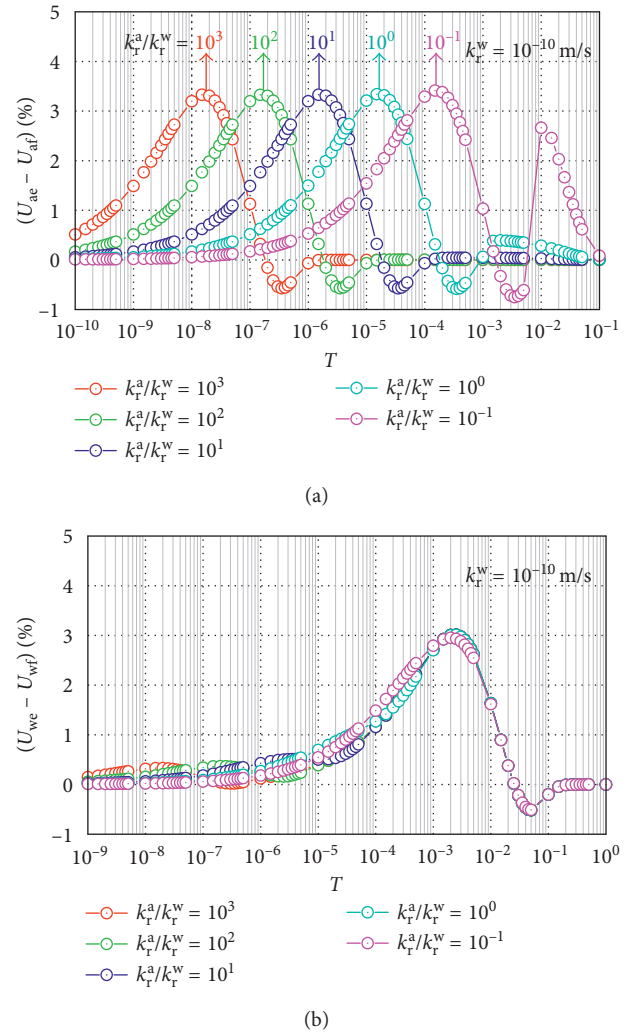


FIGURE 3: Difference of degrees of consolidation in (a) air phase and (b) water phase varying with different ratios of  $k_r^a/k_r^w$ .

dissipated almost completely, a plateau period may occur in the excess pore-water pressure patterns. At the later stage, the rate of water phase consolidation is similar to the initial stage. Besides, it can also be found that the excess pore-air pressure dissipated faster than that of the excess pore-water pressure because the permeability of air phase is greater than water phase both in the vertical drain and unsaturated soft soil foundation. Figure 4(c) presents the normalized settlement against time factor  $T$  with different values of  $r_w$ . The settlement process is similar to the consolidation process of water phase.

Figure 5 demonstrates changes in excess pore pressures and normalized settlement with different ratios of  $k^a/k^w$ . Figure 5(a) illustrates the dissipation curves of excess pore-air pressure varying with  $T$  in different ratios of  $k^a/k^w$ . As observed, when  $k^a/k^w$  increases, the excess pore-air pressure tends to dissipate faster. When  $k^a/k^w$  is very high, for instance,  $k^a/k^w = 10^3$ , the excess pore-air pressure may dissipate instantaneously. Figure 5(b) shows the dissipation curves of excess pore-water pressure varying with  $k^a/k^w$  when time elapses. It is evident that the dissipation at the initial stage of consolidation proceeds more quickly as

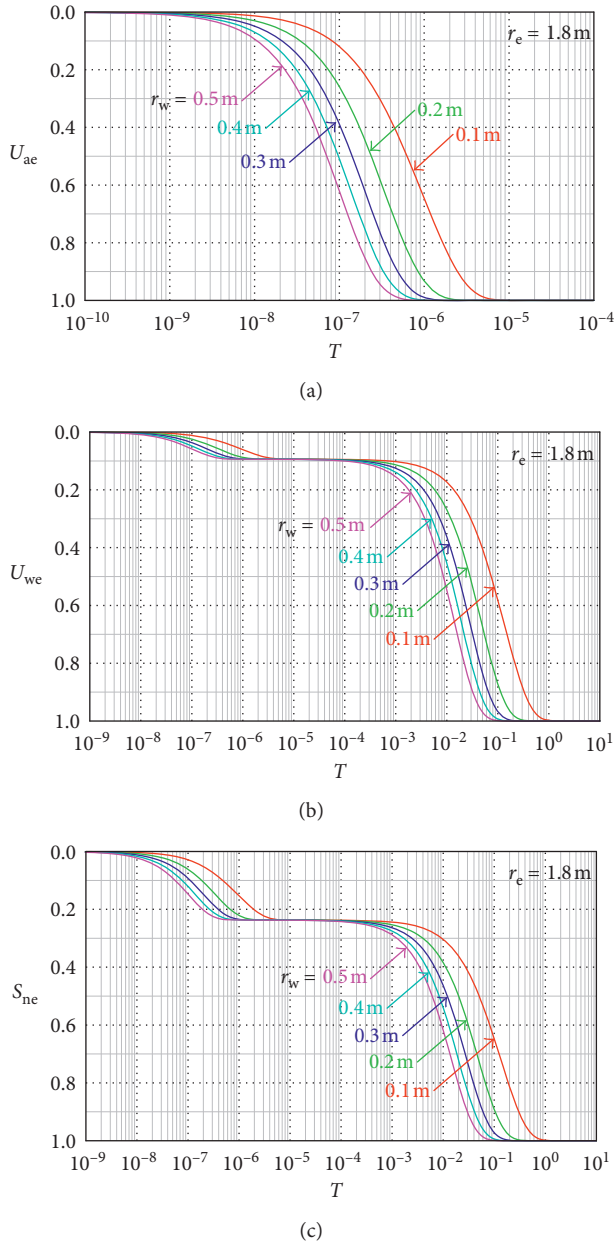


FIGURE 4: Degrees of consolidation of (a) air phase, (b) water phase, and (c) normalized settlement varying with different values of  $r_w$ .

a result of increasing  $k^a/k^w$ . After the excess pore-air pressure diminished almost fully, a plateau period may occur in the excess pore-water pressure patterns when  $k^a/k^w > 1$ . It should be noted that the greater the ratio of  $k^a/k^w$  is, the longer the plateau gets. Lastly, the curves of excess pore-water pressure dissipation converge to a single curve, and complete dissipation occurs at approximately the same time. Figure 5(c) shows the variations of the normalized settlement against time factor  $T$  with different ratios of  $k^a/k^w$ . It is worth noting that  $S_{ne}$  patterns consist of double inverse S curves when  $k^a/k^w > 0.1$ , similar to the excess pore-water pressure dissipation process. The initial stage of consolidation is governed by the simultaneous dissipation of both excess pore-air and pore-water pressures, and once the

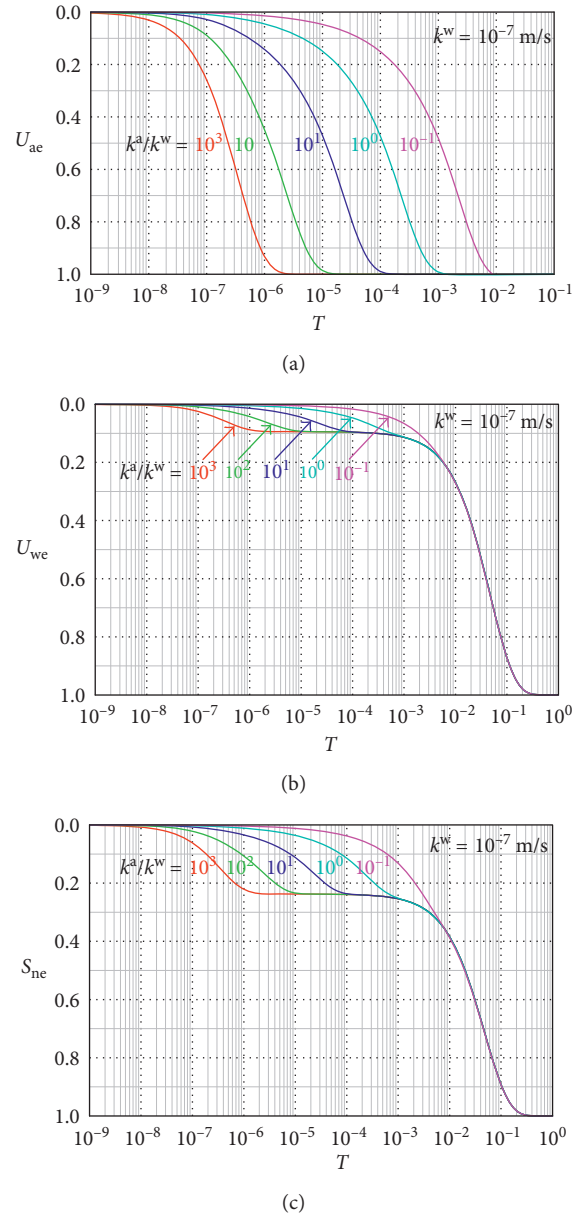


FIGURE 5: Degrees of consolidation of (a) air phase, (b) water phase, and (c) normalized settlement varying with different ratios of  $k^a/k^w$ .

excess pore-air pressure is fully dissipated in the soft soil system,  $S_{ne}$  patterns converge to only one curve and gradually approach 1 at the later stages. More remarkable, after the plateau period, the consolidation behavior is dominated by single phase (water phase) and the consolidation resembles to the classical Terzaghi's consolidation [1].

By comparing Figure 4 with Figure 5, the variation of vertical drain radius makes the normalized settlement  $S_{ne}$  a great change in the whole period of consolidation. In contrast, the difference of normalized settlement  $S_{ne}$  between different air permeabilities  $k^a$  is mainly observed before the plateau period. This is because the change of the radius of vertical drain influenced all period of consolidation process. However, the change of the air permeability of vertical drain

only had significant influence before the plateau period. After the plateau period, the consolidation process is dominated by water phase.

## 5. Summary and Conclusions

The equal-strain model established in this paper has a negligible difference for average degree of consolidation compared with the free-strain model. Parametric studies regarding well-resistance effect are graphically presented and discussed, and the key findings are summarized as follows:

- (1) The solutions calculated from the equal-strain model show good agreement with that obtained from the free-strain model. The main difference between the two models is mainly found at the earlier stage of the consolidation.
- (2) The higher the ratio of  $k_r^a/k_r^w$  is, the faster the consolidation is. With an increase of consolidation time  $T$ , the curve of average degree of consolidation for water phase gradually tends to be consistent.
- (3) With the increase of  $k^a/k^w$ , the excess pore-air and -water pressures tend to dissipate faster. After the excess pore-air pressure dissipated almost completely, a plateau period occurs in the excess pore-water pressure patterns when  $k^a/k^w > 1$ . It should be noted that the greater the ratio of  $k^a/k^w$  is, the longer the plateau gets.
- (4) Both the water and air phases of consolidation proceed more quickly with the increase of  $r_w$ , and the change of the radius of vertical drain influenced all period of consolidation process.

## Conflicts of Interest

The authors declare that they have no conflicts of interest.

## References

- [1] K. Terzaghi, *Theoretical Soil Mechanics*, John Wiley and Sons, New York, NY, USA, 1943.
- [2] R. L. Schiffman and J. R. Stein, "One-dimensional consolidation of layered systems," *Journal of the Soil Mechanics and Foundations Division*, vol. 96, no. 4, pp. 1499–1504, 1970.
- [3] J. Zhang, G. Cen, W. Liu, and H. Wu, "One-dimensional consolidation of double-layered foundation with depth-dependent initial excess pore pressure and additional stress," *Advances in Materials Science and Engineering*, vol. 2015, Article ID 618717, 13 pages, 2015.
- [4] J. C. Liu, G. H. Lei, and Y. X. Wang, "One-dimensional consolidation of soft ground considering non-Darcy flows," *Chinese Journal of Geotechnical Engineering*, vol. 33, no. 7, pp. 1117–1122, 2011, in Chinese.
- [5] Z. Liu, F. Yan, and X. Wang, "One-dimensional rheological consolidation analysis of saturated clay considering non-Darcy flow," *Chinese Journal of Rock Mechanics and Engineering*, vol. 32, no. 9, pp. 1937–1944, 2013, in Chinese.
- [6] E. Conte and A. Troncone, "One-dimensional consolidation under general time-dependent loading," *Canadian Geotechnical Journal*, vol. 43, no. 11, pp. 1107–1116, 2006.
- [7] S. C. Lu and T. W. Hsu, "Behavior of one-dimensional consolidation under time-dependent loading," *Journal of Engineering Mechanics*, vol. 132, no. 4, pp. 457–462, 2006.
- [8] R. E. Gibson, "A one-dimensional consolidation problem with a moving boundary," *Quarterly of Applied Mathematics*, vol. 18, no. 2, pp. 123–129, 1960.
- [9] W. H. Zhou and L. S. Zhao, "One-dimensional consolidation of unsaturated soil subjected to time-dependent loading with various initial and boundary conditions," *International Journal of Geomechanics*, vol. 14, no. 2, pp. 291–301, 2014.
- [10] K. H. Xie, X. Y. Xie, and W. Jiang, "A study on one-dimensional nonlinear consolidation of double-layered soil," *Computers and Geotechnics*, vol. 29, no. 2, pp. 151–168, 2002.
- [11] R. P. Chen, W. H. Zhou, H. Z. Wang, and Y. M. Chen, "One-dimensional nonlinear consolidation of multi-layered soil by differential quadrature method," *Computers and Geotechnics*, vol. 32, no. 5, pp. 358–369, 2005.
- [12] G. E. Blight, *Strength and Consolidation Characteristics of Compacted Soils*, Ph.D. dissertation, University of London, London, UK, 1961.
- [13] L. Barden, "Consolidation of compacted and unsaturated clays," *Géotechnique*, vol. 15, no. 3, pp. 267–286, 1965.
- [14] V. Dakshanamurthy, D. G. Fredlund, and H. Rahardjo, "Coupled three-dimensional consolidation theory of unsaturated porous media," in *Proceedings of the 5th International Conference on Expansive Soils*, pp. 99–103, Adelaide, SA, Australia, May 1984.
- [15] D. G. Fredlund and H. Rahardjo, *Soil Mechanics for Unsaturated Soils*, John Wiley and Sons, New York, NY, USA, 1993.
- [16] D. G. Fredlund and J. U. Hasan, "One-dimensional consolidation theory of unsaturated soils," *Canadian Geotechnical Journal*, vol. 17, no. 3, pp. 521–531, 1979.
- [17] A. F. Qin, G. J. Chen, Y. W. Tan, and D. A. Sun, "Analytical solution to one-dimensional consolidation in unsaturated soils," *Applied Mathematics and Mechanics*, vol. 29, no. 10, pp. 1329–1340, 2008.
- [18] A. F. Qin, D. A. Sun, and Y. W. Tan, "Semi-analytical solution to one-dimensional consolidation in unsaturated soils," *Applied Mathematics and Mechanics*, vol. 31, no. 2, pp. 215–226, 2009.
- [19] Z. D. Shan, D. S. Ling, and H. J. Ding, "Exact solutions for one-dimensional consolidation of single-layer unsaturated soil," *International Journal for Numerical and Analytical Methods in Geomechanics*, vol. 36, no. 6, pp. 708–722, 2012.
- [20] W. H. Zhou, L. S. Zhao, and X. B. Li, "A simple analytical solution to one-dimensional consolidation for unsaturated soils," *International Journal for Numerical and Analytical Methods in Geomechanics*, vol. 38, no. 8, pp. 794–810, 2013.
- [21] L. Ho, B. Fatahi, and H. Khabbaz, "Analytical solution for one-dimensional consolidation of unsaturated soils using eigenfunction expansion method," *International Journal for Numerical and Analytical Methods in Geomechanics*, vol. 38, no. 10, pp. 1058–1077, 2014.
- [22] Z. D. Shan, D. S. Ling, and H. J. Ding, "Analytical solution for 1D consolidation of unsaturated soil with mixed boundary condition," *Journal of Zhejiang University Science A*, vol. 14, no. 1, pp. 61–70, 2013.
- [23] A. F. Qin, D. A. Sun, and Y. W. Tan, "Analytical solution to one-dimensional consolidation in unsaturated soils under loading varying exponentially with time," *Computers and Geotechnics*, vol. 37, no. 1-2, pp. 233–238, 2010.
- [24] L. Ho and B. Fatahi, "One-dimensional consolidation analysis of unsaturated soils subjected to time-dependent loading,"

- International Journal of Geomechanics*, vol. 16, no. 2, p. 04015052, 2016.
- [25] Z. Shan, D. Ling, and H. Ding, "Analytical solution for the 1D consolidation of unsaturated multi-layered soil," *Computers and Geotechnics*, vol. 57, pp. 17–23, 2014.
- [26] E. Conte, "Plane strain and axially symmetric consolidation in unsaturated soils," *International Journal of Geomechanics*, vol. 6, no. 2, pp. 131–135, 2006.
- [27] L. Ho, B. Fatahi, and H. Khabbaz, "A closed form analytical solution for two-dimensional plane strain consolidation of unsaturated soil stratum," *International Journal for Numerical and Analytical Methods in Geomechanics*, vol. 39, no. 15, pp. 1665–1692, 2015.
- [28] L. Ho and B. Fatahi, "Analytical solution for the two-dimensional plane strain consolidation of an unsaturated soil stratum subjected to time-dependent loading," *Computers and Geotechnics*, vol. 67, pp. 1–16, 2015.
- [29] A. F. Qin, D. A. Sun, L. P. Yang, and Y. F. Weng, "A semi-analytical solution to consolidation of unsaturated soils with the free drainage well," *Computers and Geotechnics*, vol. 37, no. 7-8, pp. 867–875, 2010.
- [30] W. H. Zhou and S. Tu, "Unsaturated consolidation in a sand drain foundation by differential quadrature method," *Procedia Earth and Planetary Science*, vol. 5, pp. 52–57, 2012.
- [31] W. H. Zhou, "Axisymmetric consolidation of unsaturated soils by differential quadrature method," *Mathematical Problems in Engineering*, vol. 2013, Article ID 497161, 14 pages, 2013.
- [32] L. Ho, B. Fatahi, and H. Khabbaz, "Analytical solution to axisymmetric consolidation in unsaturated soils with linearly depth-dependent initial conditions," *Computers and Geotechnics*, vol. 74, pp. 102–121, 2016.
- [33] R. A. Barron, "Consolidation of fine grained soils by drain wells," *Transactions of the American Society of Civil Engineers*, vol. 113, pp. 718–742, 1948.
- [34] K. H. Xie and G. X. Zeng, "Consolidation theories for drain wells under equal strain condition," *Chinese Journal of Geotechnical Engineering*, vol. 11, no. 2, pp. 3–17, 1989, in Chinese.
- [35] C. J. Leo, "Equal strain consolidation by vertical drains," *Journal of Geotechnical and Geoenvironmental Engineering*, vol. 130, no. 3, pp. 316–327, 2015.
- [36] E. Conte, A. Troncone, and M. Vena, "A method for the design of embedded cantilever retaining walls under static and seismic loading," *Géotechnique*, vol. 67, no. 12, pp. 1–9, 2017.

## Research Article

# Study on Relaxation Damage Properties of High Viscosity Asphalt Sand under Uniaxial Compression

Yazhen Sun,<sup>1</sup> Zhangyi Gu,<sup>2</sup> Jinchang Wang,<sup>3</sup> Chenze Fang <sup>1</sup> and Xuezhong Yuan <sup>2</sup>

<sup>1</sup>School of Transportation Engineering, Shenyang Jianzhu University, Shenyang, China

<sup>2</sup>School of Science, Shenyang Jianzhu University, Shenyang, China

<sup>3</sup>Institute of Transportation Engineering, Zhejiang University, Hangzhou, China

Correspondence should be addressed to Xuezhong Yuan; [yuanxuezhong1@163.com](mailto:yuanxuezhong1@163.com)

Received 27 November 2017; Revised 24 January 2018; Accepted 28 February 2018; Published 1 April 2018

Academic Editor: Constantin Chaliotis

Copyright © 2018 Yazhen Sun et al. This is an open access article distributed under the Creative Commons Attribution License, which permits unrestricted use, distribution, and reproduction in any medium, provided the original work is properly cited.

Laboratory investigations of relaxation damage properties of high viscosity asphalt sand (HVAS) by uniaxial compression tests and modified generalized Maxwell model (GMM) to simulate viscoelastic characteristics coupling damage were carried out. A series of uniaxial compression relaxation tests were performed on HVAS specimens at different temperatures, loading rates, and constant levels of input strain. The results of the tests show that the peak point of relaxation modulus is highly influenced by the loading rate in the first half of an L-shaped curve, while the relaxation modulus is almost constant in the second half of the curve. It is suggested that for the HVAS relaxation tests, the temperature should be no less than  $-15^{\circ}\text{C}$ . The GMM is used to determine the viscoelastic responses, the Weibull distribution function is used to characterize the damage of the HVAS and its evolution, and the modified GMM is a coupling of the two models. In this paper, the modified GMM is implemented through a secondary development with the USDFLD subroutine to analyze the relaxation damage process and improve the linear viscoelastic model in ABAQUS. Results show that the numerical method of coupling damage provides a better approximation of the test curve over almost the whole range. The results also show that the USDFLD subroutine can effectively predict the relaxation damage process of HVAS and can provide a theoretical support for crack control of asphalt pavements.

## 1. Introduction

Relaxation modulus is a main viscoelastic parameter of an asphalt mixture and is used as an important basis for evaluating and analyzing the performance and predicting the long-term stability of a pavement. Therefore, an accurate determination of the relaxation modulus is very important. In general, the time effect in a viscoelastic material is mainly caused by the temperature, the load, the stress level, and the loading pattern. At the stages of construction and operation of a road, the stress level and the loading rate of the asphalt mixture are different. The rheological properties of the asphalt mixture are affected by the temperature, the vehicle load, and the vehicle speed. The stress in the pavement gradually dissipates with the passage of time, and stress relaxation occurs. When the temperature is very high, the stress accumulated in the pavement will dissipate quickly because of the stronger relaxation ability. However, when

the temperature is lower, the stress accumulated in the pavement will dissipate slowly because of the poor relaxation ability, and cracks may occur when the final stress is greater than the ultimate strength of the material [1]. It is necessary to study the viscoelastic properties of asphalt mixtures by relaxation tests in order to control the development of this disease in pavements.

Since the pioneering work of stress relaxation [2], there has been an increase of interest in this field [3–6]. Nowadays, there are two popular solutions for the determination of the relaxation modulus, one method is through the relaxation tests (the direct method) and another method is by the interconversion from the creep compliance (the indirect method) [7]. Hopkins and Hamming [8] discretized the time domain and established an iterative expression between the relaxation modulus and the creep compliance which was obtained from creep tests and can be transformed to relaxation modulus. However, the indirect

method is comparatively complicated [9]. In the past, stress relaxations were researched mainly through uniaxial tension tests and bending tests. In fact, the pavement surface of asphalt concrete is generally subjected to compression load. Now, a direct compression relaxation test can be carried out with the improvement of experimental technologies, with its loading pattern being analogue to the actual loading pattern. Hence, a reliable analytical solution for the determination of the relaxation modulus by uniaxial compressive relaxation tests with *high viscosity asphalt sand* (HVAS) is proposed in this paper. As suggested in the literatures, the direct compression relaxation modulus tests were carried out to get more accurate relaxation modulus.

There are initial cracks and voids in the asphalt mixture, which leads to the deterioration and damage of the materials. For such heterogeneous material as the asphalt mixture, the statistical Weibull damage model was used to reflect the deterioration of the asphalt mixture [10], and the damage probability of the asphalt mixture was described by the Weibull function [11]. Although ABAQUS provides a large number of unit libraries and solving models for users, it is inevitable that the general software is deficient in some certain fields. In view of this, ABAQUS provides a large number of user-defined subroutines to define the model [12]. During the secondary development of the UMAT subroutine, Yang [13] compiled the Mohr–Coulomb interface subroutine basing on the Rankine criterion. The results are consistent with the FLAC-3D calculation results, which indicate that the subroutine is of great value in guiding engineering practice. Fu [14], on the basis of the user material subroutine provided by UMAT, developed a modified Burgers creep model subroutine. It was proved that the subroutine could distinguish the viscoelastic deformation of the asphalt mixture correctly and made up for the deficiency of ABAQUS creep model [15]. Although the above researches demonstrate that the UMAT subroutine performs well in the fields of compression creep, the subroutine needs to determine the stress increment matrix, so the compilation process is rather complicated. With the aid of a simpler interface subroutine USDFLD (user subroutine to redefine field variables at a material point), the ABAQUS GMM is more suitable for a secondary development, which is used in the simulation of stress relaxation in this paper.

## 2. Experimental Program

**2.1. Theory.** Direct compression relaxation tests, at constant levels of input strain, were carried out on the specimens. The definition of the constant level of input strain at a given time  $t$  is

$$\varepsilon = \begin{cases} 0 & t < 0 \\ \varepsilon_0 & t \geq 0. \end{cases} \quad (1)$$

Due to the relaxation nature of the HVAS, the magnitude of the deformation is constant according to the preset program. Then the relaxation modulus can be calculated as

TABLE 1: Gradation.

Sieve size (mm)	Passing percentage
9.5	100
4.75	80.4
2.36	45.2
1.18	35.3
0.6	22.2
0.3	17.3
0.15	12.4
0.075	7.6



FIGURE 1: Prism specimen.

$$E(t) = \frac{F}{A \cdot \varepsilon_0}, \quad (2)$$

where  $F$  is the load (kN),  $\varepsilon_0$  is the constant level of input strain, and  $A$  is the cross-sectional area of the specimen ( $\text{mm}^2$ ).

**2.2. Material Properties.** A 70 penetration bitumen was used as asphalt binder for preparations of the specimens. Limestone was used as the aggregates. The ratio of binder to aggregates is 8.1% by weight. The continuous aggregate gradation, having the nominal maximum size of 10 mm, is listed in Table 1. An additional 1% activated rubber crumb and 0.7% TCA additive of the mass of asphalt mixture were added during the blending process.

**2.3. Specimen Preparations.** Track plate specimens manufactured by wheel rolling which agree with the standard test method [16] were cut into small beams with the dimensions of  $30 \times 35 \times 250 \text{ mm}^3$ .

As confirmed by the previous research, the specimen was proposed to be cylinder or nearly cube prism [15]. Since the desirable height to diameter ratio of a specimen was 2 [17], each beam was cut into  $30 \times 35 \times 70 \text{ mm}^3$  prism specimens to reduce the size effect. The specimens were polished to reduce the error in the loading area, as shown in Figure 1. During the polishing, the air blew continuously on the surface to help remove the debris generated.

**2.4. Determination of Constant Levels of Input Strain for Relaxation Tests.** Before the relaxation tests, the uniaxial



FIGURE 2: Diagonal failures of specimens under compression.

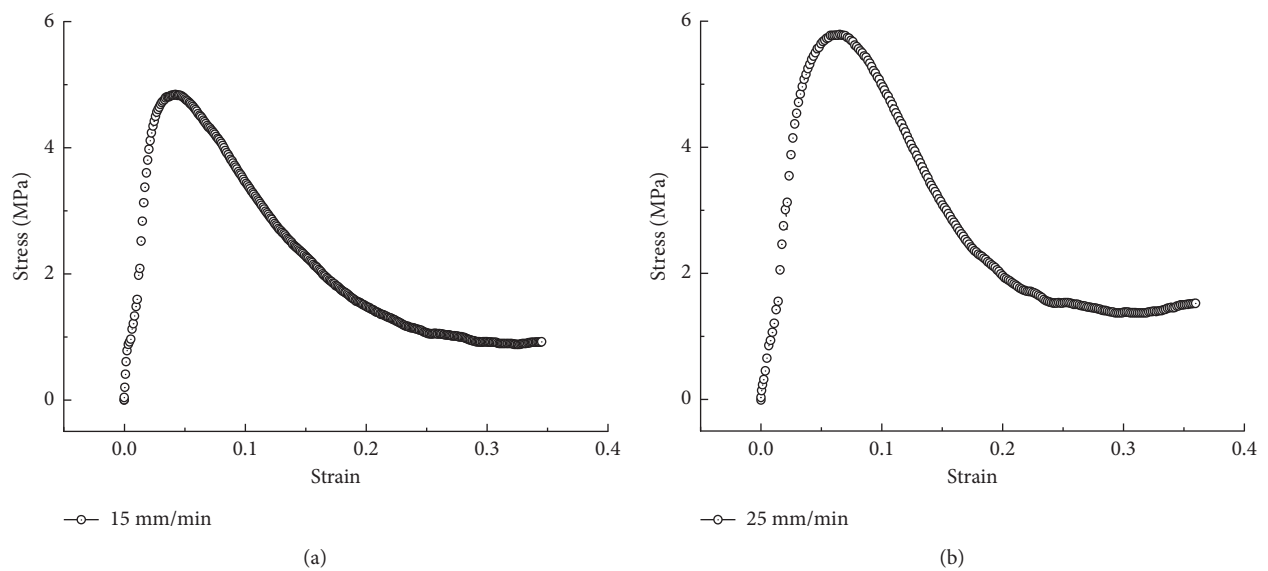


FIGURE 3: Stress-strain diagrams at different loading rates at 15°C. (a) 15 mm/min. (b) 25 mm/min.

compression strength tests were carried out, and the diagonal failures of specimens under compression are shown in Figure 2.

The stress-strain data of the compression failure tests at different loading rates were collected, and the diagrams are shown in Figure 3.

The constant level of input strain is a key parameter in the relaxation test. It should be noted that, in the uniaxial relaxation test, there was no standard evaluation method for defining the constant level of input strain until Walubita et al. [18] proposed that 20% of the maximum strain in a compressive test should be defined as the input strain. The constant level of input strain was calculated to characterize the viscoelastic behaviour of the HVAS within the undamaged limit. In general, it is widely accepted that the specimens are not damaged before the peak point of the stress-strain diagram. During the relaxation experiment, when the constant level of input strain varied from low to high, the property of the asphalt mixture changed from linear viscoelasticity to viscoplasticity [19]. Under the small-strain condition, the specimen was assumed to be not damaged (the

strain level was within the linearly viscoelastic range), so the constant level of input strain was conservatively assigned 10% of the strain at the maximum stress in our experiment. The corresponding displacement at the maximum stress, at the loading rates of 15 mm/min and 25 mm/min, respectively, was obtained from Figure 3 as 3.003 mm and 4.053 mm, respectively. The input displacements were set at 0.3 mm and 0.4 mm, respectively, after the rounding off.

**2.5. Uniaxial Compression Relaxation Tests.** The stress relaxation test is an experimental method for the determination of the viscoelastic parameters of materials, which is commonly used to evaluate the stress relaxation properties of materials. The stress response depends on the loading history as the viscoelastic material has the memory effect. Hence, the effects of loading process on the relaxation modulus were investigated. The direct compression relaxation modulus tests, at five constant levels of input strain of 0.004285, 0.012857, 0.021428, 0.042857, and 0.085714 (corresponding to the input displacements of 0.3 mm, 0.9 mm, 1.5 mm,

3 mm, and 6 mm), four temperatures of 15°C, -5°C, -15°C, and -25°C, four loading rates of 5 mm/min, 15 mm/min, 25 mm/min, and 50 mm/min, were conducted on each specimen; thus, a total of 144 tests were performed. After the specimen was put into the environmental chamber, the temperature was increased to the expected value. In order to reach thermal equilibrium inside the specimen, it should be conditioned for 4 hours or more. Vaseline was applied on the surface of the sample to reduce the friction and the boundary effect. The specimen was placed between the pressure head and the base of a WDW universal material testing machine, and then the constant level of input strain was applied.

### 3. Test Results and Analysis

**3.1. Compression Relaxation Tests at 15°C.** Figure 4 shows the effects of the loading rates on the relaxation moduli at 15°C as the input strain varies from 0.004228 to 0.08571.

As shown in Figure 4, the relaxation modulus of the HVAS at 15°C has an L-shaped curve over a wide range of time, and the modulus decreases sharply in the first half of the curve and then remains nearly constant in the second half. The L-shaped curve also agrees with the relaxation properties very well. During the test (Figures 4(a) and 4(b)), when the constant level of input strain was relative small, no obvious deterioration was observed in the specimen. As the loading rate increases, the speed of stress accumulated exceeds than that of dissipation, which leads to the increase of the peak point of the relaxation modulus. The peak point of relaxation modulus is highly influenced by the loading rate in the first half of the L-shaped curve, while the relaxation modulus is almost constant in the second half of the curve. The effect of the loading rate on the peak point of the relaxation curve is obvious with a larger constant level of input strain. When the input strain is less than 0.012857 (Figure 4 (a)), the peak point of the relaxation modulus increases proportionally to the loading rate because the material is in the elastic stage. However, when the input strain is larger (Figures 4(c)–4(e)), the peak point does not increase proportionally to the loading rate, and at 50 mm/min loading rate, it is not even the maximum modulus because the material is in the plastic stage.

In the first half of the L-shaped curve, the relaxation modulus increases with the input strain (Figures 4(a)–4(d)). However, comparing Figures 4(d) and 4(e), when the input strain exceeds 0.042857, the peak point of the relaxation modulus decreases with higher input strain because the material is in the plastic stage. This fact confirmed that the damage of the specimen contributes to the decrease of the relaxation modulus because the stress exceeds the linear viscoelastic limit.

**3.2. Compression Relaxation Tests at -5°C.** The variation tendencies of the relaxation moduli of the HVAS, at a test temperature of -5°C, are similar to the previous tests, but the relaxation moduli increase significantly at the same loading rates and the constant levels of input strains, as shown in Figure 5. The capacity of relaxation can be expressed by the

rate of change of the relaxation modulus; the higher the rate of change, the stronger the relaxation capacity. Comparing the two groups of the graphs of the effects at 15°C and -5°C (Figures 4 and 5), the HVAS has a poor relaxation capacity at -5°C, and this is resulted from the low temperature, at which the stress has accumulated significantly. For example, as shown in Figures 4(d) and 5(d), when the input strain is 0.042857 at the loading rate of 25 mm/min, the variation of the relaxation modulus is 4400 MPa at 15°C and 2000 MPa at -5°C, respectively, and we say that the HVAS has a poor relaxation capacity at -5°C. If the input strain exceeds 0.042857, both the relaxation moduli are decreased instead of increasing. This is not surprising because of the emerging of damage of the HVAS.

**3.3. Compression Relaxation Tests at -15°C.** Compared with -5°C, the peak point of the relaxation modulus decreases as the constant level of input strain is just over 0.012857. This can be explained that the superposition of the stresses caused by the applied load and temperature results in a greater stress, which leads to the damage and consequently the decrease of the relaxation modulus, as shown in Figure 6. Meanwhile, the damage occurs and the extent of damage is dependent on the input strain. Under the continuous growth of the loading rate and the input strain, the failure of the HVAS prism is inevitable, and it is not necessary to complete the remaining test according to the plan.

**3.4. Compression Relaxation Tests at -25°C.** As shown in Figure 7, the deterioration of the sample occurs at the constant level of input strain of 0.021428. In addition, comparing with -15°C, the peak point of the relaxation modulus decreases as the input strain is 0.01285. This indicates that the damage of the HVAS shifts to an earlier stage. So, as the temperature drops, the damage occurs earlier.

The relaxation tests could be completed at the constant levels of input strain that ranges from 0.042857 to 0.085714 at temperatures above -5°C; however, obvious deterioration was observed in the specimen when the input strain is only 0.042857 at temperature below -5°C, and the test came to an end. Because the determination of the relaxation modulus is highly sensitive to the temperature, it is suggested that for the HVAS relaxation tests, the temperature should be no less than -15°C.

### 4. Determination of Model Parameters

Mechanical models may be considered as different combinations of linear spring(s) and linear dashpot(s) in various series and/or parallel arrangements depending upon the complexity of viscoelastic material behaviour. These basic elements and their combinations allow the modelling of the viscoelastic behaviour of asphalt mixtures and binders better than the empirical mathematical models. The linear spring responds the same as a linear elastic material, while the basic response of a linear dashpot is the same as that of a Newtonian fluid. Combining these two basics in various series

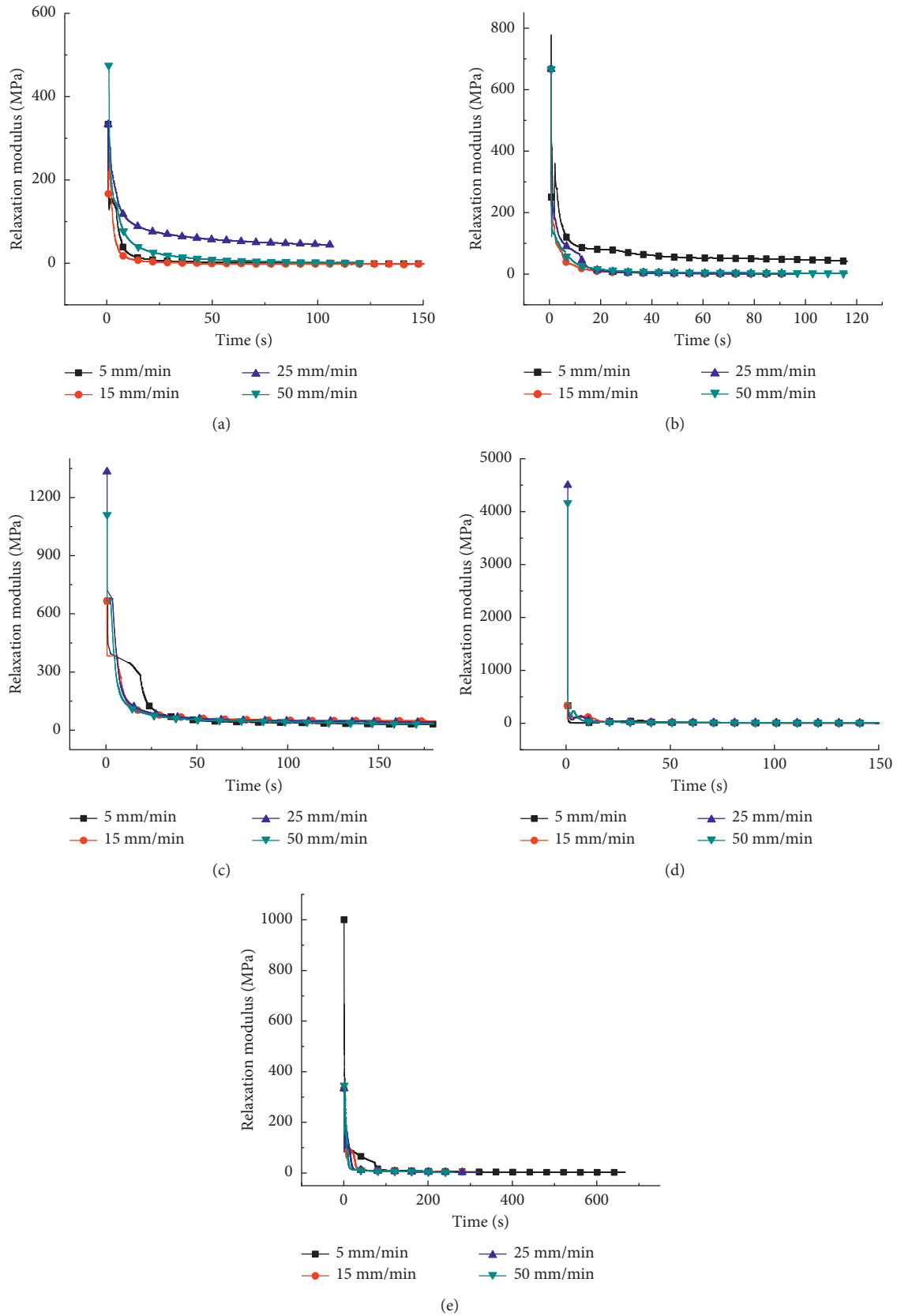


FIGURE 4: Effects of different loading rates and constant levels of input strain on relaxation moduli at 15°C. (a) 0.004285. (b) 0.012857. (c) 0.021428. (d) 0.042857. (e) 0.08571.

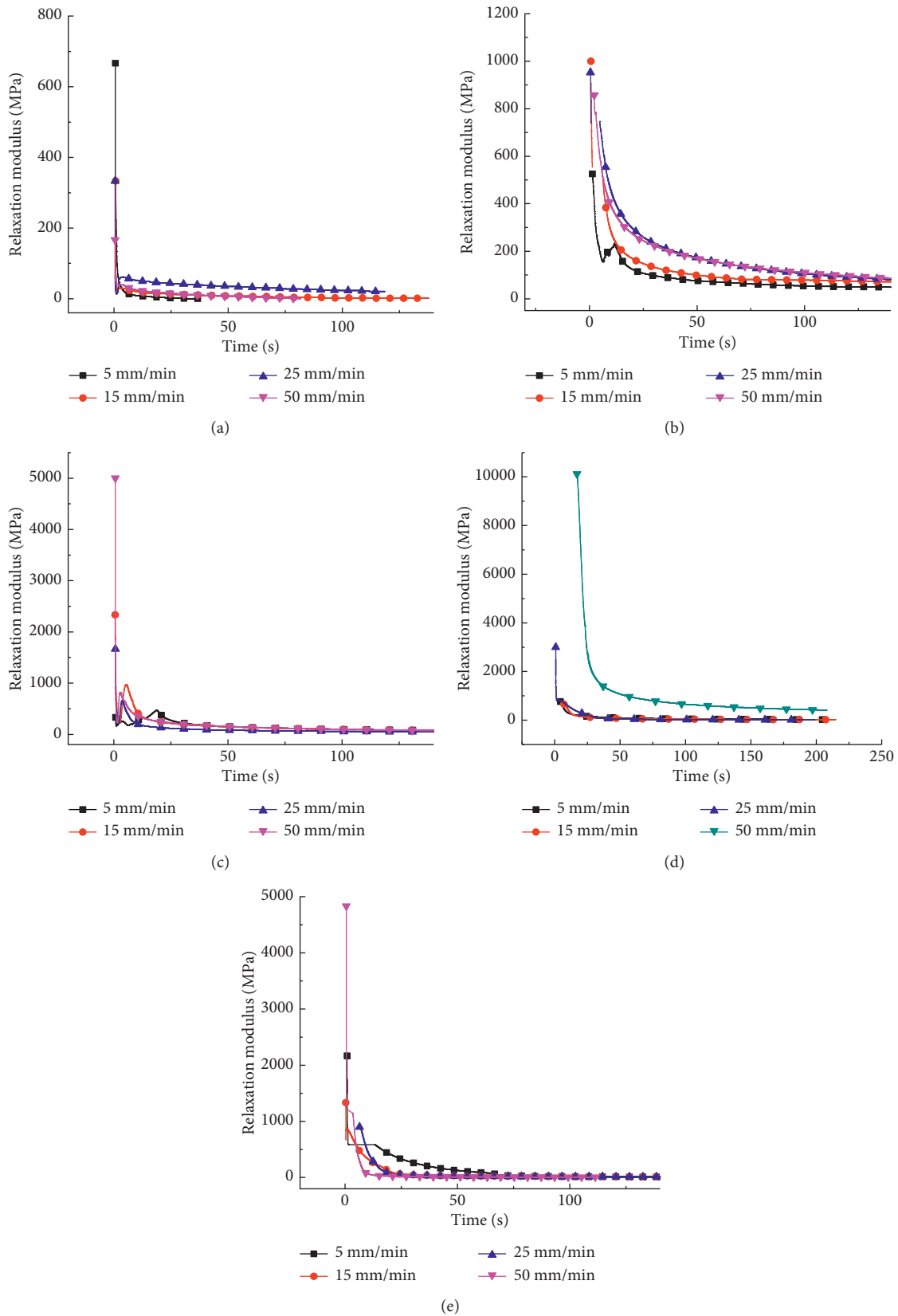
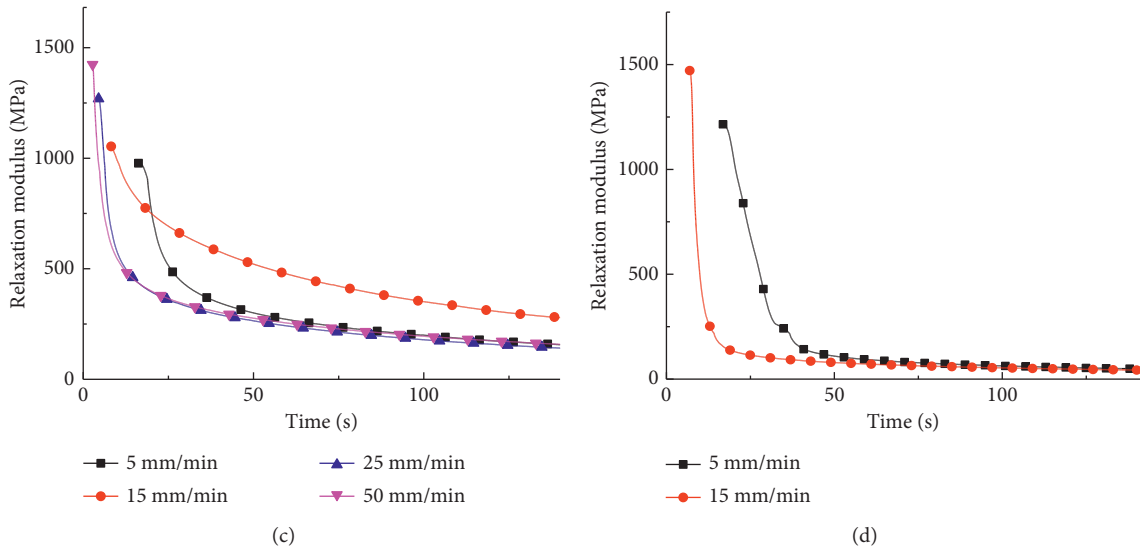
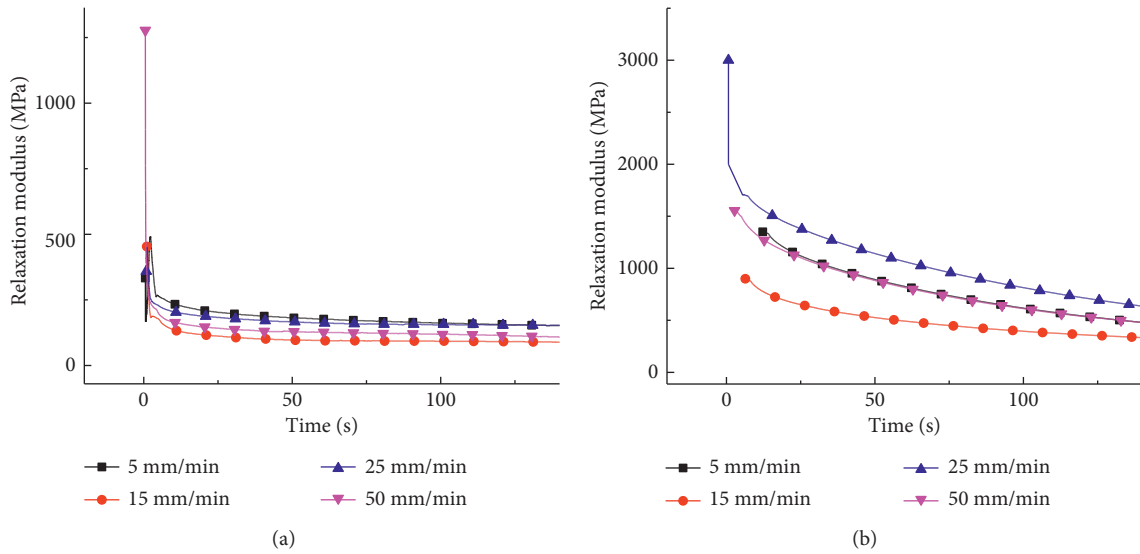


FIGURE 5: Effects of different loading rates and constant levels of input strains on relaxation moduli at  $-5^{\circ}\text{C}$ . (a) 0.004285. (b) 0.012857. (c) 0.021428. (d) 0.042857. (e) 0.085711.



(e)

FIGURE 6: Effects of different loading rates and constant levels of input strain on the relaxation moduli at  $-15^{\circ}\text{C}$ . (a) 0.004285. (b) 0.012857. (c) 0.021428. (d) 0.042857. (e) Specimen damages at  $-15^{\circ}\text{C}$ .

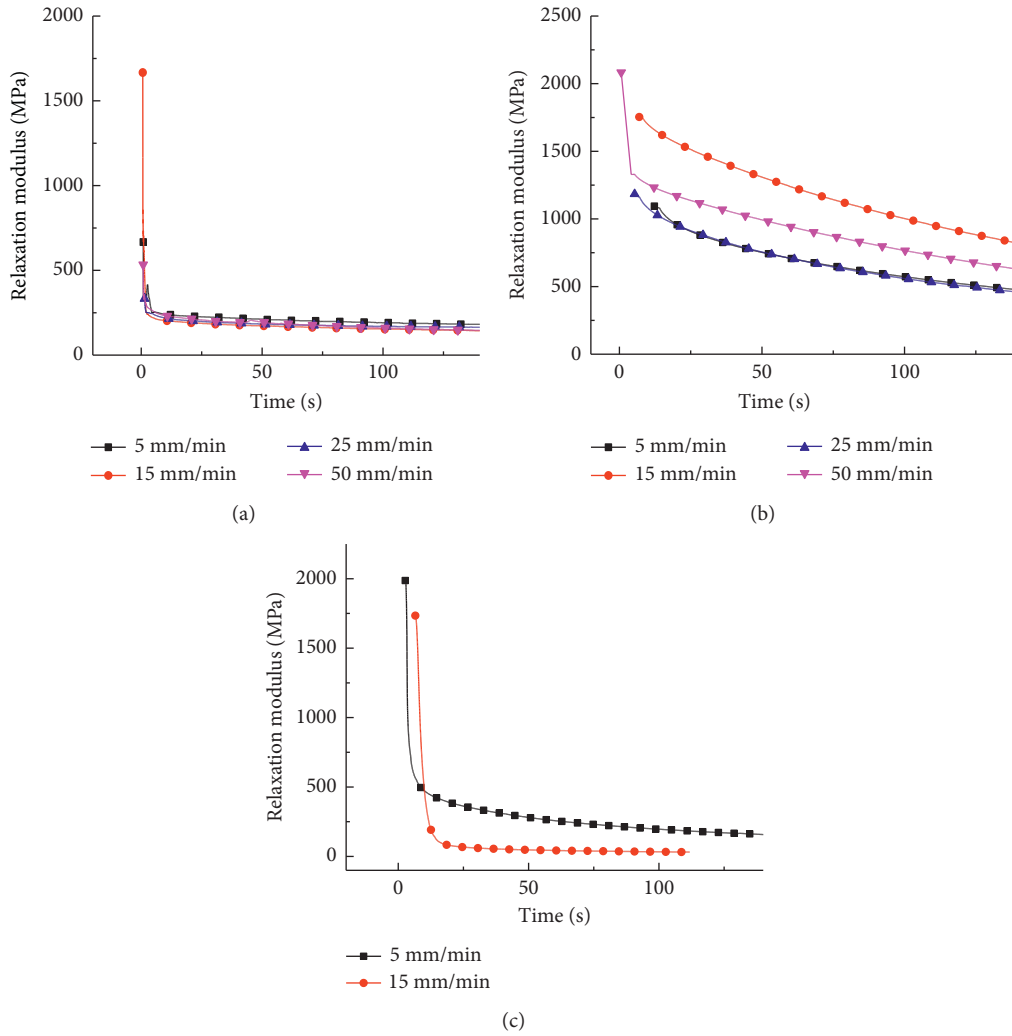


FIGURE 7: Effects of different loading rates and constant levels of input strain on relaxation moduli at  $-25^{\circ}\text{C}$ . (a) 0.004285. (b) 0.012857. (c) 0.021428.

and/or parallel arrangements produces the viscoelastic mechanical models, some of which, for example, Maxwell model and Kelvin model, are too simple to adequately model the actual behaviour of asphalt mixtures, while some other ones, for example, generalized models, may properly capture the actual behaviour of asphalt mixtures. The GMM appears to be the best phenomenological representation of the relaxation behaviour for HVAS [20].

The relaxation modulus  $E(t)$  of the HVAS can be calculated by employing GMM [21]:

$$E(t) = \sum_{i=1}^n E_i e^{-t/\tau_i}, \quad (3)$$

where  $E_i$  is the modulus for a single Maxwell model,  $t$  is the time,  $\tau_i$  is the relaxation time, and  $n$  is the number of elements for the GMM.

In agreement with the earlier results [22], the precision of the characterization of the viscoelastic behaviour varies with the number of GMM units, so 2, 4, 6, and 8 arms of GMM were used to fit the relaxation modulus at different

temperatures. An example is provided at the constant level of the input strain of 0.004285 and a loading rate of 50 mm/min, as listed in Table 2.

As shown in Table 2, the  $R^2$  value of the GMM increases with the number of units from 2 to 6. However, the  $R^2$  value decreases as the number of units increases from 6 to 8, so the GMM with 6 arms was used to characterize the relaxation of the HVAS.

Although the model parameters can express the relaxation properties of the HVAS, the more detailed damage behaviour is not depicted yet. So, there is still room for further study of the relaxation damage model.

## 5. USDFLD Development and Verification of HVAS Relaxation Damage

Relaxation often plays a crucial role in the rheological properties, so it is very important to carry out the accurate reliability analysis of the change law of the relaxation modulus. Initially, the GMM in the ABAQUS model library is used to determine the viscoelastic responses without

TABLE 2: GMM parameters at 15°C.

Model parameter	Number of units			
	2	4	6	8
$E_1$ (MPa)	182.072	2.004	1.493	15.261
$E_2$ (MPa)	1125.975	10.042	5015.853	15.261
$E_3$ (MPa)	—	18.491	41.397	41.927
$E_4$ (MPa)	—	295.548	18.603	15.199
$E_5$ (MPa)	—	—	157.825	1.214
$E_6$ (MPa)	—	—	1.409	1.214
$E_7$ (MPa)	—	—	—	1.214
$E_8$ (MPa)	—	—	—	15.199
$\tau_1/s$	10.737	6.707	4.604e21	2.433
$\tau_2/s$	0.646	39.878	1.264	2.433
$\tau_3/s$	—	80.755	26.342	11.278
$\tau_4/s$	—	5.628	1.435	2.433
$\tau_5/s$	—	—	6.398	2.436
$\tau_6/s$	—	—	1.715e21	2.436
$\tau_7/s$	—	—	—	2.437
$\tau_8/s$	—	—	—	2.433
$R^2$	0.9769	0.9896	0.9986	0.9886

TABLE 3: Damage thresholds at different constant levels of input strain at 15°C.

Input strain	0.004285	0.012857	0.021428	0.04285	0.08571
Damage threshold	0.0041	0.0093	0.017	0.021	0.047

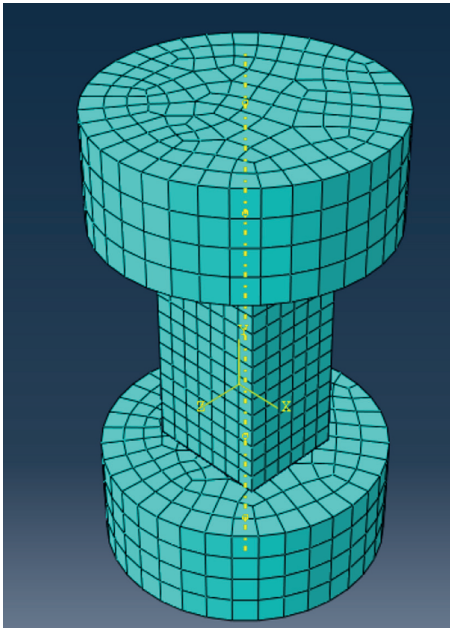


FIGURE 8: Diagram of the model mesh.

associating with the damage while the relaxation behaviour is strongly dependent on the viscoelastic damage. In order to study the relaxation damage property, a modified GMM relaxation damage model was established with the USDFLD subroutine. With the new development modified GMM relaxation damage model in ABAQUS, numerical simulations of uniaxial compression relaxation tests were carried out.

TABLE 4: Prony parameters at 15°C.

Model parameter	Input strain				
	0.004285	0.01285	0.021428	0.04285	0.08571
$E_1$	5.44E-08	0.5334	0.690846	2.14E-05	0.15845
$E_2$	0.000182	0.2115	0.014715	0.11	0.27840
$E_3$	1.50E-06	0.1214	0.104812	0.1067	0.13184
$E_4$	6.782E-07	0.0809	0.054306	0.01099	0.07601
$E_5$	5.754E-06	0.0303	0.051410	0.7688	0.07601
$E_6$	5.137E-08	0.0202	0.08353	1.76E-06	0.27828
$\tau_1/s$	4.604e21	32.12	23.4	1	1
$\tau_2/s$	1.264	191.37	1.52	18.84	3.16
$\tau_3/s$	26.342	986.68	436.43	18.84	19.5
$\tau_4/s$	1.435	7549.62	3.53	1	286.09
$\tau_5/s$	6.398	129.321	65.88	7.422	296.14
$\tau_6/s$	1.715e21	3839104	6792.17	18.84	3.16

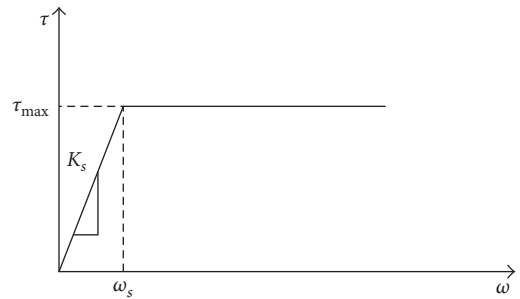


FIGURE 9: Elastic-plastic Coulomb friction model.

5.1. *Applications of USDFLD Subroutine in Damage Relaxation.* The ABAQUS built-in models have some limitations due to the fact that there are no coupling damage parameters in the models, so a modified GMM model is proposed. Firstly, the constitutive model suitable for the asphalt mixture was selected, and a USDFLD user subroutine was written by FORTRAN language to establish the correction model of coupling damage. Based on the ABAQUS software platform, not only the secondary development of the GMM constitutive model is realized, but also the damage mechanism is embedded. The subroutine is invoked by a call function in the calculation process. Some known parameters are passed by the ABAQUS main program, combined with the generalized Hooke law, to calculate the test strain, which is used to determine whether the strain exceeds the threshold value of damage, and the choice of the appropriate calculation method. Secondly, using the compiled USDFLD subroutine, a 3-D finite element model was established to study the damage relaxation behaviour of the HVAS, and the performance of the linear viscoelastic model in ABAQUS was also improved.

5.2. *Relaxation Damage Constitutive Relationship.* The 6-element-generalized Maxwell model coupling damage is chosen as the basis to simulate the stress relaxation damage process at different temperatures and constant levels of input strain.

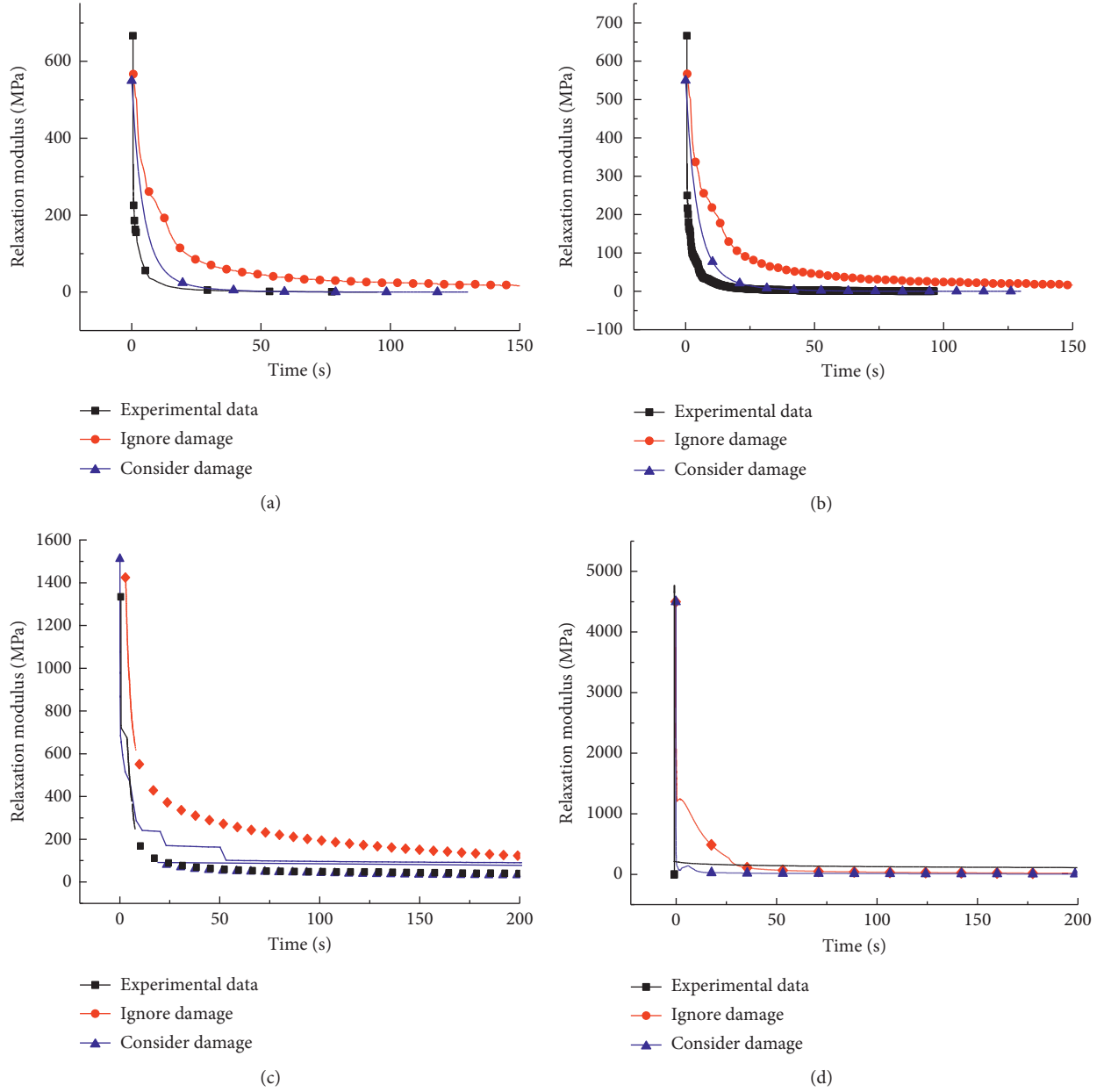


FIGURE 10: Comparisons of numerical simulation and experimental results. (a) 0.004285. (b) 0.012857. (c) 0.021428. (d) 0.042857.

The effective stress is given by [23]:

$$\tilde{\sigma}_{ij} = \frac{\sigma_{ij}}{1-D}, \quad (4)$$

where  $\tilde{\sigma}_{ij}$  is the effective stress tensor (MPa),  $\sigma_{ij}$  is the Cauchy stress tensor (MPa), and  $D$  is the damage factor.

The damage factor  $D$  is in line with the Weibull distribution:

$$D = \int_{\gamma}^{\epsilon} \frac{n}{m} (x-\gamma)^{n-1} e^{-(x-\gamma)^n/m} dx = 1 - e^{-(\epsilon-\gamma)^n/m}, \quad (5)$$

where  $m$  and  $n$  are model parameters and  $\gamma$  is the threshold of damage.

Substituting (3) into (2), the relaxation modulus is obtained:

$$E(t) = \frac{\sigma(t)}{\epsilon_0} = e^{-(\epsilon-\gamma)^n/m} \left( \sum_{i=1}^n E_i e^{-t/\tau_i} \right). \quad (6)$$

By (6), the damage thresholds can be obtained through uniaxial compression relaxation experiments. The damage thresholds corresponding to the constant levels of input strain of the uniaxial compression tests are calculated at the loading rate of 50 mm/min, as shown in Table 3.

5.3. *Establishing of a 3-D Solid Model.* ABAQUS, powerful and easily operated finite element software, is well equipped to address the problems of geometric nonlinear materials, nonlinear stress loads, boundary conditions, and nonlinear

contact. Therefore, it was used to simulate the relaxation process of the asphalt mixtures. The model size is consistent with the specimen in the relaxation test, that is,  $30 \times 35 \times 70 \text{ mm}^3$ . To better simulate the test process, two cylinders with a diameter of 80 mm and a thickness of 30 mm were established after setting up the specimen model, to simulate the pressure head and the base, as shown in Figure 8.

**5.3.1. Material Parameters.** The experimental data were fitted to obtain the parameters for the Prony series of the HVAS at 15°C, as listed in Table 4.

**5.3.2. Nonlinear Contact Model.** In the relaxation test, the contact process has nonlinear characteristics. Therefore, the contact and the friction on the interface should be considered to better simulate the reaction test process. The Coulomb friction model is usually chosen when studying contact problems involving friction in solid mechanics. In the simplified model of static linear elasticity, this law is generally considered together with the unilateral contact model which describes the possible separation of the body from the contact surface (or a rigid foundation) and the absence of penetration of the body into the surface. The interface mechanical behaviour described by the Coulomb contact model is consistent with the relaxation test, so it was used to control the interlayer contact. The nonlinearity of interlayer contact is more obvious when the friction coefficient is less than 0.6, so 0.5 is taken as the friction coefficient. The relationship between the shearing stress and the normal stress of the Coulomb friction model is shown in Figure 9. The constitutive model of contact element uses the elastic Coulomb friction model, and the relationship between the shearing stress and the normal stress is defined as

$$\begin{cases} \tau = K_S \omega & \omega < \omega_S \\ \tau = \mu p & \omega \geq \omega_S, \end{cases} \quad (7)$$

where  $\tau$  is the shearing stress,  $p$  is the normal stress,  $\omega$  is the relative displacement between the contact surface,  $\omega_S$  is the relative displacement of elastic limit, and  $\mu$  is the friction coefficient between the surfaces.

**5.4. Results and Analysis.** The relaxation stress data of the HVAS were obtained in the RPT file format. The stress relaxation curves corresponding to the constant levels of input strains are shown in Figure 10.

As shown in Figure 10, the relaxation modulus obtained by the numerical simulation has a relatively good agreement with the relaxation tests. Especially, taking into account the damage modulus, the difference of the relaxation modulus is obvious at the inflection point of the L-shaped curve. This proves that the damage has obvious effect on the relaxation characteristics of the HVAS.

After taking into account the damage modulus, the simulation values provide a better approximation for the experimental data. There is still a minor deviation between the simulation result and the experimental value at the

inflection point of the relaxation modulus curve because a linear interpolation was performed as the data were calculated by ABAQUS, and if the data density is increased, the fitting degree will be further improved.

Results show that the numerical method which takes into account the damage provides a better approximation for the experimental data over almost the whole range of the curve which illustrates that the USDFLD subroutine could effectively predict the relaxation damage process of asphalt mixtures and provide new support for crack control of asphalt pavements.

## 6. Conclusions

The effects of temperatures, loading rates, and constant levels of input strain on relaxation properties by the uniaxial compression tests were investigated. The uniaxial compression tests were employed to determine the relaxation moduli. In order to obtain reliable and reasonable test results, the size of specimens were designed and the constant levels of input strain were defined to ensure that the initial stages of the compression tests were linear elastic. The GMM is used to determine the viscoelastic responses, the Weibull distribution function is used to characterize the damage of the HVAS and its evolution, and the modified GMM is a coupling of the two models. The modified GMM was implemented through a secondary development with the USDFLD subroutine to analyze the relaxation damage process and improve the linear viscoelastic model in ABAQUS. Basing on the findings, the following conclusions can be made:

- (1) The relaxation response was significant and similar within the temperature range from  $-25^\circ\text{C}$  to  $15^\circ\text{C}$ . The relaxation modulus of the HVAS has an L-shaped curve over a wide range of time; the modulus decreases sharply in the first half of the curve and then remains nearly constant in the second half of the curve. The L-shaped curve agrees with the relaxation properties very well.
- (2) The peak point of the relaxation modulus is highly influenced by the loading rate in the first half of the L-shaped curve, while the relaxation modulus is almost constant in the second half of the curve. When the input strain is small, the peak point of relaxation modulus increases proportionally to the loading rate because the material is in the elastic stage. However, when the input strain is larger, the peak point does not increase proportionally to the loading rate.
- (3) In the first half of the L-shaped curve, the relaxation modulus increases with the input strain (Figures 4 (a)–4(d)). However, the peak point of the relaxation modulus decreases with a higher input strain because the larger input strain brings about more damage in the material.
- (4) It is evident that the curve for the relaxation property slows down significantly at low temperature, which

leads to damage and even splitting, so some tests could not be completed. The relaxation modulus is highly sensitive to the temperature, and the failure occurs earlier at low temperatures. It is suggested that for the HVAAS relaxation tests, the temperature should be no less than  $-15^{\circ}\text{C}$ .

- (5) Results show that the numerical method which takes into account the damage provides a better approximation for the experimental data over almost the whole range which illustrates that the USDFLD subroutine can effectively predict the relaxation damage process of asphalt mixtures and provide new support for crack control of asphalt pavements.

## Conflicts of Interest

The authors declare that they have no conflicts of interest.

## Acknowledgments

This research was performed at the Shenyang Jianzhu University and Institute of Transportation Engineering of Zhejiang University. The research is funded by the National Natural Science Fund (51478276) and the Natural Science Foundation of Liaoning Province (20170540770).

## References

- [1] M. Shi-bu and H. Song, "Analysis on top-down cracks and its stress intensity factor of semi-rigid pavement," *Western China Communications Science & Technology*, vol. 6, pp. 22–26, 2015.
- [2] J. C. Maxwell, "On the dynamical theory of gases," *Philosophical Transactions of the Royal Society of London*, vol. 157, pp. 49–88, 1867.
- [3] A. Stimilli, A. Virgili, F. Canestrari, and H. U. Bahia, "Estimation of low-temperature performance of recycled asphalt mixtures through relaxation modulus analysis," *Cold Regions Science and Technology*, vol. 133, pp. 36–45, 2017.
- [4] Y. Wu, J. Shi, Q. Xiao et al., "1H-NMR relaxation and application study of evaporatable water in foamed asphalt," in *Proceedings of Geo-China International Conference*, pp. 163–171, Shandong, China, July 2016.
- [5] Q. Fu, Y. J. Xie, D. T. Niu et al., "Integrated experimental measurement and computational analysis of relaxation behavior of cement and asphalt mortar," *Construction & Building Materials*, vol. 120, pp. 137–146, 2016.
- [6] Y. Wang, Y. Xiao, C. Zheng et al., "Using two-component epoxy resin for asphalt pavement applications-part b: stiffness and relaxation electrical and control engineering & materials science and manufacturing," in *Proceedings of Joint Conferences of the 6th (ICECE2015) and the 4th (ICMSM2015)*, pp. 519–525, Shanghai, China, August 2016.
- [7] S. A. Forough, F. M. Nejad, and A. Khodaii, "Comparing various fitting models to construct the tensile relaxation modulus master curve of asphalt mixes," *Road Materials and Pavement Design*, vol. 7, p. 15, 2016.
- [8] I. L. Hopkins and R. W. Hamming, "On creep and relaxation," *Journal of Applied Physics*, vol. 28, no. 8, pp. 905–909, 1957.
- [9] B. Chen and J. Liu, "Experimental study on AE characteristics of three-point-bending concrete beams," *Cement & Concrete Research*, vol. 34, no. 3, pp. 391–397, 2004.
- [10] Y. Xiaoqing, "A damaging model of jointed rock under coupled action of freezing and thawing," *Chinese Journal of Rock Mechanics and Engineering*, vol. 8, pp. 1602–1611, 2015.
- [11] X. Fan and G. Xu, "Evaluation method of remaining fatigue life for crane based on the acquisition of the equivalent load spectrum by the artificial neural network," *Journal of Mechanical Engineering*, vol. 47, no. 20, pp. 69–74, 2011.
- [12] X. Ma, *ABAQUS6.11 Finite Element Analysis Step by Step*, Tsinghua University Press, Beijing, China, 2013.
- [13] M. Yang, *Development and Application of User-Defined Material Subroutine in ABAQUS Software*, Huazhong University of Science and Technology, Wuhan, China, 2005.
- [14] K. Fu, "The secondary development of modified burgers creep model based on ABAQUS general software," *Highway Engineering*, vol. 3, pp. 132–137, 2008.
- [15] Z. Chuanjiang, *Research on Creep Damage Properties and Constitutive Model for High Viso-Elastic Asphalt Mastic*, M.S. dissertation, Vol. 12, Shenyang Jianzhu Universtiy, Shenyang, China, 2014.
- [16] JTG E20-2011, *Standard Test Methods of Bitumen and Bituminous Mixtures for Highway Engineering*, Communications Press, Beijing, China, 2011.
- [17] T. Kunyun, *Research on the Deformation Characteristics and Gas Seepage Rule of Coal Body Loaded by High Pressure Water*, China University of Mining and Technology, Beijing, China, 2014.
- [18] L. F. Walubita, *Comparison of Fatigue Analysis Approaches for Predicting Fatigue Lives of Hot-Mix Asphalt Concrete (HMAC) Mixtures*, Ph.D. thesis, Texas A & M University, College Station, TX, USA, 2006.
- [19] L. Robert and G. U. Fan, "Characteristics of undamaged asphalt mixtures in tension and compression," *International Journal of Pavement Engineering*, vol. 19, no. 3, pp. 192–204, 2017.
- [20] H. Zhang, *Mechanism Analysis of the Differences of Asphalt Fatigue Damage Under Stress and Strain Control Mode*, Harbin Institute of Technology, Harbin, China, 2014.
- [21] F. Canestrari, A. Stimilli, H. U. Bahia, and A. Virgili, "Pseudo-variables method to calculate HMA relaxation modulus through low-temperature induced stress and strain," *Materials & Design*, vol. 76, pp. 141–149, 2015.
- [22] M. B. Boubaker, "Finite element simulation of the slumping process of a glass plate using 3D generalized viscoelastic Maxwell model," *Journal of Non-Crystalline Solids*, vol. 9, p. 14, 2014.
- [23] Y. N. Rabotnov, *Creep of Structural Elements*, Nauka, Moscow, Russia, 1996.

## Research Article

# A Study on Dynamic Amplification Factor and Structure Parameter of Bridge Deck Pavement Based on Bridge Deck Pavement Roughness

Fei Han <sup>1</sup>, Dan-hui Dan <sup>1</sup>, and Hu Wang<sup>2</sup>

<sup>1</sup>Department of Bridge Engineering, Tongji University, Shanghai 200092, China

<sup>2</sup>School of Science, Chang'an University, Xi'an, Shanxi 710064, China

Correspondence should be addressed to Fei Han; 674623368@qq.com

Received 6 November 2017; Revised 8 February 2018; Accepted 21 February 2018; Published 1 April 2018

Academic Editor: Yuqing Zhang

Copyright © 2018 Fei Han et al. This is an open access article distributed under the Creative Commons Attribution License, which permits unrestricted use, distribution, and reproduction in any medium, provided the original work is properly cited.

In order to study the coupled influence of deck pavement roughness and velocity on dynamic amplification factor, a 2-DOF 1/4 vehicle model is employed to establish the vehicle-bridge-coupled vibration system. The random dynamic load of running vehicle simulated by software MATLAB is applied on bridge deck pavement (BDP) through ANSYS software. Besides, the influence of BDP parameters on control stress under static load and random vibration load is analyzed. The results show that if the surface of BDP is smooth, the dynamic magnification coefficient would first increase and then decrease with increasing of vehicle velocity and reach its maximum value when  $v = 20$  m/s; if the surface of BDP is rough, the maximal and minimum values of the dynamic amplification coefficient (DAC) occur, respectively, when the velocity reaches 10 m/s and 15 m/s. For a composite bridge deck with the cushion layer, the thickness of asphalt pavement should be not too thick or thin and better to be controlled for about 10 cm; with the increasing of cushion layer thickness, the control stress of deck pavement is all decreased and show similar change regularity under effect of different loads. In view of self-weight of structure, the thickness of the cushion layer is recommended to be controlled for about 4 cm.

## 1. Introduction

The deck pavement of long-span bridges is usually susceptible to various destructions such as cracking, lamination, steel corrosion, and concrete degradation under vehicle loads. In the interaction of tire and bridge deck, the additional dynamic load will generate because of the roughness of BDPs. Therefore, the actual vehicle load applied on BDPs is of random load, the moving constant load cannot reflect the real dynamic behavior of BDPs. However, existing mechanical analysis of BDPs is concentrated on orthotropic plate pavement system under static vehicle load. Most literatures simplify the vehicle load as moving constant load when analyzing the dynamic behavior of BDPs, and the dynamic effect of vehicle load is considered using an empirical amplification factor.

Dynamic vehicle load will bring bridges a greater effect on structural stress and deformation compared with the static vehicle load, and this response amplification phenomenon of stress and deformation caused by vehicle dynamic load is

called the impact effect [1]. Dynamic load of vehicle consists of vehicle body weight and additional dynamic load caused by surface roughness of BDPs; the specific value of dead and additional load is defined as the dynamic amplification factor (DAF). In most existing studies, the vehicle-bridge-coupled vibration is taken into consideration ignoring the effect of BDPs [2–4]. DAFs play a vital role in the practice of bridge design and condition assessment. Accurate evaluation of DAFs will lead to safe and economical designs for new bridges and provide valuable information for condition assessment and management of existing bridges. However, the evaluation of a DAF is a rather complicated issue because of the sophisticated mechanism of the vehicle-bridge interaction (VBI) and a large number of parameters influencing DAFs, including the dynamic characteristics of both the bridge and the vehicle, road surface condition, and vehicle speed, where the road surface condition and vehicle speed are two critical index affecting DAFs significantly and have been widely investigated [5–9]. Though comprehensive studies of

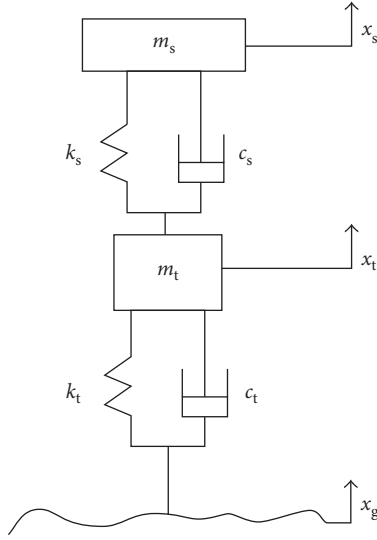


FIGURE 1: Single-wheel double-degree of freedom vehicle mode.

the DAF of highway bridges have been finished; due to the neglect of the influence of pavement layer, heavy maintenance cost of BDPs was paid during later maintenance and reinforce of the bridge. In China, BDPs were designed as an independent part isolated from the bridge girder, without considering the influence of deck pavement on structure [10]. However, BDPs are usually susceptible to cracking, lamination, steel corrosion, and concrete degradation, which accelerate the growth of damage; therefore, it is necessary to investigate the mechanical behavior of BDPs and analyze the effect of velocity and the roughness of BDPs on DAFs.

Existing researches have analyzed the dynamic response of BDPs under vehicle dynamic load considering road roughness and vehicle velocity [11], and the variation rule of vehicle load caused by structural parameters of bridge and vehicle speed has been investigated as well [12, 13]. However, the effect of DAFs caused by the design parameter of BDPs has not been studied considering the effect of road roughness. Besides, the investigation of the relation between the roughness and DAF has not been considered yet. Based on this, in this paper, the vehicle random dynamic load has been first simulated by MATLAB based on International Roughness Index (IRI) to analyze the variation law of DAF under the effect of BDP roughness and velocity. Then, the vehicle random dynamic load is applied on the finite element model of a typical bridge to investigate the relation between design parameters of BDPs and pavement stress state.

## 2. Dynamic Model of Vehicle Vibration

The most typical vehicle vibration model used for pavement mechanics analysis is the 2-DOF single-wheel vehicle model [14]. As shown in Figure 1, the total mass of bodywork, spring, and suspension is denoted by  $m_s$ ;  $m_t$  represents tire mass;  $c_s$  and  $k_s$  represent damping and stiffness of spring; and  $c_t$  and  $k_t$  represent the damping and stiffness of tires,

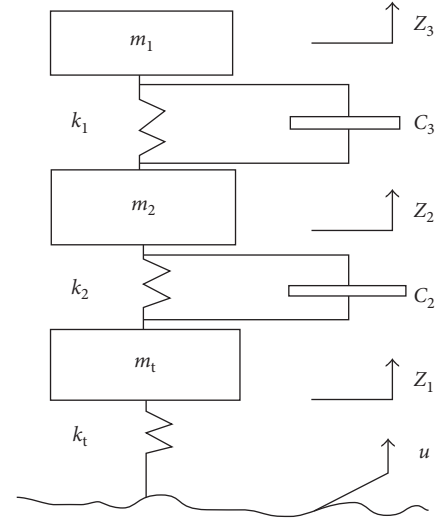


FIGURE 2: Three-mass vehicle mode.

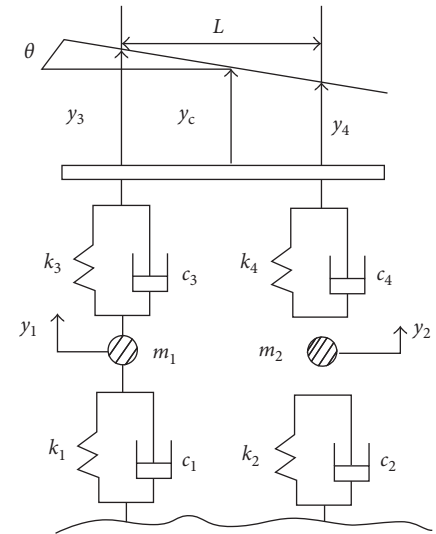


FIGURE 3: Four-degree of freedom vehicle model.

respectively. Other vehicle vibration models, such as 3-DOF single-wheel and 4-DOF vehicle vibration models, can be seen from Figures 2 and 3, respectively [15]. Though more complicated model such as biaxial 5-DOF and four-axle 10-DOF vibration models [16, 17] are raised by relevant study, 2-DOF single-wheel vehicle model is powerful and persuasive when simulating vehicle dynamic load [18]. Without loss of generality, the 2-DOF single-wheel vehicle model is employed here to analyze DAF. Vehicle system parameters of standard truck used in this paper can be seen from Table 1 [19].

According to the coordinate system shown in Figure 1, it is supposed that the vertically downward direction is positive, and the unknown displacement vector can be represented as  $U = [-x_s, -x_t]^T$ . Vehicle random dynamic load can be calculated by the following equation:

$$M\ddot{U} + C\dot{U} + KU = \bar{F}, \quad (1)$$

TABLE 1: Vehicle system parameters.

Parameter	Value
$m_s$ (kg)	9000
$m_t$ (kg)	1000
$k_s$ (N·m <sup>-1</sup> )	$480 \times 10^3$
$c_s$ (N·s·m <sup>-1</sup> )	$14 \times 10^3$
$k_t$ (N·m <sup>-1</sup> )	$1900 \times 10^3$
$c_t$ (N·s·m <sup>-1</sup> )	$3 \times 10^3$

where  $M$ ,  $U$ ,  $K$  are the mass matrix, damping matrix, and stiffness matrix of the vehicle model, respectively, and  $F$  is the vertical load of vehicle applied on the bridge deck. Bridges and vehicles are connected by the interaction of tire and deck pavements. The force vector  $F$  can be solved by the following equation:

$$F = k_i \Delta_i + c_i \dot{\Delta}_i, \quad (2)$$

where  $k_i$  and  $c_i$  the stiffness and damping of the  $i$ th tire and  $\Delta_i$  is the vertical contact displacement between the  $i$ th tire and pavement surface,

$$\Delta_i = u_i - (-r_i), \quad (3)$$

where  $u_i$  is the vertical displacement of the  $i$ th tire measured from the equilibrium position and  $r_i$  is the shape function of pavement roughness  $x_g$ .

### 3. Generation of Deck Pavement Roughness

Erratic fluctuation and pit caused by local damages of pavement are called pavement roughness, which is widely evaluated by International Roughness Index (IRI). According to Paterson's research, there are six different pavement roughness degrees, where the IRI of theoretical smooth longitudinal profile is 1; the IRI of moderate roughness is about 6, and the IRI of highly rough surfaces is 10 [20]. IRI is a dimensionless number which is customarily described by m/km. In China, deck pavement smoothness is often evaluated by the bump accumulated value BI or variance. Both of the two indexes have good linear correlation with IRI. To simulate a pavement roughness excitation, there are four existing simulated methods for the time-domain model: white noise filtration method, superposition of harmonic (namely, trigonometric series superposition method), AR (autoregression), and AMAR method based on the discrete time sequence and discrete sampling by PSD [21]. In this paper, superposition of the harmonic method is chosen because the algorithmic mechanism is clear, without too much consideration of the discretization degree of the model, and the resulting sample results are continuous. Denote that  $G_d(\omega)$  is the pavement surface power spectral density expressed in angular frequency, and  $x_g$  is the stochastic response of deck pavements, which can be expressed as follows:

$$x_g = \sum_{k=1}^M A_k \cos(\omega_k t + \phi_k), \quad (4)$$

where  $M$  is a positive integral and  $\phi_k$  is a random variable distributed in  $[0, 2\pi]$ . By substituting  $\omega = 2\pi\nu n$ , (4) can be converted to the frequency domain:

$$x_g = \sum_{k=1}^M \sqrt{3.26K_0 \Delta n} \frac{n_0}{n_k} \cos(2\pi\nu n_k t + \phi_k), \quad (5)$$

where  $\Delta n = (n_m - n_1)/M$ ,  $n_m = 2$ , and  $n_1 = 0.1$  and  $\nu$  is the velocity of vehicle. It will be more efficient to use fast Fourier transform (FFT) when simulation [22, 23]. Take  $M = 400$ ,  $n = 1$ ,  $\nu = 20$  m/s, when IRI = 2; the stochastic response of deck pavement  $x_g$  is simulated as shown in Figure 4.

After getting  $x_g$ , the dynamics differential equation of the 2-DOF vehicle vibration model in Figure 1 can be expressed as follows:

$$m_s \ddot{x}_s = -k_s (x_s - x_t) - c_s (\dot{x}_s - \dot{x}_t),$$

$$m_t \ddot{x}_t = k_s (x_s - x_t) + c_s (\dot{x}_s - \dot{x}_t) - k_t (x_t - x_g) - c_t (\dot{x}_t - \dot{x}_g), \quad (6)$$

where  $x_s$  and  $x_t$  are the vertical vibration displacement of suspension and tire, respectively, and  $x_g$  is the pavement surface roughness excitation displacement.  $F_t$  is the random load of vehicle applied on deck pavement,

$$F_t = F_d + G, \quad (7)$$

where  $F_d$  is the additional dynamic load of tire and  $G = (m_s + m_t)g$ , then

$$F_d = k_t (x_t - x_g) + c_t (\dot{x}_t - \dot{x}_g). \quad (8)$$

$F_d$  is shown in Figure 5, and the DAF  $\mu = F_d/G$ .

### 4. The Relationship between $\mu$ , $\nu$ , and IRI

To investigate the effect of  $\nu$  and IRI on  $\mu$ , let IRI be 0.5 (nearly absolutely smooth), 2 (smoothness is well), 4 (slightly rough), 6 (medium rough), 8 (highly rough), and 10 (very poor condition), the response curves of  $\mu$  for different IRIs when  $\nu$  varies from 5 m/s to 35 m/s are shown in Figure 6.

When IRI = 0.5, it can be seen from Figure 6(a) that with velocity increasing,  $\mu$  increases gradually at first and then decreases. When  $\nu = 20$  m/s,  $\mu$  reaches its maximum value and increases more than doubling compared to  $\nu = 5$  m/s. Therefore, if deck pavement is very well, the additional dynamic load of vehicle is not ever-increasing but diminishing when  $\nu > 20$  m/s with speedup; If IRI = 2, the variation curve of  $\mu$  increases rapidly at first from  $\nu = 5$  m/s to  $\nu = 10$  m/s and gets its peak value at  $\nu = 10$  m/s. Then with speedup,  $\mu$  began to decrease quickly till  $\nu = 15$  m/s, and as  $\nu$  exceeds 15 m/s, the curve increases as a whole. As IRI = 4, 6, 8, 10, respectively, we can see some common characteristics clearly from Figures 6(c) and 6(f) that there are two obvious summits and a trough of the line and the maximum will be achieved when  $\nu = 10$  m/s and minimum when  $\nu = 15$  m/s. These manners could be explained from the definition equation of additional dynamic load  $F_d$ , which is determined by the displacement  $x_g$  and its derivate  $\dot{x}_g$ . Because  $x_g$  and  $\dot{x}_g$  are the trigonometric functions of velocity  $\nu$  which can be seen from (5),  $\mu(\nu)$  must superposed by several trigonometric functions. All of these explains why  $\mu$  increases and decreases alternately with the variation of  $\nu$ . In fact, the DAF  $\mu$  fluctuates continuously as  $\nu$  changes.

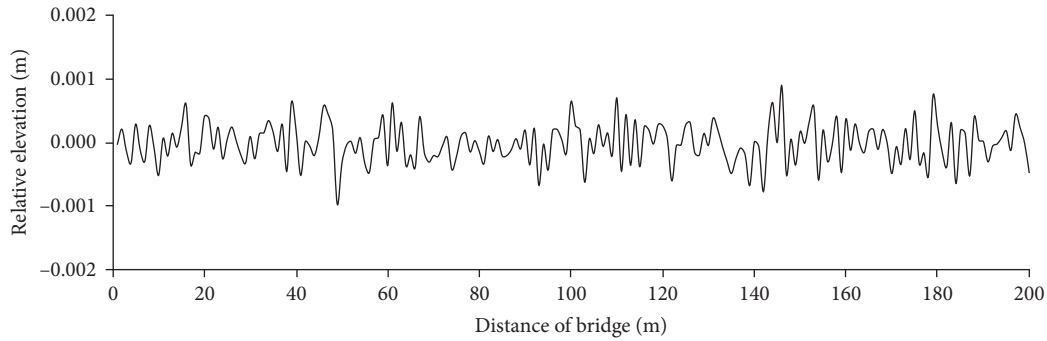


FIGURE 4: Pavement simulation with roughness when IRI = 2.

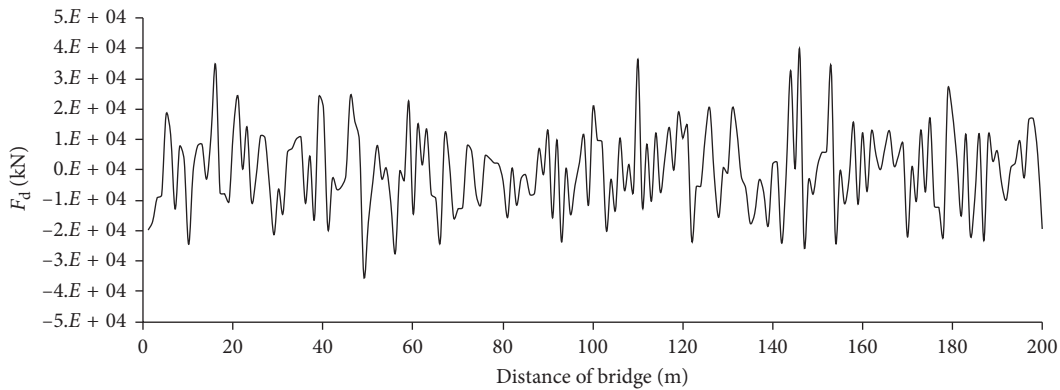


FIGURE 5: Additional dynamic load of vehicle when IRI = 2.

Based on analysis above, we can conclude that deck pavement roughness greatly affects the dynamic amplification factor, and under the same IRI, the response curve of  $\mu$  exists two obvious summits and a trough of the line and differs from that of ideal smooth pavement which first increases and then decreases. When a heavy vehicle running over the bridge whose smoothness is general or poor, the velocity should be better controlled at 15 m/s, and once the speed reaches 10 m/s or 25 m/s, the impact effect caused by vehicle vibration would significantly influence the driving comfortableness and service life of deck pavement.

If the velocity is constant and IRI is a variation, it can be seen from Figure 7 that when  $IRI < 4$ , the influence of  $v$  on  $\mu$  for different  $v$  is similar, while once  $IRI > 4$ , the character of response curves for different  $v$  differs significantly.

## 5. The Effect of Deck Pavement Structure on Pavement Stress

In existing researches, many literatures study the influence of deck pavement thickness on control stresses only under dead load or moving constant load of vehicle, regardless of the function of additional dynamic load caused by deck pavement roughness. In this section, the influence of different types of load on control stress response will be considered in order to further study the influence law of pavement structure on control stress.

**5.1. Thickness of Asphalt Pavement.** Taking a simple supported bridge with a span of 20 m and width of 12.6 m as an example, the section of the BDP is shown in Figure 8. Then, the response of control stresses under different load when asphalt layer thickness changes from 4 cm to 16 cm is investigated by software ANSYS. In this study,  $\sigma_z$  and  $\sigma_x$  represent the longitudinal and transverse tensile stress of asphalt pavement (AP), respectively;  $\sigma_1$  represents the first principle stress of the AP layer (tensile);  $\tau_{xy}$  represents the transverse shear stress in the contact surface between the AP and WP layers;  $\tau_{yz}$  represents the longitudinal shear stress in the contact surface between the AP and WP layers; and  $\sigma_y$  represents normal tensile stress in the contact surface. These six stresses are collectively referred to as the control stress of the BDP, while  $\tau_{xy}$ ,  $\tau_{yz}$ , and  $\sigma_y$  are interlayer contact stresses.

The four response curves in figures below, respectively, stand for vehicle dead load fixed in middle span (dead load), moving load without considering additional dynamic load caused by roughness (moving constant load), vehicle random dynamic load when  $IRI=4$  and  $v=10$  m/s ( $I=4$ ,  $v=10$ ), and vehicle random dynamic load when  $IRI=4$  and  $v=20$  m/s ( $I=4$ ,  $v=20$ ).

It can be seen from Figures 9–14 that (1) the response regularities of extreme values of  $\sigma_x$  and  $\sigma_1$  are similar, and both increase linearly with asphalt pavement thickness increasing. Furthermore, the response of random dynamic load is greater than that of dead load and moving constant load. The maximum value of stress response is the curve “ $I=4$ ,  $v=20$ ” and the response of dead load is no different

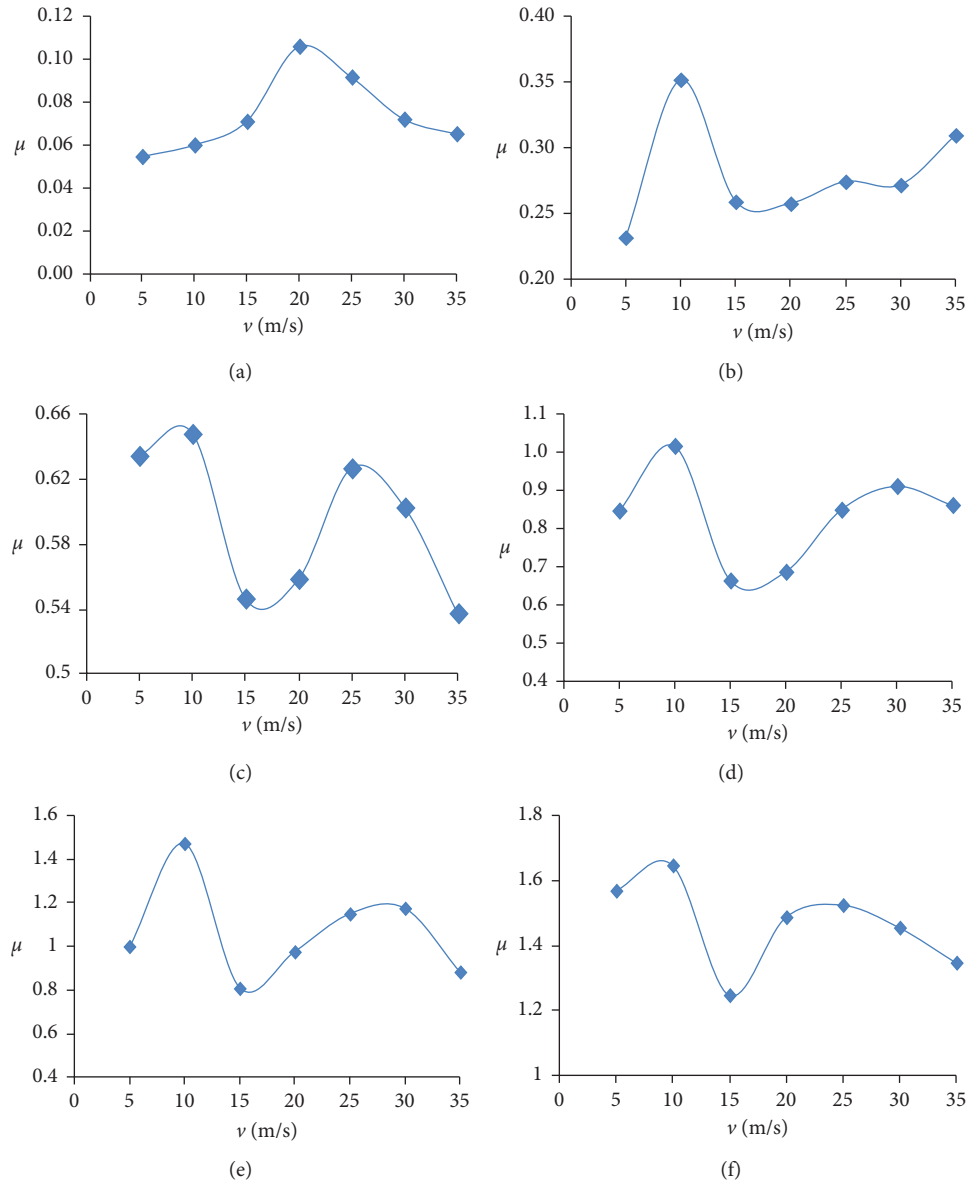


FIGURE 6: The relationship between  $v$  and  $\mu$ . (a) IRI=0.5, (b) IRI=2, (c) IRI=4, (d) IRI=6, (e) IRI=8, and (f) IRI=10.

than moving constant load; (2) the response curve of  $\tau_{xy}$  is escalating first and then descending. The maximum value will be achieved when the thickness is 6 cm. The effect of dead load and moving constant load on  $\tau_{xy}$  is similar and less than random dynamic load; (3) the extreme response of  $\sigma_y$  and  $\sigma_z$  is similar under different loads: descending rapidly with thickness increase and later escalating, the minimum value is achieved when thickness is 6 cm; (4) the variation regularity of the response curve of  $\tau_{yz}$  is relatively complicate, and the minimum value will be achieved when thickness is 10 cm.

Through comprehensive analysis we can conclude that if asphalt pavement is too thin, the extreme response of  $\sigma_y$  and  $\sigma_z$  would be too large; increase thickness properly will contribute to diminish the response, but asphalt layer should not be too thick because it will be bad for the response of  $\sigma_x$  and  $\sigma_1$ ; under the effect of stochastic dynamic load,  $\tau_{yz}$  and

$\tau_{xy}$  only reduce by 7.5% and 6.6%, respectively, when thickness increases from 10 cm to 16 cm. Besides, the increasing of thickness could not only augment the self-weight of the bridge but lead to unnecessary waste economically. So, for the composite deck pavement structure, the thickness of asphalt should be better controlled for about 10 cm.

**5.2. Design Principle.** Concrete cushion is paved above girder to protect and level the bridge deck. To analyze its effect on pavement stress, suppose that the thickness of the cushion layer changes within the range of 3 cm to 10 cm.

Through analysis we can find that overall increasing cushion thickness can help to decrease pavement stresses to some extent; the extreme responses of  $\sigma_y$ ,  $\sigma_x$  and  $\sigma_1$  all descend linearly under different loads while the stress response of dead load and moving constant load is less than

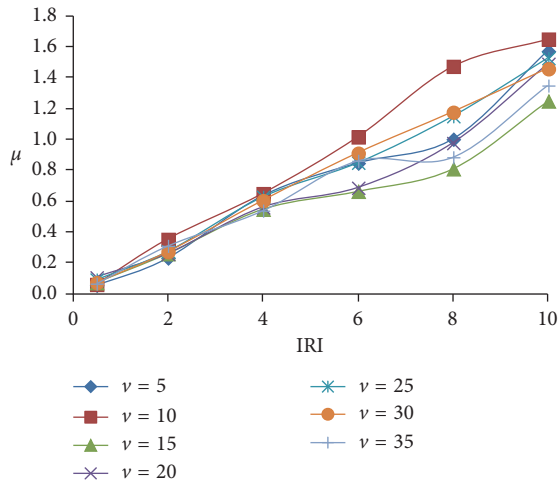


FIGURE 7: The relationship between IRI and  $\mu$ .

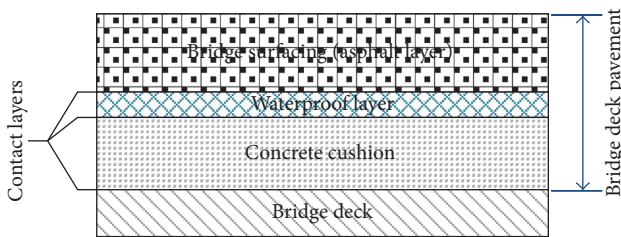


FIGURE 8: The section of bridge deck pavement.

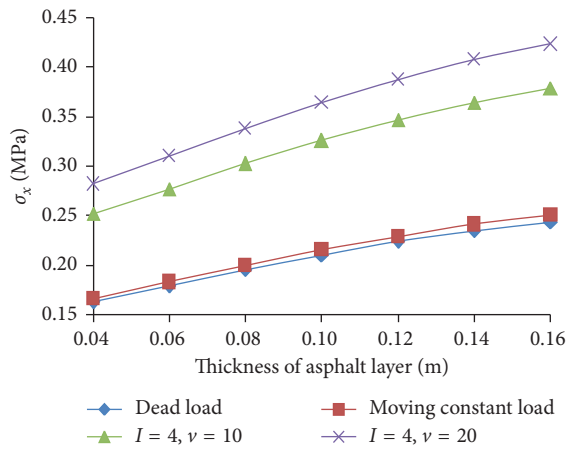


FIGURE 9: Response curve of  $\sigma_x$ .

the random dynamic load; response curves of  $\tau_{xy}$ ,  $\tau_{yz}$ , and  $\sigma_z$  are reducing greatly when cushion thickness increases from 3 cm to 4 cm and then descends slowly as thickness continues increasing. It follows that the response trend of each stress is relatively similar under action of different loads. The relative reduction of most stress extreme values is biggest when cushion thickness increases from 3 cm to 4 cm. Besides, allowing for the effect of self-weight of bridge caused by increasing cushion layer thickness, the thickness of the cushion layer should be better controlled for about 4 cm.

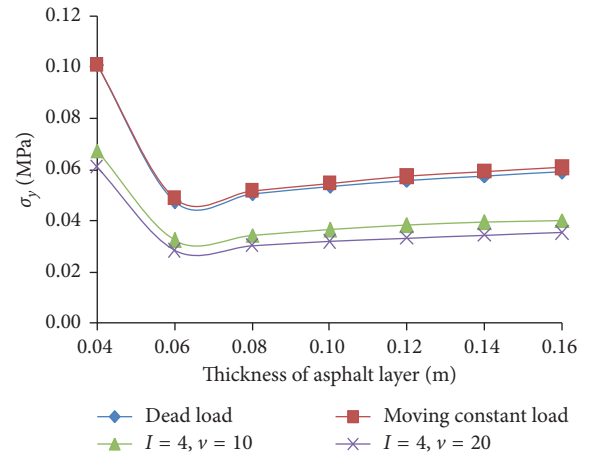


FIGURE 10: Response curve of  $\sigma_y$ .

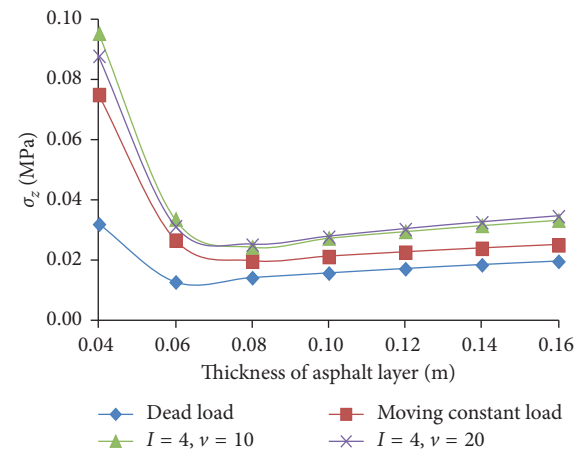


FIGURE 11: Response curve of  $\sigma_z$ .

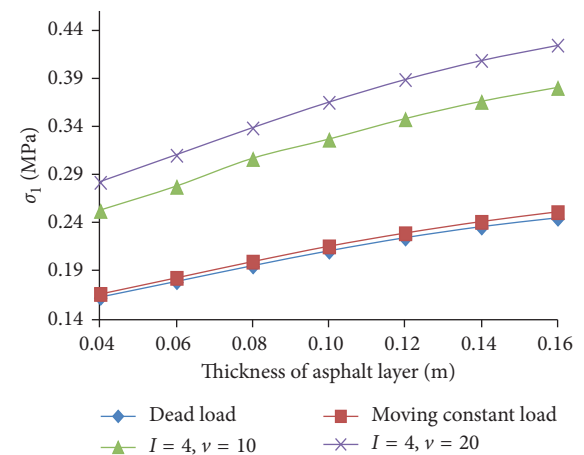
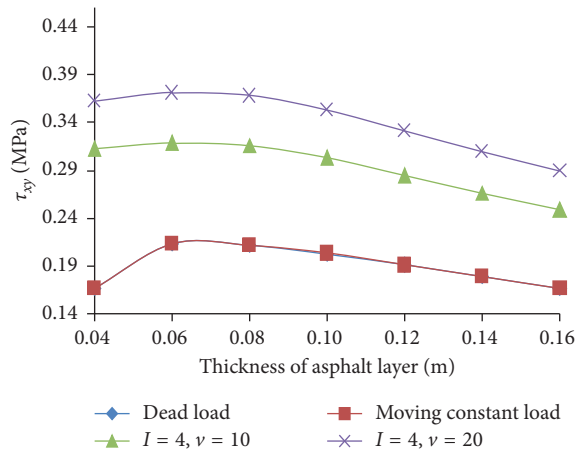
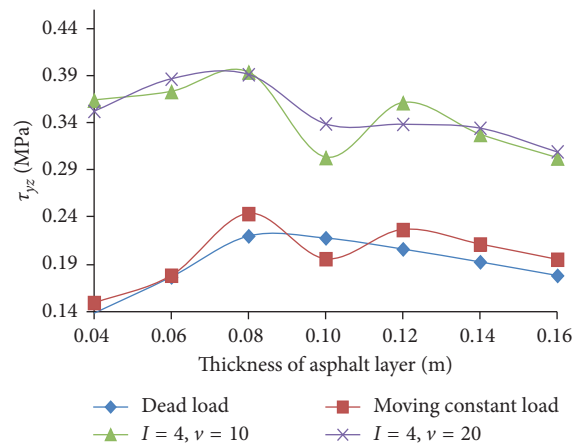


FIGURE 12: Response curve of  $\sigma_1$

5.3. Elastic Modulus of Deck Pavement Materials. The elastic modulus of common asphalt materials ranges from 1000 MPa to 2000 MPa; through analysis we can find that the extreme values of control stresses all increase in different degrees; the extreme response curves of  $\sigma_x$ ,  $\sigma_1$ ,  $\tau_{xy}$ , and  $\tau_{yz}$

FIGURE 13: Response curve of  $\tau_{xy}$ .FIGURE 14: Response curve of  $\tau_{yz}$ .

have similar variation trend, and the maximum response is caused by the random dynamic load; the relative variation of extreme values of each stress caused by increment of elastic modulus is very close.

Enhancing elastic modulus of the cushion layer can diminish pavement stress response to some extent, but the relative reduction of each stress is less than 2% for every 2 GPa, and the elastic modulus of cushion increases. It is because that the local effect on the deck pavement layer is obvious under vehicle loads, and the variation of elastic modulus of cushion can seldom improve the stress state of the upper layer.

## 6. Conclusion and Discussion

Existing researches of vehicle-bridge vibration only consider the interaction of vehicle and bridge and seldom take deck pavement into consideration. Meanwhile, the overloaded vehicles' additional dynamic load caused by pavement roughness degree is also neglected by designers during bridge's operating process. So, accurately analyzing the dynamic amplification factor caused by IRI and  $\nu$  is meaningful and necessary. In first part, this study investigated the relationship between  $\mu$  with IRI and  $\nu$ , while the second part

analyzed the influence of different types of load on control stress response and further studied the influence regularity of pavement structure on control stress so as to study the influence factor and change law of dynamic load deeply and to further guide the design of pavement structure safely and reliably. The main results are shown as follows:

- (1) The roughness of BDP greatly affects the dynamic amplification factor, and under the same IRI, the response curve of  $\mu$  exists between two obvious summits and a trough of the line and differs from that of ideal smooth pavement which first increases and then decreases. When a heavy vehicle running over the bridge whose smoothness is general or poor, the velocity should be better controlled at 15 m/s, and once the speed reaches 10 m/s or 25 m/s, the impact effect caused by vehicle vibration would significantly influence the driving comfortableness and service life of deck pavement
- (2) The increasing of thickness could not only augment the self-weight of bridge but lead to unnecessary waste economically. The thickness of asphalt should be better controlled about 10 cm.
- (3) Increasing cushion thickness can help to decrease pavement stresses to some extent, and allowing for the effect of self-weight of bridge caused by increasing the cushion layer thickness, the thickness of the cushion layer should be better controlled about 4 cm.
- (4) Enhancing elastic modulus of the cushion layer can diminish pavement stress response to some extent, but the relative reduction of each stress is less than 2% for every 2 GPa, and the elastic modulus of cushion increases. Thus, it is uneconomical to decrease pavement stress by using high-grade concrete cushion.

## Conflicts of Interest

The authors declare that they have no conflicts of interest.

## Acknowledgments

This work is supported by the State High-Tech Research and Development Plans (863) (Grant no. 2014AA110402); Shanghai Urban Construction Design Research Institute Project "Bridge Safe Operation Big Data Acquisition Technology and Structure Monitoring System Research"; the Ministry of Transport Construction Science and Technology Project "Medium-Small Span Bridge Structure Network Level Safety Monitoring and Evaluation"; and the Project of National Key Technology R&D Program in the 12th Five-Year Plan of China (Grant no. 2012BAJ11B01).

## References

- [1] Y. J. Zhou, J. Z. Cai, X. W. Shi, and Y. Zhao, "Computing method of bridge impact factor based on weighted method," *Journal of Traffic and Transportation Engineering*, vol. 13, no. 4, pp. 29–36, 2013.

- [2] X. F. Yin and Z. Fang, "Random vibration analysis of vehicle-pavement-bridge system under vehicle braking," *Chinese Journal of Computational Mechanics*, vol. 27, no. 5, pp. 936–941, 2010.
- [3] S. R. Chen and C. S. Cai, "Accident assessment of vehicles on long-span bridges in windy environments," *Journal of Wind Engineering and Industrial Aerodynamics*, vol. 92, no. 12, pp. 991–1024, 2004.
- [4] P. W. Hao, S. H. He, Y. Song et al., "Vehicle-bridge coupled vibration and its influencing factors of simple beam," *Journal of Chang'an University*, vol. 33, no. 1, pp. 59–66, 2013.
- [5] E. S. Hwang and A. S. Nowak, "Simulation of dynamic load for bridges," *Journal of Structural Engineering*, vol. 117, no. 5, pp. 1413–1434, 1991.
- [6] S. H. Ju and H. T. Lin, "A finite element model of vehicle-bridge interaction considering braking and acceleration," *Journal of Sound and Vibration*, vol. 303, no. 1-2, pp. 46–57, 2007.
- [7] L. Deng and C. S. Cai, "Development of dynamic impact factor for performance evaluation of existing multi-girder concrete bridges," *Engineering Structures*, vol. 32, no. 1, pp. 21–31, 2010.
- [8] C. C. Caprani, "Lifetime highway bridge traffic load effect from a combination of traffic states allowing for dynamic amplification," *Journal of Bridge Engineering*, vol. 18, no. 9, pp. 901–909, 2013.
- [9] L. Deng, Y. Yu, Q. Zou, and C. S. Cai, "State-of-the-art review of dynamic impact factors of highway bridges," *Journal of Bridge Engineering*, vol. 20, no. 5, p. 04014080, 2014.
- [10] CCCC Highway Consultants Co., Ltd., *JTG D60-2004 General Code for Design of Highway Bridges and Culverts*, China Communications Press, Beijing, China, 2004.
- [11] F. Han, H. Wang, and D.-H. Dan, "Dynamic response of a bridge deck pavement," *Proceedings of the Institution of Civil Engineers-Transport*, pp. 1–12, 2017.
- [12] X. Peng, X. F. Yin, and Z. Fang, "The coupled vibration analysis of elastically supported bridge with uneven surface and speed-varying vehicle," *Journal of Vibration and Shock*, vol. 26, no. 5, pp. 19–23, 2007.
- [13] X. Peng, X. F. Yin, and Z. Fang, "Vibration and TMD control of coupled system of girder bridge and vehicle with variable speeds," *Journal of Hunan University*, vol. 33, no. 5, pp. 61–66, 2006.
- [14] L. Sun and X. J. Deng, "Transient response of bridge to traveling random vehicle loads," *Journal of Vibration and Shock*, vol. 16, no. 1, pp. 142–145, 1997.
- [15] Y. Liu and Z. D. Qian, "Review of road roughness and vehicle vibration model," *Journal of Highway and Transportation Research and Development*, vol. 25, no. 1, pp. 51–57, 2008.
- [16] S. S. Law and X. Q. Zhu, "Dynamic behavior of damaged concrete structure under moving vehicle loads," *Engineering Structure*, vol. 24, no. 4, pp. 1279–1293, 2004.
- [17] H. L. Zhang and C. S. Hu, "A study on allowable differential slope of approach slab with five-degree-freedom vehicle model," *China Civil Engineering Journal*, vol. 38, no. 6, pp. 125–130, 2005.
- [18] L. Sun and T. Kennedy, "Spectral analysis and parametric study of stochastic pavement load," *Journal of Engineering Mechanics*, vol. 128, no. 3, pp. 318–327, 2002.
- [19] J. H. Li, J. He, and X. H. Li, "Dynamic response of pavement under vehicle random load and moving constant load," *Journal of Chang'an University*, vol. 35, no. 2, pp. 38–45, 2015.
- [20] W. D. Paterson and T. Watanatada, "Relationships between vehicle speed, ride quality, and road roughness," in *Measuring Road Roughness and its Effects on User Cost and Comfort*, T. D. Gillespie and M. Sayers, Eds., pp. 89–110, ASTM International, West Conshohocken, PA, USA, 1985.
- [21] Y. L. Zhang and Y. F. Zhong, "Time domain model of road undulation excitation to vehicles," *Transaction of the Chinese Society of Agricultural Machinery*, vol. 35, no. 2, pp. 9–12, 2004.
- [22] Y. Cheng and Y. K. Cheung, "Effects of random road surface roughness and long-term deflection of prestressed concrete girder and cable-stayed bridges on impact due to moving vehicles," *Computers and Mechanics*, vol. 79, pp. 853–872, 2001.
- [23] W. Schiehlen and B. Hu, "Spectral simulation and shock absorber identification," *International Journal of Non-Linear Mechanics*, vol. 38, no. 2, pp. 161–171, 2003.